arXiv:1402.2780v1 [physics.ins-det] 12 Feb 2014

Detector Optimization Studies and Light Higgs Decay into Muons at CLIC

Dissertation
zur
Erlangung des Doktorgrades (Dr. rer. nat.)
der
Mathematisch-Naturwissenschaftlichen Fakultät
der
Rheinischen Friedrich-Wilhelms-Universität Bonn

von
Christian Grefe
aus
Lüneburg

Bonn, 14.05.2012

Dieser Forschungsbericht wurde als Dissertation von der Mathematisch-Naturwissenschaftlichen Fakultät der Universität Bonn angenommen und ist auf dem Hochschulschriftenserver der ULB Bonn http://hss.ulb.uni-bonn.de/diss_online elektronisch publiziert.

Diese Dissertationsschrift wurde im Rahmen des Wolfgang-Gentner-Programms am europäischen Zentrum für Teilchenphysik CERN angefertigt. Betreuerin: Dr. Lucie Linssen.

1. Gutachter:	Prof. Dr. Klaus Desch
2. Gutachterin:	Prof. Dr. Ian Brock
Tag der Promotion:	05.10.2012
Erscheinungsjahr:	2013

Abstract

The Compact Linear Collider (CLIC) is a concept for a future e^+e^- linear collider with a center-of-mass energy of up to 3 TeV. The design of a CLIC experiment is driven by the requirements related to the physics goals, as well as by the experimental conditions. For example, the short time between two bunch crossings of 0.5 ns and the backgrounds due to beamstrahlung have direct impact on the design of a CLIC experiment. The Silicon Detector (SiD) is one of the concepts currently being discussed as a possible detector for the International Linear Collider (ILC). In this thesis we develop a modified version of the SiD simulation model for CLIC, taking into account the specific experimental conditions. In addition, we developed a software tool to investigate the impact of beam-related backgrounds on the detector by overlaying events from different simulated event samples. Moreover, we present full simulation studies, determining the performance of the calorimeter and tracking systems. We show that the track reconstruction in the all-silicon tracker of SiD is robust in the presence of the backgrounds at CLIC. Furthermore, we investigate tungsten as a dense absorber material for the hadronic calorimeter, which allows for the construction of a compact hadronic calorimeter that fulfills the requirements on the energy resolution and shower containment without a significant increase of the coil radius. Finally, the measurement of the decays of light Higgs bosons into two muons is studied in full simulation. We find that with an integrated luminosity of $2\,\text{ab}^{-1}$, corresponding to 4 years of data taking at CLIC, the respective Higgs branching ratio can be determined with a statistical uncertainty of approximately 15%.

Zusammenfassung

Der Compact Linear Collider (CLIC) ist ein Konzept für einen zukünftigen e^+e^--Linearbeschleuniger mit einer Schwerpunktsenergie von bis zu 3 TeV. Das Design eines CLIC-Experiments wird bestimmt durch die Anforderungen die sowohl aus den physikalischen Zielsetzungen als auch aus der experimentellen Umgebung herrühren. Zum Beispiel haben die kurze Zeit zwischen zwei Strahlkreuzungen von 0.5 ns und die Untergründe durch die Beamstrahlung direkte Auswirkungen auf den Aufbau eines CLIC-Experiments. Der Silicon Detector (SiD) ist eines der Detektorkonzepte, die momentan als mögliche Experimente für den International Linear Collider (ILC) diskutiert werden. In dieser Arbeit entwickeln wir eine modifizierte Version des SiD-Simulationsmodels, wobei die CLIC-spezifischen Anforderungen berücksichtigt werden. Außerdem haben wir ein Computerprogramm entwickelt, um die Effekte der strahlinduzierten Untergründe auf den Detektor zu untersuchen, indem simulierte Ereignisse aus verschiedenen Simulationen überlagert werden. Zudem stellen wir Simulationsstudien vor, in denen die Leistungsfähigkeit der Kalorimeter und der Spurdetektoren bestimmt werden. Wir zeigen, dass die Spurrekonstruktion in den in SiD vorgesehenen Siliziumspurdetektoren nicht durch die bei CLIC vorhandenen Untergründe beeinflusst wird. Des Weiteren untersuchen wir Wolfram als mögliches dichtes Absorbtionsmaterial für das hadronische Kalorimeter, was die Konstruktion eines kompakten hadronischen Kalorimeters erlaubt das sowohl die Anforderungen an die Energieauflösung als auch an die möglichst vollständige Absorbtion der Schauer erfüllt, ohne einen signifikant grösseren Spulenradius zu benötigen. Schließlich wird eine Simulationsstudie vorgestellt, in der Higgsbosonzerfälle in zwei Myonen gemessen werden. Mit einer gesammelten Luminosität von $2\,\text{ab}^{-1}$, was in etwa 4 Jahren Datennahme bei CLIC entspricht, kann das entsprechende Verzeigungsverhältnis mit einer statistischen Unsicherheit von ca. 15% bestimmt werden.

Acknowledgements

I would like to thank Prof. Dr. Klaus Desch for being my supervisor and thus giving me the possibility to write this thesis. I would also like to thank Dr. Lucie Linssen for the supervision at CERN during the past years, many useful discussions and especially for being very supportive at all times.

I would like to thank the CERN LCD group as a whole for making the last few years extremely enjoyable. I am especially thankful to Peter Speckmayer and Phillip Rohloff with whom I had the pleasure to share an office and who were always available to discuss problems. I would like to thank Dominik Dannheim for many discussions on the vertex detector and the beam-related backgrounds. In addition, I would like to thank Martin Killenberg for the discussions concerning the tracking. I am also indebted to Stephane Poss who provided endless support in fixing problems with the Grid and providing the WHIZARD files. I am thankful to André Sailer for giving useful tips concerning GEANT4 and providing many insights into the beam-related backgrounds. I would also like to thank Jan Strube for many discussions especially on the Higgs branching ratio analysis. I also would like to thank our secretary Kate Ross for helping with travel arrangements and other administrative tasks.

At SLAC I would like to thank Norman Graf and Jeremy McCormick, who helped me in many ways with the simulation and reconstruction software, as well as Richard Partridge who helped me understand the track reconstruction algorithm.

I am very grateful to those that helped improving this thesis by reading parts of it and providing many useful comments: Lucie Linssen, Dominik Dannheim, Dieter Schlatter, Phillip Bechtle and my brother Michael.

Finally, I would like to express my deep gratitude to my parents and my brother who are always there to support me.

I acknowledge the support by the Bundesministerium für Forschung und Bildung through a Wolfgang-Gentner-Stipendium.

Contents

1 Introduction **1**

2 Standard Model of Particle Physics **5**
2.1 Quantum Field Theory . . . 5
2.2 The Standard Model . . . 7
2.3 Beyond the Standard Model . . . 13

3 The Compact Linear Collider **17**
3.1 The CLIC Concept . . . 18

4 Detector Design for Collider Experiments **25**
4.1 Track Momentum and Impact Parameter Measurement . . . 25
4.2 Energy Measurement . . . 29
4.3 Detector Requirements for a CLIC Experiment . . . 33
4.4 The Particle Flow Paradigm . . . 34

5 The CLIC_SiD Detector Model **37**
5.1 Tracking System . . . 39
5.2 Calorimeters . . . 45
5.3 Solenoid and Magnetic Field . . . 47
5.4 Instrumented Yoke . . . 47
5.5 Forward Region and Beam Pipe . . . 48
5.6 Occupancies from Beam-Related-Backgrounds . . . 49
5.7 Summary . . . 55

6 Simulating High Energy Collisions and Detector Response **57**
6.1 Event Generation . . . 57
6.2 Detector Simulation . . . 58
6.3 Event Digitization and Reconstruction . . . 60

7 Tracking Performance in CLIC_SiD **73**
7.1 Track Resolution . . . 73
7.2 Jet Event Samples . . . 76
7.3 Tracking Efficiency and Fake Rate Definition . . . 78
7.4 Strategy Optimization . . . 81
7.5 Performance in Jet Events . . . 81

7.6 Summary . . . 85

8 HCal Layout Optimization **87**
8.1 Calorimeter Models . . . 87
8.2 Event Samples . . . 89
8.3 Energy Reconstruction with a Neural Network. . . . 89
8.4 Energy Resolution and Linearity . . . 91
8.5 Energy Resolution Depending on HCal Depth . . . 93
8.6 Impact of a Tail Catcher on the Energy Resolution . . . 93
8.7 Summary . . . 95

9 Calorimeter Performance in CLIC_SiD **97**
9.1 Calorimeter Calibration Procedure . . . 97
9.2 Single Particle Response . . . 98
9.3 Jet Response . . . 101
9.4 Summary . . . 104

10 Measurement of Light Higgs Decay into Muons **105**
10.1 Event Samples . . . 105
10.2 Event Selection . . . 108
10.3 Invariant Mass Fit . . . 111
10.4 Impact of Beam-Induced Background . . . 117
10.5 Impact of the Momentum Resolution . . . 120
10.6 Impact of Forward Electron Tagging . . . 122
10.7 Extracting the Higgs Coupling . . . 127
10.8 Measurement Potential at other Accelerators . . . 129
10.9 Summary . . . 130

11 Conclusion and Outlook **133**

A Units, Conventions and Notations **137**
A.1 Units . . . 137
A.2 Conventions . . . 137
A.3 Detector Coordinate Systems . . . 138

B RMS and RMS_{90} **141**

C Track Parametrization **143**
C.1 Converting Track Parameters . . . 144
C.2 Track Parameter Uncertainties . . . 144
C.3 Propagation of Track Parameter Uncertainties . . . 145

D Tracking Efficiency in Top Pair Production **147**

List of Acronyms **149**

Bibliography **153**

List of Figures **165**

List of Tables 169

CHAPTER 1

Introduction

The Standard Model (SM) of particle physics was formulated almost half a century ago [1–10]. Since then it has emerged as one of the most successful theories in modern physics. Not only did it successfully predict the existence of the heavier quarks and the massive gauge bosons of the electroweak interaction, it also succeeded in explaining all of the precision measurements of the interactions of fundamental particles performed in many collider experiments. Nevertheless, the SM is still incomplete, since it predicts the existence of a massive scalar boson—the Higgs boson—that is required to explain electroweak symmetry breaking and thus the masses of the W and Z bosons. In addition, the existence of this boson could also explain the observation of massive fermions, which would otherwise contradict the theory.

The search for the Higgs boson is one of the main tasks of the ATLAS and CMS experiments operated at the Large Hadron Collider (LHC) at CERN. With the LHC performing above expectations there is good hope to be able to proof or falsify the existence of the Higgs boson by the end of this year, at least if its interactions are as predicted by the SM. Nevertheless, this will not be the end of the journey. On one hand, if the Higgs is not found, this will require an alternative explanation of electroweak symmetry breaking. On the other hand, even if the Higgs boson is found, its true nature will still remain unclear for quite some time. All the predicted parameters of the Higgs boson including its couplings to the other particles in the SM will have to be tested.

Besides the elusive Higgs boson there are many other open questions in High Energy Physics (HEP). In the past decades, several theoretical limitations of the SM have motivated a wide range of models that extend the current theory and might lead to a deeper understanding of nature (see [11] for an overview). One direct motivation for extending the SM comes from cosmological observations. While the now established Big Bang theory (see [12] for an introduction) is another example of the success of the SM, since it consistently explains the cosmic microwave background [13, 14] and the primordial abundances of the different chemical elements in the universe [15, 16], it also leads to questions that cannot be answered directly. The apparent asymmetry in the amount of matter and anti-matter in the universe is one of the observations that cannot be explained by the SM. Another problem is the observation that the largest fraction of the matter in the universe exists in the form of dark matter [17]. This would require the existence of particles with properties that do not correspond to any particle in the SM. Some of the possible extensions of the SM introduce new particles that could well form an explanation for the dark matter in the universe. Depending on the concrete model these new particles could be in the energy range accessible to the LHC and the next generation of particle colliders.

There is broad agreement in the HEP community that the next collider at the energy frontier should be an e^+e^- linear collider with a center-of-mass energy between several hundreds of GeV and a few TeV. A lepton collider will complement the measurements at the LHC by allowing precise measurements of the properties of those particles that may be discovered in the coming years. In addition, a lepton collider would extend the discovery potential of the LHC for several hypothetical models, especially for electroweak states. One concept of a future linear collider that is currently being discussed is the International Linear Collider (ILC) [18] with a center-of-mass energy of up to 1 TeV. Another possible future linear collider is the Compact Linear Collider (CLIC). The present thesis focuses on this linear collider, with a center-of-mass energy of up to 3 TeV. The CLIC accelerator concept foresees normal conducting cavities with field gradients of approximately 100 MV/m to limit its total length to less than 50 km. The Radio Frequency (RF) power for accelerating the particles in the main beam is generated by a second particle beam—the drive beam—whose particles are decelerated in this process. This allows for almost lossless distribution of the power along the accelerator and is more efficient than the generation of RF power using klystrons. These and other aspects of the CLIC accelerator scheme are studied at the CLIC test facility 3 (CTF3) [19] and its predecessors. The feasibility of most technological challenges have been demonstrated and the current status will be reported in the accelerator volume of the CLIC Conceptual Design Report (CDR), which will be published in the coming months [20].

Two detector concepts, the International Large Detector (ILD) [21] and the Silicon Detector (SiD) [22] concepts, have been developed as possible experiments at the ILC. They are based on the particle flow paradigm. Since the requirements on the basic observables are very similar for an experiment at CLIC, these two detector concepts have been chosen as a starting point for developing a possible detector for CLIC. The main differences between the ILC and CLIC from a detector point of view are the available center-of-mass energy, leading to more energetic particles and jets at CLIC, the amount of beam-related backgrounds, mostly due to beamstrahlung, as well as the much shorter time between two bunch crossings at CLIC. In combination, the latter two differences result in higher occupancies in the subdetectors at CLIC, which have to be taken into account when designing the experiment. The physics and detector volume of the CLIC CDR, discussing the physics potential of CLIC and the performance of the two modified detector concepts CLIC_ILD and CLIC_SiD, has been published recently [23]. Some of the simulation studies of the CLIC_SiD concept that contributed to the CDR are presented in detail in this thesis.

This thesis is structured as follows. In Chapter 2 we give a brief overview of the SM and the Higgs mechanism, the limitations of the SM, as well as examples of possible extensions and their implications for the Higgs sector. Afterwards we give an introduction to the CLIC accelerator concept in Chapter 3 where we also discuss the beam-related backgrounds and their implications for an experiment. In Chapter 4 we recapitulate the basic principles of momentum and energy measurements in HEP experiments and discuss the design goals for an experiment at CLIC. Chapter 5 gives an overview of the SiD concept as proposed for CLIC, including a description of the simulation model CLIC_SiD, which is used for the studies presented in this thesis as well as those presented in the CLIC CDR. The simulation and reconstruction of collisions at CLIC are discussed in Chapter 6, including a detailed introduction to the concept of overlaying events to realistically simulate the effect of beam-related backgrounds, as well as the track reconstruction algorithm used later in the thesis. The performance of the all-silicon tracking detectors in CLIC_SiD is investigated in Chapter 7, taking into account the most important beam-related background. The basic performance is studied in simulated single muon events and the efficiency and fake rate are studied in simulated di-jet events. In Chapter 8 we show a systematic optimization study for the Hadronic Calorimeter (HCal) layout, comparing the performances of sampling calorimeters using steel and tungsten absorber plates. A performance study of the energy reconstruction in the calorimeter systems in CLIC_SiD is presented in Chapter 9. In addition to the studies of the fundamental observ-

ables, a set of detector benchmark analyses has been defined for CLIC at $\sqrt{s} = 3$ TeV [24], where each of the processes is especially demanding in one or more of the basic observables. This allows to study the simulated detector performance in the context of a realistic analysis. One of these benchmark analyses, the simulation of the measurement of the Higgs branching ratio into two muons for a light SM Higgs, is presented in Chapter 10. This measurement requires excellent momentum resolution, good muon identification and efficient electron tagging also in the forward region to reject SM backgrounds. Finally, the results of this thesis are summarized in Chapter 11.

Some supplementary information is given in the appendices. Appendix A defines the units and conventions used throughout this thesis. The RMS_{90}, an alternative measure of the spread of a distribution, is introduced in Appendix B. The track parametrization used in the tracking studies is described in Appendix C together with a derivation of the uncertainties of several physical quantities from the uncertainties of the track fit. Appendix D shows the tracking performance in simulated $\mathrm{t\bar{t}}$ events, which is a different event topology compared to the di-jet events studied in Chapter 7.

We have implemented the CLIC_SiD detector model as a modification of an existing simulation model of SiD, providing all necessary calibration files. The calculation of the total material budget in the tracking detectors was done by Astrid Münnich. A detailed description of this simulation model has been published in [25].

The software tool to overlay background events, which is essential for a realistic simulation of collisions at CLIC, has been developed in collaboration with Peter Schade who implemented the corresponding software tool in the ILD reconstruction framework. Its functionality has been documented in [26].

The results from the study of the tracking performance have been partially published in [23]. The optimization study of the HCal layout has been performed in collaboration with Peter Speckmayer and the results have already been published in [27].

The simulation study of the Higgs branching ratio into two muons has already been published in [28]. In addition, some of the results of the Higgs study have been published in [23, 29].

CHAPTER 2

Standard Model of Particle Physics

The interactions of fundamental particles can be described in the framework of relativistic quantum field theory by the Standard Model of particle physics, which combines the observed strong and electroweak interactions. The SM is a gauge invariant quantum field theory based on the $SU(3)_C \times SU(2)_L \times U(1)_Y$ gauge symmetry group, where $SU(3)_C$ is the color group describing the strong interaction and $SU(2)_L \times U(1)_Y$ describes the electroweak interaction which is spontaneously broken by the Higgs mechanism.

Many detailed discussions of quantum field theory and the SM can be found in the literature, e.g. [30, 31]. We want to briefly recapitulate some of these basic principles to motivate the interest in the Higgs sector of the SM. Section 2.1 illustrates the concept of gauge theories in the example of Quantum Electrodynamics (QED). The particles and interactions in the SM are introduced in Section 2.2 together with the Higgs mechanism, which is required to explain the observation of massive vector bosons. Section 2.3 highlights some of the shortcomings of the SM and discusses possible extensions of it.

The notations and conventions used here are defined in Appendix A. We follow the ideas presented in [31, 32].

2.1 Quantum Field Theory

In Quantum Field Theory (QFT) particles are described by fields, which act as the creation and annihilation operators of the respective particles. The field theory approach intrinsically allows the description of multi-particle interactions and also guarantees causality, which is not the case in a particle quantization. The dynamics of a system that consists of the set of fields Φ is usually described in the Lagrangian formalism, which is invariant under Lorentz transformations. The classical Lagrangian density L, usually just referred to as the Lagrangian, depends on the discrete coordinates q_i and the velocities $\dot{q}_i$, which have to be replaced by the continuous fields $\Phi(x)$ and their derivatives $\partial_\mu \Phi(x)$, respectively. The action is then given by the space-time integral of the field theoretical Lagrangian $\mathcal{L}$:

$$S(\Phi) = \int \mathcal{L}\Big(\Phi(x), \partial_\mu \Phi(x)\Big)\, \mathrm{d}^4 x. \tag{2.1}$$

The equations of motion follow from Hamilton's principle, $\delta S = 0$, and are given by the Euler-Lagrange equations

$$\partial_\mu \frac{\partial \mathcal{L}}{\partial(\partial_\mu \Phi)} - \frac{\partial \mathcal{L}}{\partial \Phi} = 0. \tag{2.2}$$

The SM contains three types of fields, spin-0 particles described by scalar fields $\phi(x)$, spin-1 particles described by vector fields $A_\mu(x)$ and spin-$\frac{1}{2}$ particles described by 4-component spinor fields $\psi(x)$.

The dynamics of a free scalar field $\phi(x)$ with the mass m is described by

$$\mathcal{L} = \frac{1}{2}(\partial_\mu\phi)^2 - \frac{m^2}{2}\phi^2. \tag{2.3}$$

The corresponding equation of motion is the Klein-Gordon equation

$$(\partial^\mu\partial_\mu + m)^2\phi = 0. \tag{2.4}$$

Its solutions are linear combinations of plane waves of the form $e^{\pm ikx}$.

The Lagrangian of a free vector field $A_\mu(x)$ is given by

$$\mathcal{L} = -\frac{1}{4}F_{\mu\nu}F^{\mu\nu} - \frac{m}{2}A_\mu A^\mu, \tag{2.5}$$

where $F_{\mu\nu}$ is the field strength tensor $F_{\mu\nu} = \partial_\mu A_\nu - \partial_\nu A_\mu$. The resulting field equation is the Proca equation

$$\left[\left(\partial^\mu\partial_\mu + m^2\right)g^{\mu\nu} - \partial^\mu\partial^\nu\right]A_\nu = 0, \tag{2.6}$$

which can be solved by linear combinations of planar waves, spanned by three linearly independent polarization vectors.

Fermions with a spin of $\frac{1}{2}$ are described by a 4-component spinor field $\psi(x)$. The dynamics of a free spinor field is described by the Dirac Lagrangian

$$\mathcal{L} = \overline{\psi}\left(i\gamma^\mu\partial_\mu - m\right)\psi, \tag{2.7}$$

where m is the fermion mass and $\overline{\psi}$ is the adjoint spinor with $\overline{\psi} = \psi^\dagger\gamma^0$. The corresponding equation of motion is the Dirac equation

$$\left(i\gamma^\mu\partial_\mu - m\right)\psi = 0, \tag{2.8}$$

which has two solutions of the form $u(p)e^{-ipx}$ and $v(p)e^{ipx}$, corresponding to the particle and anti-particle wave functions.

The interaction of fermions and vector fields can be derived by requiring that the theory is invariant under a certain group of gauge transformations. In QED we assume that the Dirac Lagrangian is invariant under global phase transformations, $\psi \to \psi' = e^{i\alpha}\psi$, where α is real. We can even assume the invariance under local phase transformations $\alpha(x)$, $\psi \to \psi' = e^{i\alpha(x)}\psi$, which define the abelian group of unitary transformations $U(1)$. This requires the presence of a vector field A_μ which has to transform as $A_\mu(x) \to A'_\mu(x) = A_\mu(x) + \frac{1}{e}\partial_\mu\alpha(x)$ in order to preserve invariance of the Lagrangian under this transformation, since the derivative in Eq. (2.7) has to be replaced by the covariant derivative $D_\mu = \partial_\mu - ieA_\mu$. The Lagrangian then reads

$$\mathcal{L} = \overline{\psi}\left(i\gamma^\mu\partial_\mu - m\right)\psi + e\overline{\psi}\gamma^\mu\psi A_\mu. \tag{2.9}$$

If we identify A_μ as the photon field and $j^\mu = e\overline{\psi}\gamma^\mu\psi$ as the electromagnetic current with the coupling e, the electron charge, this Lagrangian describes the interaction of electron and positron fields with photon fields. The kinetic term of the photon field $-\frac{1}{4}F_{\mu\nu}F^{\mu\nu}$ has to be added according to Eq. (2.5) in order

to obtain the full Lagrangian of QED. The mass term in Eq. (2.5) can be omitted since the photon is massless.

The concept of invariance under certain gauge transformations can be applied similarly to non-abelian symmetries by replacing the derivative in Eq. (2.7) by the covariant derivative and introducing several vector fields. The number of vector fields introduced is given by the number of generators of the symmetry group. Similarly to the case of QED the kinetic terms of the vector fields have to be added. The vector fields in such a theory are necessarily massless since the mass terms are not invariant under non-abelian gauge transformations. The non-abelian nature also introduces self-couplings of the vector fields through the gauge transformations, which are not present in QED. These vector fields are thus carriers of their respective charge.

2.2 The Standard Model

As mentioned above, the SM is described by the symmetry group $SU(3)_C \times SU(2)_L \times U(1)_Y$. Quantum Chromodynamics (QCD) [7–10] describes the strong interaction. It is a gauge theory invariant under local gauge transformations in the three dimensional color space, described by the color group $SU(3)_C$. The $SU(3)$ group has 8 generators which can be described by the Gell-Mann matrices, resulting in the introduction of 8 vector fields, the gluons. In the SM, only the quarks are affected by the strong interaction. They are described by a color triplet of fermion fields that transform under color transformations. The other fermions are color singlets and are not affected by the strong interaction.

The electroweak interactions [1–3] are described by the symmetry group $SU(2)_L \times U(1)_Y$. The generators of this group are the three isospin operators $I_{1,2,3}$ and the hypercharge Y. These result in 4 vector fields, the triplet $W_\mu^{1,2,3}$ and the singlet B_μ. The electric charge Q is connected to the isospin and the hypercharge by the relation

$$Q = I_3 + \frac{Y}{2}. \tag{2.10}$$

Transformation of fermions under $SU(2)$ in the SM depend on the chirality of the fermion field. One distinguishes between left-handed fermions $\psi_\mathrm{L} = \frac{1-\gamma_5}{2}\psi$ and right-handed fermions $\psi_\mathrm{R} = \frac{1+\gamma_5}{2}\psi$. Only the left-handed fermions (or right-handed anti-fermions), which carry an isospin of $I = \frac{1}{2}$, are affected by $SU(2)$ transformations and form isospin doublets. The right-handed fermions are isospin singlets and have an isospin of $I = 0$. In the SM this is realized by having two different covariant derivatives for the two chiral projections, i.e. the derivative for the other projection is 0. It should be noted that only for the case of massless fermions the left-handed and right-handed projections of Eq. (2.7) are decoupled and can be written independently. This means that massive fermions would violate gauge invariance under these $SU(2)$ transformations, which can be solved by the Higgs mechanism introduced below.

An overview of the fermions in the SM is given Table 2.1 together with their quantum numbers I_3, Y and Q. In general there could be more generations of particles, although they must be significantly heavier than the first three generations since they have not been observed yet. The strongest constraint on the existence of a fourth generation neutrino comes from the measurement of the Z boson decay width at the Large Electron-Positron Collider (LEP), which is only compatible with three neutrino generations [33]. That means that a fourth generation neutrino, if it exists, has to have at least half the Z boson mass, such that it could not be produced at LEP. This would be in strong contrast to the other three neutrinos which are assumed to be massless in the basic SM, or are at least of very small mass as discussed in Section 2.3.1.

Table 2.1: Fermions in the Standard Model. Given is the isospin I_3, the hypercharge Y and the electrical charge Q. The anti-particles are the charge conjugates of the fermions and are not listed in the table. The quark fields are color triplets, while the lepton fields are color singlets.

	Generation					
	I	II	III	I_3	Y	Q
Leptons	$\begin{pmatrix}\nu_e\\ e\end{pmatrix}_L$	$\begin{pmatrix}\nu_\mu\\ \mu\end{pmatrix}_L$	$\begin{pmatrix}\nu_\tau\\ \tau\end{pmatrix}_L$	$+1/2$ $-1/2$	-1 -1	0 -1
	e_R	μ_R	τ_R	0	-2	-1
Quarks	$\begin{pmatrix}u\\ d\end{pmatrix}_L$	$\begin{pmatrix}c\\ s\end{pmatrix}_L$	$\begin{pmatrix}t\\ b\end{pmatrix}_L$	$+1/2$ $-1/2$	$+1/3$ $+1/3$	$+2/3$ $-1/3$
	u_R	c_R	t_R	0	$+4/3$	$+2/3$
	d_R	s_R	b_R	0	$-2/3$	$-1/3$

2.2.1 The Higgs Mechanism

As mentioned in Section 2.1, vector fields in non-abelian gauge theories are necessarily massless. This contradicts the observations of the massive gauge bosons $W^{\pm}$ and Z of the weak interaction. Massive vector fields can be introduced in the theory by spontaneously breaking the $SU(2)_L \times U(1)_Y$ symmetry with the Higgs mechanism [4–6], while leaving the electromagnetic subgroup $U(1)_{em}$ unbroken.

We introduce a new isospin doublet of two complex scalar fields with an isospin of $\frac{1}{2}$ and a hypercharge of $Y = 1$

$$\phi(x) = \begin{pmatrix}\phi^+\\ \phi^0\end{pmatrix}, \tag{2.11}$$

where + and 0 denote the electrical charge. This adds another term to the Lagrangian:

$$\mathcal{L}_H = \left(D_\mu\phi\right)^\dagger \left(D^\mu\phi\right) - V(\phi), \tag{2.12}$$

where the interaction with the gauge fields enters through the covariant derivative $D_\mu = \partial_\mu - ig_2\frac{\sigma_a}{2}W_\mu^a + i\frac{g_1}{2}B_\mu$, with the two couplings of the isospin and the hypercharge $g_{1,2}$ and the Pauli matrices σ_a. The self-interaction is described by the potential $V(\phi)$. The Higgs potential is postulated as

$$V(\phi) = -\mu^2\phi^\dagger\phi + \frac{\lambda}{4}\left(\phi^\dagger\phi\right)^2, \tag{2.13}$$

where μ^2 and λ are constants. If μ^2 and λ are positive, the minimum of this potential is not found for the vacuum state $\phi = 0$. Instead, the minimum of $V(\phi)$ is reached when $\phi^\dagger\phi = \frac{2\mu^2}{\lambda}$. The Higgs doublet $\phi(x)$ has four degrees of freedom since it is complex. We chose a gauge transformation where the charged component vanishes and only the neutral component is left, referred to as the unitary gauge. The resulting vacuum expectation value of the Higgs doublet is then

$$< \phi_0 >= \frac{1}{\sqrt{2}}\begin{pmatrix}0\\ v\end{pmatrix}, \tag{2.14}$$

with $v = \frac{2\mu}{\sqrt{\lambda}}$. Expanding the field in the real component around the vacuum state yields

$$\phi(x) = \frac{1}{\sqrt{2}} \begin{pmatrix} 0 \\ v + H(x) \end{pmatrix}, \tag{2.15}$$

where $H(x)$ is a real scalar field. The imaginary component is unphysical since it can be eliminated by a suitable gauge transformation. Using this representation of the Higgs doublet, the Higgs potential in Eq. (2.13) is given by

$$V = \mu^2 H^2 + \frac{\mu^2}{v} H^3 + \frac{\mu^2}{4v^2} H^4. \tag{2.16}$$

The Higgs field $H(x)$ is thus a massive scalar field with a mass of $m_H = \mu\sqrt{2}$ and with triple and quartic self-couplings that are both proportional to m_H^2.

Using this representation of the Higgs doublet in the kinetic term of Eq. (2.12) results in mass terms for the four vector bosons of the standard model, as well as triple and quartic couplings of the H field with the vector fields. The mass terms are given by

$$\frac{1}{2}\left(\frac{g_2 v}{2}\right)^2 \left((W_1)^2 + (W_2)^2\right) + \frac{1}{2}\left(\frac{v}{2}\right)^2 \left(W_\mu^3, B_\mu\right) \begin{pmatrix} g_2^2 & g_1 g_2 \\ g_1 g_2 & g_1^2 \end{pmatrix} \begin{pmatrix} W^{3\mu} \\ B^\mu \end{pmatrix}. \tag{2.17}$$

The vector fields can be transformed into a basis that corresponds to the physical observed fields using

$$\mathrm{W}_\mu^\pm = \frac{1}{\sqrt{2}} \left(W_\mu^1 \mp W_\mu^2\right) \tag{2.18}$$

and

$$\begin{pmatrix} \mathrm{Z}_\mu \\ A_\mu \end{pmatrix} = \begin{pmatrix} \cos\theta_w & \sin\theta_w \\ -\sin\theta_w & \cos\theta_w \end{pmatrix} \begin{pmatrix} W_3^\mu \\ B_\mu \end{pmatrix}, \tag{2.19}$$

with the weak mixing angle $\cos\theta_W = \frac{g_2}{\sqrt{g_1^2+g_2^2}}$. The resulting mass terms are

$$\frac{1}{2}\left(\frac{g_2 v}{2}\right)^2 \mathrm{W}_\mu^+ \mathrm{W}^{-\mu} + \frac{1}{2}\left(\frac{v}{2}\right)^2 \left(A_\mu, \mathrm{Z}_\mu\right) \begin{pmatrix} 0 & 0 \\ 0 & 2\left(g_1^2 + g_2^2\right) \end{pmatrix} \begin{pmatrix} A^\mu \\ \mathrm{Z}^\mu \end{pmatrix}, \tag{2.20}$$

where the mass of the W boson is given by $m_\mathrm{W} = \frac{v}{2} g_2$ and the Z boson mass is given by $m_\mathrm{Z} = \frac{v}{2}\sqrt{g_1^2 + g_2^2}$. The masses of the W and Z bosons are directly connected through the weak mixing angle by $m_\mathrm{W} = m_\mathrm{Z} \cos\theta_w$. The photon field stays massless as desired. A common interpretation of the Higgs mechanism is that the three vanishing degrees of freedom of ϕ are absorbed by the three massive gauge bosons in the SM to give them their masses.

Fermion Masses

The fermion masses in the SM cannot be generated by a mass term of the form $m_f(\overline{\psi}_\mathrm{L}^f \psi_\mathrm{R}^f + \overline{\psi}_\mathrm{R}^f \psi_\mathrm{L}^f)$ as in Eq. (2.7) since this would mix left-handed and right-handed states and thus violate gauge invariance. Instead, the fermions can acquire a mass by a postulated Yukawa coupling to the Higgs field with the coupling constant g_f. The Yukawa term in the Lagrangian for the fermion f is given by

$$\mathcal{L}_Y^f = -g_f\, \overline{\psi}_\mathrm{L}\, \phi\, \psi_\mathrm{R} + \mathrm{h.c.} \tag{2.21}$$

Using Eq. (2.15) for ϕ results in the Lagrangian

$$\mathcal{L}_Y^f = -g_f \frac{v}{\sqrt{2}} \left(\overline{\psi}_\mathrm{L} \, \psi_\mathrm{L} + \overline{\psi}_\mathrm{R} \, \psi_\mathrm{R} \right) - g_f \frac{1}{\sqrt{2}} \left(\overline{\psi}_\mathrm{L} \, \psi_\mathrm{L} H + \overline{\psi}_\mathrm{R} \, \psi_\mathrm{R} H \right). \tag{2.22}$$

This includes a mass term that is identical for left-handed and right-handed fermions with $m_f = g_f \frac{v}{\sqrt{2}}$ and predicts a coupling to the scalar Higgs field, proportional to the particle mass. The choice of the coupling constant g_f is free, and thus, the fermion masses are free parameters in the SM.

In general, the mass eigenstates in Eq. (2.22) are not necessarily the flavor eigenstates of the left-handed fermions under the transformations of the $SU(2)_L$ and thus flavor mixing can occur. In the SM this is not realized for the leptons and the lepton number is conserved. The left-handed quarks in the SM are, on the other hand, not mass eigenstates, which, if formulated as diagonal mass states, leads to flavor mixing in the charge-changing weak interactions. The mixing of the left-handed quarks in the SM is described by the unitary 3×3 Cabibbo-Kobayashi-Maskawa (CKM) matrix V_CKM [34, 35]. The entries of V_CKM can be complex, which, constrained by the unitarity, leads to three mixing angles and one CP violating complex phase as additional free parameters of the SM.

It should be noted that the choice of the Higgs potential in Eq. (2.13) determines the self-interactions of the Higgs field and has to be experimentally verified by measuring the Higgs self-coupling. The choice of the gauge in Eq. (2.15) determines the mass terms of the vector bosons. Choosing the gauge which leaves the charged component of the Higgs field would, for example, result in a massive photon field and would break $U(1)_\mathrm{em}$.

2.2.2 Higgs Production in e^+e^- Collisions and Higgs Decays

As we have seen, while allowing the introduction of a mass term for all massive particles in the SM, the Higgs mechanism also introduces couplings of all of these particles to the scalar Higgs boson. If this mechanism is in fact the explanation for electroweak symmetry breaking one thus expects that the Higgs boson can be produced and observed in collider experiments.

Due to the low mass of the electron, its coupling to the Higgs boson is also very small (see Eq. (2.22)). The coupling is especially small compared to the coupling of the electron to Z and γ. It would thus require a huge amount of statistics to identify a significant signal of the resonant Higgs production, $e^+e^- \to H \to f\bar{f}$, at an e^+e^- collider over the $e^+e^- \to \gamma^*/Z^* \to f\bar{f}$ background. The most relevant Higgs production processes at an e^+e^- collider are, depending on $\sqrt{s}$, the Higgsstrahlung process, $e^+e^- \to HZ$, shown in Fig. 2.1(a) and the WW fusion process, $e^+e^- \to H\nu_e\bar{\nu}_e$, shown in Fig. 2.1(b). The cross section of the ZZ fusion process, $e^+e^- \to He^+e^-$, is suppressed approximately by one order of magnitude compared to the WW fusion process, due to the smaller coupling.

At tree-level, the total cross section of the Higgsstrahlung process is given by [36]

$$\sigma_{e^+e^- \to HZ} = \frac{G_F^2 m_Z^4}{96\pi s} \left(\left(4 \sin^2 \theta_w - 1 \right)^2 + 1 \right) \sqrt{\lambda} \frac{\lambda + 12 m_Z^2/s}{\left(1 - m_Z^2/s \right)^2}, \tag{2.23}$$

where $\lambda = \left(1 - (m_H + m_Z)^2/s \right) \left(1 - (m_H + m_Z)^2/s \right)$ and G_F is the Fermi constant

$$G_F = \frac{\sqrt{2}\, g_2^2}{8\, m_W^2}. \tag{2.24}$$

The cross section rises sharply when HZ can be produced on-shell, i.e. $\sqrt{s} = m_H + m_Z$, and drops

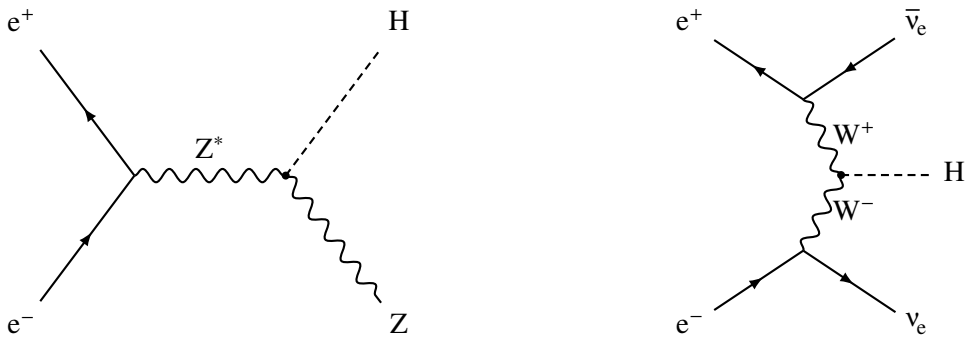

(a) $e^+e^- \to HZ$ (b) $e^+e^- \to H\nu_e\bar{\nu}_e$

Figure 2.1: Feynman diagrams of the dominant Higgs production processes at an e^+e^- collider.

with $1/s$ for high center-of-mass energies. The total cross section for the W^+W^- fusion process can be approximated by [36]

$$\sigma_{e^+e^- \to \nu_e\bar{\nu}_e H} \approx \frac{G_F^3 m_W^4}{4\pi^3\sqrt{2}} \left(\left(1 + \frac{m_H^2}{s}\right) \log\frac{s}{m_H^2} - 2 - 2\frac{m_H^2}{s} \right). \tag{2.25}$$

This cross section scales with $\log(s)$ and although it is small at low $\sqrt{s}$ it eventually becomes the dominating Higgs production process at high center-of-mass energies. Both cross sections receive important radiative corrections [37, 38] and interferences have to be taken into account if the Z decays into neutrinos [36]. Another important process is the Higgs production through radiation off a top quark $e^+e^- \to t\bar{t} \to t\bar{t}H$ [39]. Although this process does not have a large cross section it is the only way to study the Yukawa coupling to top quarks, unless $m_H > 2m_t$. The double Higgs production is induced through all processes listed above, where the Higgs decays into two Higgs bosons. There, the Higgsstrahlung process, $e^+e^- \to HHZ$, and the W^+W^- fusion process, $e^+e^- \to HH\nu_e\bar{\nu}_e$, have the highest prospects of being measurable. Figure 2.2 gives an overview of all relevant Higgs production cross sections.

The partial widths of the different Higgs decays into fermions are given by

$$\Gamma_{H\to f\bar{f}} = \frac{G_F m_f^2 m_H N_c}{4\pi\sqrt{2}} \left(1 - m_f^2/m_H^2\right)^{3/2}, \tag{2.26}$$

where N_c is the number of possible color charges, which is 1 for leptons and 3 for quarks. In addition, the Higgs can decay into the massive vector bosons as well as into two gluons or two photons. The latter two are induced through quark loops since they do not couple directly to the Higgs. The partial widths of all of these processes as well as the corresponding radiative corrections can be found for example in [41] and references therein. The total width of the Higgs boson Γ_H is then the sum of all partial widths that are kinematically allowed and the branching ratio of a certain decay is given by $BR_{H\to X} = \Gamma_{H\to X}/\Gamma_H$. The dependence of the individual branching ratios and the total width of the Higgs boson on its mass are shown in Fig. 2.3.

It should be noted, that due to its kinematics, the Higgsstrahlung process has the highest prospects of the most precise measurement of the Higgs mass through the measurement of the recoil of the Z:

$$m_H^2 = s - 2\sqrt{s}E_Z + m_Z^2. \tag{2.27}$$

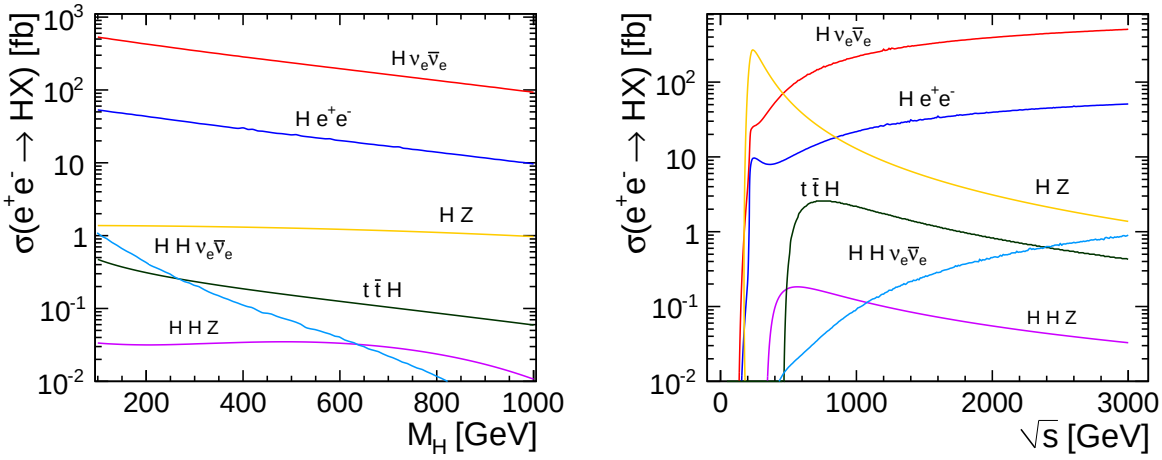

Figure 2.2: Higgs production cross section in the SM depending on the Higgs mass m_{H} for a center-of-mass energy $\sqrt{s}$ of 3 TeV (left) and depending on $\sqrt{s}$ for $m_{\mathrm{H}} = 120\,\mathrm{GeV}$ (right). Cross sections calculated with WHIZARD [40]. Figures taken from [23].

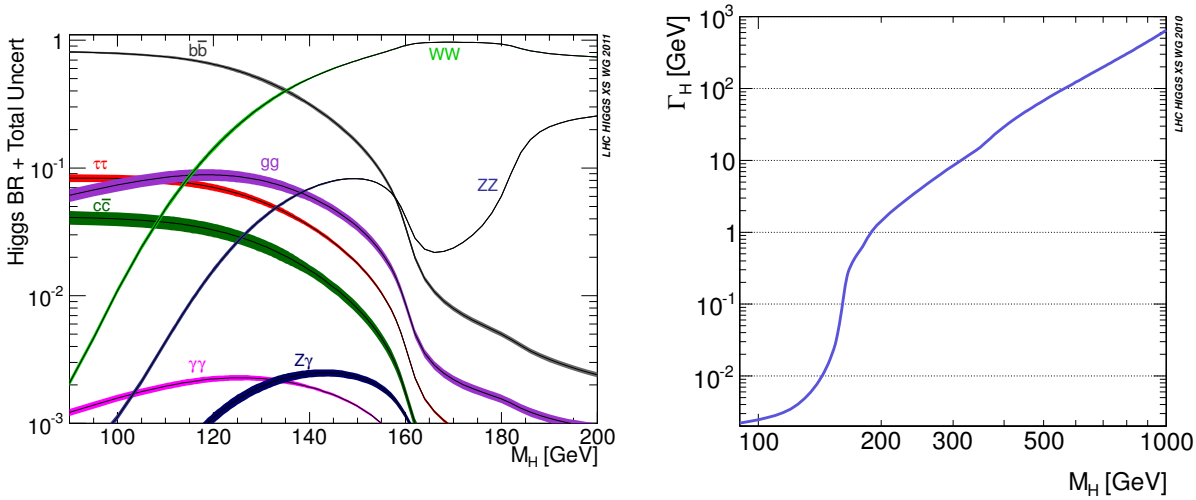

Figure 2.3: Higgs branching ratios depending on the Higgs mass, m_{H}, including uncertainties from theory calculations (left), taken from [42], and total width of the Higgs boson depending on m_{H} (right), taken from [43].

For ultimate precision a precise knowledge of $\sqrt{s}$ is required, which is only possible at a lepton collider. For example, a simulation study of this recoil mass measurement of a SM Higgs with a mass of 120 GeV at the ILC, assuming a center-of-mass energy of 250 GeV and an integrated luminosity of $250\,\mathrm{fb}^{-1}$, shows that an uncertainty on the Higgs mass of 30 MeV is achievable [44]. In addition, if only information of the Z system is used in the analysis, this process allows for the determination of the total width of the Higgs boson in a model-independent way, including possible invisible decay modes.

2.2.3 Determining the Parameters of the Standard Model

In total, the SM has 19 free parameters that have to be determined from observations. These are 9 fermion masses, 3 angles and one *CP* violating phase of the CKM matrix, the *CP* violating phase of

QCD, the three gauge coupling constants $g_{1,2,3}$ and the parameters of the Higgs potential μ and λ. The latter five parameters can also be expressed in parameters that are directly accessible to experimental observation: the fine structure constant α, the strong coupling constant α_s, and the masses m_{Z}, m_{W} and m_{H}.

Another important parameter is the Fermi constant G_F, which can be directly determined from the muon lifetime. It provides a relation between the weak boson masses and the fine structure constant

$$G_F = \frac{\pi\,\alpha}{\sqrt{2}}\left(m_{\mathrm{W}}^2 - \frac{m_{\mathrm{W}}^4}{m_{\mathrm{Z}}^2}\right)^{-1}, \tag{2.28}$$

and is a direct measure of the vacuum expectation value of the Higgs potential $v^{-1} = \sqrt{2}G_F$. Equation (2.28) is one of many possible consistency tests of the SM, since all of the parameters can be measured. Since the Higgs boson contributes to loop corrections also at lower energies, the combination of all observables, including the precise measurements of W and Z cross sections and branching ratios performed at LEP and SLD, allows to perform a global fit of the SM and thus allows to put limits on the Higgs mass. Two discussions of electroweak fits and their results can be found in [45, 46]. The latest published indirect limit on the SM Higgs mass from June 2011 is $m_{\mathrm{H}} = 80^{+30}_{-23}\,\mathrm{GeV}$ [46]. The same fit including the additional limits from the direct Higgs searches at LEP and the Tevatron yields $m_{\mathrm{H}} = 116.4^{+18.3}_{-1.3}\,\mathrm{GeV}$ [46].

In the mean time, the first results from Higgs searches at the LHC have put even more stringent limits on the possible Higgs mass in the SM. Earlier in 2012 CMS reported that a SM Higgs is excluded at the 95% confidence level for masses of $m_{\mathrm{H}} < 114.4\,\mathrm{GeV}$ and $m_{\mathrm{H}} > 127.5\,\mathrm{GeV}$ [47]. The results reported by ATLAS put stronger limits for lower Higgs masses. They report that in the SM the only Higgs masses that are not excluded at a confidence level of 95% are $117.5\,\mathrm{GeV} < m_{\mathrm{H}} < 118.5\,\mathrm{GeV}$ and $122.5\,\mathrm{GeV} < m_{\mathrm{H}} < 129\,\mathrm{GeV}$ [48]. It is expected that by the end of 2012 enough data are collected at the LHC to either exclude the SM Higgs over its full mass range or to claim its discovery with a significance of at least 5σ.

2.3 Beyond the Standard Model

Despite its great success in describing fundamental particle interactions, the SM has several limitations. For example, the Higgs mass receives quadratic corrections from fermion loops, where the heaviest fermion, the top quark, has the largest contribution. This correction can be written as

$$\Delta m_{\mathrm{H}} = -\frac{g_f^2}{8\,\pi^2}\Lambda^2 + \ldots, \tag{2.29}$$

where Λ is the ultra-violet cut-off of the theory. From measurements of the weak boson masses as well as G_F we know v and thus also that m_{H} has to be of the order of 100 GeV. If Λ is very high compared to the electroweak scale, e.g. around the reduced Planck scale of $\sim 10^{18}\,\mathrm{GeV}$, the bare Higgs mass has to be of the order of Λ^2 and fine-tuned to arrive at the observed Higgs mass. This is also referred to as the Hierarchy problem.

Although the SM offers a mechanism to assign mass terms for the massive gauge bosons and the fermions it does not explain the actual size of the different masses. Similarly the different gauge couplings, the quark mixing angles, the Higgs mass and the Higgs vacuum expectation value are free parameters of the theory. The number of generations in the SM is also not explained, as well as the observed

pattern in the values of the electrical charge and the hypercharge of the fermions. In addition, the theory does not offer a mechanism to include gravity.

A direct motivation for the incompleteness of the SM comes from cosmological observations. There is strong evidence for instance through the observations of rotational velocities of stars in galaxies [49], the observations of gravitational lensing of galaxy clusters [50], the observation of the fluctuations in the cosmological microwave background [14] and—probably the most compelling evidence—the observation of the mass distribution of the colliding galaxy clusters in the bullet cluster [51], that there is a large discrepancy between the observed gravitating matter and the expected amount of matter from observations of stars and gas in galaxies. This can be explained if a large fraction of the mass of the universe is dark matter [17], i.e. matter that only interacts gravitationally or gravitationally and weak. The only particles in the SM that fulfill this requirement are the neutrinos, but even when assuming massive neutrinos, the required dark matter largely exceeds the amount of neutrinos expected in the big bang theory. From simulations of galaxy formation processes it is evident that dark matter has to be cold [52], i.e. has to consist of non-relativistic particles. This would not be the case if neutrinos are the main constituent of dark matter. Another important cosmological observation is the absence of anti-matter in the universe [16]. This asymmetry can only be explained through CP violating processes that removed the anti particles from the universe after the big bang. The CP violation allowed in the SM is not sufficient to explain the necessary asymmetry to explain the observations.

All these are hints that the SM might be only an effective field theory which has to be extended by a suitable model.

2.3.1 Extensions of the Standard Model

The observation of neutrino oscillations [53, 54] more than a decade ago constitutes already an extension of the basic SM discussed in Section 2.2, although it does not address any of the shortcomings of the SM stated above. Similarly to the quark mixing mentioned in Section 2.2.1, mixing of the neutrino states implies that the flavor eigenstates are different from the mass eigenstates. The observation of neutrino mixing is only sensitive to mass differences but not absolute masses. Since mixing of all neutrino flavors has been observed, it can be immediately concluded that at least two of the three neutrinos are massive. This leads to two possible modifications of the SM. If the neutrinos are massive Dirac particles, it requires the existence of previously undetected right-handed neutrinos. On the other hand, if neutrinos would acquire their mass like Majorana particles, they would be their own anti-particle, which would imply violation of lepton number conservation.

Supersymmetry

An attractive extension of the SM is Supersymmetry (SUSY), reviewed for example in [55]. These models postulate a global symmetry between fermions and bosons. This symmetry introduces supersymmetric partners to all particles in the SM, also referred to as sparticles. In the Minimal Supersymmetric Standard Model (MSSM), every particle has exactly one superpartner, where the superpartners of the fermions, the sleptons and squarks, have a spin of 0 and the super partners of the gauge bosons, the gauginos or neutralinos and charginos, have a spin of $\frac{1}{2}$. In the Higgs sector, at least four additional scalar particles are predicted. The five scalar particles are two CP even neutral particles, the h and H particles, the neutral pseudoscalar particle A and two charged particles $H^{\pm}$. In many SUSY models the h is very similar to the Higgs boson in the SM, with a light mass of around 120 GeV. In most of these cases the four other Higgs particles have almost identical and rather high masses. Unfortunately SUSY introduces new couplings that violate both lepton number and baryon number, which are conserved in

the SM. These conservation laws are very well tested and have stringent limits from the minimum lifetime of the proton. This problem can be solved by postulating a new conserved quantity, the R-parity, with $P_R = (-1)^{2s+3B+L}$, where s is the spin, B is the baryon number and L is the lepton number. As a result all particles in the SM have an R-parity of 1 and all the superpartners have an R-parity of -1, thus the proton and also the lightest supersymmetric particle (LSP) are stable.

SUSY naturally solves several of the limitations of the SM discussed above. For example, the additional particles would introduce new loop corrections to the Higgs self-coupling that automatically cancel out the divergent terms and thus resolve the hierarchy problem. Similarly, the loop corrections change the dependence of the three effective gauge couplings on the transferred energy Q, allowing to unify at an energy of around 10^{16} GeV. This would allow a further unification of the strong and electroweak gauge interactions, similar to the unification of the weak and electromagnetic interactions in the SM. In addition, if the R parity is conserved and if the LSP were neutral, it would be a natural candidate for dark matter since it would be stable [56] . Even if R-parity would be slightly violated, the LSP could be an explanation for dark matter if its lifetime is large enough.

Since SUSY particles have not been observed yet, the masses of the superpartners have to be significantly higher than the masses of the SM particles. This requires that the symmetry has to be broken. In addition, the breaking of SUSY should not re-introduce quadratic divergences in the loop corrections to the Higgs self-coupling, but at most logarithmic divergences. This is referred to as soft SUSY breaking.

If SUSY is introduced as a local gauge symmetry instead of a global gauge symmetry, it requires the inclusion of gravity. A new SUSY doublet, the spin-2 graviton, which is the mediator of the gravitational force, and its super partner the spin-$\frac{3}{2}$ gravitino have to be introduced. The resulting theory is called Supergravity (SUGRA) [57, 58] and would be a natural combination of the theory of gravity and the current understanding of the other fundamental forces.

Importance of the Higgs Sector

With the introduction of new particles, like for example in the case of SUSY, new couplings to the Higgs boson(s) are predicted and thus the branching ratios of its decay modes should differ from the SM. Similarly, models that include an alternative explanation of electroweak symmetry breaking naturally predict branching ratios that are different from those in the SM. It is thus of utmost importance to not only measure the relative branching ratios of the different decay modes predicted in the SM, which leaves one ignorant to other decays, but also measure the absolute branching ratios and the total width of the Higgs boson. This will be very difficult at the LHC and is thus one of the most compelling reasons for the construction of a high-energy lepton collider. Finally, to decide between different concurring models it is important to measure all branching ratios as precisely as possible.

Extensive discussions of the Higgs sector and how to distinguish between different models can be found in [41, 59, 60].

CHAPTER 3

The Compact Linear Collider

The Compact Linear Collider is a concept for a future e^+e^- linear collider with a possible center-of-mass energy of several TeV. It will allow precise measurements of the properties of the Higgs boson, if it exists, and any other new particle that could be discovered at the LHC if it falls within the energy reach of CLIC. If it exists, the LHC experiments will only be sensitive to the couplings of the Higgs to the gauge bosons (through top loops in case of photons and gluons) and possibly to the couplings to t and b through associated production. In the lepton sector only its coupling to τ and maybe the coupling to μ will be accessible. A lepton collider like CLIC or the ILC will be able to measure all of these couplings with a much higher precision and also allows the measurement of the Higgs self coupling. While the LHC has very good chances of discovering new strongly interacting particles like squarks, a high energy lepton collider has a significantly larger discovery potential for particles in the electroweak sector, e.g. gauginos, sleptons or a Z'. Measurements at CLIC would thus be complementary to those performed at the LHC.

This interplay of hadron and lepton colliders has proven beneficial throughout the history of particle physics. For example, the W and Z bosons have been first discovered in proton-antiproton collisions at the Super Proton Synchrotron (SPS) by the UA1[61, 62] and UA2 [63, 64] experiments. Their properties have later been measured with much greater precision in the e^+e^- collisions by the experiments at LEP [33, 45]. The properties of the Z boson were also measured in e^+e^- collisions at the SLAC Large Detector (SLD) operated at the Stanford Linear Collider (SLC), the longest linear accelerator to date. The reason why proton-proton or proton-antiproton colliders are often referred to as discovery machines is that they more easily allow for a much higher collision energy. When charged particles are forced on a circular trajectory they lose energy through synchrotron radiation. In a circular collider, the energy loss through synchrotron radiation per turn scales with

$$\Delta E_{\text{synchrotron}} \propto \frac{E_{\text{beam}}^4}{m^4\,\rho} \tag{3.1}$$

where ρ is the radius of the collider and m is the mass of the particle. It is thus evident that protons, which are almost 2000 times heavier than electrons, experience a significantly lower energy loss per turn. The drawback of hadron colliders is that only one quark or one gluon of each of the colliding hadrons takes part in the hard interaction. Thus, only a fraction of the center-of-mass energy of the two hadrons is available in the hard interaction and the energy and momentum of the two partons is intrinsically unknown. Lepton colliders on the other hand collide fundamental particles, which means

that $\sqrt{s}$ of the collision is precisely known through the beam energy.

In this chapter we will introduce the CLIC accelerator concept and discuss the conditions for experiments at CLIC including the time structure of the beam, the machine-related backgrounds and the luminosity spectrum. The information summarized in this chapter is extracted from the accelerator volume of the CLIC CDR [20].

3.1 The CLIC Concept

The aim of the next e^+e^- collider is a high center-of-mass energy, covering at least the energy scale of new physics Beyond the Standard Model (BSM) (if it exists), while providing high luminosity of the order of $10^{34}\,\mathrm{cm}^{-2}\mathrm{s}^{-1}$ to allow for precise measurements of the properties of all newly discovered phenomena.

As shown in Eq. (3.1), the energy loss through synchrotron radiation in a circular collider rises with the fourth power of the beam energy. On the other hand, the energy consumption of a linear collider scales linearly with the beam energy as well as the luminosity. Already for beam energies slightly higher than those achieved at LEP a linear collider becomes more efficient than a circular collider. A linear collider requires extremely high field gradients in the acceleration structures to limit the required total length of the accelerator. The ILC proposes superconducting cavities with a gradient of $35\,\mathrm{MV/m}$ to achieve a beam energy of 250 GeV along a half-length of the collider of approximately 14 km. The maximum gradient achievable with superconducting cavities is limited and thus, if much higher beam energies are desired, normal conducting cavities are the only option without requiring an excessively long accelerator.

3.1.1 Field Gradient

For CLIC, acceleration cavities with a gradient of $100\,\mathrm{MV/m}$ and a frequency of 12 GHz are foreseen, which allows to achieve a beam energy of 1.5 TeV within an accelerator of 21 km length. The total length of CLIC, including both accelerators as well as the Beam Delivery System (BDS), is 48.3 km. A schematic view of the default layout for $\sqrt{s} = 3$ TeV is shown in Fig. 3.1. To achieve a center-of-mass energy of 500 GeV, a total length of only 13 km is required.

In addition to the high gradient in the cavities, also the breakdown rate of the RF power in the accelerating cavities has to be sufficiently low to allow for an efficient operation of CLIC. The design goal is that the probability of a breakdown happening anywhere in the accelerator is less than 1%. This translates into a maximum breakdown rate within the cavities of $3 \times 10^{-7}\,\mathrm{m}^{-1}\mathrm{pulse}^{-1}$.

3.1.2 Two-Beam Acceleration

The second crucial point is the efficient generation of the RF power required to accelerate the particles in the beam. The high number of klystrons that would be required to provide the necessary power, as well as their low efficiency is prohibitive. Instead, a two beam acceleration scheme is proposed to generate and distribute the RF power at CLIC. The drive beam that provides the power is a low-energy electron beam, with an electron energy of 2.38 GeV, at a very high intensity of 100 A within the bunch train period. This beam is decelerated in a series of Power Extraction and Transfer Systems (PETSs), where the energy is extracted to provide the accelerating field in the cavities of the main beam. The drive beam is decelerated over a length of 876 m and dumped afterwards. In total there are 24 of these sectors in each of the two accelerators. The high beam intensity of the drive beam, required to produce

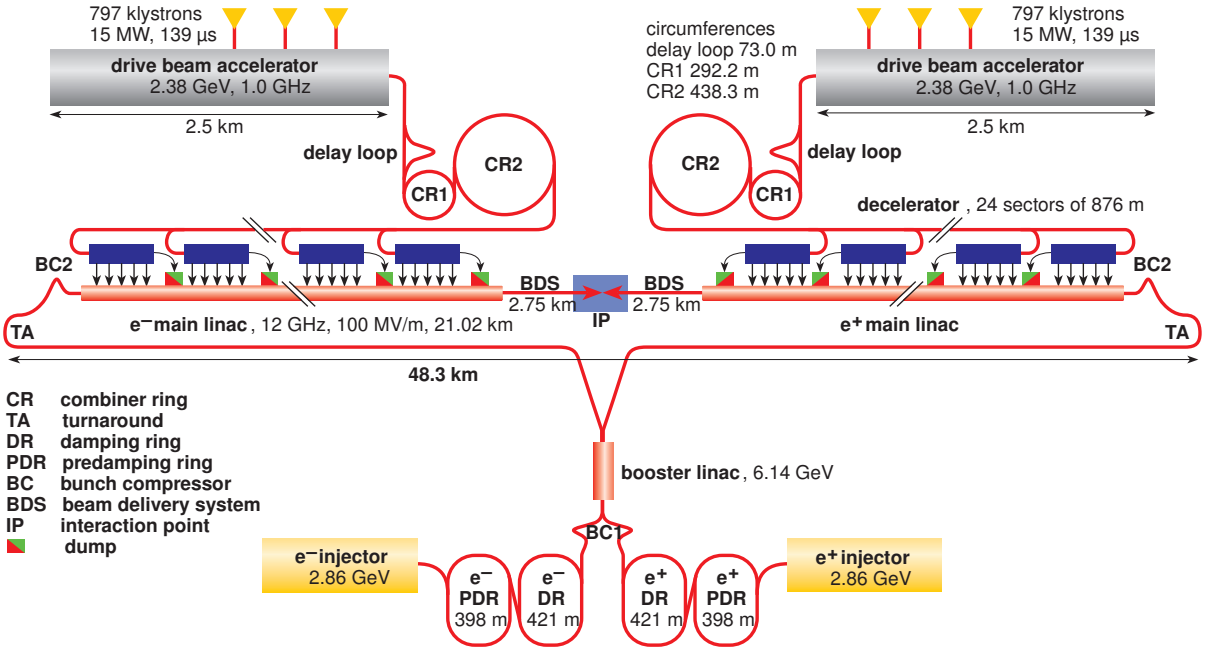

Figure 3.1: Schematic view of the CLIC layout for a center-of-mass energy of 3 TeV. Figure taken from [20].

sufficient power, is achieved by producing a beam with very short bunch spacings of 2.4 cm that is split and overlaid using a delay loop followed by two combiner rings.

The distribution of the power transport in a particle beam is almost loss-less. The most important losses are introduced in the power extraction and transfer in the PETS, which has to be very efficient ($\gg 90\%$) to provide enough power for the acceleration of the main beam.

3.1.3 Beam-Beam Effects and Beam-Related Backgrounds

The high space charge inside the two bunches leads to interactions between them when they cross each other at the interaction point. Since the bunches are of opposite charge at CLIC, the particles see an attractive force which leads to an increase in luminosity. This effect is called pinch-effect, which is discussed for example in [65]. As in the case of synchrotron radiation, the change of the trajectory due to an electromagnetic field leads to the creation of photons. The photons of this so-called beamstrahlung can interact and lead to the creation of secondary particles, mostly e^+e^- pairs [66].

The most likely process is the conversion of one of the photons into an e^+e^- pair. The photon conversion is only possible in a strong electromagnetic field, which in this case is the coherent field of all other particles seen by the photon. The e^+e^- pairs are thus called coherent pairs (see Fig. 3.2(a) for the Feynman diagram). Since the photons are created mostly collinear with the beam, the pairs are also created with very low transverse momentum. It is important to choose the opening angle of the outgoing beam pipe large enough, such that the detector is unaffected by the large flux of these high-energetic particles.

A related effect is the creation of trident pairs shown in Fig. 3.2(b), where a virtual photon converts into an e^+e^- pair in presence of the macroscopic field. The angular distribution of these pairs is very similar to that of the coherent pairs, but they are in general of lower energy. This means that they are of no additional concern for the design of the detector in the forward region.

More important for the design of the detector are the incoherent e^+e^- pairs, created from the inter-

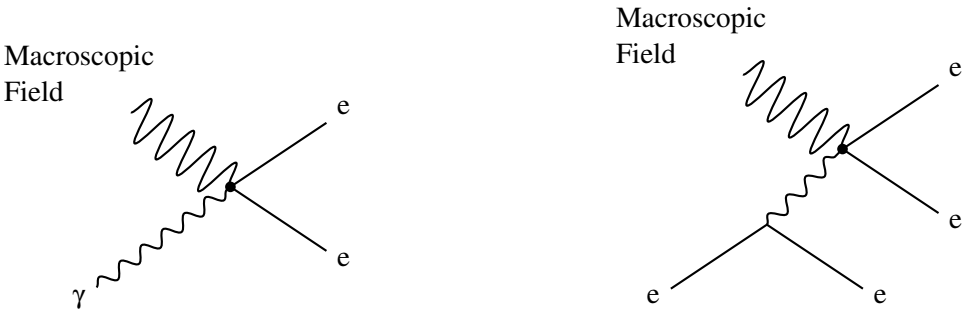

(a) Coherent Pair Production (b) Trident Pair Production

Figure 3.2: Feynman diagrams of the coherent pair production and trident pair production processes.

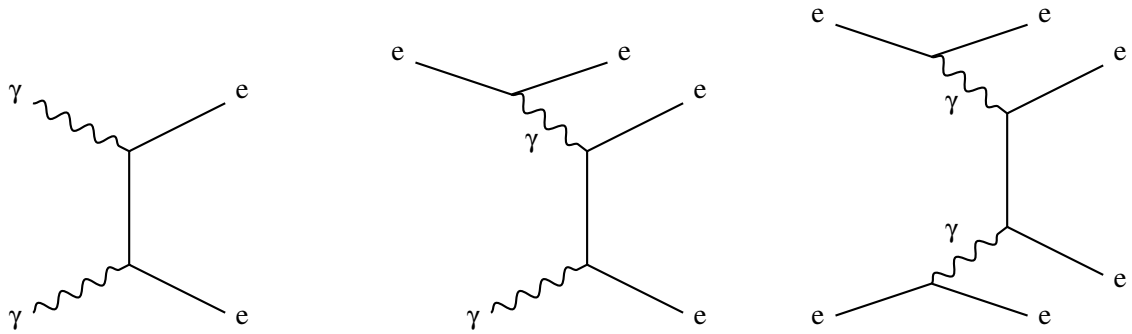

(a) Breit-Wheeler (b) Bethe-Heitler (c) Landau-Lifshitz

Figure 3.3: Feynman diagrams of the most important processes that contribute to the incoherent pair production.

action of two real or virtual photons. Figure 3.3 shows the three dominating processes contributing to their production. Although they are in general less energetic than the two previously mentioned pair backgrounds, they extend to larger polar angles. This requires a careful design of the vertex detector to avoid large occupancies as well as the forward calorimeters to avoid the creation of large amounts of backscattering particles. The strong solenoid field of the central detector helps in confining them to low radii.

All of these processes are of course also possible for all other charged fermions. Their production cross section is, however, largely reduced, due to their higher mass compared to the electron mass. The leptonic processes (other than e^+e^- production) are thus of no concern in terms of detector occupancy, although they can fake physics signatures and have to be considered when looking for a corresponding final state. The production of quark pairs is of more concern since they hadronize and create mini-jets also at large polar angles [67]. This background is referred to as $\gamma\gamma \rightarrow$ hadrons.

All of these processes are simulated with the program GuineaPig [65, 68], which is also discussed in Section 6.1.2. The resulting energy and polar angle distributions of the particles created in these processes for CLIC at 3 TeV are shown in Fig. 3.4. The particle energies extend up to the full beam energy, although they peak at low energies. The coherent pairs are emitted only within 10 mrad and the trident pairs only within 30 mrad. The incoherent pairs and the particles from $\gamma\gamma \rightarrow$ hadrons are created at all polar angles. The maximum polar angle of the coherent pairs also determines the minimum opening angle of the very forward calorimeter, i.e. the Beam Calorimeter (BeamCal), of 10 mrad.

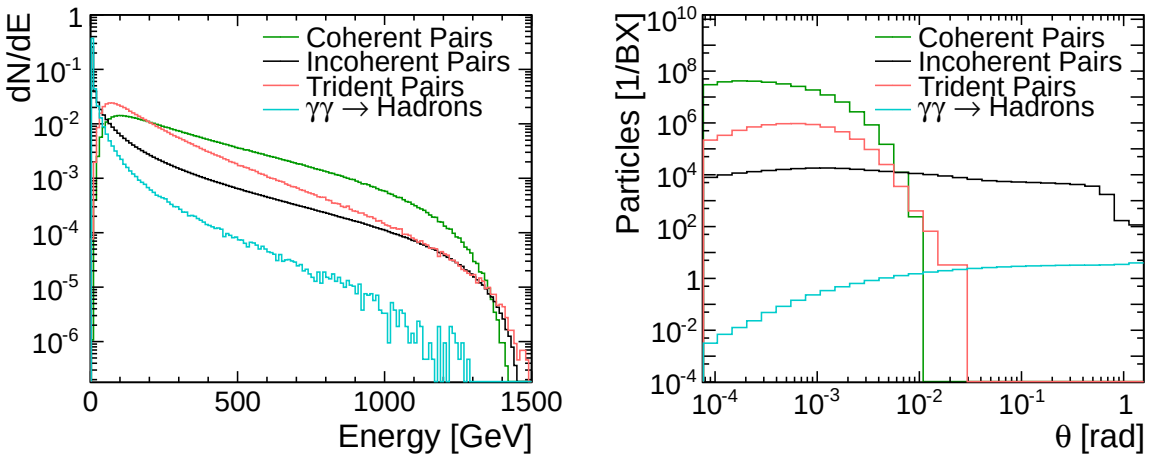

Figure 3.4: Distribution of the particle energy in the beam-induced backgrounds (left) and distribution of the polar angle of the background particles (right). The polar angle is given with respect to the outgoing beam-axis. Figures taken from [23].

3.1.4 Luminosity

The luminosity of a collider with symmetric colliding beams can be written as [65]

$$\mathcal{L} = \frac{N^2 f}{4\pi\sigma_x\sigma_y}, \tag{3.2}$$

where N is the number of particles in each bunch, f is the frequency of the Bunch Crossings (BXs), and σ_x and σ_y are the lateral extends of each bunch. In case of a linear collider that is operated in pulsed mode, i.e. the bunches arrive in trains that are short with respect to the distance between them, the frequency has to be replaced by $f = f_{\text{train}} \cdot n_{\text{bunches}}$, where f_{train} is the frequency of the trains and n_{bunches} is the number of bunches in each train. A high luminosity thus requires both, a very high bunch charge, i.e. a large number of particles in each beam, as well as very collimated beams. The total length of each train is limited by the choice of the normal conducting technology, since the electric field in the cavities dissipates quickly. The pulse length generated by the PETS is 176 ns. The total length of each train at CLIC has to be shorter and is chosen to be 156 ns, where each train consists of 312 bunches. For the ILC on the other hand, much longer bunch trains of 1 ms are proposed. Figure 3.5 shows a schematic view of the typical beam structure at a linear collider and gives the numbers for the ILC and CLIC to highlight the very different time structures of the two proposed accelerator concepts.

While the luminosity scales with $1/\left(\sigma_x\sigma_y\right)$, the amount of energy lost in beamstrahlung scales with $1/\left(\sigma_x+\sigma_y\right)^2$ [65]. This means that an asymmetric shape of the bunch in xy-direction with very different σ_x and σ_y is the optimal choice. The minimum size in any of these directions is limited by the feasible emittance of the beam, as well as the achievable stability of the beam position, due to the stability of the focusing elements in the BDS, especially that of the final focusing quadrupole (QD0). The parameters chosen for the default layout of CLIC for a center-of-mass energy of 3 TeV are given in Table 3.1.

The short spacing between two bunches leads to interactions between incoming and outgoing bunches, especially if the beams are not perfectly aligned. This and the desired placement of the QD0 as close as possible to the Interaction Point (IP) infers a minimum crossing angle of the accelerator of 20 mrad [69].

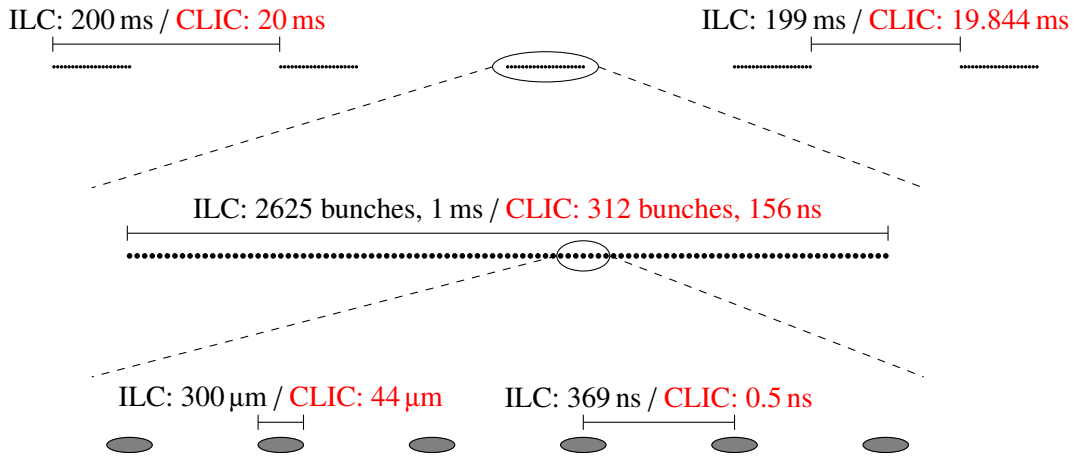
ILC: 200 ms / CLIC: 20 ms
ILC: 199 ms / CLIC: 19.844 ms
ILC: 2625 bunches, 1 ms / CLIC: 312 bunches, 156 ns
ILC: 300 µm / CLIC: 44 µm
ILC: 369 ns / CLIC: 0.5 ns

Figure 3.5: Schematic view of the time structure of a beam at the ILC at $\sqrt{s} = 500\,\text{GeV}$ (black numbers) and at CLIC at $\sqrt{s} = 3\,\text{TeV}$ (red numbers). The beam is split into trains with a large gap in between (top). Each train consists of several bunches as indicated in the lower two sketches. Pictures are not to scale. Numbers for CLIC from [20]. Numbers for ILC correspond to the nominal design in [18].

3.1.5 Luminosity Spectrum

In any particle accelerator the energy of the colliding particles is subject to an intrinsic spread. At CLIC this energy spread is expected to be 0.35% around the nominal beam energy of 1.5 TeV. In addition, the mean beam energy is expected to fluctuate by approximately 0.1% [23]. The biggest effect on the center-of-mass energy at CLIC originates from the beamstrahlung introduced above. The potentially large energy loss of one or both of the colliding particles at the interaction point leads to long tails to low energies in the distribution of the effective center-of-mass energy: the luminosity spectrum. This effect is illustrated in Fig. 3.6. For the nominal CLIC parameters, shown in Table 3.1, the fraction of collisions within the highest 1% of the nominal energy corresponds only to 35% of the total luminosity. This mostly affects the measurement of processes with production thresholds close to the nominal center-of-mass energy. On the other hand, processes which can be produced at lower $\sqrt{s}$ will benefit from a significantly larger fraction of the total luminosity. In any case this luminosity spectrum has to be taken into account when calculating production cross sections at CLIC.

We want to stress that the long tail in the luminosity spectrum is mostly caused by the beam-beam effects which can not be avoided if a high total luminosity is desired. A CLIC accelerator at lower center-of-mass energies of $\sqrt{s} = 500\,\text{GeV}$ would have a much narrower luminosity spectrum with almost 75% of the luminosity within the highest 1% of the energy, but with a lower total luminosity of only $2.0 \times 10^{34}\,\text{cm}^{-2}\text{s}^{-1}$ [23].

3.1.6 Staged Construction

The configuration of the accelerator and especially the beam delivery system is chosen to optimize the available luminosity for the nominal center-of-mass energy. Although the accelerator can also be operated at lower $\sqrt{s}$ this will result in a significantly lower total luminosity. For certain scenarios, e.g. a threshold scan, the accelerator will need to be operated far from its nominal energy. It is thus beneficial to construct CLIC in several stages with increasing center-of-mass energies. The chosen energy stages will depend strongly on the new physics scenarios discovered at the LHC. One possible scenario involving three energy stages is investigated in [70]. There, the first stage is designed for a

Table 3.1: Parameters of the default CLIC layout for $\sqrt{s} = 3$ TeV. Given is the crossing angle θ_c, the repetition rate of the bunch trains f_{train}, the number of bunches in each train n_{bunches}, the time between two bunch crossings Δt, the number of particles in each bunch N, the orthogonal bunch sizes $\sigma_{x,y,z}$, the total luminosity $\mathcal{L}$, the luminosity within the highest 1% of the nominal beam energy $\mathcal{L}_{1\%}$, the number of beamstrahlung photons per beam particle n_γ, the fraction of the beam energy lost in beamstrahlung $\Delta E/E$, the number of coherent pair particles per BX N_{coh}, the total energy of all coherent pair particles per BX E_{coh}, the number of incoherent pair particles per BX N_{incoh}, the total energy of all incoherent pair particles per BX E_{incoh}, and the number of $\gamma\gamma \rightarrow$ hadrons events per BX n_{had} with a minimum transferred energy of 2 GeV. Table adapted from [23]. A full set of machine parameters for CLIC, also for other $\sqrt{s}$, can be found in [20].

Parameter	Value
θ_c	20 mrad
f_{train}	50 Hz
n_{bunches}	312
Δt	0.5 ns
N	3.72×10^9
σ_x	$\sim$ 45 nm
σ_y	$\sim$ 1 nm
σ_z	44 µm
$\mathcal{L}$	$5.9 \times 10^{34}\,\text{cm}^{-2}\text{s}^{-1}$
$\mathcal{L}_{1\%}$	$2.0 \times 10^{34}\,\text{cm}^{-2}\text{s}^{-1}$
n_γ	2.1
$\Delta E/E$	0.28
N_{coh}	6.8×10^8
E_{coh}	2.1×10^8 TeV
N_{incoh}	3.0×10^5
E_{incoh}	2.3×10^4 TeV
n_{had}	3.2

nominal center-of-mass energy of 500 GeV, which allows to precisely measure the Higgs mass and some of its couplings in HZ production as well as to precisely measure the top mass in a $\text{t}\bar{\text{t}}$ threshold scan. The second stage is then chosen to be at $\sqrt{s} = 1.4$ TeV based on the mass spectrum in the SUSY scenario that was chosen for this particular study. The final stage will then be the 3 TeV configuration presented here.

3.1.7 Demonstration of Feasibility

Most of the key technological challenges have been achieved in prototypes. For example, the generation of a high intensity beam using a delay loop followed by one combiner ring has been demonstrated at CTF3. Similarly, the efficient power extraction using a series of PETSs demonstrated at CTF3, which then has been used to demonstrate the concept of two-beam acceleration. In addition, a gradient of 106 MV/m in combination with a maximum breakdown rate of $3.1 \times 10^{-7}\,\text{m}^{-1}\text{pulse}^{-1}$ has been achieved in individually tested acceleration structures [20].

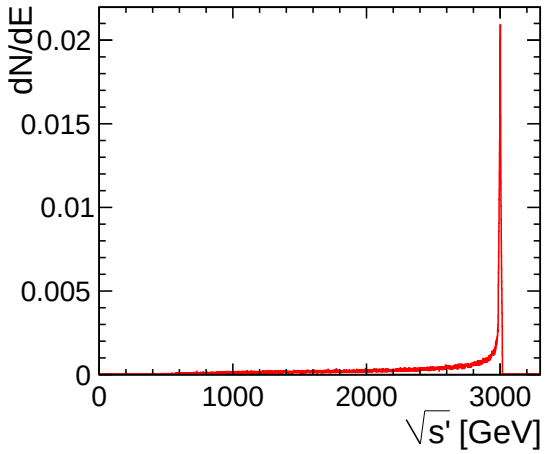

Figure 3.6: Distribution of the effective center of mass energy $\sqrt{s'}$ at CLIC for a nominal center-of-mass energy of 3 TeV. Figure taken from [23].

CHAPTER 4

Detector Design for Collider Experiments

High energy collisions are studied by measuring the four momenta, i.e. the energies and the momenta, of ideally all particles that were created in the collision. All other observables are derived from these two quantities and the quality of their measurement determines the success of an experiment.

In this chapter we discuss the basic concepts of momentum measurement (see Section 4.1) and energy measurement (see Section 4.2) in HEP collider experiments, and motivate the formulae typically used to parametrize the detector performance. Subsequently the detector requirements for an experiment at CLIC are discussed in Section 4.3. The particle flow paradigm, which is driving most detector designs for future collider experiments is introduced in Section 4.4.

4.1 Track Momentum and Impact Parameter Measurement

Charged particles are deflected in a magnetic field through the Lorentz force. In a homogeneous magnetic field the resulting particle trajectory is a helix defined only by the particle momentum $\vec{p}$, its charge q and the magnetic field $\vec{B}$. This allows the measurement of the particle momentum in a known magnetic field. The momentum measurement can be divided into the measurement of the transverse momentum in the plane perpendicular to the magnetic field and the measurement of the polar angle θ:

$$p = \frac{p_{\mathrm{T}}}{\sin\theta}. \tag{4.1}$$

An illustration of the two track projections and more information on the track parameters can be found in Appendix C.

4.1.1 Curvature Measurement

Assuming a perfect solenoid field parallel to the z-axis, the magnetic field inside the solenoid is $\vec{B} = (0, 0, B)$. The circular path of the particle with a charge q in the $r\phi$-plane is then given by the centripetal force introduced by the Lorentz force

$$\frac{m v_{\mathrm{T}}^2}{\rho} = q\, v_{\mathrm{T}}\, B, \tag{4.2}$$

where ρ is the radius, m is the particle mass and v_T is the absolute value of the particle velocity projected to the $r\phi$-plane. Using $mv_\mathrm{T} = p_\mathrm{T}$ the radius and the curvature κ are given by

$$\frac{1}{\kappa} \equiv \rho = \frac{p_\mathrm{T}}{qB}. \tag{4.3}$$

Charged particles that are living long enough to form a measurable track carry unit charge, $\pm e$. Omitting the sign of the charge, which defines the orientation of the helix, and using units commonly used in HEP, the transverse momentum can be calculated as

$$p_\mathrm{T} = \frac{0.3\ B}{\kappa} \frac{\mathrm{GeV}}{\mathrm{T\ m}}. \tag{4.4}$$

The arc length S of the projected track in the $r\phi$-plane can be calculated from the azimuthal angle φ between the start point and the end point of the helix:

$$S = \rho\varphi = \frac{p_\mathrm{T}\ \varphi}{0.3\ B} \frac{\mathrm{T\ m}}{\mathrm{GeV}}. \tag{4.5}$$

The uncertainty of the curvature measurement using N individual measurement points with an uncertainty of $\sigma(r\phi)$ and which are equally distributed along S can be estimated using the Glückstern formula [71]

$$\sigma(\kappa) \approx \sqrt{\frac{720}{N+4}} \frac{\sigma(r\phi)}{S^2}. \tag{4.6}$$

This formula is derived using a parabola as an approximation of the circular track projection and only holds for small curvatures and $N \gg 3$. An exact solution for circular tracks can be found in [72].

Using Eqs. (4.4) and (4.6) the relative uncertainty of the transverse momentum due to the point resolution can be approximated as

$$\left.\frac{\sigma(p_\mathrm{T})}{p_\mathrm{T}}\right|^{\mathrm{track}} \approx \sqrt{\frac{720}{N+4}} \frac{\sigma(r\phi) p_\mathrm{T}}{0.3\ B\ S^2} \frac{\mathrm{T\ m}}{\mathrm{GeV}}. \tag{4.7}$$

For almost straight tracks, S is equivalent to the distance between the innermost and outermost measurement point. This means that the radius of the detector is the most powerful variable to improve the momentum resolution for high momentum tracks.

4.1.2 Polar Angle Measurement

The projection of the track in the curved Sz-plane is a straight line described by

$$z = z_0 + S\ \cot(\theta), \tag{4.8}$$

where z_0 is the z-position of the track origin in the xy-plane. For tracks with a small curvature the track projection in the rz-plane can be approximated by a straight line. The uncertainty on the measurement of the polar angle from N measurements with a point resolution of $\sigma(\xi)$ which are equally distributed along a straight line of the length L is given by [71]

$$\sigma(\theta) \approx \frac{\sigma(\xi)}{L} \sqrt{\frac{12(N-1)}{N(N+1)}}. \tag{4.9}$$

The point resolution $\sigma(\xi)$ is perpendicular to the track. This has to be translated into the detector point resolution which is parallel to the detector layer. For barrel detectors which are parallel to z this results in $\sigma(\xi) = \sigma(z)\sin(\theta)$. For disk detectors which are perpendicular to z this results in $\sigma(\xi) = \sigma(r)\cos(\theta)$. It should be noted that the length L used here is the total length of the track along the helix

$$L = \frac{S}{\sin(\theta)} = S\sqrt{1 + \cot(\theta)}. \tag{4.10}$$

4.1.3 Multiple Scattering

A charged particle that traverses material is deflected by multiple Coulomb scattering. The distribution of the scattering angle is described by Molière's theory of multiple scattering [73]. For small scattering angles α within a plane parallel to the original direction of the particle, the distribution of α can be described by a Gaussian distribution centered around $\alpha = 0°$. For particles with $q = \pm e$, its width $\sigma(\alpha)$ is then given by the approximation [74, 75]

$$\sigma(\alpha) \approx \frac{13.6\,\text{MeV}}{\beta\, p}\sqrt{\frac{X}{X_0}}\left(1 + 0.038\ln\left(\frac{X}{X_0}\right)\right), \tag{4.11}$$

where X is the thickness of the material along the particle trajectory and X_0 is the radiation length of the material. Since the second term in parentheses is only a small correction it will be neglected below.

For an estimation of the impact of multiple scattering on the track measurement we treat the scattering in θ and ϕ directions independently. The transverse momentum measurement is only affected by the multiple scattering in ϕ which introduces an additional uncertainty in φ. Using Eq. (4.5) we find

$$\frac{\sigma(p_\text{T})}{p_\text{T}} = \frac{\sigma(\varphi)}{\varphi} = \frac{\sigma(\varphi)\, p_\text{T}}{0.3\, B\, S}\frac{\text{T m}}{\text{GeV}}. \tag{4.12}$$

In order to use Eq. (4.11) to describe the uncertainty in φ due to multiple scattering we have to project the scattering angle into the $r\phi$-plane which gives $\alpha_{r\phi} = \alpha/\sin\theta$. We also assume a homogeneous material distribution along the track such that $X = L$. The resulting uncertainty on the transverse momentum due to multiple scattering is then

$$\left.\frac{\sigma(p_\text{T})}{p_\text{T}}\right|^\text{MS} \approx \frac{0.045\; p_\text{T}\;\text{T m}}{\beta\; p\; B\; S\;\sin\theta}\sqrt{\frac{L}{X_0}} = \frac{0.045\;\text{T m}}{\beta B\;\sin\theta\;\sqrt{L\,X_0}}. \tag{4.13}$$

It should be noted that for multiple individual layers the scattering angles introduced by different layer are correlated. In addition, when calculating the traversed length L' of track in a layer, the direction in ϕ in which a layer is crossed has to be considered as well as the angle in θ.

Using Eq. (4.7) and Eq. (4.13) it is evident that the relative transverse momentum resolution can be parametrized as

$$\frac{\sigma(p_\text{T})}{p_\text{T}} = a p_\text{T} \oplus \frac{b}{\sin\theta}. \tag{4.14}$$

The impact of multiple scattering on the measurement of the polar angle can be estimated similarly. Like above we assume a homogeneous material distribution along L. The additional uncertainty on θ is then directly given by Eq. (4.11)

$$\sigma(\theta)|^\text{MS} \approx \frac{13.6\,\text{MeV}}{\beta\, p}\sqrt{L/X_0}. \tag{4.15}$$

As shown in [76] the total momentum resolution is given by

$$\frac{\sigma(p)}{p} \approx \sqrt{\left(\frac{\sigma(p_\mathrm{T})}{p_\mathrm{T}}\right)^2 - \cot^2\theta\,\sigma^2(\theta)}. \tag{4.16}$$

4.1.4 Impact Parameter Measurement

The impact parameter d_0 is defined as the distance of closest approach to the IP of the helix projection in the xy-plane. It defines the origin $S = 0$ of the helix projection. The z-position of P_0 is called z_0.

The measurement of d_0 is the extrapolation of the azimuthal measurement to the point of closest approach, which we can approximate by a parabola for sufficiently small curvatures [76]

$$d_0 \approx R\phi - R\varphi + \frac{\kappa}{2}R^2, \tag{4.17}$$

where R is the radius of the measurement layer. The track curvature has to be small compared to R, otherwise the track would not pass through multiple layers. We can thus neglect the last term, and the resulting uncertainty on d_0 is given by

$$\sigma(d_0) \approx \sigma(R\phi) \oplus R\sigma(\varphi), \tag{4.18}$$

when also neglecting correlations. We can identify $\sigma(R\phi)$ with the point resolution $\sigma(r\phi)$ in the measurement layer. In addition, the term $\sigma(\varphi)$ recieves a contribution from multiple scattering. Using Eq. (4.11) projected into the $r\phi$-plane for the additional uncertainty on φ results in

$$\sigma(d_0) \approx \sigma(r\phi) \oplus R\sigma(\varphi) \oplus \frac{R\ 13.6\,\mathrm{MeV}}{\beta\ p \sin\theta}\sqrt{\frac{X}{X_0}}. \tag{4.19}$$

For high track momenta the multiple scattering term and the uncertainty on the angular measurement should be small compared to $\sigma(r\phi)$, which then determines the impact parameter resolution. For low momenta only the multiple scattering term is relevant. In a barrel like detector with constant thickness $d = X \sin\theta$ we can write

$$\sigma(d_0) \approx \sigma(r\phi) \oplus \frac{R\ 13.6\,\mathrm{MeV}}{\beta\ p\ \sqrt{\sin\theta}}\sqrt{\frac{d}{X_0}}, \tag{4.20}$$

which corresponds to the canonical parametrization

$$\sigma(d_0) \approx a \oplus \frac{b}{p\ \sqrt{\sin\theta}}. \tag{4.21}$$

The measurement of z_0 is a linear extrapolation of the track slope from the innermost measurement position z

$$z_0 = z - S(z)\ \cot\theta. \tag{4.22}$$

Neglecting correlations, the uncertainty of the z_0 measurement is given by

$$\sigma(z_0) \approx \sigma(z) \oplus \frac{S\ \sigma(\theta)}{\sin(\theta)}. \tag{4.23}$$

Like in the case of d_0 only the second term recieves corrections due to multiple scattering. Using

Eq. (4.11) to estimate the uncertainty on the polar angle yields

$$\sigma(z_0) \approx \sigma(z) \oplus \frac{S\ \sigma(\theta)}{\sin(\theta)} \oplus \frac{S}{\sin(\theta)} \frac{13.6\,\text{MeV}}{\beta\ p} \sqrt{\frac{X}{X_0}}. \tag{4.24}$$

If the distance to the IP is sufficiently small, $\sigma(z_0)$ is determined by $\sigma(z)$ in the central region and by $\sigma(\theta)$ for lower θ. For low momenta $\sigma(\theta)$ is dominated by multiple scattering which then also dominates the impact parameter measurement. Assuming a constant material budget $d = X \sin(\theta)$ we get the usual parametrization

$$\sigma(z_0) = a \oplus \frac{b}{p\ \sqrt{\sin\theta}}, \tag{4.25}$$

which is similar to the one for d_0.

4.2 Energy Measurement

The particle energy is measured in the calorimeters. In this process the particle loses its energy through various interactions until all its energy is deposited in the calorimeter. These interactions usually lead to the creation of secondary particles. In this way, a shower cascade is created in the calorimeter.

The basic mechanisms of the shower development and the most important influences on the energy resolution are discussed below following the detailed discussions in [77].

4.2.1 Electromagnetic Showers

The dominant electromagnetic processes that lead to energy loss of a charged particle that passes through matter are either ionization of the nuclei in the passed material or creation of Bremsstrahlung photons for high particle energies. The transition of these two regimes is characterized by the critical energy of the particle ϵ_c at which the energy loss of these two processes is equivalent. ϵ_c depends both on the electron density in the absorber and the mass of the particle

$$\epsilon_c \propto \frac{m^2}{Z}, \tag{4.26}$$

where Z is the atomic number of the material. The critical energy for electrons is well below 100 MeV in most materials, while for muons the critical energy is typically of the order of several hundred GeV. Coulomb scattering, introduced in Section 4.1.3, does affect the particle direction and thus contributes to the lateral expansion of the shower, but does not contribute to the energy loss.

The mean energy loss of charged particles heavier than electrons through ionization of the surrounding material can be approximated by the Bethe formula [78]

$$\frac{dE}{dx} = Kz^2 \frac{A}{Z} \frac{1}{\beta^2} \left(\frac{1}{2} \ln \frac{2m_e c^2 \beta^2 \gamma^2 E_{\text{max}}}{I^2} - \beta^2 - \frac{\delta(\beta\gamma)}{2} \right), \tag{4.27}$$

where A is the atomic number of the absorber material, I is the mean excitation energy, E_{max} is maximum transferred energy for each interaction and $\delta(\beta\gamma)$ is a density dependent correction factor. With the electron mass m_e and the classical electron radius $r_e = \frac{e^2}{4\pi\epsilon_0 m_e c^2}$ the constant K is given by $K = 4\pi N_A r_e^2 m_e c^2$. The Bethe formula is a good approximation in the range $0.1 < \beta\gamma < 1000$. Particles with an energy loss around the minimum of the Bethe formula are called Minimum Ionizing Particles (MIPs).

The energy loss of a MIP is described by a Landau distribution [79] which is asymmetric and has a long tail towards high energies. If the energy transfer in an ionization process is high, the resulting free electron is called a δ electron. Due to its high energy it will lead to more ionization along its path.

The dominating interactions of photons with matter are the photoelectric effect for very low energies (hundreds of GeV and less), Compton scattering for intermediate energies and e^+e^--pair production for high energies (several MeV and more). For positrons, the annihilation with an electron is another process of energy deposition and leads to the creation of a secondary photon.

If a highly energetic particle enters material, its energy is successively reduced by the processes listed above until it is eventually absorbed. The secondary particles that are created, i.e. photons and e^+e^--pairs, also lose their energies through these processes and produce more secondary particles such that the energy of the initial particle is distributed over a shower of secondary particles. The shower builds up to a maximum until the average energy of the secondary particles drops below the energies where pair production or Bremsstrahlung are dominating, such that the number of particles does not multiply further.

The longitudinal shower development can be described in a material independent way by the radiation length X_0. The radiation length is defined as the average pathlength in an absorber material after which the initial energy of an electron or positron is reduced by approximately 63.2% ($E = E_0/e$). The radiation length of any given material can be approximated by [78]

$$X_0 = \frac{716.4\ A}{Z(Z+1)\ln(287/\sqrt{Z})}\frac{\mathrm{g}}{\mathrm{cm}^2}. \tag{4.28}$$

In the limit of very high energies, the radiation length also describes the mean free path length of photons, which can be approximated as $\frac{9}{7}X_0$.

The lateral shower size can be characterized similarly in a material independent way. The Molière radius, which is defined as the radius of the cylinder around the shower axis that contains on average 90% of the shower energy, is given by [77]

$$\rho_\mathrm{M} = m_e\ c^2\sqrt{\frac{4\pi}{\alpha}}\frac{X_0}{\epsilon_\mathrm{c}} \approx 21.2\,\mathrm{MeV}\frac{X_0}{\epsilon_\mathrm{c}}. \tag{4.29}$$

4.2.2 Hadronic Showers

Hadrons will lose their energy in strong interactions with the nuclei of the absorber material, when passing through matter. Charged hadrons also lose some of their energy through ionization or pair production, as explained above, but will eventually enter a nuclear interaction.

The inelastic scattering of a highly energetic hadron with a nucleus usually leads to spallation of the nucleus. In the first stage of the nuclear reaction, a cascade of intranuclear reactions leads to the release of high energetic mesons and nucleons in direction of the incident particle. In the slower evaporation phase of the spallation, low energetic nucleons, α-particles and photons are released isotropically from the excited nucleus. The fraction of a hadronic shower energy that is lost in the binding energy through the release of fragments of a nucleus is intrinsically invisible.

The spallation protons lose a large part of their energy through ionization. The neutrons on the other hand can lose their energy only through nuclear interactions that can produce secondary α-particles and photons. For kinetic energies below 1 MeV, elastic scattering is the dominant interaction for neutrons. The maximum transferred energy in these elastic scattering processes is proportional to $1/A$. This is the reason that an active material that contains hydrogen is especially sensitive to the neutron component of

a hadronic shower.

A hadronic shower always contains also an electromagnetic component. This is due to the creation of π^0 and η-particles, which both decay into two photons. The average fraction of the shower energy that is deposited via electromagnetic processes depends on the absorber material as well as the energy and the type of the initial hadron. Proton showers do not produce π^0s in the initial hadronic interaction and thus have a considerable smaller electromagnetic component.

The longitudinal development of hadronic showers is characterized by the mean free path length of a hadron in a material, also referred to as nuclear interaction length λ_I. In addition to the absorber material, the interaction length depends on the particle type and can be up to 50% longer for pions than for protons. In this thesis λ_I always refers to the interaction length of a proton.

4.2.3 Energy Resolution

The resolution of a calorimeter is influenced by a large number of factors. These factors depend differently on the particle energy. Since they are mostly uncorrelated the energy resolution can be parametrized as

$$\frac{\sigma(E)}{E} = \frac{s}{\sqrt{E}} \oplus \frac{n}{E} \oplus c, \tag{4.30}$$

where s is the *sampling* term, n is the *noise* term and c is the *constant* term. The effects contributing to these three terms are briefly discussed below.

Sampling Term

The energy that is measured in a calorimeter is deposited discretely, e.g. in ionization electrons or Čerenkov photons. The number of energy depositions N is proportional to the energy, $N = kE$. Ideally, the calorimeter response is also proportional to number of individual energy deposits, such that the only uncertainty originates from the Poisson fluctuations of the number of created energy deposits. This leads to the stochastic uncertainty in the energy resolution

$$\frac{\sigma(N)}{N} = \frac{1}{\sqrt{N}} \tag{4.31}$$

$$\Rightarrow \left.\frac{\sigma(E)}{E}\right|^{\text{sampling}} = \frac{a}{\sqrt{E}}, \tag{4.32}$$

where a depends on k convolved with the signal collection efficiency of the detector.

In case of a sampling calorimeter only a fraction of the deposited energy is directly measured. The average measured energy in an active layer is proportional to the total deposited energy, while each individual energy deposition fluctuates following the Poisson statistics. This introduces another uncertainty described by Eq. (4.32), where the factor a depends by the ratio of material thicknesses between active and passive layers, the sampling fraction.

In addition to these two effects which apply to electromagnetic and hadronic showers, the uncertainty due to the fluctuation of the fraction of invisible energy, i.e. energy lost in binding energy, in hadronic showers also scales with $\sigma(E)/E \propto 1/\sqrt{E}$. Similarly, the fluctuation of the electromagnetic shower content in a hadronic shower fluctuates from event to event and introduces another uncertainty only observed in hadronic showers. This uncertainty scales with $\sigma(E)/E \propto E^{-j}$, where j is typically less than 0.5. The value of j of a given calorimeter depends on the different response of the calorimeter to electromagnetic and hadronic energy deposits. The deterioration of the resolution due to this effect can

be avoided if the calorimeter is compensating, which is discussed in Eq. (4.34).

Due to these additional effects, the energy resolution of hadronic showers is necessarily worse than the resolution for electromagnetic showers. In addition, the sampling fluctuations in hadronic showers are much larger than in electromagnetic showers since the energy deposited through ionization by charged hadrons as well as slow spallation protons is usually very different from the minimum ionization energy.

Noise Term

Electronic noise inevitably adds some energy to the energy collected from the shower. This amount of noise depends on the detector technology, thresholds, amplification factors and the number of channels used to calculate the energy sum of the shower. It is independent of the shower energy and thus results in an uncertainty on the energy measurement of

$$\left.\frac{\sigma(E)}{E}\right|^{\text{noise}} = \frac{n}{E}. \tag{4.33}$$

Constant Term

If the shower is not fully contained in the calorimeter only a part of the shower energy is measured. The amount of leakage depends on the particle energy, which fluctuates strongly for each event, since it strongly depends on the position of the first hard interaction as well as the random shower development. The leakage thus leads to an energy dependent uncertainty that translates to a constant term in the relative energy resolution

$$\left.\frac{\sigma(E)}{E}\right|^{\text{constant}} = c. \tag{4.34}$$

Compensation

As described in Eq. (4.30), a different response to electromagnetic and hadronic showers in a calorimeter will lead to an additional uncertainty in the energy measurement. This can be avoided in two ways. If the calorimeter is designed in a way that these responses are identical it is called a compensating calorimeter. This can be tested for example by comparing the response of the calorimeter to electron and pion showers. The effect can also be reduced by applying different weighting factors depending on the particle type, e.g. proton or pion. An effective correction can only be achieved by determining the electromagnetic shower content on an event by event basis, since the electromagnetic shower content is fluctuating.

4.2.4 Digital Calorimetry

Since most of the energy of a shower is deposited through ionization which are roughly of similar energy one can also estimate the shower energy by counting these energy deposits, referred to as digital calorimetry. This is only possible if the cells in the calorimeter are small compared to the typical shower size. This technology significantly reduces the amount of data required to read out from each calorimeter cell, which is an essential prerequisite for having very small cell sizes that are read out individually. The option of a digital HCal has been first proposed for a TESLA detector assuming $1 \times 1\,\text{cm}^2$ cells [80].

This technology can be refined by using one or more additional thresholds to separate between high and low energetic deposits. This is referred to as semi-digital calorimetry [81].

4.2.5 Linearity

The energy measurement of a calorimeter is only useful if its response is proportional to the deposited energy. Saturation effects can lead to a non-linear behavior at high energies and are more common in electromagnetic showers which deposit the energy in a smaller volume. Energy dependent weighting factors can be used to correct for this and can improve the linearity.

4.2.6 Jet Energy Measurement

The measurement of the energy of a jet, which consists of several particles that enter the calorimeter in a narrow region, strongly depends on the type of particles in the jet. This composition fluctuates strongly on an event by event basis due the randomness of the hadronization of the original quark(s). If the jet can not be resolved into individual calorimeter clusters for the individual particles in the jet, the achievable energy resolution is necessarily worse than the resolution for a single hadronic particle, since an additional uncertainty on the electromagnetic content of the shower is introduced.

4.3 Detector Requirements for a CLIC Experiment

The design of any future experiment is directly motivated by the requirements imposed by its physics goals. The physics case for a future linear collider experiment is the precision measurement of various observables of the SM and investigations of possible extensions of the SM or deviations from it, as discussed in Chapter 2. The implications for the detector design of a future linear collider experiment have been formulated for TESLA [82], the ILC [18, 21, 22] and recently for CLIC [23]. Despite differences in the available center-of-mass energy and thus in the physics reach of the experiments at these colliders, the resulting detector requirements are rather similar. The requirements on the basic observables are summarized from [23] together with their physics motivation.

Track Momentum Resolution The precise measurement of leptonic final states requires excellent momentum resolution, $\sigma(p_T)/p_T^2$, of the order of $2 \times 10^{-5}\,\mathrm{GeV}^{-1}$ or better. This requirement ensues from the Higgs boson mass measurement through Higgsstrahlung process discussed Section 2.2.2. Similar requirements are imposed by the measurement of the cross section times branching ratio of Higgs into two muons, as discussed in Section 10.5.

Jet Energy Resolution The jet energy resolution $\sigma(E)/E$ has to be around 3.5%-5% in the range from 1 TeV to 50 GeV, to precisely identify hadronic final states. Many BSM scenarios predict multi-jet final states, like the chargino pair production process, $e^+e^- \to \tilde{\chi}_1^+\tilde{\chi}_1^- \to W^+W^-\tilde{\chi}_1^0\tilde{\chi}_1^0$, in supersymmetric models. These require the identification and separation of hadronic decays of W, Z and h bosons to supress background processes [83].

Impact Parameter Resolution The precise reconstruction of secondary vertices requires an excellent impact parameter resolution and is necessary for efficient flavor tagging. This is for example important for identifying b jets like in the measurement of the Higgs coupling to b quarks [84] or the measurement of the triple Higgs coupling, $e^+e^- \to h\nu_e\bar{\nu}_e \to hh\nu_e\bar{\nu}_e$. Using the parametrization for the d_0 resolution given in Eq. (4.21) the desired resolution is $a \leq 5\,\mu\mathrm{m}$ for the point resolution and $b \leq 15\,\mu\mathrm{m} \cdot \mathrm{GeV}$ for the term depending on the material budget.

In addition, the particle identification capabilities, especially for leptons, should be excellent to correctly identify event topologies. This goes together with the required excellent coverage of the detector

also in the forward region to correctly identify event topologies with particles created at low polar angles.

4.4 The Particle Flow Paradigm

Traditionally the jet energy is measured as the energy sum of the energy deposits in the calorimeters in a region around the jet axis. The desired jet energy resolution of 3.5% to 5% (see Section 4.3) translates into a energy resolution of $\sigma(E)/E \approx 30\%/\sqrt{E/\mathrm{GeV}}$ [85], which is significantly better than what has been achieved in previous experiments using sampling calorimeters and thus novel approaches are required to reach this energy resolution.

One solution to this problem might be dual-readout calorimetry [86, 87] which aims for ultimate hadronic energy resolution. By individually measuring the response to the electromagnetic and hadronic shower components (see Section 4.2.2) the largest uncertainty in the energy measurement of hadronic showers and jets is removed. In this case, a compensating calorimeter, as explained in Eq. (4.34), is not required and the calorimeter can be optimized for the best intrinsic sampling resolution.

The second approach is particle flow [88, 89], which aims at identifying the showers of the individual particles that constitute the jet and measure their individual four momenta. This idea has evolved from the concept of energy flow which has for example been used in the ALEPH [90] experiment to successfully improve its jet energy resolution.

The average particle content in a jet has been measured at LEP [91] and consists approximately of 62% charged particles, 27% photons, 10% neutral hadrons and 1.5% neutrinos. If the showers of these particles can be resolved, the total jet energy resolution can be significantly improved. Especially the energy of charged particles can be determined from the track momentum measurement with far greater accuracy than achievable in the calorimeters. For photons the energy resolution in the Electromagnetic Calorimeter (ECal) applies, which leaves only a small fraction of the jet energy, the neutral hadrons, that has to be measured in the HCal directly.

The main goal of particle flow is thus not the actual energy measurement but the correct identification of the individual showers. This requires a highly segmented calorimeter (laterally and longitudinally) as well as a sophisticated pattern recognition. The largest source of uncertainty in a particle flow energy reconstruction comes from confusion. For example, if a shower from a neutral particle is not resolved from that of a neighboring charged particle and the energy of the charged particle determined from its momentum is used, the total reconstructed energy will be too low. On the other hand, if a subcluster of a charged particle shower is identified as an individual neutral shower, the total energy will be overestimated. This shows that, despite not being used for most of the direct energy measurement, a good energy resolution of the calorimeter is still important to identify discrepancies between the energy determined from the track momentum and the energy of the corresponding calorimeter shower. Significant leakage will also contribute to the confusion if the algorithm compensates longitudinal energy loss by identifying neighboring neutral clusters as parts of a charged cluster instead.

It should be noted that $\sigma(p_\mathrm{T})/p_\mathrm{T}$ scales with p_T, as shown in Eq. (4.14), while $\sigma(E)/E$ scales mostly with $\sqrt{E}$. The energy measurement of an energetic charged particles can thus ultimately be more precise in the calorimeters if the contribution of the constant term, i.e. leakage, is small enough. It has been demonstrated in simulation that even at typical jet energies at a CLIC experiment, particle flow will perform better than a pure calorimetric energy measurement [85].

In addition to the requirements on the segmentation of the calorimeters, which depend mostly on ρ_M, X_0 and λ_I of the absorber materials used, the inner radius of the calorimeters and the magnetic field strength are of importance for particle flow. Charged particles will be deflected from their original

trajectory by the magnetic field, and will thus be separated from the neutral particles in a jet and reduce the possible confusion. The strength of the magnetic field and the path length, i.e. the inner radius of the ECal, determine the typical separation and can thus also affect the choice of the lateral segmentation. It has been shown that for ultimate particle flow performance, a larger radius is preferable over a larger magnetic field [85]. This has been driving the design decisions of the ILD concept. The SiD concept, which aims at a more cost effective solution, deviates from that and prefers using a higher magnetic field with a smaller inner radius of the calorimeters. The desired lateral segmentation of the calorimeter has been determined in simulation studies to be 5 mm for the ECal and 30 mm for the HCal [85].

A definitive test of the particle flow paradigm can only be achieved in a full sized experiment since both momentum and energy measurements have to be performed in jet events. Nevertheless, there are efforts to test parts of the concept using test beam data. For example, two events taken in a beam test can be merged offline by displacing them in the calorimeter and adding their signals. This allows to test the effectiveness of a Particle Flow Algorithm (PFA) using real data as demonstrated in [92]. The results indicate that there is no noticeable difference in the performance of PandoraPFA using simulated events or test beam data.

Particle flow event reconstruction is also used in the CMS experiment, which was not designed for that purpose, to improve the jet energy resolution significantly in several event topologies [93].

CHAPTER 5

The CLIC_SiD Detector Model

The Silicon Detector [22] is a concept for an experiment at a future e^+e^- collider. It was originally designed for the ILC [18]. It is an example of a typical 4π multi-purpose detector for high energy collider experiments with highly granular calorimeters according to the particle flow paradigm introduced in Section 4.4. Despite originally being designed for a center-of-mass energy of 500 GeV the concept is an excellent starting point for a detector concept used at collision energies of several TeV. Nevertheless, we have introduced several modifications to the detector concept to account for the different experimental conditions at CLIC.

- The vertex detector layout had to be adapted to avoid high occupancies due to beam induced background.
- The forward region had to be changed completely due to the placement of the final focusing quadrupole and the requirements on its stability.
- The hadronic calorimeters had to be made significantly deeper to avoid leakage due to the higher jet energies.

While the first two points are specific to the CLIC accelerator, the last point is purely due to the higher center-of-mass energy of the collisions compared to the default parameters of the ILC.

This chapter describes the CLIC_SiD model as it is implemented in the GEANT4 simulations used in the CLIC CDR studies and the studies presented in this thesis. Although the simulation model contains some details, as for example cabling and support structures in the tracking detectors, it is still a simplified model. For example, an engineering model has been developed of CLIC_SiD for machine-detector integration studies [94]. In that model, the size of the yoke has been increased to provide sufficient shielding for the magnetic field, which thus yields a more realistic estimate of the overall dimensions.

With an overall length of 12.39 m and a total height of 12.50 m, the detector is rather compact and smaller than for example CMS. An overview of the parameters of the main detector components is given in Table 5.1. Figure 5.1 shows one quadrant of the detector model in the *xy*-plane as well as in the *xz*-plane.

The tracking system is described in Section 5.1. It consists of the vertex detector with five barrel layers in the central region and four disk layers of silicon pixel detectors in the endcaps. The vertex detector is surrounded by the main tracking system, consisting of five barrel layers of silicon strip detectors and four disks of silicon stereo-strip detectors on each side. The tracking system is completed

Table 5.1: Parameters for the main elements of the CLIC_SiD_CDR detector model. The parameters $z_{\text{min/max}}$ are the beginning and end in one half of the detector. While $r_{\text{min/max}}$ are the radii of the inscribing circles for the polygons given in the last column. The polygon column gives the number of corners for polygonal shaped detector elements. All other elements are cylindrical.

	z_{min} [mm]	z_{max} [mm]	r_{min} [mm]	r_{max} [mm]	Polygon
ECal Barrel	0	1765	1265	1404	12
HCal Barrel	0	1765	1419	2657	12
Coil	0	3575	2770	3571	
Yoke Barrel	0	3575	3581	6251	8
ECal Endcap	1657	1796	210	1250	12
HCal Endcap	1805	3395	500	2657	12
Yoke Plug	3395	3675	690	2657	12
Yoke Endcap	3675	6195	690	6251	8
LumiCal	1805	1976	64	240	
BeamCal[A]	2486	2671	0	130	

[A] The BeamCal is centered around the detector axis. The holes for the incoming and outgoing beam pipes, which are not in the center, are described in Section 5.5.2.

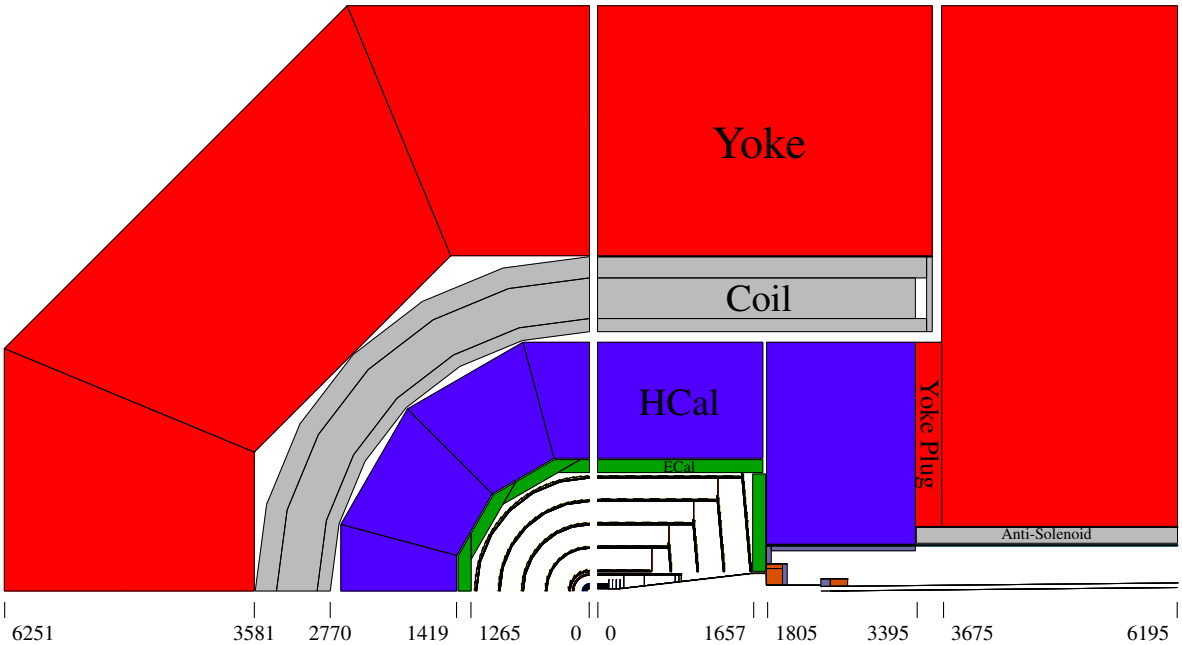

(a) xy (b) zx

Figure 5.1: One quadrant of the CLIC_SiD_CDR detector model in the xy-plane (a) and in the zx-plane (b). Values are given in millimeters.

by three additional silicon pixel disks in the forward region. A solenoidal field of 5 T is provided by a superconducting coil outside of the calorimeters and is described in Section 5.3.

Between the coil and the tracking systems are the calorimeters which are discussed in Section 5.2. The silicon-tungsten ECal and the HCal are highly granular sampling calorimeters following the particle flow paradigm. The HCal is instrumented with scintillator plates and steel is used as the absorber material in the endcaps. Tungsten is used as the absorber material in the HCal barrel in order to keep the size of the coil feasible.

The iron yoke, which surrounds the whole detector, is instrumented with Resistive Plate Chambers (RPCs). It helps with the identification of muons and serves as a tail-catcher for the HCal and is described in Section 5.4.

Section 5.5 describes the far forward region of the detector. There, the Luminosity Calorimeter (LumiCal) and the BeamCal complement the coverage for electromagnetic showers provided by the ECal. The design of the forward region is driven by the requirements for the QD0. The QD0 is placed behind the BeamCal and has to be supported by a large support tube from the tunnel walls in order to achieve the required stability.

The occupancies due to the machine-induced backgrounds in the tracking detectors are discussed in Section 5.6.

5.1 Tracking System

The all-silicon tracking system in CLIC_SiD is designed to provide excellent point resolution combined with low material budget. The pixel detectors (see Section 5.1.1) and the main tracking system (see Section 5.1.2) form an integrated system that provides at least ten precisely measured points for all tracks down to a polar angle of about 15° and at least six measured points down to a polar angle of about 8°, as shown in Fig. 5.2. A cut through the tracking region of CLIC_SiD is shown in Fig. 5.3.

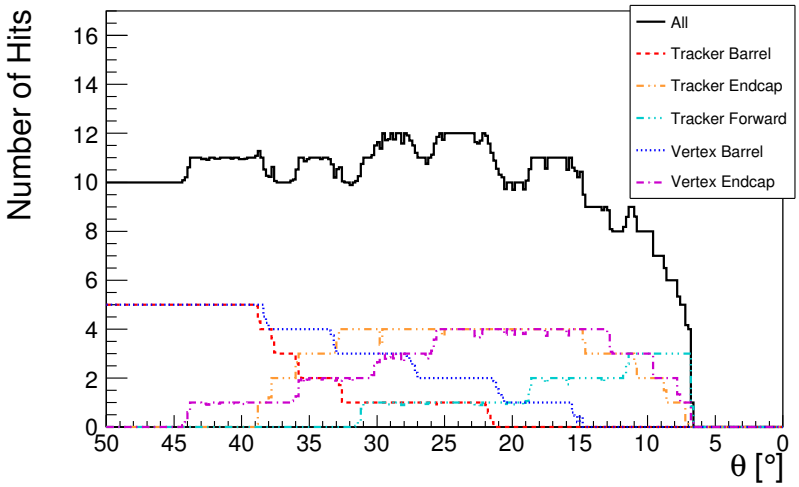

Figure 5.2: Coverage of the tracking systems with respect to the polar angle θ. Shown is the average number of hits created by a 500 GeV muon in full simulation. At least six hits are measured for all tracks with a polar angle down to about 8°.

The layers of the tracking detectors are made up of individual modules including realistic overlaps. Beyond that, the modules are not segmented in the simulation model, instead, the segmentation into strips and pixels is applied during the digitization step of the reconstruction, as discussed in

Section 6.3.2. Nevertheless, the assumed pitches for the strip and pixel detectors are given here for completeness.

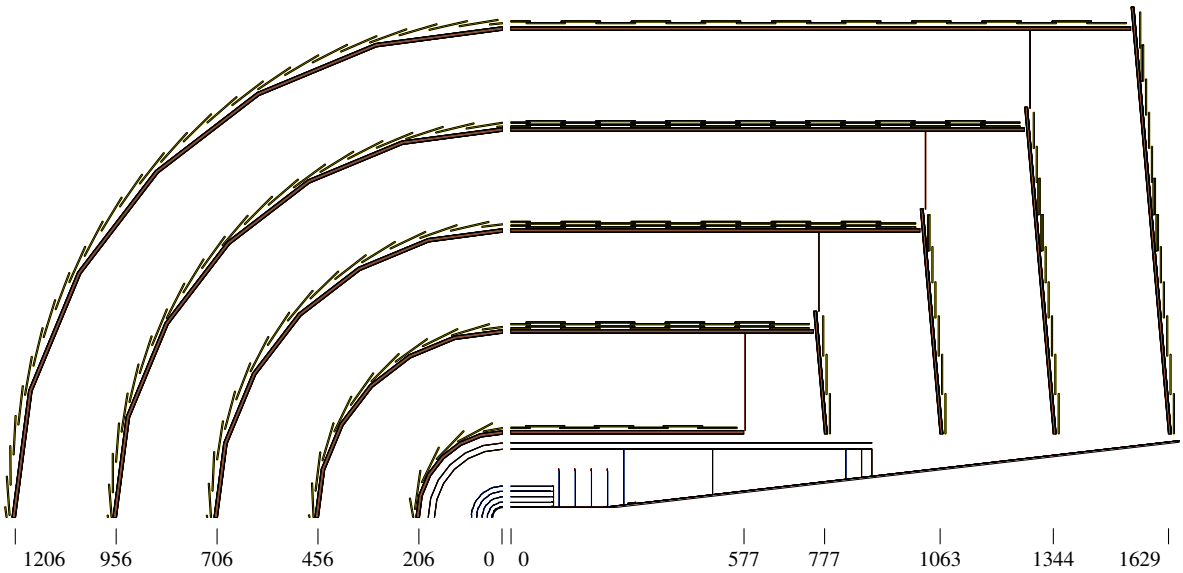

(a) *xy* (b) *zx*

Figure 5.3: Layout of the tracking system in CLIC_SiD in the *xy*-plane (a) and in the *zx*-plane (b). The main tracker modules are displayed in yellow and support structures are displayed in brown. A detailed view of the vertex detector can be found in Fig. 5.4 and Fig. 5.5. Values are given in millimeters.

5.1.1 The Vertex Detector

The layout of the vertex detector system has been changed significantly with respect to the default SiD layout to account for the background from incoherent pairs. For example, the radius of the first layer has been increased from 15 mm to 27 mm. All other radii are changed accordingly. The length of the barrel section has been increased from 62.5 mm to 100 mm to provide a similar coverage in the polar angle. The disk detectors have been moved out accordingly and the distances between the disks, especially in case of the forward disks, has been modified to a more equidistant layout. A systematic fast simulation study of various vertex detector layouts including varying assumptions on the material budget can be found in [95].

Vertex Detector Barrel

The vertex barrel detector consists of five concentric layers. Each layer is made up by several modules as described in Table 5.2. Each module consists of 50 µm of silicon ($\approx 0.053\% X_0$) followed by 130 µm of carbon ($\approx 0.061\% X_0$) as support. The silicon is segmented into 20×20 µm ^{2} pixels. Figure 5.4 shows the arrangement of the layers and the modules in the vertex barrel detector.

The vertex detector for CLIC will have to combine high spatial resolution with a low material budget. While these requirements are similar to those of an ILC vertex detector, CLIC will require also high time resolution to mitigate the high occupancy due to beam induced backgrounds. There is currently no pixel technology available that fulfills all requirements of the CLIC vertex detector. In terms of

material budget, the key issue will be the use of power pulsing, i.e. switching off the detector between two bunch trains, to reduce the power consumption. In the current design no cooling except for air cooling is foreseen. The alternative would be evaporative cooling using CO_2, which would increase the material budget due to the required pipes. For the pixel technologies multiple integrated pixel solutions are pursued, like for example designs based on the TimePix chip [96], the MIMOSA sensors [97], the CHRONOPIXEL sensors [98] or fully integrated solutions based on Silicon On Insulator [99] or 3D architectures [100]. For a detailed discussion on the possible pixel technologies we refer to [23].

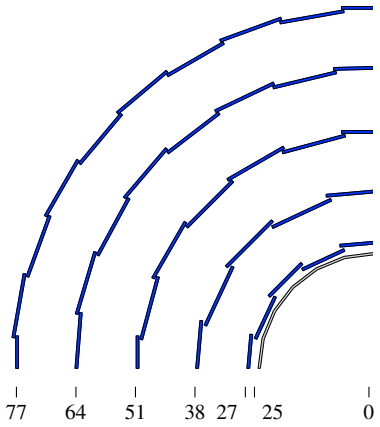

Figure 5.4: Layout of the vertex barrel detector in the xy-plane. Values are given in millimeters.

Table 5.2: Parameters for the vertex detector barrel layers. The number of modules N in the layer, the mean radius r of the layer, the half-length z of the module and width w of the module are given. Each module consists of a layer of 50 µm of silicon followed by 130 µm of carbon fiber.

Layer	N	r [mm]	z [mm]	w [mm]
1	18	27.0	98.5	9.8
2	18	38.0	98.5	13.8
3	24	51.0	98.5	13.8
4	30	64.0	98.5	13.8
5	36	77.0	98.5	13.8

Vertex Detector Endcap and Forward Tracking Disks

There are seven pixel disks covering the forward and far-forward region of the detector. The first four disks are close together and are considered part of the vertex detector. The three forward tracking disks extend the coverage of the tracker endcap to the beam pipe. All pixel disks consist of several trapezoidal modules as described in Table 5.3. Like in the vertex barrel each module consists of 50 µm of silicon ($\approx 0.053\% X_0$) followed by 130 µm of carbon ($\approx 0.061\% X_0$), with the silicon being segmented into 20×20 µm ^{2} pixels. For the pixel technology the same applies as for the vertex barrel detector.

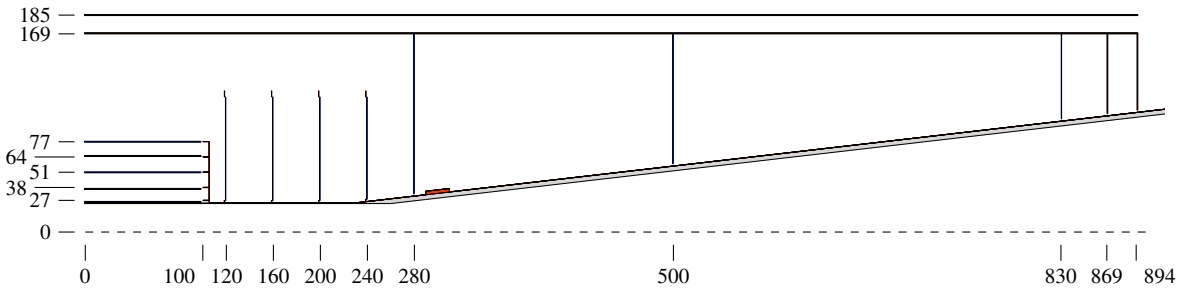

Figure 5.5: Layout of the vertex region in CLIC_SiD in the zx-plane. Shown are the vertex barrel layers, the vertex endcap disks and the forward tracking disks together with the vertex support, cabling and the central beam pipe. All values are given in millimeters.

Table 5.3: Parameters for the vertex endcap and forward tracking disks. The number N of trapezoidal modules, the inner radius r_{in}, the outer radius r_{out}, the inner width w_{in}, the outer width w_{out} and the position in z of the modules are given. Each module consists of a layer of 50 µm of silicon followed by 130 µm of carbon fiber.

Disk	N	r_{in} [mm]	r_{out} [mm]	w_{in} [mm]	w_{out} [mm]	z [mm]
1	16	27.0	115.0	10.8	45.1	120.0
2	16	27.0	115.0	10.8	45.1	160.0
3	16	27.0	115.0	10.8	45.1	200.0
4	16	28.1	115.0	11.3	45.1	240.0
5	16	32.8	168.7	13.1	66.2	280.0
6	16	58.2	168.7	23.3	66.2	500.0
7	16	96.4	168.7	38.6	66.2	830.0

Vertex Detector Support and Cabling

The vertex detector and the forward tracking disks are supported by a double-walled carbon fiber tube with an inner radius of 168.7 mm, an outer radius of 184.7 mm and a half length of 894.8 mm. This tube is supported from the beam pipe by two carbon fiber disks at each end of the tube. The first one is placed at 868.8 mm in z with an inner radius of 100.9 mm and the second one is placed at 894.3 mm in z with an inner radius of 103.9 mm. The outer radius for both disks is 168.7 mm. The thickness of each carbon fiber wall and disk is 0.5 mm. The support tube fits inside the main tracker, as shown in Fig. 5.3(b) and the vertex detector can thus be removed together with the beam pipe when opening the detector.

Some estimation of required cabling is included in the simulation model. Copper disks are placed at the end of the barrel layers connecting down to the beam pipe. A copper layer around the beam pipe represents the connection to the outside of the detector. Routing the cables along the support tube instead of the beam pipe might be beneficial for the impact parameter in the far forward region since it removes some material in front of the first measurement layer.

5.1.2 Main Tracking System

The main tracking system is unchanged with respect to the SiD concept since the requirement on the momentum resolution are very similar. The segmentation is sufficient to provide robust pattern recognition also in presence of the $\gamma\gamma \rightarrow$ hadrons background at CLIC as shown in Chapter 7.

Main Tracker Barrel

The main tracking barrel detector consists of five layers of silicon strip detectors. The overall dimensions of the layers are given in Table 5.4. Each layer is made from several square modules with a size of 97.8×97.8 mm^2. Each module consists of 0.3 mm of sensitive silicon ($\approx$ 0.32% X_0) and 2.6 mm of support and electronics ($\approx$ 0.19% X_0). A detailed description of the material in each module can be found in Table 5.5(a). The readout assumed for the strip detectors is the KPiX ASIC [101] developed for the SiD concept. It is designed to provide time resolution of several hundred nanosecons, which is sufficient to resolve individual bunch crossings at the ILC. For CLIC this has to be improved to a time resolution of the order of 5 ns.

The silicon strips run along the z-direction and, with a length of 92.03 mm, span almost the whole module. Their pitch is 25 µm, with only every second strip being read out directly, while the intermediate strip is read out via capacitive coupling (see Section 6.3.2). The readout pitch is thus 50 µm.

Table 5.4: Parameters for the barrel tracker layers. The number N of modules in the layer in z and ϕ, the mean radius of the layer r and the half-length of the layer z are given. Each module consists of 300 µm of silicon and 2.6 mm of support material (see Table 5.5(a)).

Layer	N_z	N_ϕ	r [mm]	z [mm]
1	13	20	230.0	578.0
2	17	38	483.0	749.8
3	23	58	725.5	1013.9
4	29	80	988.5	1272.3
5	35	102	1239.0	1535.7

Table 5.5: Materials and corresponding thicknesses d in each of the modules in the tracker barrel (a) and in the tracker endcap (b), ordered as seen from the interaction point. The carbon fiber and ROHACELL31 used in the main tracker modules have only half of their nominal densities and thus twice the radiation length.

(a) Tracker barrel module

Material	d [µm]
Copper	3.8
Kapton	38.0
Silicon (passive)	4.8
Silicon (sensitive)	300.0
Carbon Fiber (50%)	160.0
Epoxy	175.0
ROHACELL31 (50%)	1800.0
Carbon Fiber (50%)	160.0
PEEK	200.0

(b) Tracker endcap module

Material	d [µm]
Copper	5.2^{A}/ 7.9^{B}
Kapton	51.0^{A}/ 78.0^{B}
Silicon (passive)	4.8
Silicon (sensitive)	300.0
Carbon Fiber (50%)	160.0
Epoxy	175.0
ROHACELL31 (50%)	1800.0
Carbon Fiber (50%)	160.0
Silicon (sensitive)	300.0
Silicon (passive)	4.8.0
Kapton	51.0^{A}/ 78.0^{B}
Copper	5.2^{A}/ 7.9^{B}

A Material in the inner three rings.
B Material in the outer rings.

Main Tracker Disks

The tracker endcap consist of four silicon stereo strip layers. Each layer consists of several rings of trapezoidal modules. The rings are arranged to follow a conical shape, as shown in Fig. 5.3(b)). A detailed description of the dimensions of the individual disks is given in Table 5.6.

Each module in the tracker endcap has two layers of 0.3 mm of sensitive silicon, since they are modelled as stereo strip detectors, amounting to about 0.64% X_0, and other material representing support and electronics, as described in detail in Table 5.5(b). The modules used in the inner three rings have a radial extent of 100.1 mm and the modules in the outer rings have a radial extent of 89.8 mm.

Like for the tracker barrel, the silicon strips have a pitch of 25 µm, while the readout pitch is 50 µm. The readout is assumed to be the KPiX chip mentioned above. The strips in the first sensitive layer are perpendicular to one side of the trapezoid, while the strips in the second sensitive layer are perpendicular to the other side of the trapezoid, which then automatically defines the stereo angle. The layout of the

inner and outer modules is chosen, such that in both cases the stereo angles between the two sensitive layers is 12°.

Table 5.6: Parameters for the tracker endcap disks, which are made of trapezoidal modules that are arranged in rings. The number of modules N, the inner radius r_{in}, the outer radius r_{out}, the two widths of the trapezoid $w_{\text{in/out}}$ and the position in z of the modules within the ring are given. The material budget of the modules is described in Table 5.5(b).

Disk	N	r_{in} [mm]	r_{out} [mm]	w_{in} [mm]	w_{out} [mm]	z [mm]
1	24	206.7	306.7	72.2	93.3	787.1
	32	304.0	404.0	72.2	93.3	778.8
	40	399.2	499.2	72.2	93.3	770.5
2	24	206.7	306.7	72.2	93.3	1073.3
	32	304.0	404.0	72.2	93.3	1065.0
	40	399.2	499.2	72.2	93.3	1056.7
	40	493.5	583.5	90.5	109.4	1048.5
	48	580.7	670.7	90.5	109.4	1041.1
	54	658.7	748.7	90.5	109.4	1033.7
3	24	206.7	306.7	72.2	93.3	1353.8
	32	304.0	404.0	72.2	93.3	1345.5
	40	399.2	499.2	72.2	93.3	1337.2
	40	493.5	583.5	90.5	109.4	1329.0
	48	580.7	670.7	90.5	109.4	1321.6
	54	658.7	748.7	90.5	109.4	1314.2
	58	748.4	848.4	90.5	109.4	1306.8
	64	829.2	919.2	90.5	109.4	1299.5
	68	913.4	1003.4	90.5	109.4	1292.2
4	24	206.7	306.7	72.2	93.3	1639.2
	32	304.0	404.0	72.2	93.3	1630.8
	40	399.2	499.2	72.2	93.3	1622.6
	40	493.5	583.5	90.5	109.4	1614.3
	48	580.7	670.7	90.5	109.4	1606.9
	54	658.7	748.7	90.5	109.4	1599.6
	58	748.4	841.4	90.5	109.4	1592.2
	64	829.2	919.2	90.5	109.4	1584.9
	68	913.4	1003.4	90.5	109.4	1577.6
	72	996.0	1096.0	90.5	109.4	1570.2
	78	1079.2	1169.2	90.5	109.4	1562.9
	84	1161.9	1251.9	90.5	109.4	1555.6

Main Tracker Support and Cabling

The barrel modules are mounted on carbon fiber cylinders. The endcap modules are mounted on conical disks made of carbon fiber as indicated in Fig. 5.3(b). In addition copper disks are added at the end of each of the barrel layers to represent cables. Like for the vertex detector only air cooling is assumed and no material is added for other cooling mechanisms. Thus, also here power pulsing with the repetition

rate of the bunch trains is an essential requirement.

5.1.3 Tracker Material Budget

The total amount of material in the vertex detector amounts to approximately 1% X_0, including the beam pipe discussed in Section 5.5.3 but excluding the vertex detector support tube. The whole tracking region amounts to approximately 7% X_0 at a polar angle of 90°. This value slowly increases towards lower polar angles, as shown in Fig. 5.6. At $\theta \approx 42°$ the material budget rises sharply because of the forward disks which are traversed at a shallow angle. For even lower polar angler the total material budget decreases in steps, depending on how many of the main tracker disks are traversed. The conical part of the beam-pipe is designed to be pointing (see Section 5.5.3) and thus results in a huge material budget at its opening angle of $\theta \approx 7°$. Otherwise the total material budget of the tracking region never exceeds 20% X_0.

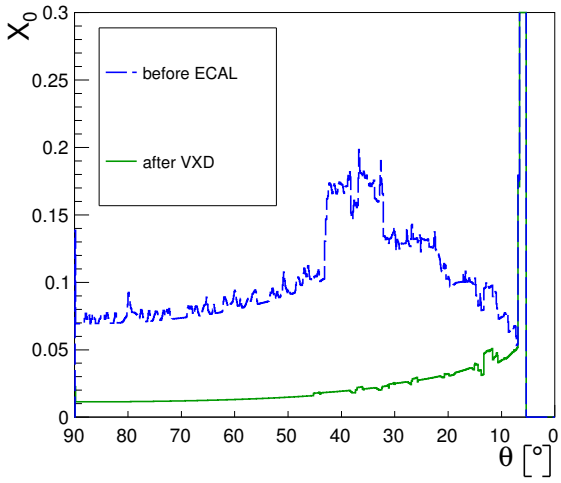

Figure 5.6: The material budget in the tracking region given in radiation lengths X_0, with respect to the polar angle θ. The conical beam pipe causes the sharp peak at $\theta \approx 7°$. Figure kindly provided by Astrid Münnich.

5.2 Calorimeters

As discussed in Section 4.4, the main goal of particle flow calorimetry is to minimize confusion by providing high lateral and longitudinal segmentation. This paradigm also drives the design of SiD and CLIC_SiD.

5.2.1 Electromagnetic Calorimeter

The ECal is a highly segmented tungsten sampling calorimeter with silicon as the sensitive material. The innermost layer of the ECal consists only of a sensitive layer. It is followed by 20 layers with an absorber thickness of 2.5 mm and another 10 layers with an absorber thickness of 5 mm. The absorber material is tungsten. Each layer consists of the absorber material followed by an air gap of 0.25 mm, 0.32 mm of silicon (sensitive), 0.05 mm of copper, 0.3 mm of Kapton and another air gap of 0.33 mm. The cell size in all layers is 3.5×3.5 mm^2. The total material corresponds to approximately 1.0 λ_I or 25.7 X_0. The ECal barrel consists of twelve modules with non-pointing gaps, illustrated in Fig. 5.7(a).

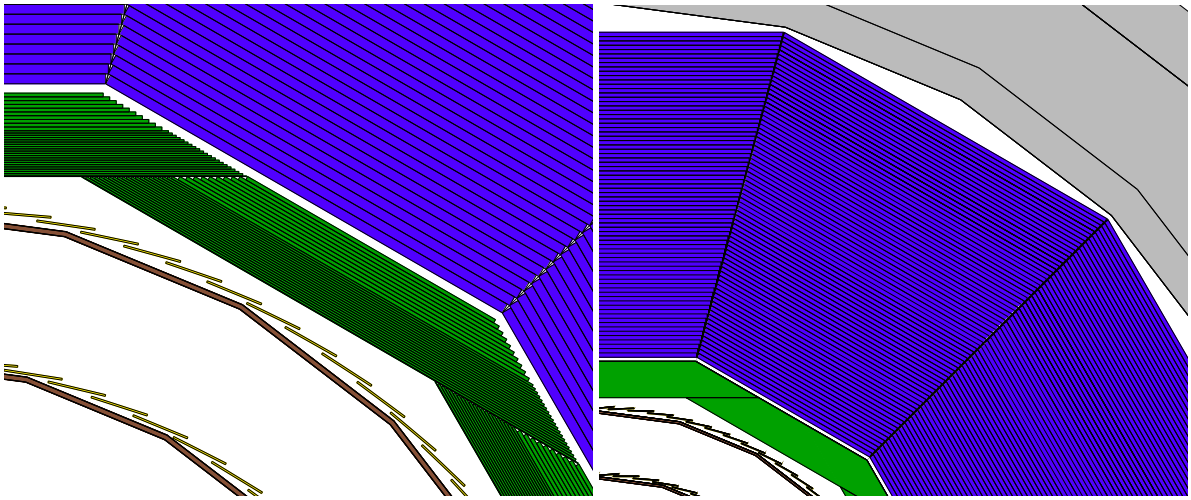

(a) (b)

Figure 5.7: Cut through the barrel region of the electromagnetic calorimeter (a) and the hadronic calorimeter (b), showing the layers and modules.

This layout is identical to that forseen in the SiD model. The total depth is sufficient for most electromagnetic showers also at CLIC and the highly granular HCal works as a tail catcher. The baseline technology for the ECal in SiD is hexagonal silicon pixels with an area of 13 mm^2 which we approximate here using square pixels. The readout has to be fully embedded to minimize the gap sizes. It is forseen to use the KPiX chip [101].

5.2.2 Hadronic Calorimeter

The HCal is a sampling calorimeter with polystyrene plates as the sensitive material. The polystyrene plates have a thickness of 5 mm and are segmented into 30×30 mm^2 cells. In addition to the sensitive layer and the absorber plates described below, there is an air gap of 1.5 mm in each layer. There is no material included to represent electronics. This does not affect the overall material budget significantly. The total gap size of 6.5 mm should be sufficient to accommodate sensitive material and electronics for all sampling calorimeter technologies currently being discussed.

There are 75 layers in the barrel with 10 mm tungsten absorber plates arranged in twelve modules with pointing gaps (see Fig. 5.7(b)). The total material corresponds to 7.9 λ_I. This amount of material does provide sufficient absorption for hadronic showers at CLIC energies, and the sampling provides the best energy resolution in the given space as shown in Chapter 8. In the endcaps there are 60 layers with 20 mm steel plates as absorber material, which corresponds to 7.6 λ_I. There is no need to replace the absorber material in the endcap, since only the size of the HCal barrel is constrained by the coil.

There are many different technologies being considered for the HCal in SiD. Several prototypes have been built and operated in beam tests. These options include scintillators with analog readout using Silicon Photomultipliers (SiPMs) [102] or RPCs with pads that are read out digitally [103]. Alternative gaseous detector options are using MPGD like GEM foils [104] or MicroMegas [105] instead of the pad readout. The baseline for SiD is the digital RPC option with 1×1 cm^2 pads. For CLIC_SiD the analog scintillator option has been chosen since the PandoraPFA algorithm which was chosen as default particle flow algorithm was only validated for analog calorimeter signals.

Another important difference compared to the SiD concept is the increased inner radius of the HCal

endcap of 50 cm to accommodate the support tube for the QD0 as discussed in Section 5.5.4. This results in a significantly reduced acceptance.

5.3 Solenoid and Magnetic Field

The superconducting coil is modelled as an aluminium cylinder, which represents the conductor and the mandrel. It is surrounded by a vacuum layer and a steel layer, which represent the vacuum vessel. The vaccum vessel is closed by steel at its ends. The total thickness of the coil corresponds to approximately 1.5 λ_I. An overview of the parameters of the coil is shown in Table 5.7.

The solenoidal magnetic field is a homogeneous field of 5 T parallel to the detector axis throughout the volume inside of the coil. The field outside of the coil is 1.5 T pointing in the opposite direction of the inner field. There is no field beyond the end of the coil in z-direction.

The coil radius is increased by 18 cm with respect to the SiD design to allow calorimeters of similar depth in the CLIC_ILD and CLIC_SiD models. This radius corresponds approximately to that of the CMS coil [106] which has a nominal field strength of 4 T. Constructing a coil of similar size and with 5 T field will require novel technologies like reinforced conductors [107, 108].

Table 5.7: Parameters of the coil elements. For all elements the material, the longitudinal extent in one half of the detector $z_{min/max}$ and the radial extent $r_{min/max}$ are given.

Material	z_{min} [mm]	z_{max} [mm]	r_{min} [mm]	r_{max} [mm]
Steel	0	3515	2770	2800
Vacuum	0	3515	2800	2910
Aluminium	0	3395	2910	3344
Vacuum	0	3515	3344	3531
Steel	0	3515	3531	3571
Vacuum	3395	3515	2910	3344
Steel	3515	3575	2770	3571

5.4 Instrumented Yoke

The coil is surrounded by an iron return yoke, which shields the experimental area from the magnetic field as well as from radiation. It is instrumented with double-layers of RPCs to help identifying muons.

Each layer consists of two RPC layers, followed by an air gap of 10 mm and the absorber material. There are 18 layers in the barrel and the endcap with 100 mm of iron as absorber material for each layer. The first barrel layer has only 50 mm of iron to give a finer sampling directly after the coil. The second and the last absorber layer in the barrel are twice as thick, in order to take the stress. Unlike the barrel, the yoke endcap begins with an absorber layer and ends with a sensitive layer. The 18 endcap layers have iron absorber plates of 100 mm thickness and are instrumented like the barrel layers.

In addition, a yoke plug fills the gap between HCal and yoke in the endcap region inside of the coil. It is instrumented with an RPC double-layer between two iron layers of 150 mm and 90 mm thickness.

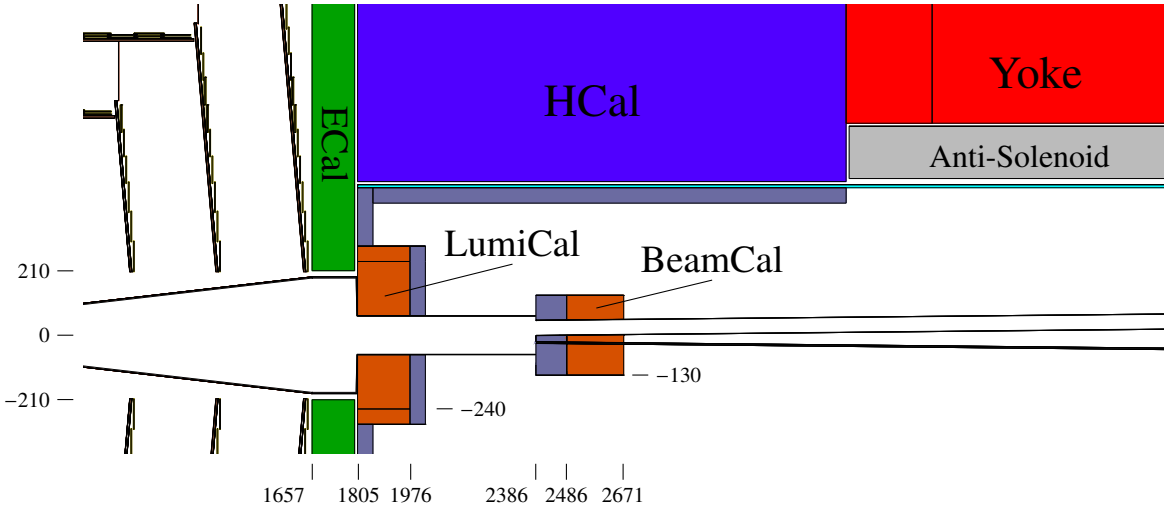

Figure 5.8: Layout of the forward region in CLIC_SiD. The BeamCal and the LumiCal are shown together with the forward part of the beam pipe, the support tube and several shielding and mask elements. Not included are the QD0 which will be placed around the beam pipes inside of the anti-solenoid, a vacuum valve which will be placed between LumiCal and BeamCal and beam monitoring equipment which will be placed behind the BeamCal. All values are given in millimeters.

5.5 Forward Region and Beam Pipe

5.5.1 LumiCal

The LumiCal extends the coverage for the identification of electromagnetic showers down to 64 mm, which corresponds to an opening angle of about 35 mrad. It is placed behind the ECal at a z-position of 1805 mm. The outer radius of 240 mm creates enough overlap with the ECal to avoid a gap in the coverage. Its main purpose is the measurement of the luminosity spectrum through the measurement of Bhabha scattering events but is also important for identifying other forward processes as shown in the analysis in Chapter 10.

The instrumentation is very similar to the one of the ECal described in Section 5.2.1. It also consists of two sections with different absorber thicknesses. The first 20 layers have a tungsten thickness of 2.71 mm and the last 15 layers have a tungsten thickness of 5.43 mm. Each layer consists of the absorber material followed by 0.32 mm of silicon (sensitive), 0.05 mm of copper, 0.3 mm of Kapton and an air gap of 0.33 mm. The cell size is 3.5×3.5 mm^2 and the total material corresponds to 1.4 λ_I or 34.8 X_0. A tube of G10 with a thickness of 50 mm is placed around the LumiCal as a placeholder for readout electronics.

In the simulation model the LumiCal is placed symmetric to the detector axis. This is a simplification since it should be placed centered around the outgoing beam axis.

5.5.2 BeamCal

The BeamCal completes the forward coverage of the electromagnetic calorimeters. It is has an outer radius of 130 mm and it starts at a z of 2486 mm. The BeamCal has two holes for the incoming and outgoing beam pipes. The radius of the hole for the incoming beam pipe is 2.55 mm and the radius for the outgoing beam pipe is 24.91 mm, which corresponds to an opening angle of 10 mrad. This opening

angle is enough to avoid the majority of the coherent pair background (see Section 3.1.3).

The BeamCal consists of 50 layers of 2.71 mm tungsten, 0.32 mm of silicon (sensitive), 0.05 mm of copper, 0.3 mm of Kapton and an air gap of 0.33 mm. Like the other electromagnetic calorimeters, the sensitive layer is segmented into 3.5×3.5 mm^2 cells. Due to the high radiation dose at these low angles, the sensitive detectors have to be radiation hard like for example diamond sensors [109].

A graphite layer of 100 mm is placed in front of the BeamCal in order to absorb backscattered particles [110, 111]. The position in z of the BeamCal including the graphite mask is thus 2386 mm.

5.5.3 Beam Pipe

The central part of the beam pipe is made of beryllium because of its low radiation length. It has an outer radius of 25 mm and a thickness of 0.5 mm. The conical parts and the elements in the far forward region are made of steel. The beam pipe becomes conical at a z of 260 mm with an opening angle of 6.6°. The thickness of the conical beam pipe is 4 mm in radial direction. It has been shown that this amount of steel effectively removes most of the backscattered particles that are created from the beam-related backgrounds in the far-forward region of the detector [110]. The beam pipe reaches a radius of 190 mm at the front face of the ECal and then becomes cylindrical again. This radius is small enough to allow an opening scenario of the detector where the vertex detector is removed together with the beam pipe.

The thickness of the beam pipe in front of LumiCal is 1 mm. A cylindrical beam pipe with an outer radius of 63 mm and a thickness of 1 mm is inside of the LumiCal and continues to the front face of the BeamCal. Two cylindrical beam pipes which are centered around the incoming and outgoing beam axis are placed inside of the BeamCal holes and continue until the end of the detector volume. The outgoing beam pipes are simplified in this model and should instead be conical with an opening angle of 10 mrad.

5.5.4 Accelerator Components

The QD0 has to placed as close to the IP as possible to provide the necessary beam focusing for high luminosity. Alternatively the QD0 would have to be placed outside of the detector which would result in a significantly reduced luminosity [20]. The QD0 has to be stable to around 1 nm during a bunch train which can not be achieved if it is supported from the detector. All of the far-forward detectors and the QD0 will thus be supported from a support tube which is mounted on the tunnel wall to fulfill the stability requirements on the QD0. This support tube is simulated as a iron cylinder inside the HCal and yoke endcaps. The QD0, which would be placed around the incoming beam pipe behind the BeamCal is not represented in the detector simulation.

In addition there are several shielding elements to avoid backscatters from the BeamCal and other far-forward elements to reach the calorimeters. These are modelled as a layer of 50 mm of tungsten behind the LumiCal and the ECal and right inside of the support tube within the HCal endcap.

An anti-solenoid placed right outside of the support tube in the region of the yoke endcap. It is there to protect the QD0 magnet, which includes a permanent magnet, from the field of the central solenoid. The anti-solenoid is also modelled as an iron cylinder.

5.6 Occupancies from Beam-Related-Backgrounds

The occupancies from beam-related backgrounds have been studied in CLIC_ILD [110, 111]. The main differences between the ILD and SiD concepts are the solenoid field strength, i.e. 4 T for ILD and 5 T which affect the angular distributions of charged background particles, as well as the tracking systems, which will be the focus of this section. However, we want to mention one important result

from [110]: the train occupancies in the endcap calorimeters can reach up 60% in the ECal mostly from the $\gamma\gamma \rightarrow$ hadrons background and up to 1100% at the innermost radii in the HCal from incoherent pairs interacting in the outgoing beampipes. This shows that the highly granular calorimeters serve an important purpose at CLIC beyond their intended use for particle flow calorimetry. A highly granular calorimeter gives the possibility to disentangle energy deposits from beam-related backgrounds and physics. For more details on the occupancies in the calorimeters and estimations of radiation doses we refer to those two studies.

5.6.1 Simulation Samples

We study the occupancy using two background samples generated from GuineaPig [65, 68] for the nominal CLIC parameters at a center-of-mass energy of 3 TeV. The incoherent pairs corresponding to one full bunch train and another for the $\gamma\gamma \rightarrow$ hadrons background, corresponding to approximately 10000 bunch trains. Each bunch crossing of incoherent pair background contains approximately 300000 electrons and positrons and can thus not be simulated as one event. Instead, each particle is passed through the full detector simulation individually. The resulting tracker hits are merged together into events corresponding to the signal from 1000 incoherent pair particles, i.e. $\sim 1/300$ of a bunch crossing, before passing it through the hit digitization. For the $\gamma\gamma \rightarrow$ hadrons background we simulate and digitize each event individually, while we expect about 3.2 events in each bunch crossing (see Table 3.1). The steps involved in the simulation and hit digitization are explained in Chapter 6. Consequently each hit represents a reconstructed cluster, i.e. several pixel or strip hits. The resulting hit rates using full digitization are comparable to the rates obtained from counting all simulation hits that deposit more energy than $1/5$ of a MIP as done in [110]. However, using digitized hits allows to directly estimate the occupancy based on resulting cluster sizes.

5.6.2 Hit Densities

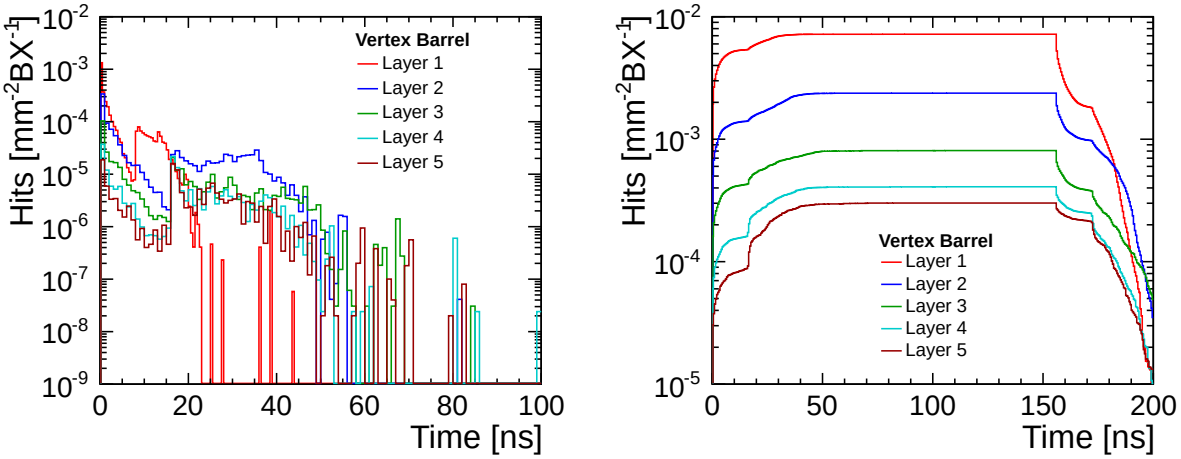

(a) Time structure of hits from a single BX

(b) Time structure of hits in a full bunch train

Figure 5.9: Time dependence of the hit densities in the five vertex barrel layers from incoherent pairs. Shown is the time structure of the hits from a single BX (a) and for a full bunch train (b).

The hits originating from the incoherent pair background originate in parts from backscatters that are

significantly displaced in time as shown in Fig. 5.9(a). These are mostly created in the very forward region, i.e. the BeamCal as well as the outgoing beam pipe. The time delay between these direct and indirect hits is given by the distance of the BeamCal from the IP. A careful design of the BeamCal and its mask is essential to keep these backscatters at manageable levels. A thick conical beam pipe is similarly important to shield the central detectors from these backscatters [110]. A thinner beam pipe, as foreseen in the ILC detectors, results in an increase of hits due to backscatters of one order of magnitude. They would thus constitute the dominating contribution to the total occupancy [110]. The resulting time structure for the full bunch train is shown in Fig. 5.9(b). We obtained the distribution by repeatedly displacing the average time distribution of a single BX and thus, no statistical fluctuations are visible. In the first 15 ns of a bunch train the vertex barrel detectors only experience direct hits. Afterwards backscatters start to arrive in time with the particles from the IP. The highest occupancy levels are reached after 30–40 ns. As a result of this time structure there are hits visible in the detector until 40 ns after the end of a bunch train.

Low p_T particles are confined to small radii by the magnetic field. This does not necessarily apply for backscatters. Thus, for large radii the importance of backscatters increases. The maximum hit density within a bunch train, on the other hand, decreases significantly with larger radii from 7×10^{-3} Hits/mm^2/BX in the first barrel layer of the vertex detector to 2.5×10^{-4} Hits/mm^2/BX in the fifth layer.

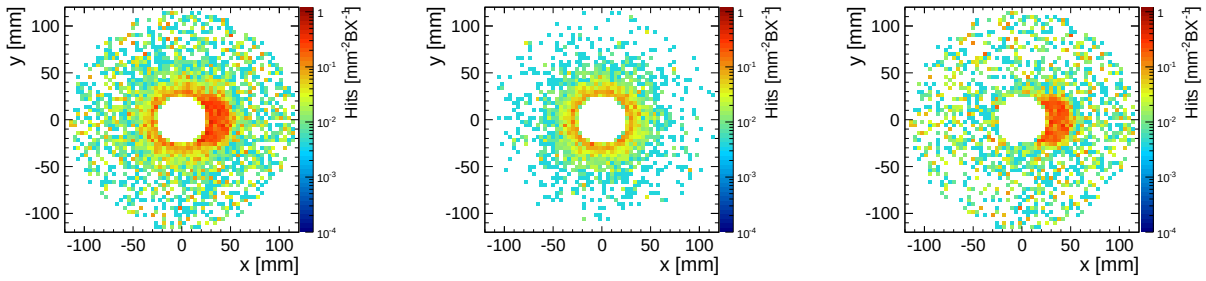

(a) All hits from one BX (b) $t < 15$ ns (c) $t > 15$ ns

Figure 5.10: Hit densities from incoherent pair background in the innermost vertex endcap layer depending on x and y.

The hits that originate from backscatters are not distributed uniformly. They have a strong dependency on the azimuthal angle ϕ originating from the asymmetric shape of the forward region. For example, backscatters created in the outgoing beam pipe can re-enter the detector only through the opening of the BeamCal. This results in hot spots in the tracking detectors from the projection of this opening as shown in Fig. 5.10.

The structure of the hits from the $\gamma\gamma \rightarrow$ hadrons events is quite different from those from the incoherent pairs. The particles are created not as forward and no strong azimuthal dependence of the backscatters is present. The hit densities in all tracking detectors are shown for both backgrounds in Figs. 5.11 to 5.15. In the innermost vertex barrel layers the amount of hits from incoherent pairs exceeds the number of hits for $\gamma\gamma \rightarrow$ hadrons events by one order of magnitude. For higher radii the hit densities are comparable. This is also visible in the distributions of the hit densities in the vertex endcaps (see Fig. 5.13) and the forward tracking disks (see Fig. 5.14) which are similar at all radii greater than 50 mm. At lower radii the backscatters from the incoherent pair background are the dominating background. In the main tracker endcaps the $\gamma\gamma \rightarrow$ hadrons background is dominating, as shown in Fig. 5.15. While the incoherent pair background consists of individual particles the hadronic background consists

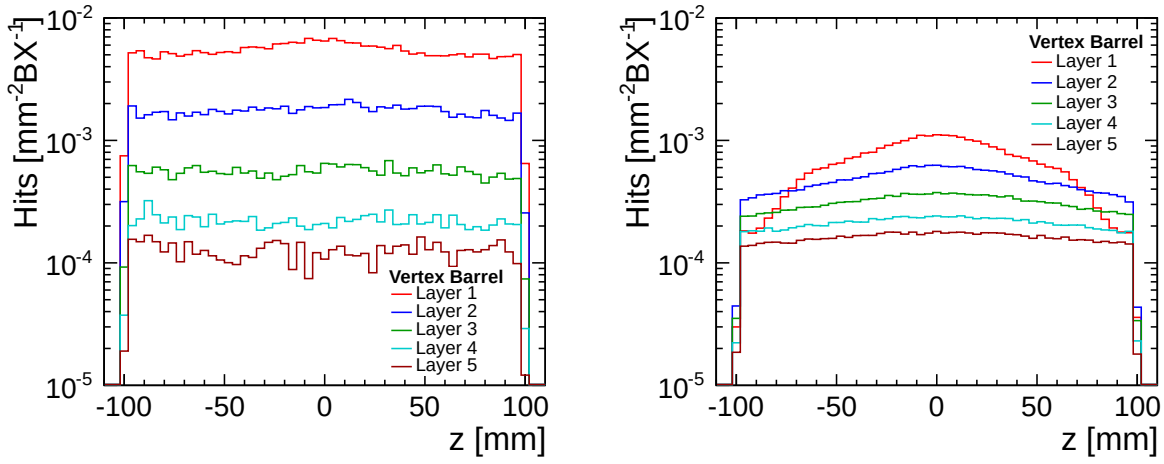

(a) Incoherent pairs

(b) $\gamma\gamma \rightarrow$ hadrons

Figure 5.11: Hit densities in the five vertex barrel layers from incoherent pairs (a) and the $\gamma\gamma \rightarrow$ hadrons background (b) depending on z.

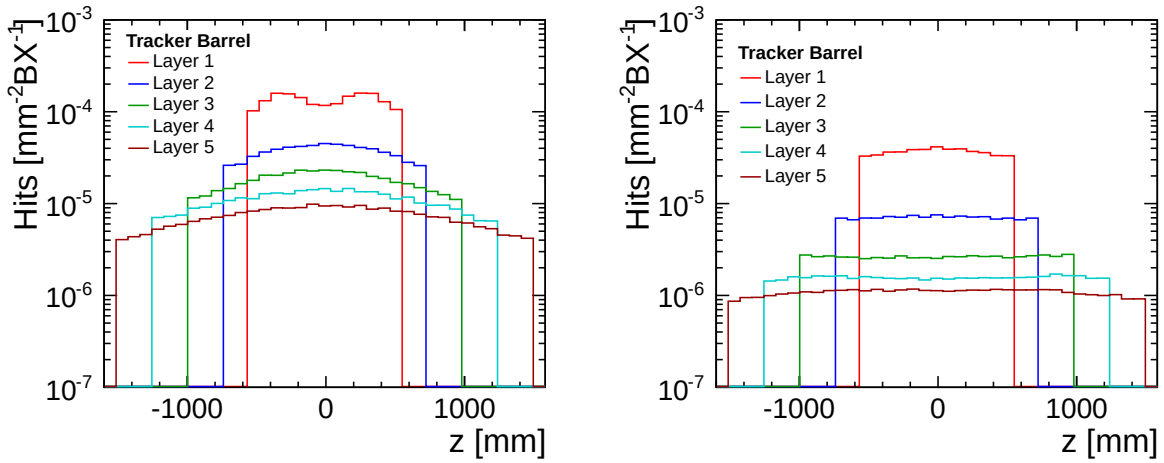

(a) Incoherent pairs

(b) $\gamma\gamma \rightarrow$ hadrons

Figure 5.12: Hit densities in the five main tracker barrel layers from incoherent pairs (a) and the $\gamma\gamma \rightarrow$ hadrons background (b) depending on z.

of low energetic jets. Higher local densities lead to more ghost hits in the stereo strip detectors of the endcaps and thus result in the higher hit rates due to the $\gamma\gamma \rightarrow$ hadrons background.

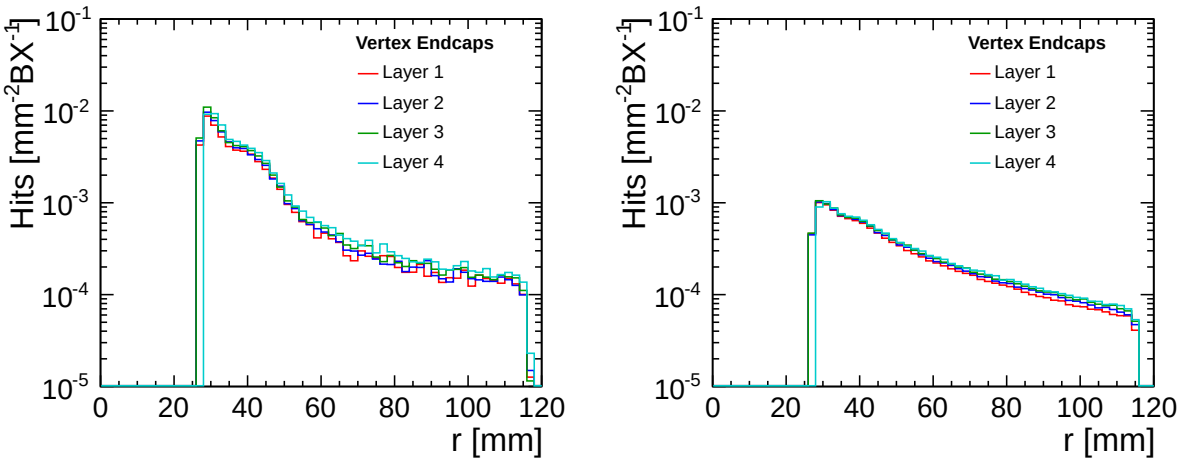

(a) Incoherent pairs

(b) $\gamma\gamma \rightarrow$ hadrons

Figure 5.13: Hit densities in the four vertex endcap layers from incoherent pairs (a) and the $\gamma\gamma \rightarrow$ hadrons background (b) depending on r.

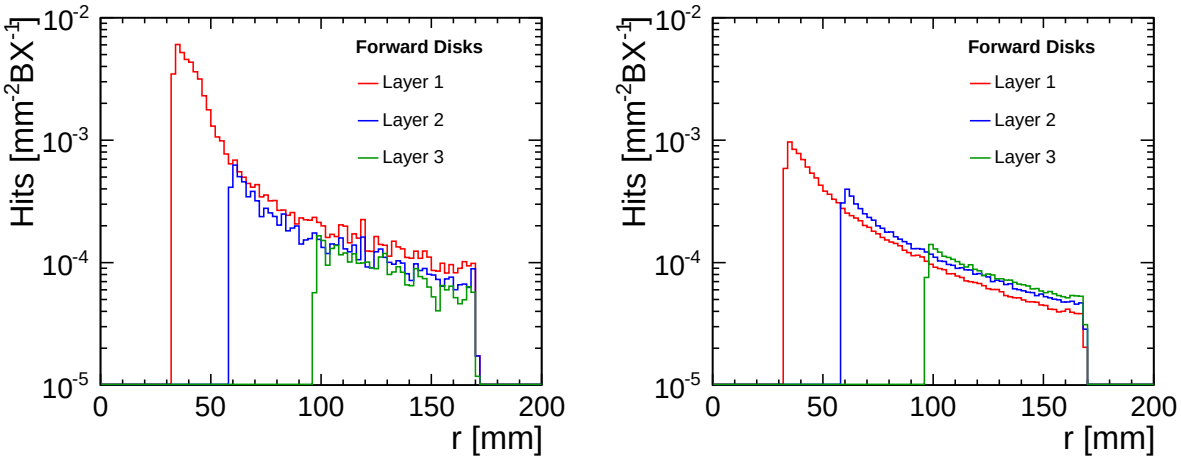

(a) Incoherent pairs

(b) $\gamma\gamma \rightarrow$ hadrons

Figure 5.14: Hit densities in the three forward tracking pixel disks from incoherent pairs (a) and the $\gamma\gamma \rightarrow$ hadrons background (b) depending on r.

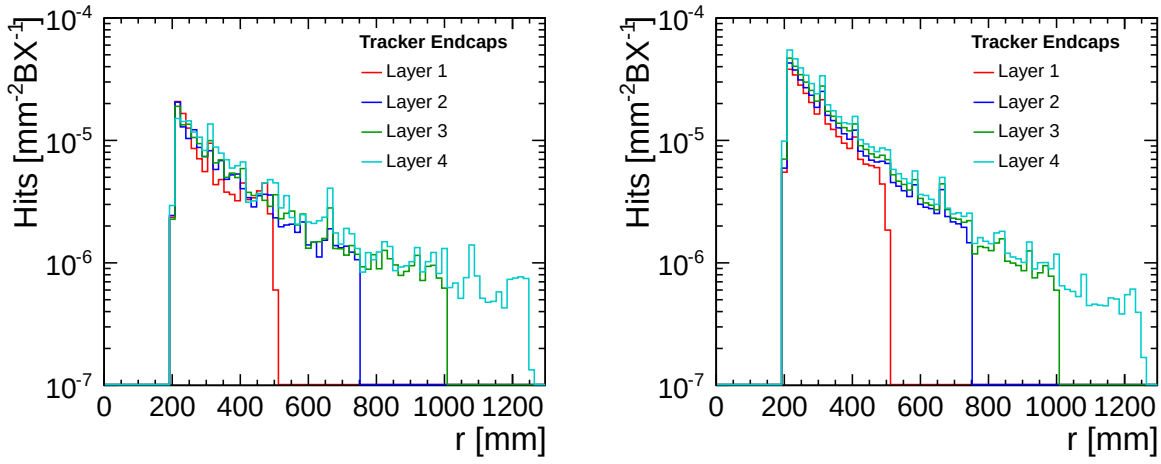

(a) Incoherent pairs

(b) $\gamma\gamma \rightarrow$ hadrons

Figure 5.15: Hit densities in the four main tracker endcap layers from incoherent pairs (a) and the $\gamma\gamma \rightarrow$ hadrons background (b) depending on r.

5.6.3 Occupancies

From the hit densities shown above we can estimate the expected occupancies for the different subdetectors. We assume the nominal segmentation of the subdetectors, i.e. $20 \times 20\,\mu\text{m}^2$ for the pixel detectors and $50\,\mu\text{m} \times 985\,\text{mm}$ for the strip detectors, and use the average reconstructed cluster sizes. The distribution of the reconstructed cluster sizes in the tracking detectors is shown in Fig. 5.16. If a pixel is hit in the pixel detectors, all directly neighboring pixels are usually hit as well, resulting in an average cluster size of 4.6. Similarly, in the strip detectors the two neighboring strips are hit resulting in an average cluster size of 2.7. The clusters in the stereo strip detectors of the main tracker endcap detectors are more than twice that size. The number of hits seen in a stereo strip layer is the multiplication of the number of the hits in the two strip layers. The average cluster size in the stereo strip detectors is thus 7.2. For the occupancy we count each stereo layer as a single layer, we thus have to use 3.6 as the average cluster size. We apply an additional safety factor of 5 to the occupancy from incoherent pairs to account for uncertainties and fluctuations in the background rates. The amount of backscatters estimated from the full simulation constitutes the largest source of uncertainty and can not be easily verified. For the $\gamma\gamma \rightarrow$ hadrons background we use a safety factor of 2, since it is causing significantly less amounts of backscatters.

Using these assumptions, the highest occupancies are reached in the innermost layer of the tracker barrel which experiences a maximum occupancy of 200–300% from incoherent pairs, depending on the azimuthal angle and the position in z, when intergrating over a full bunch train. An occupancy of 15–30% resulting from the $\gamma\gamma \rightarrow$ hadrons background has to be added to this value. Similarly critical are the innermost regions of the main tracker endcaps which have an occupancy of up to 35% from $\gamma\gamma \rightarrow$ hadrons hits and an additional 30% from incoherent pairs over a full bunch train. This occupancy drops quickly for larger radii and is below 5% for $r > 600\,\text{mm}$. The pixel detectors are of much less concern. The innermost vertex barrel layer has an occupancy of 1.5–2.0% for a full bunch train, depending on the azimuthal angle. The numbers for the pixel disks are similar and drop below 0.5% for radii greater than 50 mm.

Since we simulated and digitized only small fractions of a bunch train simultaneously, the numbers

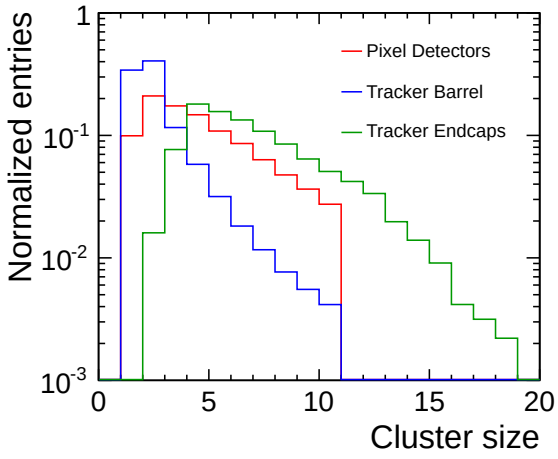

Figure 5.16: Distribution of the sizes of the reconstructed clusters in the tracking detectors.

for the stereo strip detectors are underestimated. For occupancies as high as stated above a significant amount of additional ghost hits will be reconstructed. This problem does not occur for the other detectors where we overestimate the occupancy since some of the clusters would overlap.

It is evident that at least for the innermost main tracker barrel layer and the inner parts of the main tracker endcaps multi-hit readout capability is necessary to keep occupancies at a manageable level. Alternatively one could replace the modules in that region with pixel detectors, which could have larger pixels than those used in the vertex detectors. The desired time resolution for all sub detectors at CLIC is of less than 10 ns [23] which would reduce the occupancies by a factor of approximately 15. It should be noted that the numbers obtained here agree very well with the study performed for CLIC_ILD for those detector regions which are dominated by direct background hits. For regions which are dominted by hits from backscattered particles we find significantly higher hit rates. Several optimizations of the layout of the forward region were applied to the CLIC_ILD model [111], which are not present in the CLIC_SiD model. This suggests that the hit rates at high radii are probably overestimated.

5.6.4 Other Sources Of Backgrounds

As discussed in Section 3.1.3, the coherent pair background and the trident pair background are only relevant at very low angles and do not have any direct impact on the tracking systems. Their impact on the tracking system through backscatters remains to be studied but is assumed to be covered within the safety factors. Another source of background particles are muons that can be created from the beam halo during the collimation in the BDS. This background can be reduced by placing magnetized iron spoilers along the BDS to deflect the muons. Simulation studies suggest that it is realistic to assume an average of one muon per 20 BX traversing the detector volume [20, 23]. This rate is completely negligible compared to the other backgrounds.

5.7 Summary

We have presented the CLIC_SiD simulation model which was used for the CLIC CDR simulation studies as well as the studies presented in this thesis. The most important changes with respect to the SiD detector model are the layout of the vertex region to avoid large amounts of direct hits from the

beam-related backgrounds, the replacement of the HCal barrel absorber material with a denser material together with an increase in the inner radius of the coil to accommodate a sufficiently deep calorimeter and the redesign of the forward region due to the required stability of the QD0.

We have also studied the occupancies in the tracking detectors due to particles from incoherent pairs and the $\gamma\gamma \rightarrow$ hadrons background. With the current design of the tracking systems the most critical regions are the innermost layer of the main tracker barrel and the inner modules of the main tracker endcaps. In both regions occupancies of 100% or more are reached when integrating over a full bunch train and when including a safety factor of 5. In addition to the desired < 10 ns time resolution this could be mitigated by increasing the segmentation in these parts of the detectors.

CHAPTER 6

Simulating High Energy Collisions and Detector Response

A problem including many convolved effects, which is probably even impossible to solve analytically, can be solved using the Monte Carlo method. This method allows to determine the result of a complicated chain of steps if the probability distributions of the possible results for each step are known. Generating a random outcome for each of the steps yields a final result. Repeating this exercise will result in the probability distribution for the original problem.

Determining the response of a complicated detector model is an ideal example of the Monte Carlo method. All possible interactions of the particles with matter are usually well understood and the problem arises only from the convolution of these countless effects. By repeatedly simulating the random passage of some particle through the model we can estimate the expected distribution of an observable. Another application of the Monte Carlo method in HEP is the event generation where it is used to determine the phase space distribution of particle interactions. Finally, a simulation offers the unique ability to disentangle effects in cases which are not directly accessible to a measurement, e.g. a hypothesis can be tested by simulating the outcome of the experiment and comparing it with the observation.

In this chapter we want to briefly discuss the different steps that are necessary for a realistic detector simulation and event reconstruction. First, we introduce the event generation step Section 6.1 which produces the samples used in all other steps. Afterwards, we discuss full detector simulations in GEANT4 in Section 6.2. The major part is the description of the event reconstruction in Section 6.3, where we put emphasis on the event overlay which is necessary for the simulation of CLIC experimental conditions as well as the tracker hit digitization and the track reconstruction used later in Chapter 7

6.1 Event Generation

The first step in each physics simulation is the event generation, e.g. the creation of a list of particles with all relevant attributes which are required to be properly propagated through the detector simulation.

6.1.1 Physics Samples

Event samples that represent high energy particle collision processes have to be generated with correct distributions and correlations for all variables of interest, like angles, momentum and energy. These samples are usually used to compare measurements from experiments with expectations from physics

models. They are also useful to estimate the performance of a future experiment to measure a certain quantity of an assumed model, like the possible measurement of the $h \to \mu^+\mu^-$ branching ratio at CLIC, presented in Chapter 10.

The event generator WHIZARD [40] is used for generating the jet samples used in the tracking studies in Chapter 7, the calorimetry studies in Chapter 9 as well as for producing the physics samples for the $h \to \mu^+\mu^-$ branching ratio analysis. WHIZARD is optimized for calculating cross sections of e^+e^- collisions. The matrix elements are calculated on tree-level and generated by O'Mega [112]. The effect of the luminosity spectrum (see Section 3.1.5) and the initial state radiation (ISR) are taken into account in the event generation. Both effects lead to lower energy of the colliding electrons and modified cross sections. The ISR photons are forced to be collinear with the outgoing beam. The hadronization of the quarks is handled in PYTHIA [113], which also takes care of the generation of final state radiation (FSR). The hadronization parameters in PYTHIA are tuned to the results of the OPAL experiment [114]. The decays of τ leptons of some of the simulated background processes for Chapter 10 are performed using TAUOLA [115].

The file format used for the physics sample is the binary format StdHep [116].

6.1.2 Beam-Beam Interactions

The generation of the samples of beam-induced backgrounds, which we discussed in Section 3.1.3, require several simulation steps. First the particles are tracked through the Linear Accelerator (LINAC) and the BDS as described in [117] to determine the beam parameters at the interaction point. Afterwards, the beam-beam interactions are simulated in GuineaPig [65, 68], which produces the event samples for the produced electron pairs, photons and hadrons as well as a file containing the luminosity spectrum. The hadronic pairs have a minimum invariant mass of 2 GeV. After the event generation they have to be run through PYTHIA for the fragmentation of the hadrons. More details on the simulation of the $\gamma\gamma \to$ hadrons background are given in [118].

6.1.3 Individual Particles

Fundamental detector parameters like resolutions and efficiencies are usually obtained using dedicated samples of certain particles with a well defined angular and energy distribution. The General Particle Source (GPS) provided by Geant4 (see below) allows to generate various particle types at fixed angles and energies or following user provided distributions. Event samples generated by the general particle source are used for example in the tracking studies in Chapter 7, the calorimeter layout optimization in Chapter 8 and the calorimeter calibration in Chapter 9.

6.2 Detector Simulation

The simulation of the interaction of the particles with the detector model is performed using the program SLIC [119, 120]. SLIC is a thin wrapper around Geant4 [121, 122] that allows to easily define a detector geometry in an XML format. The initial particles for the simulation can either be defined by a file in the StdHep format or by using Geant4 GPS interface. The output files containing the simulated events are produced in the LCIO [123, 124] file format. All simulations presented in this thesis use SLIC version 2.9.8 together with Geant4 version 9.3.2.

Since the events are generated in WHIZARD as head-on collisions the crossing angle of the beams at the interaction point has to be taken into account in the detector simulation. All initial particles are boosted according to the crossing angle of 20 mrad at the beginning of the simulation.

6.2.1 Particle Transport in GEANT4

The particles are propagated by GEANT4 through the detector volume in discrete steps. The length of each step is the shortest value of either the mean free path length in the respective material, the distance to the boundary of the respective volume or a defined maximum step length. The interaction of the particle within each step is then randomly selected from a list of possible processes defined in the physics list (see below), according to their probability. The energy loss in this step is then calculated accordingly and the particle momentum and position after the step are set. If one or more secondary particles are created, e.g by Bremsstrahlung or pair production, they are propagated individually through the detector afterwards, starting from the position of their production. If the energy of a particle is below a certain minimum energy, all its energy is deposited in the step and the particle is stopped. More precise results are achieved for shorter step lengths and lower minimum energy limits. This will result in longer computing time required to simulate the event such that the parameters are always a trade-off between precision and performance of the simulation.

For those detector volumes that are declared as active detectors, the energy deposited by a particle traversing the volume is written out as a hit. In addition to the energy, the simulation hit also stores the time and a reference to the particle(s) that created the hit. Each energy deposit in the tracking detectors creates an individual hit, since the volumes are not segmented into strips or pixels within the simulation model. The calorimeters, on the other hand, are segmented into individual cells and each hit is a list of all energy deposits within the respective cell during the simulation of the event.

6.2.2 Physics Lists in GEANT4

GEANT4 offers various models to describe the different interactions of particles with matter. Reference physics lists offer validated combinations of these models and the choice of the physics list depends on the focus of the simulation. The `QGSP_BERT` physics list is the reference physics list used for the simulation for the LHC experiments. It has been shown that this list offers good agreement between simulations and data obtained from beam tests for the energy and the shower shape, e.g. in [125].

The models can be grouped into models for electromagnetic interactions and hadronic interactions. The electromagnetic models are fairly well understood and the same combination of models is used in almost all of the reference physics lists. These models include descriptions for energy loss through ionization, multiple Coulomb scattering, Bremsstrahlung, pair production and annihilation of anti-electrons. The models for photons include the photoelectric effect, Compton scattering and conversion into e^+e^- pairs. Details about the electromagnetic models can be found in [126] and references therein.

For the inelastic scattering of hadrons a wide range of models exist in GEANT4. The `QGSP_BERT` physics list uses the Bertini cascade model [127, 128] for energies below 9.9 GeV and the quark-gluon string model [129, 130] for energies higher than 12 GeV. As a transition, a low energy parametrization model is used from 9.5–25 GeV and in regions where more than one model is defined, one is randomly chosen for each interaction. The elastic scatterings involving hadrons are modeled using the Chiral Invariant Phase Space model (CHIPS) [131–133]. In addition, models for neutron capture and neutron induced fission are included in `QGSP_BERT`. All details concerning this and the other hadronic physics lists are given in [134].

Most physics lists only differ in details and the level of agreement between data and simulation depends on which observable is of interest. For example, the jet energy resolution achieved with PANDORAPFA (see Section 6.3.6) is not very sensitive to the choice of the physics list [85]. In addition, these differences only matter when comparing simulations with data, especially in high precision measurements, but usually do not apply to the simulation studies currently being performed for future linear

colliders. One notable exception is the QGSP_BERT_HP physics list. It offers precise neutron tracking down to lowest energies and is used in the HCal study in Chapter 8.

6.3 Event Digitization and Reconstruction

The hits created during the detector simulation have to be passed through various pattern recognitions to reconstruct the original event. These include track reconstruction and identification of clusters in the calorimeters which are then combined into reconstructed particles. To simulate a realistic event reconstruction, the hits have to be passed through a digitization step that models the response of an actual detector to the deposited energy. This can include threshold effects, noise, cross-talk of neighboring channels, smearing of the signal and conversion into a digital signal with limited precision.

The digitization and reconstruction is performed in several steps using the `org.lcsim` [135] framework and the slicPandora software package. The individual steps that are performed are explained below.

6.3.1 Overlay of Beam-Induced Background

An essential part of realistic detector simulations for CLIC is the inclusion of the high levels of beam-induced backgrounds. This allows to estimate the impact of hits and energy deposits from background particles on the pattern recognition in the tracking system or the reconstruction of clusters in the calorimeters. The background overlay has to be performed before the digitization step of the event reconstruction to correctly account for a realistic energy deposit within each channel. This is particularly important when incorporating measurement thresholds and saturation effects.

For the CLIC detector studies the background events are simulated independently and then merged with the physics events at a later stage. This approach removes the overhead in computing resources used when simulating background particles together with a physics event. It also allows to study the impact of the background on an event by event basis since each event can be reconstructed with and without the background particles.

We have developed a software tool for `org.lcsim` that allows for overlaying events from different simulated events in a flexible way. The *OverlayDriver* [26] allows to merge a user defined number of background events with a signal event by merging the individual simulated hits. Signal and background events are shifted in time with respect to each other if desired, thus, effectively recreating the beam structure as seen by the detector. The time of each hit is shifted depending on when the background event happened with respect to the signal event. In addition, a readout time window can be defined for every collection[1].

Time Structure and Amount of Background

The beam structure is simulated in the *OverlayDriver* as follows. First, the time between two bunch crossings and the total length of a train are defined. The signal event is then either placed randomly at one of the bunch crossings or at a user defined bunch crossing. By default the time of the collision in the signal event, t_{signal}, is chosen as the reference time $t_0 = 0\,\text{ns}$. Afterwards, for each bunch crossing in the train a number is drawn from a Poisson distribution to determine the number of background events that occur at that bunch crossing. The corresponding number of background events is then merged

[1] In the simulation each subdetector writes its hits to a different collection. A collection in LCIO is an ordered list of arbitrary objects which can have meta data attached to it.

successively with the signal event, shifting the times of all hits and particles according to the time of the bunch crossing. A schematic display of the resulting time structure is shown in Fig. 6.1.

A bunch train of 60 bunch crossings with a bunch spacing of 0.5 ns was used for the background overlay in the CLIC CDR and the studies presented in this thesis. This corresponds only to approximately one fifth of the bunch train at CLIC but is sufficient to have realistic background levels throughout the readout time windows of 10 ns, as described below. In these studies only the $\gamma\gamma \rightarrow$ hadrons background is included systematically with an expectation value of 3.2 events per bunch crossing. The signal event is placed at the tenth bunch crossing within the bunch train to guarantee realistic amounts of background throughout the whole time window.

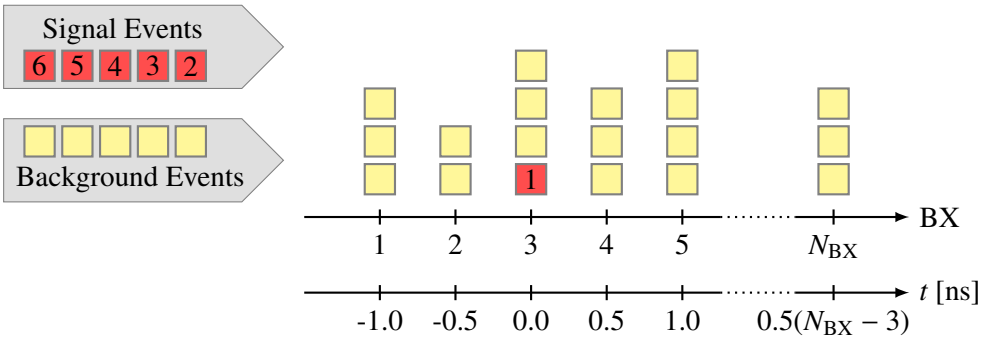

Figure 6.1: Example of a bunch train structure created by the *OverlayDriver* assuming a time of 0.5 ns between two bunch crossings. One signal event is placed at a random bunch crossing. A random number of background events is added to each bunch crossing in the train. The signal event determines the reference time.

Read-out Time Windows

In a CLIC experiment the readout will be triggerless. Each subdetector will read out continuously for the duration of the train and a time stamp of a certain resolution will be applied to each signal. The reconstruction software will then have to reconstruct the full event in sliding time windows by looking at different combinations of adjacent readout cycles to identify the hard interaction. This procedure is not implemented in the current reconstruction software. Read-out time windows can be defined instead for each subdetector, assuming that the hard interaction can be identified and constrained to the corresponding time window. These time windows present the subsequent digitization and reconstruction software following the *OverlayDriver* with a single event.

The readout time windows have a defined length for each of the collections present in the event, $\Delta t_{\text{collection}}$. All hits outside the respective time window are removed. The starting point of the time windows is defined by t_{signal}. This simplification assumes that the correct time window of the signal has been identified and avoids removing late parts of the developing showers. In addition, a time-of-flight correction based on the hit position $\vec{x}_{\text{hit}}$ is applied, assuming that the particles move with the speed of light c along the line-of-sight from the interaction point. The time window for a certain hit is defined by its limits t_{min} and t_{max} which can be written as

$$t_{\text{min}} = t_{\text{signal}} + \frac{|\vec{x}_{\text{hit}}|}{c}, \tag{6.1}$$

$$t_{\text{max}} = t_{\text{min}} + \Delta t_{\text{collection}}. \tag{6.2}$$

Figure 6.2 shows the time structure of the hits in an arbitrary event with and without addition of

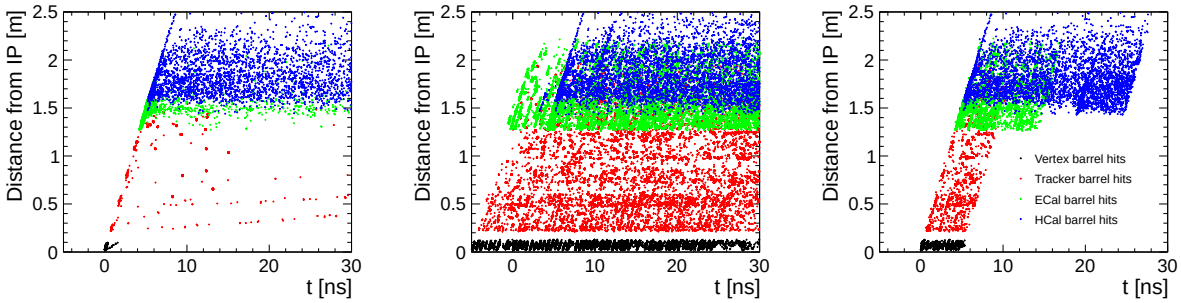

Figure 6.2: Time structure of the hits in the barrel detectors in the signal event (left), together with a bunch train of $\gamma\gamma \rightarrow$ hadrons events (center) and after introducting readout time windows (right). The readout time windows used here are 5 ns for the vertex detector (black) and the main tracker (red), 10 ns for the ECal (green) and 20 ns for the HCal (blue).

$\gamma\gamma \rightarrow$ hadrons background events. While most hits in the tracking systems are produced shortly after the expected time from the time-of-flight, the shower development in the calorimeter leads to much later hits.

For the CLIC CDR a readout time window of 10 ns is assumed throughout all subdetectors, except for the HCal barrel which uses tungsten as absorber material. Hadronic showers in tungsten have a larger neutron component compared to steel absorbers, which tend to have a later calorimetric response. The time window of the HCal barrel is thus set to 100 ns, which is feasible since the occupancy from the beam induced backgrounds at these radii is low compared to the forward detectors.

Treatment of Tracker Hits

The tracking detectors are segmented into modules in the simulation model as described in Section 5.1.2. Individual strips or pixels are not implemented in the simulation. Thus, each tracker hit represents a localized energy deposit and not a pixel or strip hit. These pixel or strip hits are only created during the digitization step taking into account all energy deposits that would belong to the same readout channel. This leaves the *OverlayDriver* only with the task of shifting the hits in time according to their bunch crossing and removing all hits that do not fall within the defined time window.

Treatment of Calorimeter Hits

Calorimeter hits represent the total energy deposition within a certain readout cell of the calorimeter. They can consist of several individual energy depositions that occurred during the simulation within the corresponding volume. Each of those energy deposits has a time stamp and the information of which particle it originates from. The time window cuts are applied to the individual energy deposits instead of the calorimeter hit as a whole, since he time of the hit is simply defined as the time of the earliest of its energy depositions. Multiple calorimeter hits corresponding to the same cell are merged into a single calorimeter hit by merging all of their energy depositions within the respective time window.

Treatment of Monte Carlo Particles

The list of all Monte Carlo particles in the signal event is kept to maintain the full true event information. The number of background particles can be very high and they are usually only of limited interest. Only those background particles that are associated with a hit that passed the time window selection are kept

and placed into the list of Monte Carlo particles together with the full hierarchy of their respective ancestors. Two lists of pointers are created to identify which of the particles originated from the signal event and which ones are background particles. The production times of all particles are modified according to the time of the bunch crossing at which they occur.

Multiple Sources of Backgrounds

The *OverlayDriver* was intended from the beginning to allow overlaying different types of background from different sources. For this, multiple instances can be run one after the other using different parameters. A label can be set to distinguish the individual lists of background Monte Carlo particles. The parameters defining the placement of the signal event have to be set carefully to avoid inconsistencies. For example, if the signal event should be placed randomly within the bunch train, the beginning of the bunch train has to be selected as t_0 in the first overlay step. Then, for all following instances of the *OverlayDriver* the signal has to be forced to the first bunch crossing since the output of the first overlay has set its time structure relative to the first bunch crossing in the train.

6.3.2 Tracker Hit Digitization and Clustering

The digitization of the tracker hits transforms energy deposits from the GEANT4 simulation into signals as they would be seen from a detector readout, i.e. Analog to Digital Converter (ADC) counts for each readout channel. Since the simulation model only defines modules and not individual strips or pixels the respective modules have to be segmented virtually and the individual tracker hit positions have to be identified with their respective channel. Afterwards, the charge build-up in each channel due to the simulated energy deposition has to be simulated and translated into the resulting measurable signal height. Finally, a clustering algorithm is used to combine signals from neighboring channels and identify the most probable hit position.

The digitization code that is used is the *SiSim* package [136] implemented in `org.lcsim`. The algorithm is explained in some detail below since no written documentation exists to date.

Segmentation of Tracker Modules

The segmentation of the tracking modules are defined for each subdetector individually by setting the desired sensor pitch. For pixel sensors values are set for the pitches in x and y-direction, which are the local dimensions parallel to the sensor plane. For strip detectors only one pitch has to be defined for the strip width since the strip length is defined by the module extent. The direction of the strips in the barrel detector is parallel to the z-axis. In case of the stereo strip detectors in the tracker endcaps, the strips are placed perpendicular to the sides of the trapezoidal modules (see Section 5.1.2). The chosen stereo angle is 12° for all stereo strip modules. This step also sets the transfer efficiencies for all subdetectors. They represent the efficiency of charge transport within the silicon as well as from the surface of the sensitive material to the readout and reduce the signal height as explained below.

It is forseen that only every other strip in the strip detectors is read out directly to lower the number of required readout channels. The intermediate strips are connected via capacitive coupling to their neighboring strips which allows to maintain a high spatial resolution of the hit position as shown in [137]. This is taken into account in the silicon simulation by defining a readout pitch of twice the sensor pitch. The charge collected in the intermediate strips is added to both neighboring strips that are read out directly using a lower transfer efficiency.

In CLIC_SiD the sensitive and readout pitch for all pixel detectors are set to 20 µm in x and y and the transfer efficiency is set to 1. For all strip detectors the sensitive pitch is set to 25 µm, while the readout

pitch is set to 50 µm. For the strips that are read out directly a transfer efficiency of ~ 99% is assumed. The intermediate strips, which are read out via capacitive coupling by both neighboring strips is set to a value of ~ 40%, which is significantly lower than half of the efficiency assumed the directly read out strips.

Silicon Simulation

The simulation of the charge deposition and distribution is implemented for a generic silicon sensor device. Generic variables like the bias and depletion voltages, the doping concentration, as well as the electron and hole concentrations are used to describe the sensor material. For the basic principles of semi-conductor sensors we refer to [138]. The readout device is similarly defined in a generic way by its threshold and noise level.

First all simulated tracker hits that deposited energy in the respective sensitive volume are identified. A simulated hit is defined by its position in the center of the sensitive medium, its energy deposit and the two points where the particle that it originated from entered and left the sensitive plane. For a realistic charge simulation a single energy deposition in the center of the medium is not sufficient. Instead, the energy is evenly distributed in small steps throughout the material along the path of the particle as shown in Fig. 6.3. The particle trajectory is determinded from the two endpoints and divided into small track segments. Each segment has a maximum length of 1/10 of the sensor pitch. The local deposited energy for each segment is then converted into the corresponding number of electron-hole pairs that are created in the doped silicon. The amount of charge is then corrected for its collection inefficiency due to local charge trapping. Afterwards, the diffusion of the charge during its drift to the electrodes is calculated taking into account the electric field created by the bias and depletion voltages. The impact of the magnetic field is neglected. As a result the charge is distributed in a 2 dimensional Gaussian distribution on the electrode surface.

Once the charge distribution of all track segments of all hits in a module has been calculated, the charge collected within the surface of each readout channel is combined. The transfer efficiency is applied to calculate the visible signal. Randomly generated noise can be added to the signal of each channel, which was not done for the CLIC CDR studies. Finally, the charge in the cell is converted to an integer value which represents the digital signal of the ADC. If the resulting signal is above the desired threshold it is added to the list of digitized hits. The time of the hit is not used during the digitization. The only constraint on the time of the hits comes from the background overlay time windows introduced in Fig. 6.1.

Clustering

The digitized hits are clustered together using a nearest neighbor algorithm. Two threshold values have to be defined for each subdetector. The first value defines the minimum signal height for a hit to be used as a seed, while the second threshold defines the minimum signal height for a neighboring cell to be clustered together with a seed.

The identified clusters are converted into tracker hits to be used by the track finding algorithm explained in Section 6.3.5. The position of the tracker hit is calculated as the signal weighted center of the cluster. The uncertainties of the hit position are calculated from the readout pitch of the cell, w_{cell}, and a correction factor f which depends on the cluster width, w_{cluster}, in the relevant direction

$$\sigma = w_{\text{cell}} \cdot f(w_{\text{cluster}}). \tag{6.3}$$

The correction factors used are given in Table 6.1.

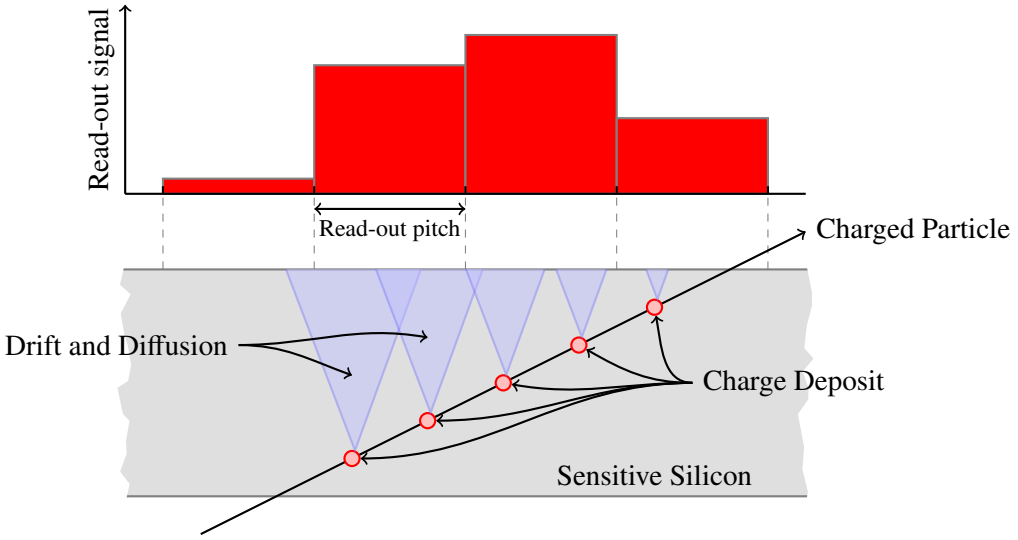

Figure 6.3: Illustration of the charge deposition in the sensitive material, charge drift to the electrode and conversion into signals in the readout cell as simulated by the tracker hit digitization code. See text for details.

Table 6.1: Correction factors f used for the calculation of the tracker hit uncertainty depending on the cluster width w_{cluster}.

w_{cluster}	f
1	$1/\sqrt{12}$
2	1/5
3	1/3
4	1/2
5	1

6.3.3 Removal of Tracker Hits

The layers of the tracking system in the CLIC_SiD detector model are made of individual sensitive modules, which are partially overlapping. This leads to a more realistic material budget in the full simulation, but it also creates multiple tracker hits within a single layer when a particle passes through such overlapping modules. The track reconstruction algorithm, described in Section 6.3.5, was originally written for a simpler geometry description using cylindrical and disk tracking layers. In those geometries overlaps are not existing and only a single hit from every layer is allowed to be assigned to a track. The additional hits in the overlapping region can lead to a performance drop, since more combinations are possible, or, in the worst case, lead to the creation of fake tracks.

This shortcoming of the tracking algorithm is circumvented by removing those hits before the track finding is run. All layers are checked for multiple tracker hits belonging to the same Monte Carlo particle and every hit except for the one that occurred first is removed. This driver is the only one using Monte Carlo truth information throughout the reconstruction chain, which was done for simplicity. A similar result could be obtained by implementing a hit removal that is based on the pure geometrical overlap of the individual modules.

Ideally the additional information should be used in the pattern recognition as a short vector defining the track direction in the overlap region.

6.3.4 Removal of Muon Chamber Hits

The return yoke in the CLIC_SiD detector model is modelled with 18 equidistant sensitive layers for muon identification (see Section 5.4). It has been shown, that an efficient muon identification can be achieved with a significantly smaller number of layers, i.e. three groups of three instrumented layers throughout the yoke thickness [139]. This is taken into account in the event reconstruction by ignoring all hits in the return yoke except of those in the layers 1–3, 8–10 and 16–18.

6.3.5 Track Reconstruction

The tracks are reconstructed from the digitized tracker hits with the *SeedTracker* algorithm [140] implemented in `org.lcsim`. This algorithm is a generic tracking algorithm intended for silicon based tracking detectors with only a small number of hits along a track. The geometry information of the detector is decoupled from the algorithm by relying on a set of strategies that encapsulate the required geometry information. In addition, it uses generalized three dimensional tracker hits for the track fitting and does not rely on certain hit types. Thus, this algorithm is especially suited for detector design studies where the detector geometry is frequently changed.

Track Finding Steps

The track finding is controlled by strategies. Each strategy assigns a certain role to each of the layers in the tracking system that should be considered. Three layers are defined as seed layers, one layer is defined as the confirmation layer and usually all other layers are defined as possible extension layers. There is no requirement on the order of seed and confirmation layers, i.e. inside-out and outside-in tracking strategies are possible. There is also no requirement to chose adjacent layers as seed and confirmation layers although this is beneficial for the track finding.

In addition to the roles of each tracking layer, the strategy defines a minimum number of hits that are required to form a track candidate, N_{min}, a maximum total χ^2 for the track fit, χ^2_{max}, a constraint on the minimum transverse momentum for the track, $p_{\text{T,min}}$, and a constraint on the distance of closest approach of the track to the IP in $r\phi$ and z, referred to as $d_{0,\text{max}}$ and $z_{0,\text{max}}$, respectively. The vertex constraint is required to reduce the number of fake tracks in case of a low number of required hits and should be chosen rather loosely to avoid that tracks from displaced vertices fail the reconstruction. Secondary decays that occur far away from the IP can not be found by this algorithm due to this vertex constraint. It has been shown that these tracks can be found efficiently by a second tracking algorithm that uses the track stubs created by MIPs in the ECal as seeds [141]. The high granularity of the ECal allows a sufficiently precise determination of the track parameters to extrapolate the trajectory back into the tracking region and identify the associated hits. This calorimeter assisted tracking algorithm was not used in the tracking studies presented in this thesis since it is incompatible with the digitization code used.

For tracking systems consisting of multiple subdetectors, several strategies are required to cover the necessary layer combinations of seed and confirmation layers to be able to find all the tracks within the acceptance of the detector. This is usually the case, since barrel and endcap detectors are treated as individual subdetectors in the simulation. The set of strategies then has to cover all necessary combinations of seed layers from different subdetectors to also find tracks in the transition region. The training procedure for obtaining a full set of strategies is explained below.

The track finding is performed for each of the strategies and results in a single list of reconstructed tracks. It is performed in steps corresponding the three different roles that are assigned to the different layers in that strategy. During these steps hits are successively added to a track candidate by checking

its consistency with a helical fit explained below. The hit is only added to the track candidate if the fit succeeded and the total χ^2 of the fit does not exceed the χ^2_{max}.

Seeding The hits in the seed layers defined by the strategy are used to form the initial track candidates. This list contains all possible combinations of hits from the three different layers. An initial helix fit is performed to determine the track parameters of each track candidate.

Confirming All track candidates resulting from the seeding are tested for a successful helix fit with any of the hits in the confirmation layer fulfilling $\chi^2 \leq \chi^2_{\text{max}}$. It is possible to create multiple confirmed seeds from a single track candidate.

Extending The list of confirmed seeds is tested if they can be extended to a full track. For each track candidate all the hits in each of the extension layers are tested if they pass a helix fit ($\chi^2 \leq \chi^2_{\text{max}}$). Once the number of remaining layers to be tested drops below the number of hits still required to form a track, the candidate is discarded. Each resulting track candidate is checked if it shares more than one hit with any of the previously reconstructed tracks. If this is the case, the only the best track candidate is kept. The best track candidate is defined as the one with the most hits associated and in case of equal number of hits the one with the smallest χ^2.

The hits in each layer are grouped into sectors in ϕ and z which allows to check only the hits in the sectors consistent with the current set of helix parameters when confirming and extending the track seeds. While hits have to be present in the seed and confirmation layers to find a track, extension layers can be skipped if there are sufficient hits in other extension layers to fulfill the N_{min} criterion.

Helix Fitting

The track fit used throughout the *SeedTracker* algorithm assumes a helical track path. This helix fit consists of a non-iterative circle fit [142] in the $r\phi$-plane followed by a straight line fit in the zS-plane, where S is the arc length from the z position of the point of closest approach in the xy-plane, z_0, to the position of interest along the helix. A definition of the coordinates can be found in Appendix C. The hit uncertainties in $r\phi$ and z are a assumed to be uncorrelated. For stereo strip hits the hit position and covariance matrix is depending on the direction at which the layer is passed. The track parameters from the previous fit are used to calculate the corrected covariance matrix.

If possible, i.e. at least three pixel hits are available, only those hits are used in the linear fit of the slope, since those hits have a far better z-resolution compared to the long strips[2]. A χ^2 penalty is added if the resulting track parameters exceed the limits for $p_{T,\text{min}}$, $d_{0,\text{max}}$ or $z_{0,\text{max}}$. The total χ^2 of the track fit is the combination of the individual fit χ^2 and the different penalties,

$$\chi^2 = \chi^2_{\text{circle}} + \chi^2_{\text{line}} + \left.\frac{(\kappa - \kappa_{\text{max}})^2}{\sigma_\kappa}\right|_{\kappa>\kappa_{\text{max}}} + \left.\frac{(d_0 - d_{0,\text{max}})^2}{\sigma_{d_0}}\right|_{(d_0-d_{0,\text{max}}} + \left.\frac{z_0 > z_{0,\text{max}})^2}{\sigma_{z_0}}\right|_{z_0>z_{0,\text{max}}}, \tag{6.4}$$

where χ^2_{circle} and χ^2_{line} are the χ^2 of the circle and the line fit, respectively.

Multiple Scattering

The material budget is taken into account for each helix fit beyond the initial fit performed during the seed step. This is done by combining the uncertainty due to multiple scattering with the uncertainty of the single point resolution of each hit.

[2] This is always possible in the CLIC_SiD detector

First, the width of the scattering angle distribution introduced by each layer is calculated taking into account the angle at which the layer is crossed and the track candidate momentum. This requires some track parameters and is thus only possible after the initial fit has been performed. The layers considered for the multiple scattering estimation are the physical layers present in the tracking volume which includes support material in addition to the sensitive layers.

The uncertainty due to the scattering angle is estimated for each layer passed using Eq. (4.11). Although the incident angle of the particle is taken into account when calculating the pathlength within the material, the curvature of the particle trajectory within the material is ignored. These multiple scattering uncertainties are then extrapolated to the position of the candidate hit for all layers that are closer to the IP than the hit. The uncertainties for all layers are extrapolated individually and added in quadrature. This neglects any correlations between the multiple scattering uncertainties introduced by the individual layers which underestimates the total uncertainty. Finally, the total multiple scattering uncertainty is added in quadrature to the uncertainty of the hit position.

Once a hit is added to a track candidate the helix parameters are changed based on the new fit and the calculation of the multiple scattering explained above has to be repeated. Since confirmation and extension steps are done per layer and only one hit is added per layer this calculation has to be done once per layer and track candidate.

Strategy Training

Since the number of strategies required to cover the full geometry can be very high, depending on the number of different layers in the detector and the desired minimum number of hits to form a track, a software tool is available to generate the list of necessary strategies.

A sample of training events covering the desired angular and momentum range is used to map out the possible combinations of layers that can be hit by individual particles. A minimum transverse momentum can be set to select only those particles that are desired to be found. Then, the set of particles is reduced to those that created at least the minimum number of hits required to form a track. All combinations of 4 different layers are generated from the available tracking layers, representing the three seed layers and the confirmation layer of the strategies. This set of strategy candidates is then used to obtain the smallest set of strategy candidates required to find all of the particles in the training sample.

Each layer can have a weight assigned and in case of redundant strategy candidates only the one with the highest combined weight is used in the final strategy list. By default, all layers which are not used as seed layers are defined as extension layers for that strategy. If desired, the strategy builder enforces symmetry between strategies involving one of the endcap layers.

6.3.6 Calorimeter Clustering, Particle Flow and Particle Identification

The identification of the calorimeter clusters and the creation of Particle Flow Objects (PFOs), i.e. reconstructed particles, is performed in the PandoraPFA framework [85, 143]. The client application SlicPandora takes care of the reading and writing of the event, digitizes the hits before passing them to PandoraPFA and provides the detector geometry.

Calorimeter Hit Digitization

The calorimeter hit digitization is very basic and only applies a threshold cut to the hit energy. In addition, only hits within the first 100 ns of the event are taken into account, modeling the read-out cycle of the calorimeters. The energy of the hits in the muon chambers, which are instrumented with a digital RPC readout, is set to 1 if the deposited energy is above threshold. All other hits are ignored.

Pandora Particle Flow Algorithm

The PandoraPFA framework offers a wide range of clustering algorithms that can be used for the identification of clusters. A short overview of the steps performed in PandoraPFA is given below. Details of these steps can be found in [85, 143].

- The energy of the hits is corrected by the sampling fraction of the respective calorimeter layer. Different sampling fractions for electromagnetic and hadronic showers are foreseen and both hypothesis for the hit energy are calculated. The final decision on which sampling fraction to use for calculating the shower energy is done after the particle identification step.

- Individual hits that are most likely caused by slow neutrons are removed, since they are hard to attribute to specific showers.

- Initial clusters are formed from the calorimeter hits using a cone-based algorithm starting in the first layer of the calorimeter. The direction of tracks that reach the calorimeters are used as seeds. This step tends to produce small clusters which can be merged at a later stage.

- Neighboring clusters are merged based on their topology, i.e. the observed pattern matches a typical topology of two subclusters. Clusters that are consistent with a purely electromagnetic shower hypothesis are not merged with neighboring clusters.

- Clusters are merged with reconstructed tracks based on the topology. If the energies of the track and the cluster do not match, several re-clustering algorithms try to improve the match by breaking up the cluster or merging it with neighboring clusters.

- PFOs are created from the clusters. If the PFO has a track, its momentum is directly taken from the track and the energy is calculated assuming the particle mass from the particle identification, as explained below. For neutral hadrons and photons the energy is set to the cluster energy. The momentum is calculated from the energy and the direction of the cluster. A mass of 0 is used for the calculation of the momentum since no proper identification of neutral hadrons is performed.

6.3.7 Particle Identification in PandoraPFA

PandoraPFA offers a basic particle identification. If a track is associated with the PFO, the particle is identified as a charged pion or, if the cluster size resembles the size of a purely electromagnetic shower, it is identified as an electron. Similarly, if no track is associated with the cluster it is identified as a neutron or, if the shower is a purely electromagnetic shower, it is identified as a photon.

A dedicated algorithm to identify muons [144] is used as the first step in PandoraPFA. All hits associated with a muon are removed before any of the other algorithms are run.

6.3.8 PFO Selection and Truth Linking

The final part of the reconstruction is again performed in `org.lcsim`. It applies several selection cuts to the reconstructed particles in order to reduce the amount of beam-induced background. It also creates the truth links between Monte Carlo and reconstructed particles required for performance studies.

Table 6.2: One set of cuts used for the PFO selection at CLIC. Given is the minimum transverse momentum $p_{\mathrm{T,\,min}}$ for particles that are kept, the maximum transverse momentum for particles that are removed $p_{\mathrm{T,\,max}}$, and the maximum reconstructed production time of the PFO at the IP. These selction cuts depend on the reconstructed polar angle range and the particle type.

Particle type	Polar angle region	$p_{\mathrm{T,\,min}}$ [GeV]	$p_{\mathrm{T,\,max}}$ [GeV]	t_{max} [ns]
Photons	$\cos\theta \leq 0.975$	0.75	4.0	2.0
		0.0	0.75	2.0
	$\cos\theta > 0.975$	0.75	4.0	2.0
		0.0	0.75	1.0
Neutral hadrons	$\cos\theta \leq 0.975$	0.75	8.0	2.5
		0.0	0.75	1.5
	$\cos\theta > 0.975$	0.75	8.0	2.5
		0.0	0.75	1.5
Charged particles	All angles	0.75	4.0	3.0
		0.0	0.75	1.5

PFO Selection Cuts and Truth Links

The readout windows applied to collections, as described in Fig. 6.1, partially remove the beam-induced background by reducing the number of bunch crossings that are reconstructed together with the signal event. Once the reconstructed particles are available, a more sophisticated background rejection is possible using the combined time information from reconstructed clusters [145].

It is assumed that the calorimeter readout will provide time information for individual calorimeter hits on the order of 1 ns, which is possible when using for example fast SiPMs [146]. The truncated mean time of a reconstructed calorimeter cluster is known to sub-nanosecond precision. This mean cluster time is then propagated back to the interaction point, either along the line of sight for neutral particles or along the helix of the reconstructed track for a charged particle to calculate a precise time of the particle creation. The time of flight calculation is taking into account the mass of the particle based on its particle type. Using this procedure it is possible to select particles that were created within a certain time window around the signal event that is much narrower than the original readout time windows. It thus allows to efficiently identify and select only those particles that originate from the physics event together with those that are produced in-time with the physics event.

Different PFO selection cuts are defined for each type of particle—charged particles, photons and neutral hadrons—and depend on whether the particle was reconstructed in the forward region of the detector, which is experiencing a much higher background occupancy. Two cuts on the transverse momentum define which particles are affected by the selection cuts. Particles below the limit are always rejected and particles with a higher p_{T} are always kept. The *loose* selection cut defined for the CLIC CDR studies is given as an example set of PFO selection cute in Table 6.2. This set of cuts was used in the Higgs analysis in Chapter 10.

Truth Linking

Reconstructed high level objects like tracks, calorimeter clusters and PFOs have no intrinsic link to the Monte Carlo particles that they originated from. This connection is required to asses the quality of the event reconstruction and to quantify reconstruction efficiencies. We have implemented a truth linker in

`org.lcsim` to provide these links by creating weighted relations between Monte Carlo particles and the reconstructed objects mentioned above [147]. These links are used to identify the true particles for the tracking performance studies in Chapter 7.

The relations for tracks and clusters are evaluated based on the truth information of the contributing hits. The weight of the relation is the fraction of hits that a Monte Carlo particle contributed to a track, or, in case of a calorimeter cluster, the fraction of energy that it contributed to the total true energy. The relations for the reconstructed particles are based on the contributing tracks in case of charged particles and the contributing clusters for neutral particles. This resembles how the information is used in the PFA, which only uses the track momentum to calculate the particle energy, if available, because it has usually much higher accuracy.

CHAPTER 7

Tracking Performance in CLIC_SiD

In this chapter the performance of the tracking system of the CLIC_SiD model is studied. First, the performance in determining the fundamental observables is studied in single muon events in Section 7.1. In Section 7.2 we introduce the samples used to study the performance in jet events. Furthermore we motivate our definition of the track finding efficiency and the fake rate in Section 7.3. Afterward we present a parameter scan used to determine the optimal track finding efficiency strategies in Section 7.4. Finally, in Section 7.5, we determine the performance in di-jet events from track finding efficiency and fake rates including the impact of the $\gamma\gamma \rightarrow$ hadrons background.

7.1 Track Resolution

7.1.1 Momentum Resolution

As we have discussed in Chapter 4 the momentum is one of the main observables in a HEP experiment. In case of particle flow, a precise measurement of the track momentum is also essential for the energy measurement of charged particles. It is especially important for channels that involve only leptonic final states like for example the analysis of the Higgs decay into muons in Chapter 10.

Figure 7.1 (left) shows the transverse momentum resolution of the CLIC_SiD detector versus the momentum for single muons at different polar angles θ. The points show the result obtained from a Gaussian fit on 10000 fully simulated and reconstructed tracks at the respective angle and momentum. The dashed lines shows a fit to Eq. (4.14) for fixed θ. The resulting fit parameters are given in Table 7.1. The desired momentum resolution of $\sigma_{p_T}/p_T^2 \approx 2 \cdot 10^{-5}\,\text{GeV}^{-1}$ is achieved for central tracks with a momentum above 100 GeV. For forward tracks with a polar angle of 30° this resolution is only reached for very energetic particles of 500 GeV or more. The parameter b is increasing towards lower θ, which is expected due to the higher material budget in the forward region (see Fig. 5.6). Although the material budget assumed in the simulation model is rather ambitious it is still the limiting factor for the momentum resolution up to very high momenta. The dependence of the transverse momentum resolution on the polar angle is shown in Fig. 7.1 (right) for different track momenta. The strong θ-dependence originates from the dependence of p_T on θ.

The Δp_T-distribution of the reconstructed momenta follows a Gaussian distribution for all simulated samples. This is expected, since there is no confusion when reconstructing single tracks which could induce errors beyond the normal distributed errors due to multiple scattering and the measurement of the curvature. For high momentum forward tracks of $\theta \leq 30°$ the reconstructed momentum is slightly

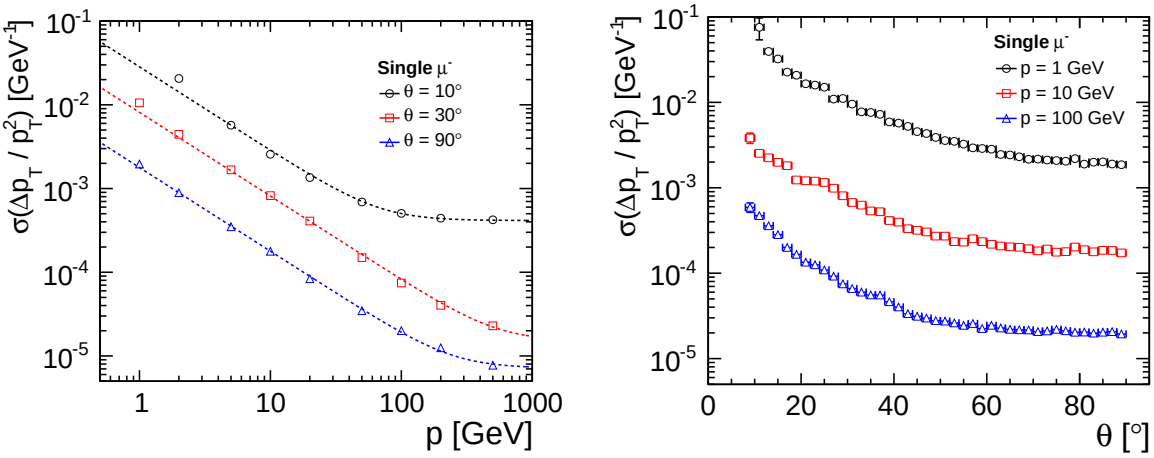

Figure 7.1: Transverse momentum resolution depending on the momentum p for single muons at polar angles of 10°, 30° and 90° (left). Transverse momentum resolution depending on the polar angle θ for single muons of 1 GeV, 10 GeV and 100 GeV (right).

Table 7.1: Transverse momentum resolution $\sigma(\Delta p_T/p_T^2)$ in CLIC_SiD for single muons, parametrized by Equation 4.14.

θ [°]	$a\left[\text{GeV}^{-1}\right]$	b
90	$7.3 \cdot 10^{-6}$	$2.0 \cdot 10^{-3}$
30	$1.9 \cdot 10^{-5}$	$3.8 \cdot 10^{-3}$
10	$4.0 \cdot 10^{-4}$	$5.3 \cdot 10^{-3}$

biased, depending on the charge, as shown in Fig. 7.2 (left). This shows that the curvature fit is biased towards one direction in ϕ for these tracks, resulting in too low curvatures for negatively charged tracks and too high curvatures for positively charged tracks. It remains to be understood if this effect is due to the detector geometry, e.g. the fact that the modules in the disk detectors are overlapping in one direction, or is caused by the algorithm itself. Since only a very specific group of tracks is affected, this problem was not considered problematic for the CDR studies.

The pull of the transverse momentum is defined as $\Delta p_T/\delta p_T$, where δp_T is the uncertainty calculated by the track fit. It allows to test the uncertainty calculated by the track fit. Ideally, the pull-distribution follows a Gaussian distribution with a width of 1. To calculate the pull we first need to propagate of the uncertainty from the track parametrization to the desired physical quantity which is shown in Appendix C. The resulting pull distribution is shown in Fig. 7.2 for muons of 10 GeV at three different polar angles. The widths of all distributions are significantly larger than 1 which means that the uncertainties are underestimated by the fit. This was expected, as the correlations between the multiple scattering corrections introduced by each traversed layer are neglected. While the error is underestimated by approximately 50% for the muons at 10° the difference for muons at 90° is more than a factor of 3.

The momentum resolutions for single muons is shown in Fig. 7.3. It is much less dependend on the polar angle than the transverse momentum resolution, which dominates the momentum resolution only in the central region. The polar angle resolution, which we discuss below, dominates the momentum resolution in the forward region (see Eq. (4.16)).

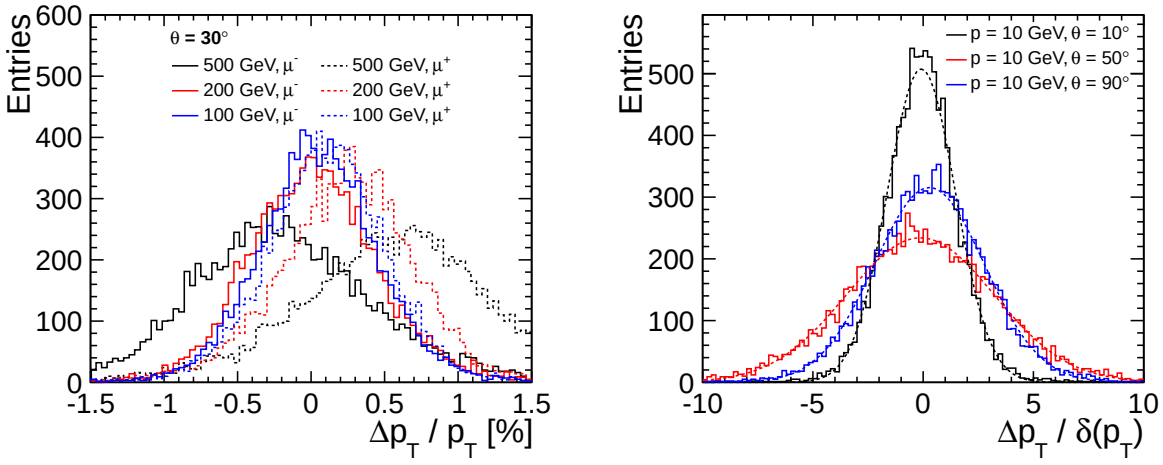

Figure 7.2: Δp_T-distribution for high energetic muons at a polar angle of 30° (left). Pull-distribution of the transverse momentum measurement for muons of 10 GeV (right).

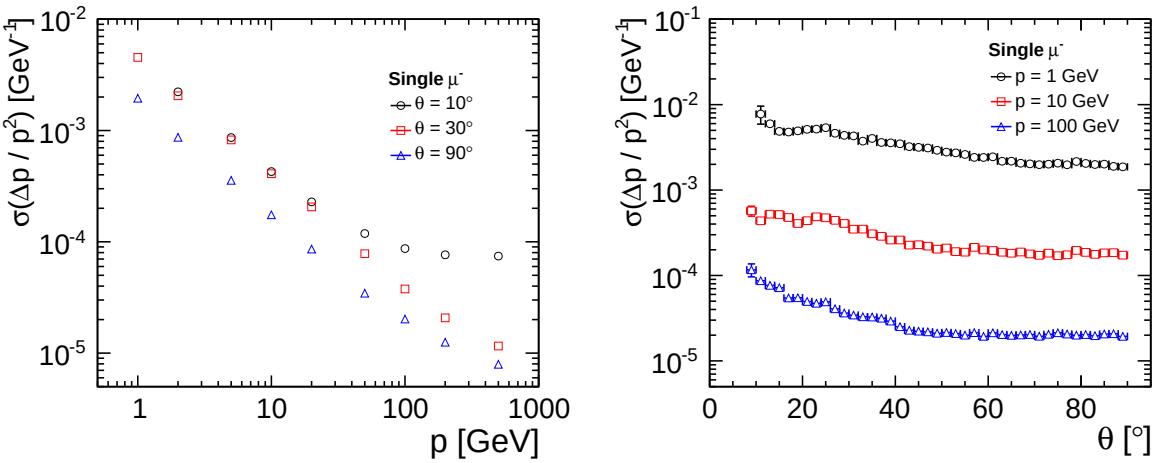

Figure 7.3: Momentum resolution depending on the momentum p for single muons at polar angles of 10°, 30° and 90° (left). Momentum resolution depending on the polar angle θ for single muons of 1 GeV, 10 GeV and 100 GeV (right).

7.1.2 Angular Resolution

The dependence of the polar angle resolution on the polar angle is shown in Fig. 7.4 (left). For low energies the resolution dependency is almost flat and is given by the multiple scattering contribution. For high track momenta, on the other hand, it has some distinct features. These originate from the fact that only pixel hits are used in the fit of the slope (see Section 6.3.5). This results in a very short lever arm for the fit of the slope in the central region. Using Eq. (4.9) we can estimate the expected polar angle resolution for a given angle. For example, using $\sigma(\xi) \approx 0.00577\,\text{mm}$, $L \approx 50\,\text{mm}$ and $N = 5$ yields a resolution of approximately $\sigma(\theta) \approx 0.0065°$ which is slightly better than the number in Fig. 7.4 since we have neglected the multiple scattering term. The complete angular dependency of the $\sigma(\theta)$-resolution for high momentum tracks can be explained from Eq. (4.9), as $\sigma(\xi)$, L, $N = 5$ vary with the

polar angle. The resolution can not be easily improved by using the strip hits in the fit due to their large point resolution in z. This effects has no impact on the momentum resolution as shown in Fig. 7.3.

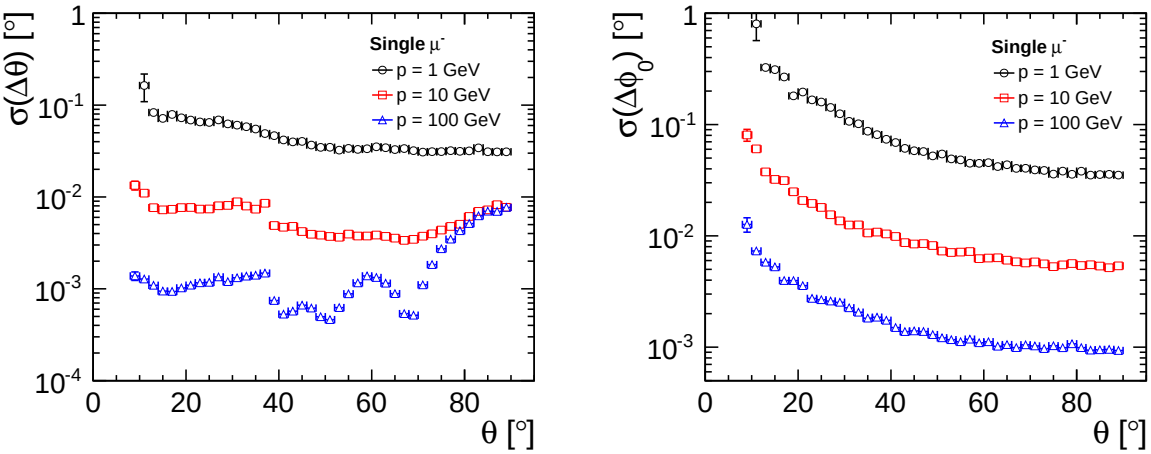

Figure 7.4: Polar angle resolution depending on the polar angle for single muons (left). Azimuthal angle resolution depending on the polar angle for single muons (left).

The dependency of the azimuthal angle resolution on the polar angle, shown in Fig. 7.4 (right), is similar to the behavior of the transverse momentum resolution. This is expected since they are directly connect via Eq. (4.5).

7.1.3 Impact Parameter Resolution

Figure 7.5 (left) shows the impact parameter resolution for d_0. As expected, the d_0-resolution dependency on the polar angle is similar to the azimuthal angle dependency and reaches a few µm for high momentum tracks. The reconstructed d_0 is significantly biased depending on the track charge for tracks with a momentum above 10 GeV. This effect, which can be seen in Fig. 7.5 (right), shows that the track fitting is currently underestimating the curvature of very straight tracks.

The z_0 resolution, shown in Fig. 7.6, is clearly dominated by the polar angle resolution with an added $1/\sin\theta$ dependence according to Eq. (4.23). This limits the z_0 resolution in the central region to values significantly larger than 1 µm.

7.2 Jet Event Samples

The tracking performance in jets is studied in di-jet events from the decay of a hypothetical Z′ with a mass of 3 TeV which has been produced at rest and is presented in Section 7.5. These events offer two highly energetic jets with high local track densities which are particularly challenging for the pattern recognition. The performance in jet events was also studied in $t\bar{t}$ events with a center-of-mass energy of 3 TeV which can be found in Appendix D. These events offer quite a different topology with two to six jets, depending on the decay mode of the two W bosons. The $t\bar{t}$ events have a more complex topology compared to the di-jet events but are slightly less challenging for the pattern recognition, which is limited by local occupancy instead of global occupancy.

The distributions of the polar angle and the transverse momentum of the findable particles in the jet events are shown in Fig. 7.7 (see Section 7.3 for the definition of findable particles). While the angular

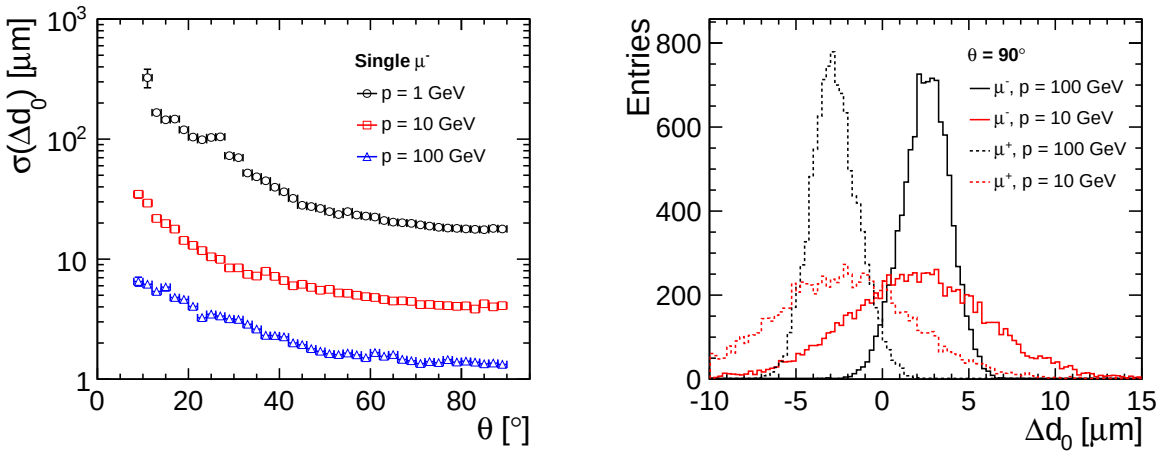

Figure 7.5: Impact parameter d_0 resolution depending on the polar angle θ for single muons of different energies (left). Δd_0-distribution for μ^+ and μ^- of 10 GeV and 100 GeV at a polar angle θ of 90° (right).

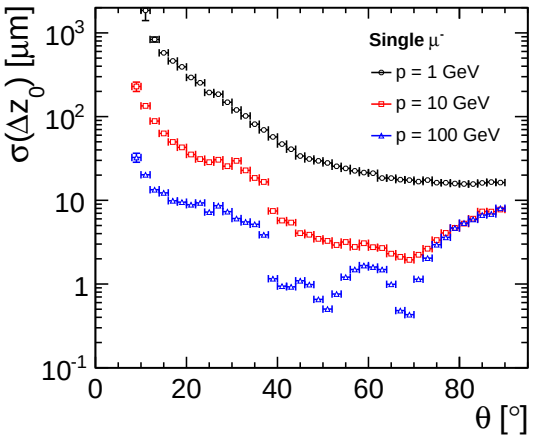

Figure 7.6: Impact parameter z_0 resolution depending on the polar angle θ for single muons of different energies.

distribution is similar in both cases with most of the tracks inside the barrel region of $\theta > 40°$, the transverse momentum distribution extends to higher momenta in case of the di-jet events. This is due to the fact that the same amount of energy is distributed over fewer tracks.

The track multiplicity is shown in Fig. 7.8 (left). The average number of findable tracks in di-jet events is 64.6, while it is 77.6 in $t\bar{t}$ events. Despite the higher track multiplicity, the local occupancy is lower in $t\bar{t}$ events since the tracks are distributed over up to six jets and those jets are less pencil like due to the lower track momentum. This can be seen in Fig. 7.8 (right) which shows the closest distance from any of the track hits to any other hit. Any hit closer than 40 µm will not results in a separate digitized cluster and can thus not be resolved. In both types of events a large number of tracks has at least one hit within its direct vicinity. The peak for $t\bar{t}$ events is around 190 µm, while for di-jet events it is below the threshold that can be resolved.

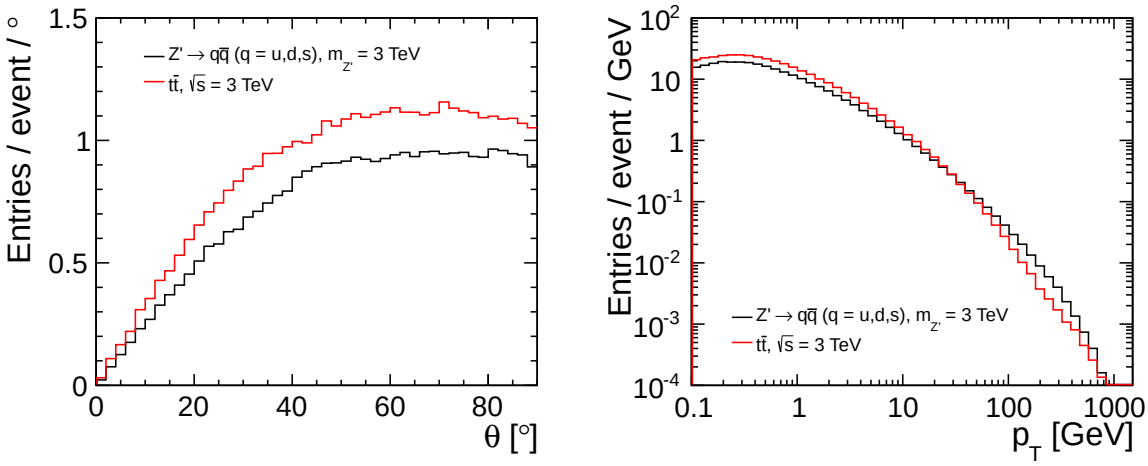

Figure 7.7: Distribution of polar angles θ (left) and distribution of transverse momenta p_T (right) of findable particles in $Z' \to qq(q = uds)$ and $t\bar{t}$ events.

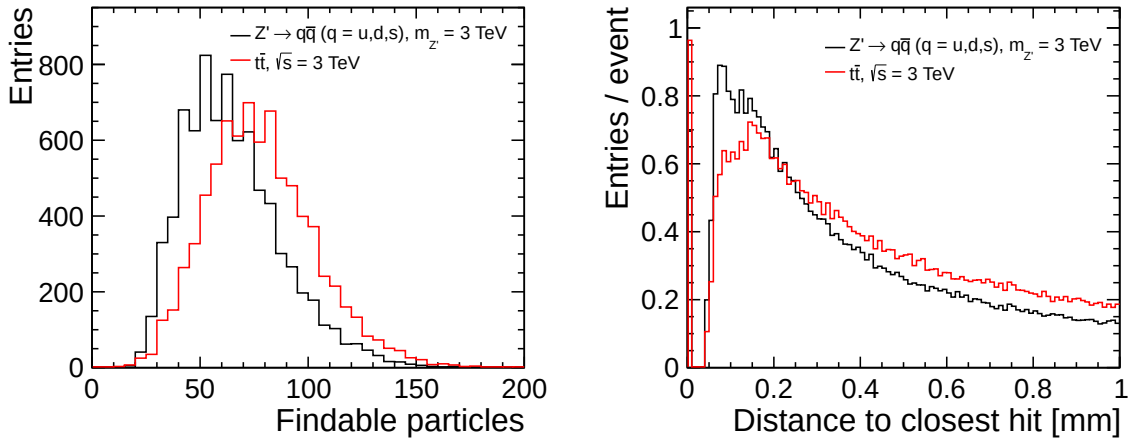

Figure 7.8: Distribution of number of findable particles (left) and the distance to the closest hit not originating from these particle (right) in $Z' \to qq(q = uds)$ and $t\bar{t}$ events.

7.3 Tracking Efficiency and Fake Rate Definition

An important aspect of the tracking performance is the efficiency of reconstructing a particle track. First the reconstructed tracks have to be matched to Monte Carlo particles. This is done using the truth linking explained in Table 6.2. The particle contributing to the majority of hits that have been associated to the track during the track reconstruction is considered the true particle. In addition, if this particle contributed to multiple reconstructed tracks it is only considered the true particle for the track to which it contributed most of its hits. The tracking efficiency can then be expressed as

$$\epsilon = \frac{N_{\text{reconstructed}}}{N_{\text{findable}}}, \tag{7.1}$$

where $N_{\text{reconstructed}}$ is the number of findable particles that have been matched to a reconstructed track and N_{findable} is the number of particles that are supposed to be found. The definition of what to call a findable particle is strongly dependend on which type of tracking efficiency is looked at. Throughout this Chapter two types of tracking efficiencies are used.

Algorithmic tracking efficiency is a measure of how efficient the tracking algorithm finds tracks of particles that fulfill all requirements that are intrinsic to the algorithm: the minimum transverse momentum, maximum impact parameter, minimum number of total hits and sufficient number of hits in the seed layers. This tracking efficiency is neither sensitive to the geometric coverage nor the coverage by the chosen tracking strategies.

Total tracking efficiency —further referred to as just tracking efficiency—includes inefficiencies due to the algorithm and the geometric coverage and represents the efficiency relevant to any realistic physics analysis. Nevertheless, some selection cuts have to be applied to the particles in order to select only those that are actually relevant for a physics analysis. First, only those charged particles that travel at least 5 cm, measured along their helical path, are considered findable particles to suppress those intermediate particles short life times. In addition, only those particles originating from within a sphere with a radius of 5 cm from the interaction point are taken into account. This cut does not reject particles originating from typical secondary vertices but removes particles created from bremsstrahlung in the tracking volume.

Two additional selection cuts are applied depending on the variable that is plotted if not stated otherwise. For efficiency plots versus θ a minimum transverse momentum of 1 GeV is required. Similarly, for plots versus p_{T} a minimum polar angle of 15° is implied. This is done to disentangle the effects of detector acceptance and low efficiency for low momentum tracks.

All selection cuts are applied to both the reconstructed and findable particles. An additional quality cut is applied to the reconstructed particles to ensure that the parameters of the reconstructed track resemble those of the original particle. This quality cut is based on the number of false hits that have been assigned to a reconstructed track. A hit is considered a false hit if the truth matched particle did not contribute to the hit. Fig. 7.9 shows the transverse momentum resolution depending on the track momentum and the $\frac{\Delta p_{\text{T}}}{p_{\text{T}}^2}$-distribution for central tracks in di-jet events with different numbers of false hits. Fig. 7.10 shows the impact parameter resolution depending on the track momentum and the Δd_0-distribution for central tracks in di-jet events with different numbers of false hits. Both resolutions are degrading strongly if one or more false hits have been assigned to a track and large non-Gaussian tails can be seen in the distributions. For this reason, the RMS_{90} method was preferred over a Gaussian fit to obtain the resolutions.

Requiring a pure track with no false hits reduces the track reconstruction efficiency, as shown in Figure 7.11. This effect is most strongly seen in the barrel region, where due to the missing information on the z-coordinate of the strip detectors it is more likely to pick up a false hit. Thus, the definition of a good track is always a tradeoff between ultimate resolution and good efficiency. For the remainder of this chapter the maximum number of false hits on a track is one for those tracks that are counted as reconstructed tracks in the efficiency calculation.

The fake rate is a measure of the number of tracks that are reconstructed but that do not correspond to any of the true particles. It can be expressed as

$$f = \frac{N_{\text{fake}}}{N_{\text{reconstructed}}}, \tag{7.2}$$

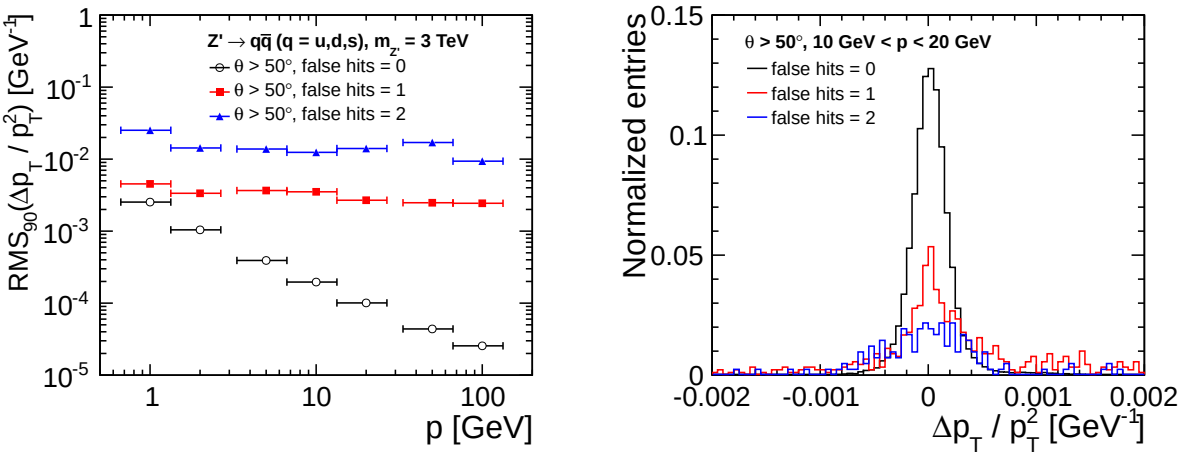
Z' → qq̄ (q = u,d,s), m_Z' = 3 TeV
θ > 50°, false hits = 0
θ > 50°, false hits = 1
θ > 50°, false hits = 2
RMS90(Δp_T / p_T^2) [GeV^-1]
p [GeV]
θ > 50°, 10 GeV < p < 20 GeV
false hits = 0
false hits = 1
false hits = 2
Normalized entries
Δp_T / p_T^2 [GeV^-1]

Figure 7.9: Momentum resolution depending on the track momentum (left) and the $\frac{\Delta p_T}{p_T^2}$-distribution for 10 GeV $< p <$ 20 GeV (right) for reconstructed tracks in the central region of the detector with different numbers of false hits in di-jet events.

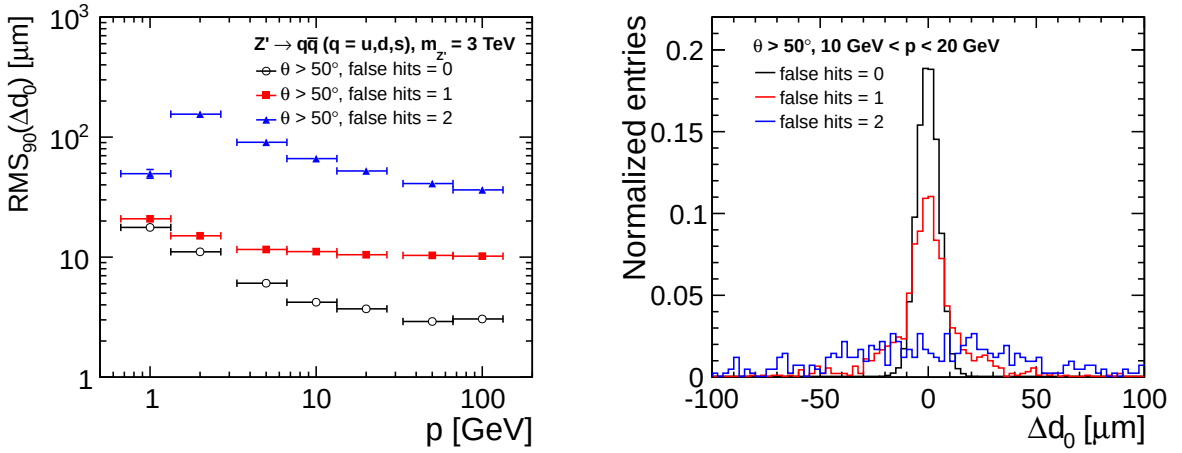
Z' → qq̄ (q = u,d,s), m_Z' = 3 TeV
θ > 50°, false hits = 0
θ > 50°, false hits = 1
θ > 50°, false hits = 2
RMS90(Δd0) [μm]
p [GeV]
θ > 50°, 10 GeV < p < 20 GeV
false hits = 0
false hits = 1
false hits = 2
Normalized entries
Δd0 [μm]

Figure 7.10: The d_0 impact parameter resolution depending on the track momentum (left) and the Δd_0 distribution depending on the polar angle (right) for reconstructed tracks with different numbers of false hits in di-jet events.

where N_{fake} is the number of fake tracks and $N_{\text{reconstructed}}$ is the number of all reconstructed tracks. One type of fake tracks is purely combinatorial fakes where a track is reconstructed from random hits. A bad track on the other hand is a track that correctly identifies the hits originating from a single particle but has picked up additional hits and results in track fit parameters far from those of the original particle. Both effects mostly depend on the occupancy in the tracking detectors. Here the second, much stricter, definition is used and the fake rate is given as the fraction of tracks that have more than one false hit.

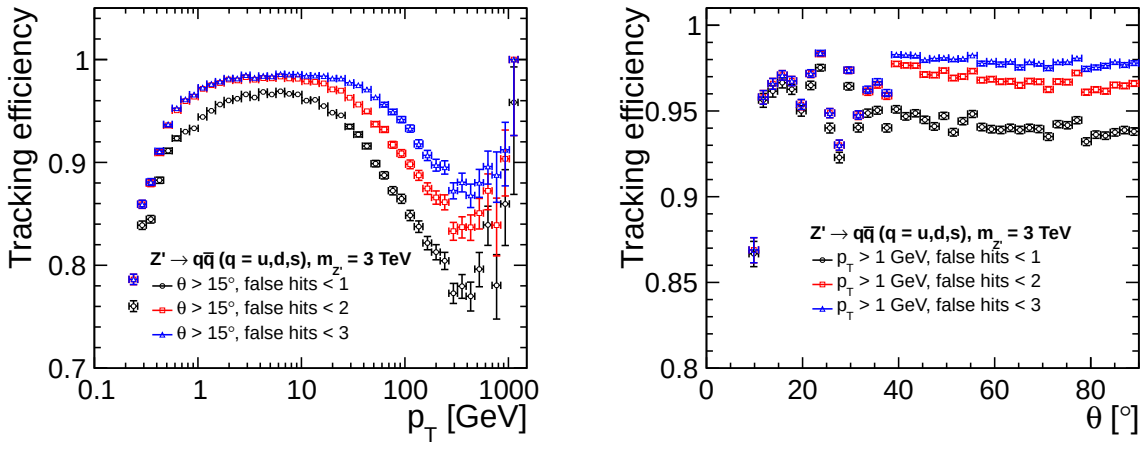

Figure 7.11: Tracking efficiency depending on the transverse momentum (left) and the polar angle (right) for reconstructed tracks with different numbers of false hits in di-jet events.

7.4 Strategy Optimization

As explained in Section 3.1.3, the track finding is steered by a set of strategies which can be trained automatically. For this training, a dedicated event sample of 100000 single muon events is used. The muons are uniformly distributed in p between 0.1 GeV and 50 GeV, in θ between 5° and 175° and between 0° and 360° in ϕ. The minimum transverse momentum for the strategy training is set to 0.2 GeV. The layer weights are set such that vertex layers are preferred for seeding with decreasing weights for layers further away from the interaction point, resulting in inside-out tracking strategies.

The incoherent pair background, introduced in Section 3.1.3, could not be included in the track reconstruction due to its huge number of particles. In order to not overestimate the track finding performance, the two innermost vertex layers are excluded as seed layers. Their occupancy is considerably higher than those of the outer layers, as shown in Section 5.6. Nevertheless, these layers are allowed as extension layers and thus their hits are used for the track fit.

The χ^2_{max} and N_{min} (see Section 6.3.5) for the final set of tracking strategies were chosen by a parameter scan and the resulting impact on the tracking efficiency in di-jet events. Fig. 7.12 shows the tracking efficiency depending on p_{T} and θ for different N_{min} and a fixed χ^2_{max}. Requiring a large number of hits for a track results in lowered tracking efficiency for low momentum tracks, which are less likely to pass a sufficient number of layers, as well as a smaller acceptance in the very forward region of $\theta < 10°$. The final strategy set thus requires a minimum of 7 hits with an exception of barrel only tracks which require only 6 hits to improve finding of central low momentum tracks. The impact of varying the χ^2_{max} is shown in Fig. 7.13 where the minimum number of hits is kept at 7. For χ^2_{max} below 10 the performance is degrading significantly, while for higher values the performance is almost constant. The final strategy set uses a χ^2_{max} of 10 for all strategies.

7.5 Performance in Jet Events

This section discusses the tracking performance in di-jet events. The performance in $\text{t}\bar{\text{t}}$ events is slightly different due to the different topology and can be found in Appendix D.

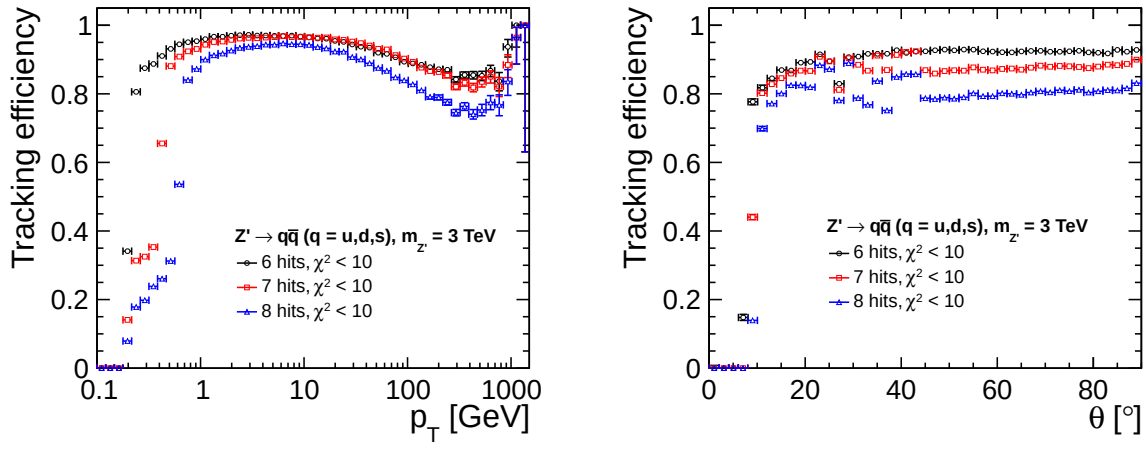

Figure 7.12: Tracking efficiency depending on the transverse momentum p_T (left) and depending on the polar angle θ (right) for various strategy sets requiring a minimum of 6, 7 or 8 hits for a reconstructed track in $Z' \rightarrow qq(q = uds)$ events.

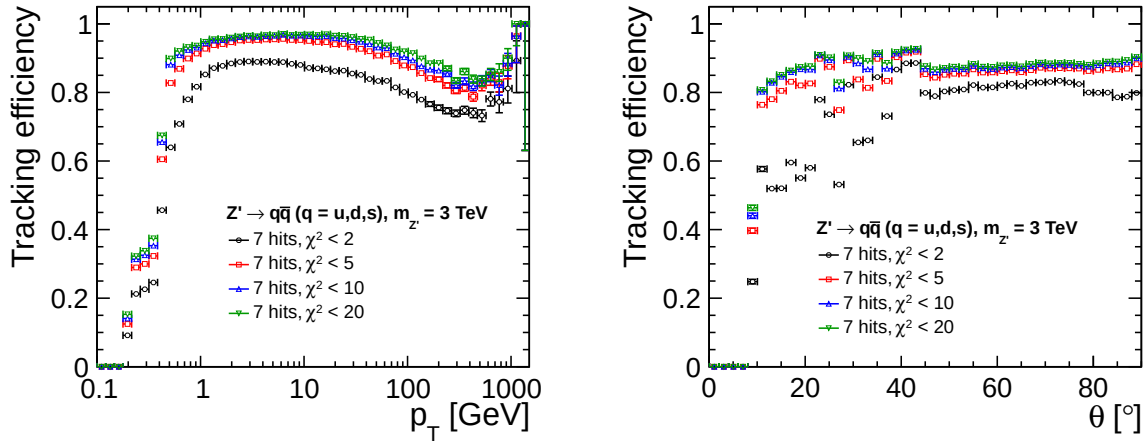

Figure 7.13: Tracking efficiency depending on the transverse momentum p_T (left) and depending on the polar angle θ (right) for various strategy sets with different χ^2_{max} and a minimum of 7 hits for the track finding in $Z' \rightarrow qq(q = uds)$ events.

7.5.1 Track Finding Efficiency

The tracking efficiency in di-jet events depending on the polar angle and the transverse momentum is shown in Fig. 7.14. The highest tracking efficiency of 97% to 98% is achieved for tracks with a transverse momentum between 1 GeV and 20 GeV which constitutes the majority of the tracks. The efficiency drops to below 85% for tracks with a high transverse momentum of around 400 GeV. The efficiency increases for higher momentum tracks which have a higher probability of being isolated, since they carry a very large fraction of the jet energy. The efficiency depending on the polar angle is rather constant in the barrel region going from 96% for very central tracks to about 98% for tracks with a polar angle of 40°. In the forward region, below 40°, the tracking efficiency shows large fluctuations

depending on the local material budget, resulting in efficiencies between 92% and 98%. The efficiency drops sharply for angles below 10° due to the detector acceptance.

Overlaying typical amounts of $\gamma\gamma \rightarrow$ hadrons background expected at CLIC has no significant effect on the track finding efficiency.

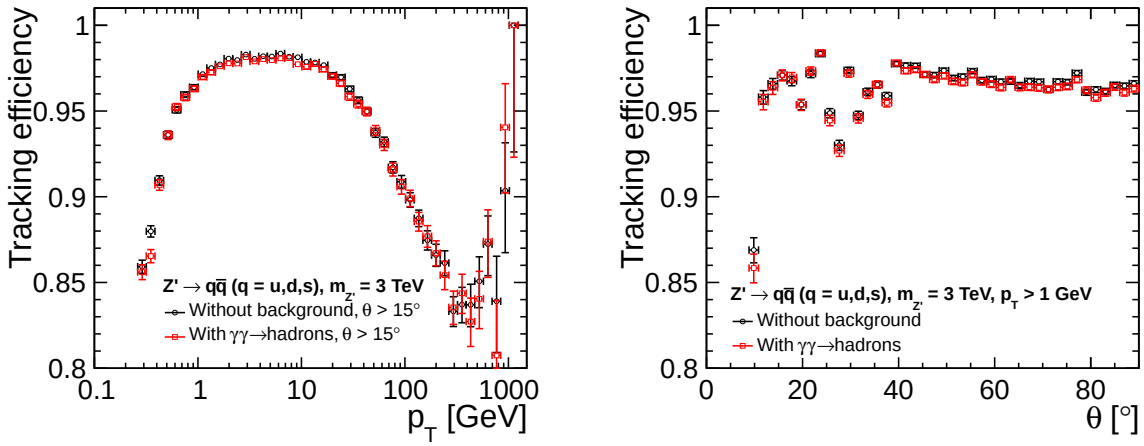
Tracking efficiency
p_T [GeV]
Z' → qq̄ (q = u,d,s), m_Z' = 3 TeV
Without background, θ > 15°
With γγ→hadrons, θ > 15°
Tracking efficiency
θ [°]
Z' → qq̄ (q = u,d,s), m_Z' = 3 TeV, p_T > 1 GeV
Without background
With γγ→hadrons

Figure 7.14: Tracking efficiency depending on the transverse momentum p_{T} (left) and the polar angle θ (right) in $\mathrm{Z}' \rightarrow qq(q = uds)$ events with and without $\gamma\gamma \rightarrow$ hadrons background.

High momentum tracks are most likely in the center of the jet, as shown in Fig. 7.15 (left). The local occupancy is highest in the center of the jets which leads to a higher probability of confusing hits and not finding proper tracks. Fig. 7.15 (right) shows the efficiency depending on the distance to the closest hit along the track. The track finding efficiency is very high (> 97%) for tracks that do not have another hit within 130 µm but drops quickly for tracks that do have a very close hit from another particle.

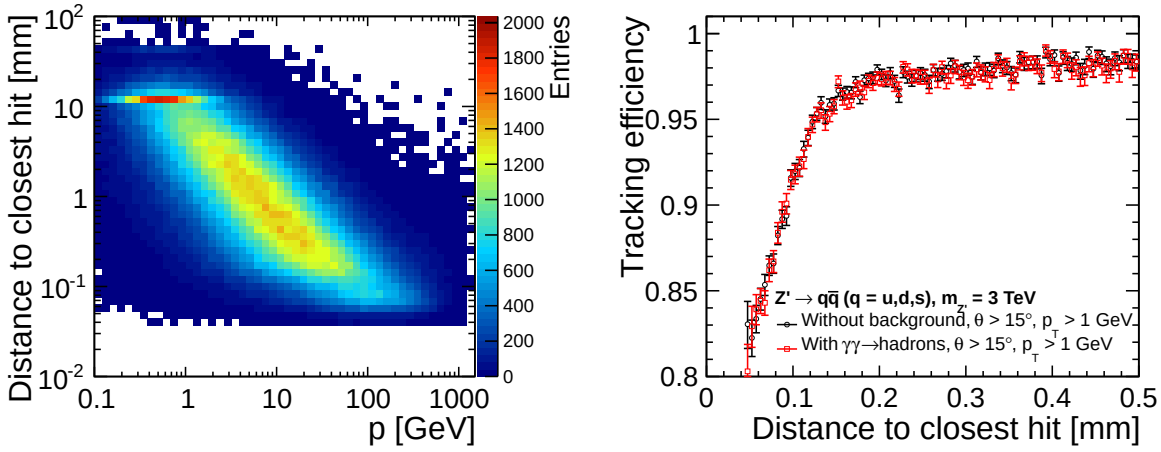
Distance to closest hit [mm]
p [GeV]
Entries
Tracking efficiency
Distance to closest hit [mm]
Z' → qq̄ (q = u,d,s), m_Z' = 3 TeV
Without background, θ > 15°, p_T > 1 GeV
With γγ→hadrons, θ > 15°, p_T > 1 GeV

Figure 7.15: Correlation between track momentum p and the distance to the closest hit in $\mathrm{Z}' \rightarrow qq(q = uds)$ events (left). Tracking efficiency depending on the distance to the closest hit in $\mathrm{Z}' \rightarrow qq(q = uds)$ events with and without $\gamma\gamma \rightarrow$ hadrons background (right).

The algorithmic tracking efficiency is shown in Fig. 7.16. In most regions the results are better by

1–2% than the efficiencies found with the more general definition of the tracking efficiency shown in Fig. 7.14. These 1–2% of the tracks are not findable by the algorithm with the set of strategies that we used. The most important features of the θ and p_T dependency are also visible in the algorithmic tracking efficiency, although less pronounced. As we already discussed, these effects are caused by high local occupancies which the algorithm can not resolve, although, from their parameters these tracks should be findable. In principle it should thus be possible to recover these tracks if the segmentation were sufficiently increased or the algorithm would be improved. One possible improvement could be an iterative approach to the track finding, where hits belonging to an identified track are removed from the list of available hits to allow for a second track finding step to recover tracks that were missed in the first iteration.

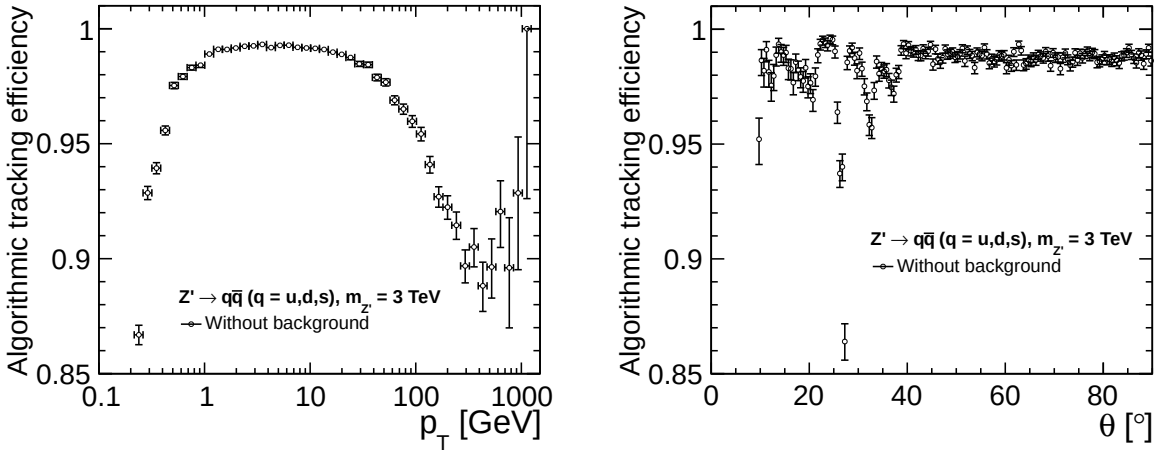

Figure 7.16: Algorithmic tracking efficiency depending on the transverse momentum p_T (left) and the polar angle θ (right) in $Z' \to qq(q = uds)$ events.

7.5.2 Fake Rate

The fake rate in di-jet events is shown in Fig. 7.17. It is highest in the barrel region with between 1% and 2% of fake tracks, when considering each track with two or more false hits as being a fake. This is caused by the low point resolution in z due to the long strip length of the strip detectors in the main tracker barrel. It drops by more than a factor of ten in the forward region where picking up false hits is less likely due to the smaller point resolutions. High p_T tracks are especially likely to be fake tracks since they are in the center of the jets (see Fig. 7.15).

If one uses a stricter definition where each track that has a single false hit is also considered a fake, the fake rate increases by a factor of two to ten.

Like for the tracking efficiency, the fake rate is almost unaffected by the addition of the $\gamma\gamma \to$ hadrons background. The only effect is a significantly lower fake rate for tracks around 1 GeV since the background adds a large amount of tracks to the events with that transverse momentum that are mostly well reconstructed.

7.5.3 Track Purity

The impact of the $\gamma\gamma \to$ hadrons background on the track purity is illustrated in Fig. 7.18. The probability of reconstructing a pure track drops from 96.2% to approximately 95.5% when adding the

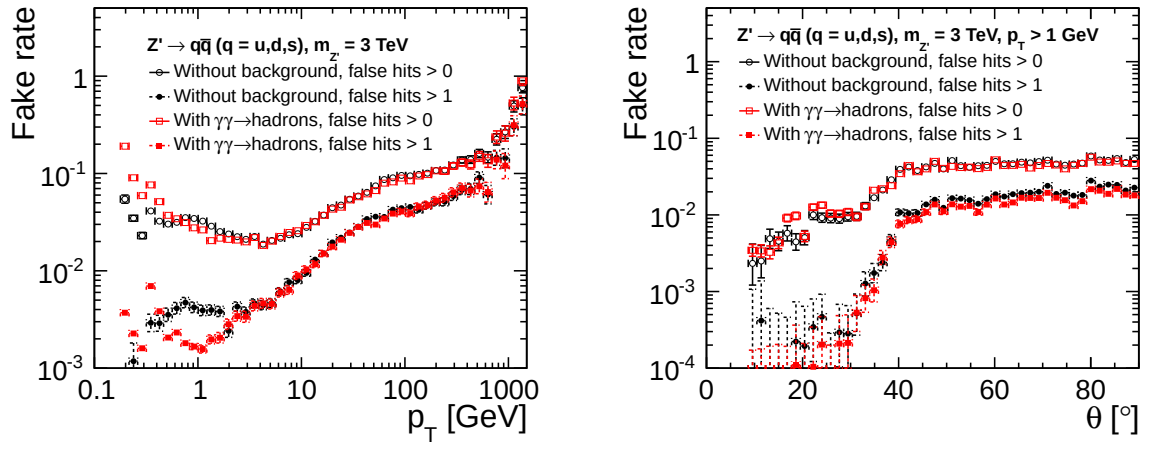
Fake rate
Z' → qq̄ (q = u,d,s), m_Z' = 3 TeV
Without background, false hits > 0
Without background, false hits > 1
With γγ→hadrons, false hits > 0
With γγ→hadrons, false hits > 1
p_T [GeV]
Z' → qq̄ (q = u,d,s), m_Z' = 3 TeV, p_T > 1 GeV
θ [°]

Figure 7.17: Fake rate depending on the transverse momentum p_{T} (left) and the polar angle θ (right) in $\mathrm{Z}' \rightarrow qq(q = uds)$ events with and without $\gamma\gamma \rightarrow$ hadrons background.

$\gamma\gamma \rightarrow$ hadrons background. In turn, the probability to reconstruct a track with one false hit increases from 2.6% to 3.2%. The probability to reconstruct a track with two false hits is almost unchanged at around 0.8%. The number of tracks with even higher numbers of false hits are negligible. In terms of the purity only the tracks with a low number of total hits are affected significantly. The average purity of tracks with 6 hits is reduced from 96.3% to 94.2%, while the purity for tracks with 7 hits is reduced to 95.7% from 96%.

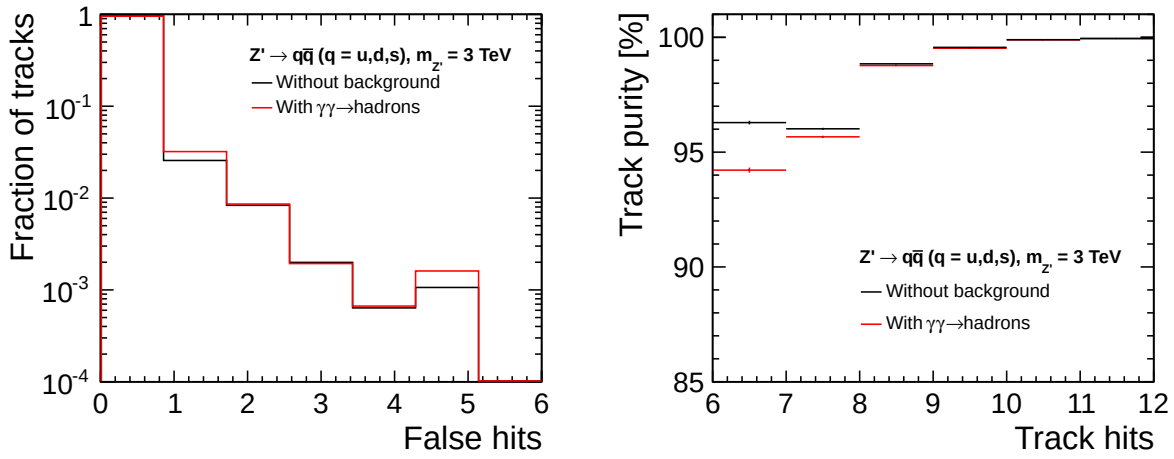

Figure 7.18: Probability of reconstructing a track with a certain number of false hits (left) and average track purity depending on the number of hits on a reconstructed track (right) in $Z \rightarrow qq(uds)$ with and without $\gamma\gamma \rightarrow$ hadrons.

7.6 Summary

It has been shown that the all-silicon tracker designed for the SiD detector concept is also suitable as the main tracking device in a CLIC detector at 3 TeV. It offers excellent momentum and impact $d0$

resolution and despite the low number of tracking layers achieves an excellent pattern recognition with high track finding efficiency, high purity and a low fake rate. The high purity is essential to the tracking performance in this layout with a minimal number of layers since already a single false hit deteriorates the track fit significantly. Some shortcomings of the current track fitting algorithm have been identified and remain to be investigated. In addition, the short lever arm in the vertex barrel detector was identified as the limiting factor in the θ resolution and thus also limits the z_0 resolution. If a better resolution is desired this would require at least one highly segmented layer at a large radius.

The amount of beam-related background assumed in these studies does not significantly affect the track reconstruction. Instead, the high local occupancy in multi-TeV jets is the most important source of inefficiencies in the track finding. This effect is most notable in the barrel region where the low z-resolution of the strip detectors can lead to confusion. The impact of increasing the longitudinal segmentation in one or more of the barrel tracker layers should thus be investigated in the future.

CHAPTER 8

HCal Layout Optimization

The design of the calorimeter system has to take into account several parameters. Most important is the desired energy resolution, which is driven by the sampling fraction, the choice of the absorber material as well as the active material and the readout technology. A good energy resolution also relies on a linear response over the full energy range as well as on minimal leakage, which means that the calorimeter depth has to be well adapted to the expected shower energies. Finally, cost and feasibility have to be taken into account as well.

The aim for excellent jet energy resolution as discussed in Section 4.3 requires that both the ECal and the HCal are placed inside of the solenoid to avoid large amounts of dead material in the region most important to the energy measurement—the shower maximum. The desired magnetic field in the inner detector of 5 T for the SiD concept implies a strong constraint on the maximum coil radius through cost and technical feasibility. This translates directly into the maximum radius of the calorimetric system. When modifying the ILD and SiD detector concepts for the CLIC scenario it was decided to keep the inner and outer radii of the calorimeter systems and replace the iron absorber plates in the HCal with a denser absorber material. This requires a re-assessment of the absorber thickness to achieve optimal performance. There is no need to modify the ECal since the ILC concepts already foresee dense tungsten absorber plates with a total depth of approximately 25 X_0. In addition, the highly granular HCal offers sufficient performance to measure the tails of electromagnetic showers that might leak out of the ECal.

This chapter presents a systematic simulation study to identify the optimal sampling fraction for the HCal in a CLIC detector, comparing different calorimeter configurations using steel and tungsten absorber plates. The different calorimeter geometries that were used in the simulations are explained in Section 8.1. The energy reconstruction is performed using a Neural Network (NN), which is discussed in Section 8.3. Section 8.4 shows the intrinsic resolution that results from the different sampling frequencies and Section 8.5 discusses the energy resolution that is achievable when a finite detector length and leakage are taken into account. The impact of additional calorimetric information from a tail catcher that is placed behind the coil is shown in Section 8.6.

8.1 Calorimeter Models

To optimize the sampling fraction of a calorimeter a simplified detector model is sufficient. The simulation models used in this study consist of simple HCal stacks with varying absorber materials and absorber plate thicknesses. The sampling fraction is homogeneous within each stack and thus, no ded-

Table 8.1: List of all simulated HCal geometries. Given is the absorber material, the thickness of the absorber layer, the average nuclear interaction length λ_I and the average radiation length X_0 for each full layer including the passive and active material.

absorber material	absorber thickness [mm]	λ_I per layer	X_0 per layer
tungsten	5	0.06	1.37
tungsten	10	0.11	2.72
tungsten	15	0.16	4.07
tungsten	20	0.21	5.42
steel	10	0.07	0.60
steel	15	0.10	0.89
steel	20	0.13	1.18
steel	25	0.16	1.47
steel	30	0.19	1.76
tungsten-steel	10	0.09	1.66
tungsten-steel	15	0.13	2.48
tungsten-steel	20	0.17	3.30
steel-tungsten	10	0.09	1.66
steel-tungsten	15	0.13	2.48
steel-tungsten	20	0.17	3.30

icated ECal is present in the models. The absorber materials studied are tungsten and steel as well as combinations of both materials, where each absorber layer consists of two slices of each material, each with a thickness of half the total thickness. The models with both absorber materials were simulated in two configurations, such that each material is used as the first material in direction of the particle. The order of the material has an impact mostly on the electromagnetic shower component since the X_0 of steel and tungsten are very different. In total, 15 different configurations have been simulated. They are listed in Table 8.1. The depth of each calorimeter stack model is chosen large enough ($> 20\lambda_I$) such that longitudinal leakage is negligible. With a plate size of $5 \times 5\,\mathrm{m}^2$ the lateral leakage can also be ignored.

The tungsten alloy used in the simulation, simply referred to as tungsten, consists of 93% W, 6.1% Ni and 0.9% Fe (by volume), which results in a radiation length of 0.37 cm and the nuclear interaction length is 10.16 cm For the steel we assume a typical structural steel (*steel 235*) with 99.8% Fe, 0.02% Cu and a density of $7.85\,\mathrm{g/cm}^3$. The radiation length is 1.73 cm and the nuclear interaction length is 16.87 cm. The active material thickness and the readout is the same in all setups. Each active layer consists of 5 mm of plastic scintillator (Polysterene), followed by 2.5 mm of G10, a fibre-reinforced plastic that serves as a placeholder for the readout electronics and cabling present in each layer. The layers are segmented into $1 \times 1\,\mathrm{cm}^2$ cells with analog readout. The scope of this study is not the optimization of the lateral segmentation and only showers originating from single particles are simulated. In addition, only variables that are not strongly dependent on the lateral segmentation are used to describe the shower shape (see Section 8.3).

The minimum energy of a hit to be considered in the reconstruction is 250 keV. This represents a noise cut that would be applied in any real experiment. The simulation does not include noise hits.

The depth of the calorimeter is varied by ignoring all simulated hits in those layers that are not considered part of the detector. This also allows to study the impact of large inactive areas within the calorimeter and is used to study the impact of the coil position, as discussed in Section 8.6.

8.2 Event Samples

An event sample of single pions is used to study the hadronic energy measurement. A data set of 100000 π^+ events was simulated in each of the detector configurations described above. Since a NN is used to reconstruct the pion energy, a sample with a continuous energy distribution is used for the training in order to avoid overtraining. The particle energy is chosen to be in the range between 1 GeV and 300 GeV and follows an exponential distribution with

$$N \propto 0.5^{E/300\,\mathrm{GeV}} \tag{8.1}$$

to provide slightly more statistics at lower particle energies. This energy range represents the typical energy of individual particles in jets at the TeV scale, e.g. as shown in Figure 7.8 (left). The pions are generated using the GEANT4 particle gun and are shot perpendicular onto the center of the first calorimeter layer. A small angular spread of $\pm 1^\circ$ is added to the particle direction to avoid a bias due to the impact position of the particle.

The neutron content of hadronic showers increases with the atomic mass of the materials traversed. The response of plastic scintillators is especially sensitive to signals from elastic neutron scattering due to the high fraction of hydrogen. The higher cross section for neutron capture in tungsten compared to steel leads to an enhanced slow shower component and a significantly different time structure of the signal. In combination, this means that the simulation of the neutron shower component requires special attention when simulating tungsten-scintillator sampling calorimeters. GEANT4 offers special high precision physics list for low energetic neutrons that are denoted by an appended `HP` to the name of the physics list. These physics lists allow for tracking of neutrons with kinetic energies below 20 MeV down to thermal energies [148]. Unlike the other simulation studies presented in this thesis, which use the `QGSP_BERT` physics list (see Section 6.2), the simulations presented in this chapter are performed using the `QGSP_BERT_HP` physics list. The differences of the two physics lists for the tungsten absorber case are discussed in [149]. First results from a test beam campaign with a tungsten HCal prototype [150] indicate that simulations using the `QGSP_BERT_HP` physics list are in good agreement with the observed time development of hadronic showers [151].

8.3 Energy Reconstruction with a Neural Network.

The standard approach of energy reconstruction in a sampling calorimeter is a linear model where the sampling fraction is used to calculate the particle energy from the sum of the visible energy. This often requires to apply ad-hoc corrections for leakage as well as weightings depending on the shower type to obtain a good energy resolution. A multivariate classifier allows to directly use the maximum information of the shower topology in the energy reconstruction, taking into account possible correlations of the variables. Simulation studies performed for various HEP experiments, e.g. H1 [152], CMS [153] and ATLAS [154], have found that an energy reconstruction using NN performs usually much better than the respective standard energy reconstruction of the experiments. For the HCal optimization study presented here, the particle energy is therefore reconstructed from the energy deposited in the active scintillator material using the Neural Network classifier implemented in the Toolkit for Multivariate Data Analysis (TMVA) [155]. Using shower shape information is especially beneficial when assessing the impact of the coil position and a possible tail catcher, which requires an estimation of the energy deposited in the dead region from adjacent layers.

The Neural Network is created with two hidden layers of $N + 30$ and $N + 20$ nodes, where N is the number of variables used. The network is trained with the true particle energy as the target value on

half of the simulated events. For each of the detector configurations an individual network is trained using the hits from a calorimeter depth of approximately 3 λ_I, 4 λ_I, 5 λ_I, 6 λ_I, 7 λ_I, 8 λ_I, 9 λ_I and the full calorimeter stack. Specific NNs are also trained for the various tail catcher configurations. This way the leakage is implicitly taken into account in the training. The training events are not used in the analysis discussed in Sections 8.4, 8.5 and 8.6.

8.3.1 Neural Network Variables

Since only single particles are simulated, no clustering algorithm is necessary and all hits with an energy above the threshold of 250 keV define the cluster. The following variables are used in the NN to reconstruct the particle energy.

- The total energy of the cluster

$$E_{\text{cluster}} = \sum_{i}^{N_{\text{cells}}} E_{\text{cell},i}, \tag{8.2}$$

  where $E_{\text{cell},i}$ is the deposited energy in the cell with the index i and with $E_{\text{cell},i} > E_{\text{threshold}}$.

- The energy density in the cluster

$$\rho_{\text{E,cluster}} = \frac{E_{\text{shower}}}{N_{\text{cells}}}. \tag{8.3}$$

- The energy weighted center of the cluster in z direction

$$\bar{z}_{\text{cluster}} = \frac{1}{E_{\text{cluster}}} \sum_{i}^{N_{\text{cells}}} z_{\text{cell},i} E_{\text{cell},i}, \tag{8.4}$$

  where $z_{\text{cell},i}$ is the z position of the cell with the index i.

- The energy weighted distance of the cluster from the z axis

$$\bar{r}_{\text{cluster}} = \frac{1}{E_{\text{cluster}}} \sum_{i}^{N_{\text{cells}}} r_{\text{cell},i} E_{\text{cell},i}, \tag{8.5}$$

  where $r_{\text{cell},i}$ is the distance from the z axis of the cell with index i.

- The length of the cluster in z, estimated by the Root Mean Square (RMS) of the energy weighted z position

$$\text{RMS}_{z,\text{cluster}} = \frac{1}{E_{\text{cluster}}} \sqrt{\sum_{i}^{N_{\text{cells}}} \left(z_{\text{cell},i} - \bar{z}\right)^2 E_{\text{cell},i}^2}. \tag{8.6}$$

- The width of the cluster, estimated by the RMS of the energy weighted distance from the z axis

$$\text{RMS}_{r,\text{cluster}} = \frac{1}{E_{\text{cluster}}} \sqrt{\sum_{i}^{N_{\text{cells}}} \left(r_{\text{cell},i} - \bar{r}\right)^2 E_{\text{cell},i}^2}. \tag{8.7}$$

- Three additional energy sums are calculated similarly to Eq. (8.2) for different regions of the calorimeter. The energy deposited within the first λ_I of the calorimeter, the last λ_I of the calorimeter and the energy deposited in between these two regions.

- In case of the tail catcher studies, the sum of the energy visible in the tail catcher is used as an additional variable. The tail catcher is defined as a region of the calorimeter that follows an inactive volume with a length of approximately $2\,\lambda_I$ which represents the coil.

8.4 Energy Resolution and Linearity

The energy resolution is determined as the $\mathrm{RMS}_{90}(E_{\mathrm{reco}}/E_{\mathrm{true}})$ in 13 intervals of the true particle energy in the range between 40 GeV and 270 GeV. The intervals are chosen such that the ratio $E_{\mathrm{reco}}/E_{\mathrm{true}}$ is almost constant over the interval. The RMS_{90}, which is explained in Appendix B, is preferred over a Gaussian fit to describe the width of the reconstructed energy. It takes into account possible non-Gaussian tails while rejecting strong outliers at the same time. The energy dependence of the resolution can be described by the parametrization given in Eq. (4.30). The noise term can be ignored since noise is not part of the simulation. The parametrization used for the fit is thus

$$\frac{\sigma(E)}{E} = \frac{s}{\sqrt{E}} \oplus c. \tag{8.8}$$

The energy resolution of a calorimeter is limited by its sampling fraction. The best resolution for a given active material is achieved in the limit of a homogeneous calorimeter without any absorber plates.

Figure 8.1 shows the energy resolution for different tungsten absorber thicknesses in the full calorimeter stack where leakage is negligible. The best resolution of $32.3\%/\sqrt{E/\mathrm{GeV}} \oplus 0.0\%$ is achieved for the finest sampling with an absorber thickness of 5 mm. For coarser samplings the resolution function worsens to up to $56.6\%/\sqrt{E/\mathrm{GeV}} \oplus 1.3\%$ for an absorber thickness of 20 mm. The constant term is always very small since leakage is not an issue in these detector setups and non-uniformities of the cells are not simulated. The reconstructed energy stays within ±1.5% of the true energy over the whole energy range (see Fig. 8.2), which confirms that the NN provides a good calibration.

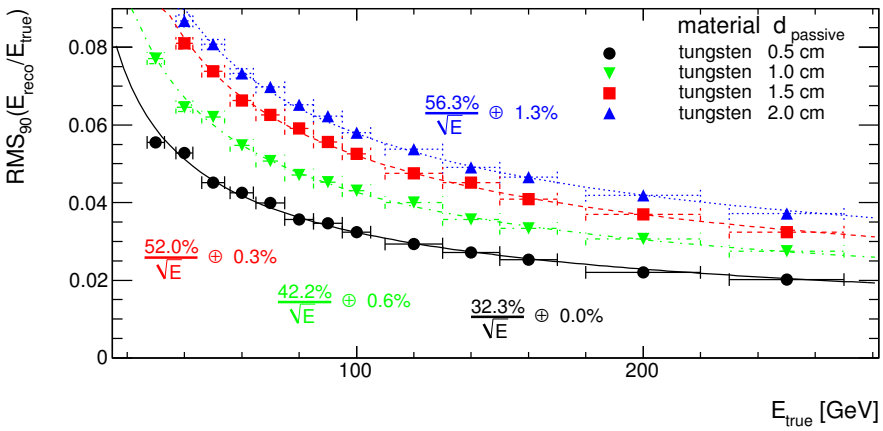

Figure 8.1: Energy resolution for π^+ depending on the true particle energy for different tungsten absorber thicknesses, d_{passive}, in the full calorimeter stack.

The energy resolution of the steel calorimeter stacks is shown in Fig. 8.3. The resolution is considerably better than in the tungsten case for similar interaction lengths per layer. For example, when comparing the tungsten 15 mm configuration and the steel 25 mm configuration with both approximately

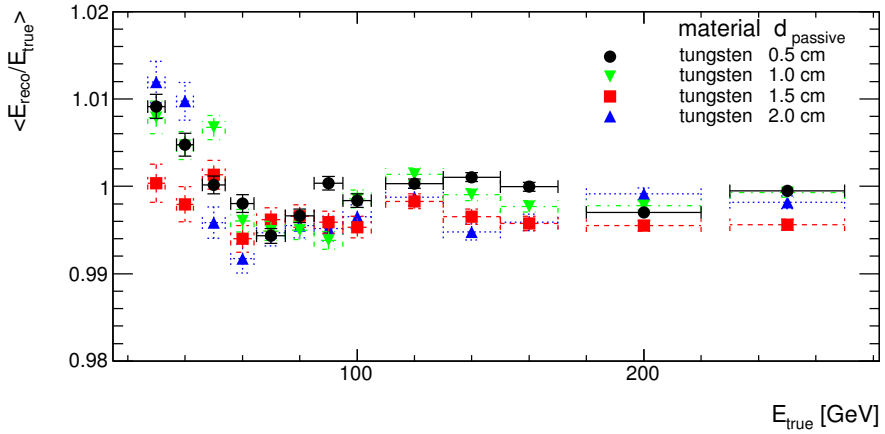

Figure 8.2: Linearity for π^+ depending on the true particle energy for different tungsten absorber thicknesses, d_{passive}, in the full calorimeter stack.

0.16 λ_I per layer, the resolution in the steel 25 mm case is $31.3\%/\sqrt{E} \oplus 0.6\%$ and $52.0\%/\sqrt{E} \oplus 0.3\%$ in the tungsten 15 mm configuration. This can be explained by the large differences in the radiation length of the two absorber materials: A steel calorimeter offers a much finer sampling of the electromagnetic shower content.

The deviations from a linear energy response in the steel configurations, which is shown in Fig. 8.4, is similar to the tungsten case and never exceeds ±1.5%.

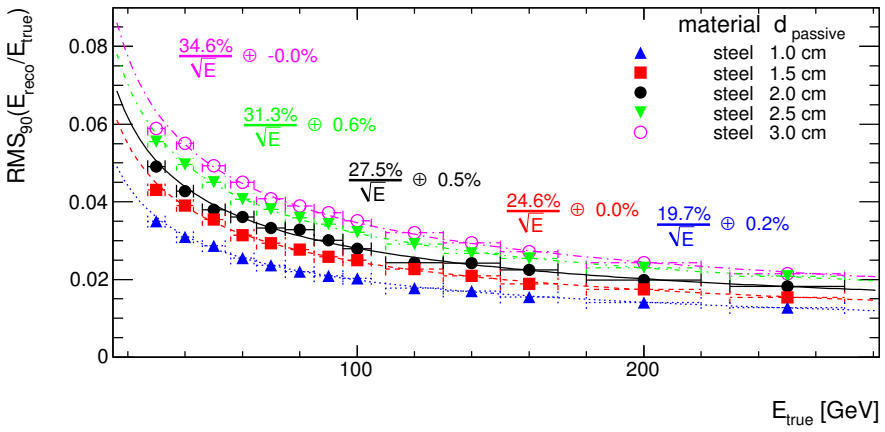

Figure 8.3: Energy resolution for π^+ depending on the true particle energy for different steel absorber thicknesses, d_{passive}, in the full calorimeter stack.

The configurations with the mixed absorber plates, i.e. tungsten-steel and steel-tungsten, performed in between the pure tungsten and steel configurations, as expected from the relative density. No significant difference was observed when changing the order of the absorber materials.

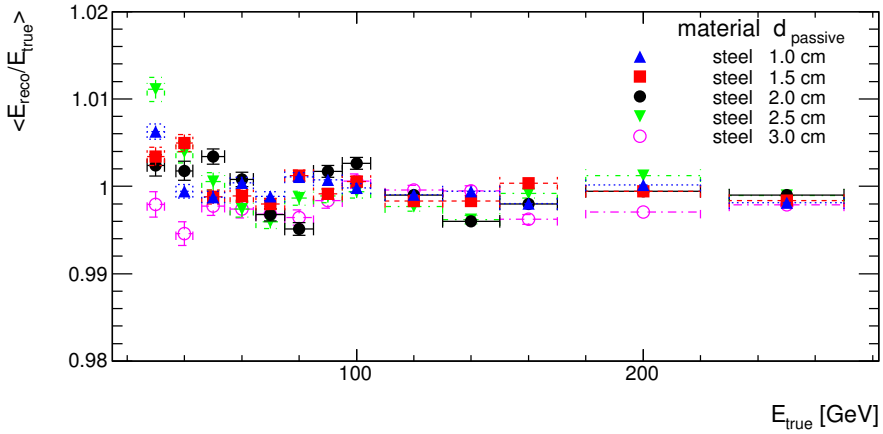

Figure 8.4: Linearity for π^+ depending on the true particle energy for different steel absorber thicknesses, d_{passive}, in the full calorimeter stack.

8.5 Energy Resolution Depending on HCal Depth

The intrinsic resolution due to the sampling fraction discussed in Section 8.4 is only reached for an infinite calorimeter. In case the calorimeter depth is limited, leakage reduces the achievable resolution. For the SiD concept the depth of the calorimeter is limited by the radius of the coil.

The energy resolution for high energy pions of 250 ± 20 GeV as a function of the total depth of the calorimeter is shown in Fig. 8.5 for tungsten and in Fig. 8.6 for steel. The energy resolution is worst for very short calorimeters where the resolution is clearly dominated by leakage. For longer calorimeters the resolution improves until it reaches a plateau which is determined by the intrinsic resolution given by the sampling fraction of the configuration.

These figures allow to choose the optimal calorimeter configuration for a given calorimeter thickness. In case of the CLIC detectors, the available space between the ECal and the coil is approximately 120 cm. For this thickness (and a gap size of 7.5 mm) the optimal configuration is the tungsten calorimeter with an absorber thickness of approximately 10 mm, which corresponds to an HCal depth of approximately 7.5 λ_{I}. In addition to offering the best resolution, the tungsten 10 mm configuration is also in the plateau region of the resolution at a thickness of 120 cm, which means that leakage is negligible. The energy resolution in the steel configurations, on the other hand, are dominated by leakage for this thickness. In case of a particle flow energy reconstruction, full shower containment is preferred over better intrinsic resolution, since most of the information that is used comes from the shower topology.

8.6 Impact of a Tail Catcher on the Energy Resolution

The added value of a tail catcher is studied by using a slightly modified setup. The first 8 λ_{I} of the calorimeter stack are considered as the main calorimeter, i.e. ECal and HCal, followed by a dead region of 2 λ_{I} representing the coil, and a tail catcher of varying length. The tail catcher here uses the same sampling as the HCal which overestimates the performance, since a typical tail catcher only consists of the sparsely instrumented return yoke outside of the coil.

The resolution for a calorimeter of 8 λ_{I} with 10 mm tungsten absorber plates and varying tail catcher configurations is shown in Figure 8.7. The resolution improves by less than 1% when information from

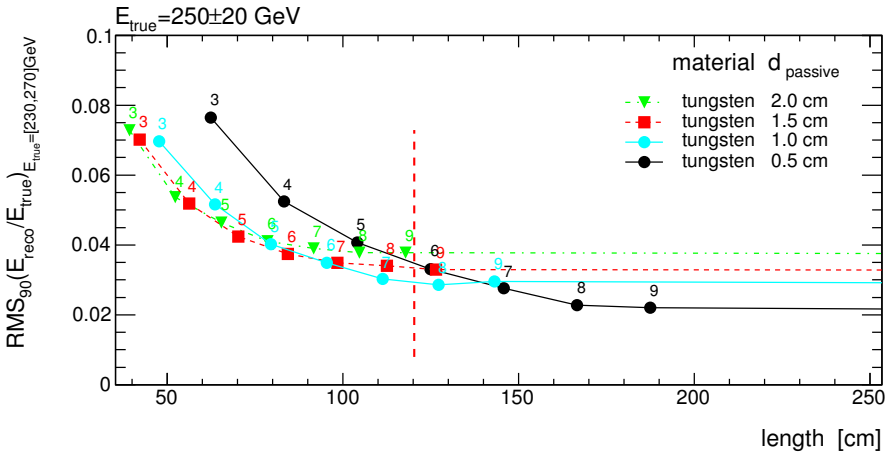

Figure 8.5: Energy resolution for π^+ with an energy of 250 ± 20 GeV depending on the calorimeter depth for tungsten calorimeters with different absorber thicknesses d_{passive}. The numbers next to the data points denote the calorimeter thickness in interaction lengths. The dashed vertical line indicates the approximate size foreseen for the HCal.

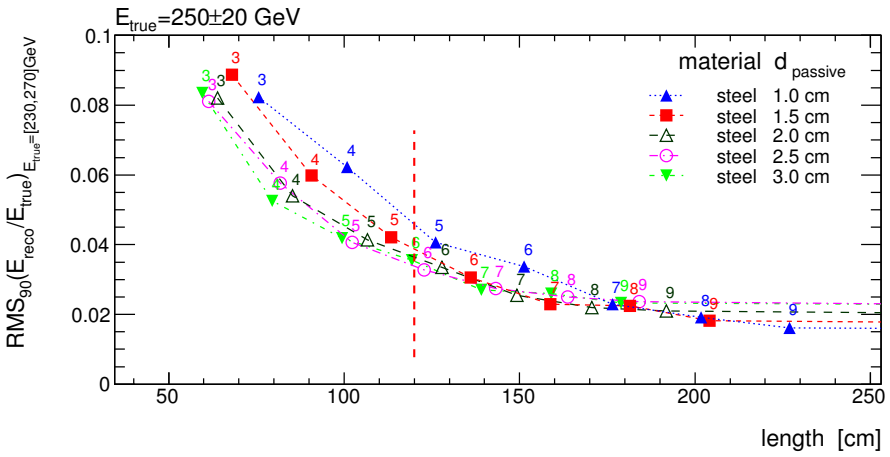

Figure 8.6: Energy resolution for π^+ with an energy of 250 ± 20 GeV depending on the calorimeter depth for steel calorimeters with different absorber thicknesses d_{passive}. The numbers next to the data points denote the calorimeter thickness in interaction lengths. The dashed vertical line indicates the approximate size foreseen for the HCal.

a tail catcher is added. As expected, mainly the constant term is improved, since some of the leakage is recovered. The size of the tail catcher is almost irrelevant, as long as some information from the tail catcher is used. The large size of the calorimeter of 8 λ_I provides sufficient depth to contain the majority of the shower and the leakage correction from the tail catcher only leads to a small improvement. In addition, the variables used for the energy reconstruction implicitely allow for longitudinal leakage correction without using tail catcher information by using the shower position, longitudinal extent as well as the amount of energy in the last λ_I of the calorimeter.

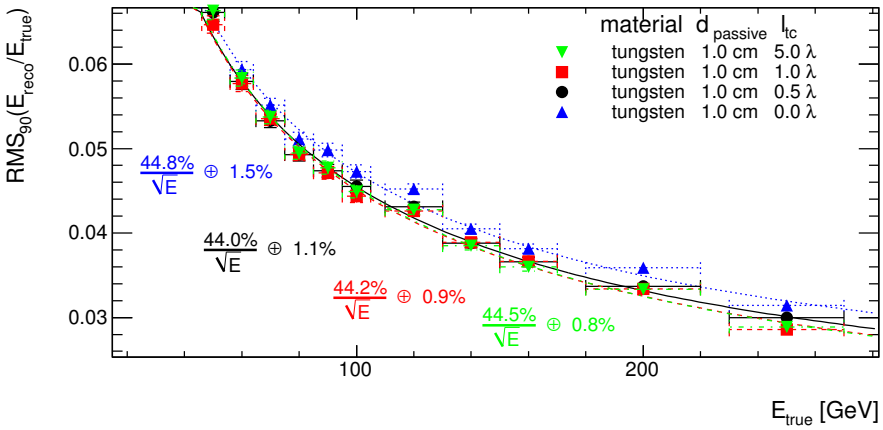

Figure 8.7: Energy resolution for π^+ depending on the true particle energy for a calorimeter of $8\,\lambda_I$ using 10 mm tungsten absorber plates followed by a coil of $2\,\lambda_I$ and a tail catcher of varying thickness, l_{tc}. In case of $l_{tc} = 0\,\lambda_I$ no tail catcher information is used.

8.7 Summary

The aim of this study was to compare the relative calorimetric performance of steel and tungsten sampling calorimeters. For this we developed an energy reconstruction using a NN with several variables to describe the shower shape. An individual NN was trained for each of the calorimeter setups to guarantee optimal performance. There are several caveats when comparing the resolutions presented here with those achieved in other studies. First of all this is a simplified study where only the relative performance of different sampling ratios are studied. Detector effects like noise are not taken into account. In addition, the differences between RMS_{90}, RMS or a Gaussian width have to be taken into account, as discussed in Appendix B. Nevertheless, using more information of a calorimeter shower than its total energy does certainly result in a significantly improved energy reconstruction. For example, it has been shown in test beam data from the CALICE analog HCal prototype that the energy resolution can be improved significantly when the local shower densities in a highly granular calorimeter are used to correct for electromagnetic shower content [156]. This correction leads to relative improvement of the energy resolution by 20%. Another recent study using data from the same prototype applies a leakage correction using the information from the high longitudinal segmentation [157]. The variables used for the leakage correction are the shower start and the energy sum in the last four layers, which is very similar to the variables that we use to describe the shower shape. This leakage correction results in a relative improvement of the energy resolution by 25%.

The simulation study presented in this chapter shows that for the given space in the CLIC detector concepts a tungsten sampling calorimeter performs better than a steel sampling calorimeter. The optimal performance is achieved for a tungsten absorber plate thickness of approximately 10 mm when assuming a gap size of 7.5 mm for each active layer. The simulation study assumes an analog scintillator readout but the result will be applicable to other readout technologies as long as the gap size does not deviate significantly from the number used here. It was found that for a calorimeter depth that corresponds to $8\,\lambda_I$, information from a tail catcher that is placed behind the coil can slightly improve the energy measurement. The findings concerning optimal HCal depth were later confirmed by an independent study using PandoraPFA, where only the total depth of the HCal was varied [23]. In combination, these

studies lead to the decision for the current HCal layout used in the CLIC_ILD and CLIC_SiD models.

A tungsten HCal prototype has been built within the CALICE collaboration to verify the simulation results with test beam data. This prototype has been successfully operated in two test beam campaigns at the PS and SPS at CERN using analog scintillator detectors [150]. Preliminary results show good agreement between simulation and data [158].

CHAPTER 9

Calorimeter Performance in CLIC_SiD

In this chapter we discuss the calorimetric performance of CLIC_SiD after the modifications of the HCal, which we motivated in Chapter 8.

The energy of a calorimeter cluster is calculated from the sum of the energy in hits associated with that cluster. Since we are using sampling calorimeters, a correction factor has to be applied to account for the energy deposited in the absorber layers, which depends on the sampling fraction of the respective layer. In addition, we use different sampling fractions depending on the shower type to account for the potentially different responses of electromagnetic and hadronic showers, as discussed in Section 4.2.

First, we discuss the calibration procedure used to obtain the different sampling fractions in Section 9.1. Afterwards, we discuss the performance of the reconstruction of showers from individual neutral particles in Section 9.2, which allows us to deduce the intrinsic calorimetric resolution of CLIC_SiD. The energy reconstruction in di-jet events using PandoraPFA is discussed in Section 9.3. Since we are interested in the basic performance, all events are simulated without the $\gamma\gamma \rightarrow$ hadrons background.

9.1 Calorimeter Calibration Procedure

The sampling fractions for the different calorimeters are calculated from the response of simulated single particle events at several energies. The simulated events that are used, are single photon events to determine the electromagnetic sampling fractions and single K_L^0 events for the hadronic sampling fractions. Both particle types are generated with the Geant4 particle gun and are simulated for kinetic energies of 1 GeV, 2 GeV, 5 GeV, 10 GeV, 20 GeV and 50 GeV. Samples are generated for polar angles of 90° and 30° to determine the sampling fractions for the barrel and endcap calorimeters independently. Each sample contains 10000 events.

The calorimeter consists of two ECal sections with different longitudinal sampling and the HCal section, which has an even coarser sampling. In addition, the absorber material and the sampling fraction of the HCal in the barrel region differs from those in the endcap. The energy reconstruction has to account for all these differences by using different correction factors for each of these subdetectors. If we assume a linear response in all of the individual calorimeters the energy of the particle in one event is given by

$$E = \sum_{i=0}^{N} \frac{E_i}{c_i}, \tag{9.1}$$

Table 9.1: Electromagnetic and hadronic sampling fractions used for the different calorimeters in CLIC_SiD.

Sampling fraction		$ECal_1$	$ECal_2$	HCal
Barrel	Electromagnetic	0.0168	0.00816	0.0485
	Hadronic	0.0173	0.00939	0.0461
Endcap	Electromagnetic	0.0173	0.00845	0.0334
	Hadronic	0.0156	0.00907	0.0350

where the index i denotes the calorimeter compartment with the sampling fraction c_i and the sum of the deposited energy in its active layers E_i. The sum of the deposited energy E_i takes into account only those hits that are above the threshold of the respective calorimeter, as given in Section 6.3.6. In addition, a cone based clustering algorithm with a fixed opening angle of 0.5 is used to identify the main cluster of each event. Hits not attributed to the cluster are ignored. E is given by the true generated energy of the initial particle, taking into account the particle mass in case of the Kaons. Together with the calculated sums for all E_i, the optimal sampling fractions can be determined using the least-squares method.

Since the clustering in the actual event reconstruction is performed in PandoraPFA which uses additional topological information to refine the clustering, a second iteration is required to determine the final sampling fractions. The calibration events are passed through SlicPandora using the initial sampling fractions. The resulting clusters from PandoraPFA are then used to re-calculate the values for E_i and the final sampling fractions are again determined with the least-squares method.

The resulting sampling fractions are given in Table 9.1. As expected, the sampling fractions for the second ECal are approximately half of the first ECal section, since the absorber thickness differs by that amount (see Section 5.2.1). For hadronic showers a slightly higher weight is put on the second ECal section due to the fact that the first section usually lies before the shower start and mostly sees energy deposits from backscattering evaporation protons and neutrons. Especially the slow protons, which can deposit significantly more energy than a MIP on a given path length, should in fact be weighted less. The sampling fractions for electromagnetic and hadronic showers are within 5% of each other for the hadronic calorimeters and slightly further apart for the ECals. This shows that the calorimters are almost compensating and only a limited degradation of the hadronic energy resolution due to this effect is expected.

9.2 Single Particle Response

The basic performance of the calorimeter system was tested with several simulated single particle event samples. Only neutral particles can be used since the particle flow algorithm always uses the track momentum to determine the particle energy of a charged particle. 10000 events of single γ, π^0, K^0_S and K^0_L have been simulated for each of the kinetic energies of 1 GeV, 2 GeV, 5 GeV, 10 GeV, 20 GeV, 50 GeV, 100 GeV, 200 GeV and 500 GeV. The polar angles of the particles have been restricted to $5^\circ < \theta < 175^\circ$ and the azimuthal angle was left free. The events have been passed through the standard event reconstruction, as explained in Section 6.3. In this case, PandoraPFA is only used to determine the calorimeter clusters, which is trivial in the single particle case. The resulting energy resolution can be interpreted as the intrinsic calorimeter performance. For the analysis, the energy of the original particle, E_{true}, is compared with the total reconstructed energy, E_{reco}. The resolution is determined as the RMS of the $E_{\text{reco}}/E_{\text{true}}$ distribution for each of the simulated energies. A cut on the polar angle of the initial particle of $\theta > 30^\circ$ was introduced to restrict the sample to fully contained showers. The linearity is

determined as the mean of the $E_{\text{reco}}/E_{\text{true}} - 1$ distribution.

The resulting linearity is shown in Fig. 9.1 (left) over the full energy range. Especially for the hadronic showers the reconstructed energies deviates significantly from the true energy for very low energies. For example, the reconstructed energy for 1 GeV K_L^0 is approximately 20% too low. For π^0 particles of $E_{\text{kin}} = 1$ GeV the reconstructed energy is by approximately 4% too low. For photons the difference never exceeds 1%. For higher energies, the difference between true and reconstructed energy becomes significantly smaller and approaches asymptotically 0. An especially large deviation is observed for K_L^0 of 10 GeV, which is caused by the physics list, since this deviation occurs directly in the transition region of the models for the inelastic scattering of hadrons (see Section 6.2.2). The effect of significantly reduced visible energy for hadrons with energies in the transition region of `QGSP_BERT` is discussed in [149]. The K_S^0 particles on the other hand almost never reach the calorimeters and thus the available energy of the hard interaction is only that of its decay products. This effect, although much less pronounced, can be seen for K_S^0 of 20 GeV.

The linearity was fitted with a linear equation

$$E'_{\text{reco}} \equiv a \cdot E_{\text{reco}} + b = E_{\text{true}} \tag{9.2}$$

to obtain correction factors that can be applied to the reconstructed energy. The point corresponding to 10 GeV K_L^0 was excluded from the fit to avoid a bias. The resulting parameters are given in Table 9.2. Using these corrections a much better linearity is achieved as shown in Fig. 9.1 (right). Even for low energetic Kaons the mean reconstructed energy does not deviate more than 2% from the true energy.

Although this correction significantly improves the reconstructed energy of low energetic neutral hadrons it depends on the particle type and thus requires particle identification. Since there is no particle identification for neutral hadrons in the current reconstruction software, as mentioned in Section 6.3.7, this correction can not be used. Applying this correction should also improve the reconstructed energy of jets, which still has to be investigated.

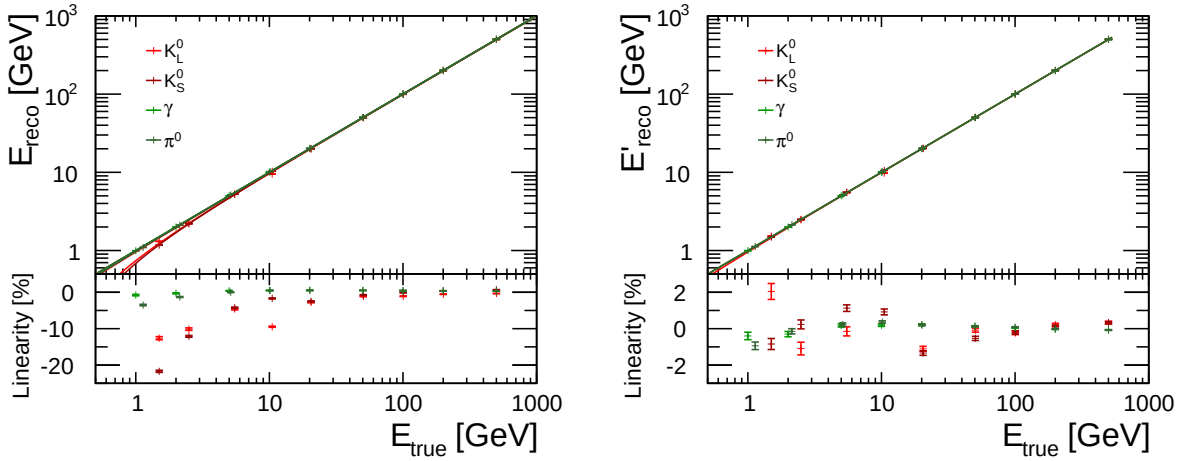

Figure 9.1: Linearity for single neutral particles in the CLIC_SiD detector. The left plot shows the linearity of the reconstructed energy obtained from the mean of the reconstructed energy for the respective sample. The right plot shows the improved linearity after a correction has been applied. The lines correspond to a linear fit as discussed in the text.

The energy resolution, which is shown in Fig. 9.2, has been fitted for all particles with the parametriza-

Table 9.2: Correction to the reconstructed particle energy to improve the linearity in CLIC_SiD. Given is the particle type with the corresponding correction factors a and b according to Eq. (9.2).

Particle	a	b [GeV]
γ	0.996	0.009
π^0	0.996	0.034
K^0_S	0.996	0.351
K^0_L	1.008	0.299

tion given in Eq. (8.8). The resulting parameters of the fit to Eq. (8.8) for all of the particle types are given in Table 9.3. The energy resolution achieved for photons and π^0s is almost the same, which is expected, since π^0 particles decay almost exclusively into two photons. The calorimetric energy resolution for electromagnetic showers in CLIC_SiD is thus approximately $19.1\%/\sqrt{E/\mathrm{GeV}} \oplus 1.0\%$. The calorimetric energy resolution for hadronic showers is given by the resolution for K^0_L, which is $50.3\%/\sqrt{E/\mathrm{GeV}} \oplus 6.5\%$. The situation for K^0_S is a bit more complex, since they most likely decay in flight before reaching the calorimeters. The two relevant decays are $K^0_S \to \pi^+\pi^-$ and $K^0_S \to \pi^0\pi^0$, with branching ratios of $\sim 69.2\%$ and $\sim 30.7\%$ [78], respectively. The later decay mode will further decay into 4 photons before reaching the calorimeters due to the short lifetime of the π^0s. Due to the late decay of the K^0_S, the tracks of the charged pions can not be reconstructed with the current tracking algorithm, as discussed in Section 6.3.5. The corresponding showers are thus reconstructed as neutral hadrons and the total resolution for K^0_S particles is between the electromagnetic and the hadronic resolution of the calorimeters.

The numbers for the energy resolution given here are obtained from the uncorrected reconstructed energy. Calculating the energy resolution for E' gives very similar results.

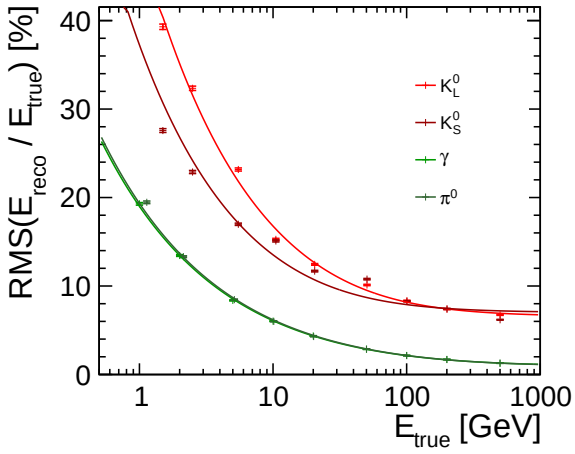

Figure 9.2: Energy resolution for single neutral particles in the CLIC_SiD detector calculated from the RMS of the reconstructed energy for the different test samples. The line shows the fit of the energy resolution as discussed in the text.

Table 9.3: Energy resolution for single neutral particles in CLIC_SiD. Given is the particle with the sampling term s and the constant term c according to Eq. (9.2).

Particle	s [%]	c [%]
γ	19.1	1.0
π^0	19.3	0.9
K_S^0	38.7	6.9
K_L^0	50.3	6.5

9.3 Jet Response

The performance of the energy reconstruction of jet events was studied using di-jet samples from Z′ decaying at rest. These are the same event samples that are used to evaluate the tracking performance in jets. In addition to the sample with a Z′ mass of 3 TeV discussed in Section 7.2 we also use samples with lower masses in the range from 91 GeV to 3 TeV to study the dependence of the jet energy resolution on the jet energy. No jet finding is used in the event reconstruction to avoid a bias depending on the choice of the algorithm and its parameters. Instead, the energy of all reconstructed particles, i.e. PFOs, is summed up to find the reconstructed energy E_{reco} of the di-jet system. The energy of each jet is assumed to be $E_{\text{reco}}/2$. The resolution is then calculated as the RMS_{90} of the distribution of E_{reco} and the resolution for each individual jet is calculated as $\sigma(E_{\text{jet}}) = \sqrt{2}\sigma(E_{\text{reco}})$. Since no jet clustering is used, we define the polar angle of the jet as the polar angle of the original quark[1].

The jet energy resolution for central jets, which is shown in Fig. 9.3 (left), is between 3% and 5%, depending on the jet energy and when using RMS_{90}. The best resolution is achieved for jet energies of approximately 500 GeV and drops significantly for lower jet energies. For higher jet energies it degrades moderately. The energy is underestimated in the reconstruction by 3–5%, as shown in Fig. 9.3. Since this effect is almost constant over the full energy range, the result can be improved by rescaling the reconstructed energy by a constant factor of 1.050 which was obtained from the slope of the linearity in Fig. 9.3 (right). It is assumed that this systematic bias in the jet energy reconstruction is caused by confusion when soft neutral showers are not resolved from large neighboring charged particle showers. It should be noted that the configuration of the algorithms in PandoraPFA was originally tuned for CLIC_ILD and not specifically adapted to CLIC_SiD. The smaller inner radius of the calorimeters in CLIC_SiD, compared to CLIC_ILD might be the cause of this, but further studies are required.

Figure 9.4 shows a comparison of the PFA performance and a pure calorimetric energy measurement. The calorimeter energy is obtained as the sum of all hit energies corrected by the respective sampling fractions given in Table 9.1, where the electromagnetic sampling fraction was used in the ECal and the hadronic sampling fraction was used in the HCal. In addition, the total reconstructed energy is scaled such that the slope of the linearity is 1. Similarly, we applied the energy scaling of 1.050 to the PFA energy as discussed above. The energy reconstruction using PFA is significantly better than using just the energy measurement in the calorimeter over the full energy range. These results are consistent with the results found for an ILD-like detector geometry, as discussed in [85]. The distribution of the total reconstructed energies, shown in Figure 9.5, also highlights the large advantage in using momentum information to reconstruct the jet energy. It also shows that the distributions have long asymmetric tails which motivates the use of RMS_{90}.

The angular dependence of the jet energy resolution can be seen in Fig. 9.6(a). The jet energy reso-

[1] The quarks are created back-to-back and can thus be identified with a single polar angle in the interval $[0°, 90°]$

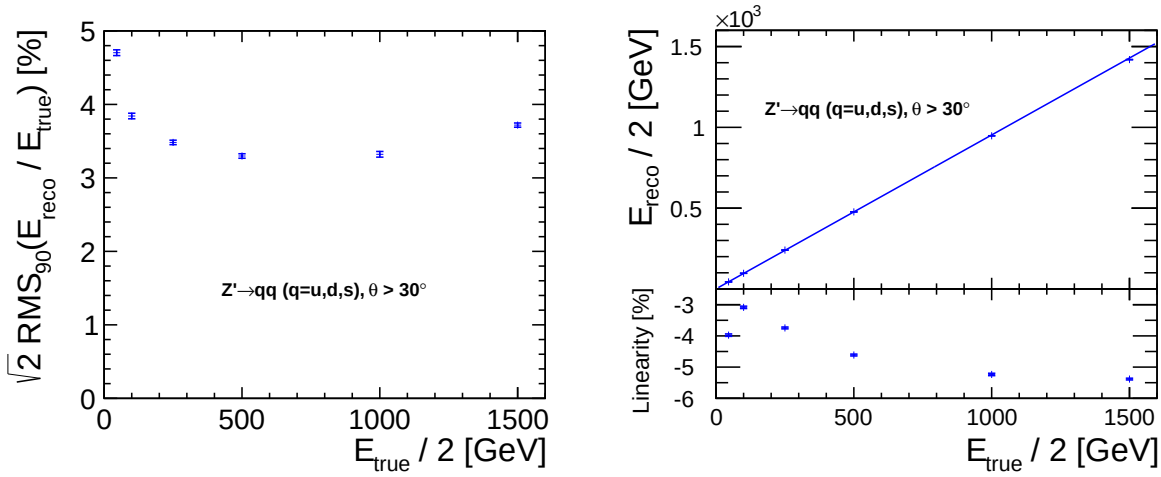

Figure 9.3: PFA response for single jets in di-jet decays of a Z′ at rest, depending on the jet energy. Shown is the jet energy resolution (left) and the linearity (right) obtained from the energy sum of all reconstructed PFOs.

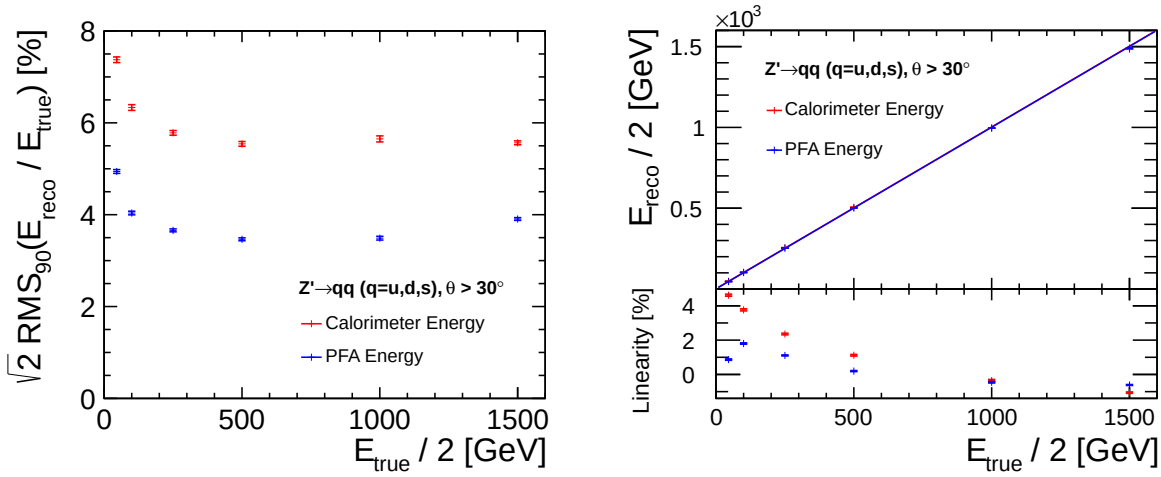

Figure 9.4: Calorimeter response for single jets in di-jet decays of a Z′ at rest, depending on the jet energy. Shown is the jet energy resolution (left) and the linearity (right) using either the energy sum of all reconstructed PFOs or the energy sum of all corrected calorimeter hits.

lution is almost constant for all polar angles θ throughout the central region of the detector and drops significantly for jet angles lower than 20°. This drop in the performance is to some extent due to the degrading momentum resolution in the forward region but mostly due to the acceptance of the calorimeters in that region, where especially the HCal acceptance is limited due to the support tube necessary for stabilizing the QD0 (see Section 5.5.4). The effect of the acceptance can be seen more directly in the dependence of linearity on the polar angle, which is shown in Fig. 9.6(b). The energy is underestimated by 4–5% in the central region, which increases to 10–20% for polar angles of less than 20°. While we have discussed possible explanations of this discrepancy in the central region, the showers in the very forward region are clearly not fully contained. These effects are more pronounced for high energy jets at all polar angles. In the transition region between barrel and endcap calorimeters at $\theta \approx 40°$ the reconstructed energy is especially low for high jet energies. This shows that the energy loss in the gap

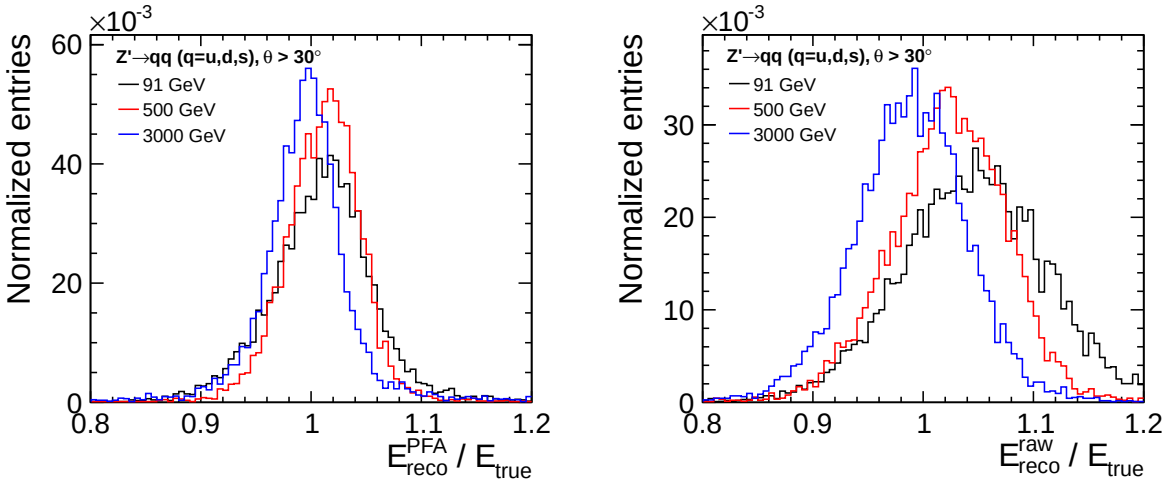

(a) PFA energy (b) Cluster energy

Figure 9.5: Distribution of the reconstructed energy in di-jet decays of a Z′ at rest for different Z′ masses, using the energy sum of all reconstructed PFOs (a) and using the energy sum of all calorimeter hits (b).

between these two calorimeter regions is not correctly accounted for.

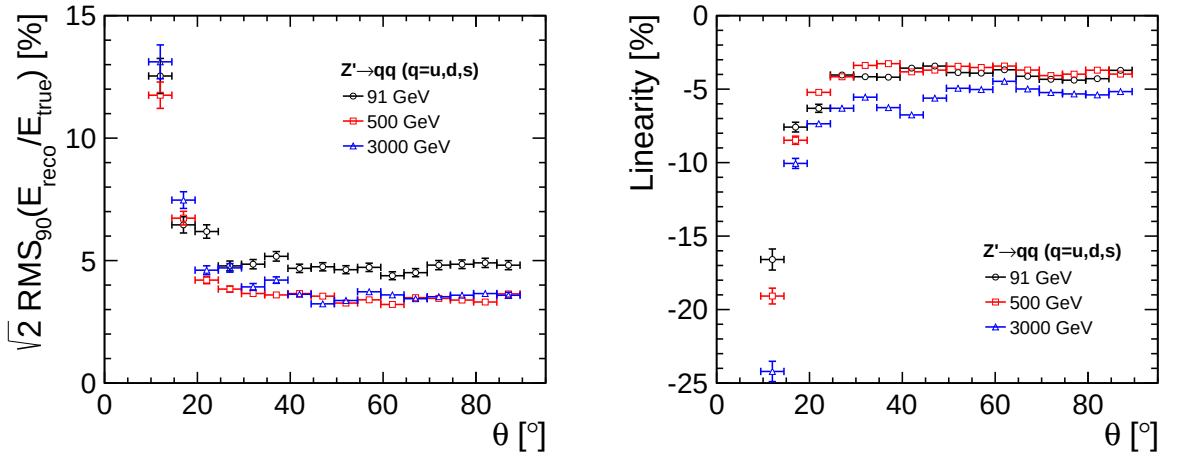

(a) (b)

Figure 9.6: Calorimeter response for single jets in di-jet decays of a Z′ at rest, for different Z′ masses, depending on the polar angle θ of the jet. Shown are the resolution (left) and the linearity (right) using the energy sum of the reconstructed PFO.

For completeness we summarize some of the findings presented in [159] concerning the impact of the $\gamma\gamma \rightarrow$ hadrons background. This background significantly increases the reconstructed energy in each event. Depending on the event topology a suitable jet clustering algorithm might be sufficient to retain the original event information. The K_t-algorithms [160] have proven especially useful at CLIC conditions, as for example shown in the squark mass measurement benchmark study [161]. In more complex event topologies rejecting reconstructed particles based their reconstructed production time is necessary using the method explained in Section 6.3.8. Although this method is extremely efficient,

tight selection cuts also degrade the jet energy resolution by removing particles from the original event. This effect is only noticeable for low energetic jets, since the individual particles in $\gamma\gamma \rightarrow$ hadrons events are of low energy and thus, only low energetic particles are removed by the cuts. In these cases, the jet energy resolution can degrade by up to a factor of two.

One example of the effectiveness of these timing cuts is the gaugino and neutralino pair production benchmark analysis [83].

9.4 Summary

We have presented the method that is used to determine the sampling fractions for the CLIC_SiD detector model. A set of simulated single photon and K_L^0 particle events at various energies and two polar angles is used to determine the optimal sampling fractions of all subdetectors in a least-squares fit. The resulting calibration is tested using independent samples of single particles and di-jet events, not taking into account the $\gamma\gamma \rightarrow$ hadrons background.

For single particles we found that, especially for very low energetic Kaons, the reconstructed energy is too low by up to 20%. A linear correction can be used to improve this significantly but requires particle identification also for neutral hadrons which is not available in the current reconstruction software. The energy resolution for electromagnetic showers was found to be $19.1\%/\sqrt{E/\mathrm{GeV}} \oplus 1.0\%$. As expected, the hadronic energy resolution is significantly worse with $50.3\%/\sqrt{E/\mathrm{GeV}} \oplus 6.5\%$.

The jet energy resolution in di-jet events was found to be in between 5% and 3.5% (using RMS_{90}) for jet energies of 45 GeV to 1.5 TeV. We have shown that PFA improves the jet energy resolution significantly. It remains to be studied if the performance of PandoraPFA can be improved by tuning some of its algorithms specifically for CLIC_SiD.

CHAPTER 10

Measurement of Light Higgs Decay into Muons

As discussed in Chapter 2, the measurement of the Higgs branching ratios is an important test of the SM. The SM makes precise predictions of the Higgs branching ratios with the mass of the Higgs boson being the only unknown parameter. A deviation from these predictions would be a strong indication of new physics. Measuring the Higgs decay into muons is especially challenging because of its very small branching ratio of 0.028% for a Higgs boson mass of 120 GeV.

This chapter presents the cross section times branching ratio measurement for the W^+W^- fusion process, $e^+e^- \to h\nu_e\bar{\nu}_e$, with the Higgs decaying into two muons, at CLIC with a center-of-mass energy of 3 TeV. This analysis is part of the detector benchmark analyses [24] described in the CLIC CDR [23] with the aim of demonstrating the detector performance in realistic physics analyses. This channel, requiring the precise reconstruction of two muons of medium energies, challenges the momentum resolution of the tracking system at all angles. The analysis is performed in the CLIC_SiD detector model which is described in Chapter 5. A total integrated luminosity $\mathcal{L}$ of $2\,\text{ab}^{-1}$ is used for the analysis. This corresponds to about 4 years of data taking with an instantaneous luminosity of $5.9 \times 10^{34}\,\text{cm}^{-2}\text{s}^{-1}$, assuming 200 days of operation per year with an efficiency of 50%. This analysis has already been published in [28].

We begin by describing the event samples which are used in the analysis in Section 10.1. In Section 10.2 we introduce the event selection procedure used and in Section 10.3 we discuss the invariant mass fit used to extract the number of signal events as well as the resulting uncertainties on the cross section times branching ratio measurement. In Section 10.4 we investigate the impact of the $\gamma\gamma \to$ hadrons background on this analysis. The dependency of the uncertainty of the branching ratio measurement on the momentum resolution is studied in a fast simulation study presented in Section 10.5. Moreover, the importance of efficient electron tagging in the forward calorimeters is demonstrated in Section 10.6. Furthermore, the translation of the measured cross section branching ratio into the corresponding coupling constant g_μ is discussed in Section 10.6. Finally, we compare the achievable uncertainty at CLIC with the potential for measuring this branching ratio at the ILC and at the LHC in Section 10.8.

10.1 Event Samples

This section introduces the different event samples used throughout this analysis. An overview is given in Table 10.1 showing the cross sections of all processes and the number of events that were simulated.

Table 10.1: List of processes considered for the $h \to \mu^+\mu^-$ analysis with their respective cross sections σ and the number of simulated events N_{events}.

Process	σ [fb]	N_{events}	Short label
$e^+e^- \to h\nu_e\bar{\nu}_e$; $h \to \mu^+\mu^-$ (signal)	0.120	21000	$h \to \mu^+\mu^-$
$e^+e^- \to \mu^+\mu^-\nu\bar{\nu}$	132	5000000	$\mu^+\mu^-\nu\bar{\nu}$
$e^+e^- \to \mu^+\mu^-e^+e^-$	346[A]	1350000	$\mu^+\mu^-e^+e^-$
$e^+e^- \to \mu^+\mu^-$	12[B]	10000	$\mu^+\mu^-$
$e^+e^- \to \tau^+\tau^-$	250	100000	$\tau^+\tau^-$
$e^+e^- \to \tau^+\tau^-\nu\bar{\nu}$	125	100000	$\tau^+\tau^-\nu\bar{\nu}$
$\gamma\gamma \to \mu^+\mu^-$ (generator level only)	20000[B]	1000000	$\gamma\gamma \to \mu^+\mu^-$

[A] Including a cut of 100 GeV $< M(\mu\mu) <$ 140 GeV and requiring a minimum polar angle for both muons of 8°.
[B] Including a cut of 100 GeV $< M(\mu\mu) <$ 140 GeV.

10.1.1 Signal Sample

At a center of mass energy of 3 TeV the most relevant production processes for a light Higgs are gauge boson fusion processes, as discussed in Section 2.2.2. The Higgs production through W^+W^- fusion, $e^+e^- \to h\nu_e\bar{\nu}_e$, has a cross section of 422 fb when the CLIC luminosity spectrum is taken into account. The corresponding Feynman diagram is shown in Fig. 10.1. The cross section of the ZZ fusion process $e^+e^- \to he^+e^-$ is 42.6 fb which is about 10 times smaller. The Higgs branching ratios depend on the Higgs boson mass and are calculated using PYTHIA. The $BR_{h\to\mu^+\mu^-}$ is only 0.028% for a 120 GeV SM Higgs, which is compatible with latest theoretical calculations [42]. For an integrated luminosity of 2 ab^{-1} one thus expects about 236 events from the W^+W^- fusion process and only 24 events from the ZZ fusion process. Therefore, the Higgs boson production through W^+W^- fusion is chosen for this study. The final state of the signal is thus $\mu^+\mu^-\nu_e\bar{\nu}_e$, which will further be referred to as $h \to \mu^+\mu^-$. The event topology of interest comprises two muons and missing energy.

The number of events from the ZZ fusion channel with this signature is very low. The selection efficiency is on the few per cent level, depending on the final cuts. Taking it into account in the signal and background hypothesis is not expected to have a noticeable effect on the final results.

The signal events used in this analysis have been created by generating events with a final state of $h\nu_e\bar{\nu}_e$ using WHIZARD. The Higgs boson was forced to decay into two muons in PYTHIA. Since final state particles have to be stable in WHIZARD, the width of the Higgs boson is not taken into account. The width of a Standard Model Higgs with a mass of 120 GeV is 3.6 MeV, which is considerably smaller than the invariant mass resolution of the detector and is thus negligible.

For this analysis 21000 $h \to \mu^+\mu^-$ events were generated and simulated. They were reconstructed with and without overlaying the $\gamma\gamma \to$ hadrons background in order to study the impact of this background on the analysis result.

10.1.2 Main Backgrounds

The two main background processes are the $e^+e^- \to \mu^+\mu^-\nu\bar{\nu}$ and the $e^+e^- \to \mu^+\mu^-e^+e^-$ processes where the muons are not produced by a Higgs boson and, in the case of the second process, the electrons escape the detector through the beam pipe. Their total cross sections are 132 fb and 5.4 pb, respectively. Both

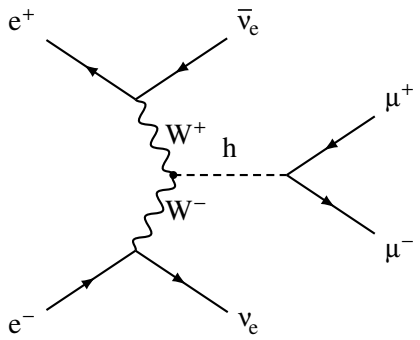

Figure 10.1: Feynman diagram of the Higgs production through W^+W^- fusion with the Higgs decaying into two muons.

were generated as inclusive final states in WHIZARD, where the diagrams including a Higgs boson were kinematically forbidden by artificially setting the Higgs mass to 12 TeV.

Because of the large cross section of the $e^+e^- \to \mu^+\mu^-e^+e^-$ process, several generator level cuts were introduced to limit the number of events that needed to be simulated and reconstructed. The invariant mass of the di-muon system, $M(\mu\mu)$, was limited to masses between 100 GeV and 140 GeV and the minimum polar angle of the muons was set to 8°. The cross section of the $e^+e^- \to \mu^+\mu^-e^+e^-$ process including these cuts is 346 fb. These cuts introduce no bias, since the pre-selection requires $105\,\text{GeV} < M(\mu\mu) < 135\,\text{GeV}$ and the detector acceptance to reconstruct muons is around 10°, as discussed in Section 10.2.1.

Because of its final state of only two muons, 5 million events were simulated and reconstructed for the $e^+e^- \to \mu^+\mu^-\nu\bar{\nu}$ background process, which corresponds to an integrated luminosity of almost $40\,\text{ab}^{-1}$. The simulation and reconstruction of the $e^+e^- \to \mu^+\mu^-e^+e^-$ process is considerably slower and thus only 1.35 million events were generated for this background, corresponding to an integrated luminosity of approximately $2\,\text{ab}^{-1}$. In both cases no $\gamma\gamma \to$ hadrons background was overlaid since it would have significantly increased the reconstruction time per event and the impact is only minor. For a discussion of this background see Section 10.4.

10.1.3 Additional Background Samples

Several other two and four fermion final states were simulated to verify that they can be easily identified as background events. The $e^+e^- \to \mu^+\mu^-$ process has a total cross section of about 350 fb. It was generated with an invariant mass of the di-muon system between 100 GeV and 140 GeV which reduces the cross section to about 12 fb. The processes $e^+e^- \to \tau^+\tau^-$ and $e^+e^- \to \tau^+\tau^-\nu\bar{\nu}$ have cross sections of 250 fb and 125 fb, respectively. They can mimic the signal topology if both taus are decaying into muons, which happens in about 3% of the cases. In addition to the large reduction by requiring two muons, the invariant mass of the di-muon system allows to distinguish these channels from the signal events.

Finally, a sample of beam-induced incoherent pair background was generated with WHIZARD, using a photon spectrum generated by GuineaPig [65, 68]. The $\gamma\gamma \to \mu^+\mu^-$ background has a large cross section of 20 pb even after requiring the invariant mass of the di-muon system to be in the range from 100 GeV to 140 GeV. This sample was not put through full simulation since it became clear that all of its events can easily be rejected by cutting on the transverse momentum of the di-muon system (see Section 10.2.3).

10.2 Event Selection

The event selection is done in two steps. First, the pre-selection reduces the samples to the relevant invariant mass region around the Higgs mass peak. Then, the final event selection using several kinematic variables in a boosted decision tree classifier is applied to separate signal and background events.

10.2.1 Pre-Selection

For the analysis only events with at least two reconstructed muons are used. In addition to the PFO selection cuts given in Table 6.2, each reconstructed particle is required to have a transverse momentum of 5 GeV or larger, which removes most of the particles from the $\gamma\gamma \rightarrow$ hadrons background, see Section 10.4. In case there are more than two muons reconstructed, the two most energetic muons are used. In this analysis, the most energetic muon is referred to as μ_1 and the second most energetic muon is referred to as μ_2. In addition, the invariant mass of the two muons, $M(\mu\mu)$, is required to be between 105 GeV and 135 GeV. This limits the background events used for the training of the classifier to the region relevant to the fit of the Higgs mass peak.

The muon reconstruction efficiency is a combination of the track finding efficiency and the muon identification efficiency. As shown in Fig. 10.2 (right) it is very high within the detector acceptance. There are two small regions with slightly lower efficiencies around 27° and 37° which are due to the barrel-endcap transition in the tracking system and the calorimeters, respectively. The average reconstruction efficiency for muons with a polar angle θ_μ larger than 10° is 99.6% in the $h \rightarrow \mu^+\mu^-$ sample. The efficiency drops quickly for polar angles below 10° due to the tracker acceptance. The efficiency to reconstruct both muons is dominated by this acceptance and is 78.7% for the $h \rightarrow \mu^+\mu^-$ sample, since a sizable amount of muons is produced at low polar angles, as shown in Fig. 10.2 (left). The pre-selection cut on the invariant mass of the di-muon system reduces the selection efficiency further to 74.1%. Table 10.2 summarizes the impact of the pre-selection cuts on all simulated samples.

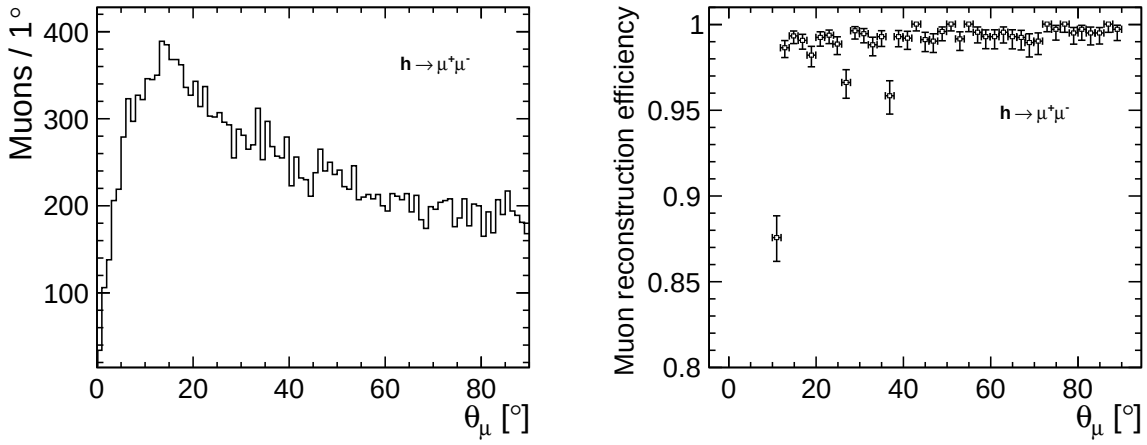

Figure 10.2: Distribution of the true polar angles of the muons θ_μ (left) and the muon reconstruction efficiency depending on the true polar angle θ_μ (right) in $h \rightarrow \mu^+\mu^-$ events.

Table 10.2: Selection efficiencies ϵ and number of selected events N_{events} in $\mathcal{L} = 2\,\text{ab}^{-1}$ when applying the pre-selection cuts to the simulated samples.

	Two muons reconstructed		$105\,\text{GeV} < M(\mu\mu) < 135\,\text{GeV}$	
Process	ϵ	N_{events}	ϵ	N_{events}
$h \to \mu^+\mu^-$	78.7%	187.6	74.1%	176.6
$\mu^+\mu^-\nu\bar{\nu}$	43.3%	127700	1.0%	2563
$\mu^+\mu^-e^+e^-$	81.4%	564400	57.1%	395600
$\mu^+\mu^-$	27.7%	6638	16.6%	3974
$\tau^+\tau^-$	0.7%	3368	0.02%	105.9
$\tau^+\tau^-\nu\bar{\nu}$	1.4%	3456	0.007%	17.79

10.2.2 Boosted Decision Tree

The event selection is done using the boosted decision tree classifier implemented in TMVA [155]. The goal of the classification is to reject the $e^+e^- \to \mu^+\mu^-e^+e^-$ background, while the $e^+e^- \to \mu^+\mu^-\nu\bar{\nu}$ background is indistinguishable from the signal except for the di-muon invariant mass distribution. The $e^+e^- \to \mu^+\mu^-$, $e^+e^- \to \tau^+\tau^-$ and $e^+e^- \to \tau^+\tau^-\nu\bar{\nu}$ samples are not used in the training and are only used to verify that they are removed by the final event selection. Thus, the Boosted Decision Tree (BDT) training is performed using only events from the $h \to \mu^+\mu^-$ and $e^+e^- \to \mu^+\mu^-e^+e^-$ samples. 10000 $h \to \mu^+\mu^-$ events and 500000 $e^+e^- \to \mu^+\mu^-e^+e^-$ events were used for the training, which leaves sufficient statistics for the actual analysis.

The variables used for the event selection by the BDT are chosen to distinguish resonant di-muon production as in case of the Higgs decaying into muons and radiative processes which are dominating in the $\mu^+\mu^-e^+e^-$ background. The following variables are being used:

- The visible energy excluding the two reconstructed muons, E_{vis}.
- The scalar sum of the transverse momenta of the two muons, $p_T(\mu_1) + p_T(\mu_2)$.
- The helicity angle $\cos\theta^*(\mu\mu) = \frac{\vec{p}'(\mu_1)\cdot\vec{p}(\mu\mu)}{|\vec{p}'(\mu_1)|\cdot|\vec{p}(\mu\mu)|}$, where $\vec{p}'$ is the momentum in the rest frame of the di-muon system. Since the two muons are back-to-back in the rest frame of the di-muon system, there is no additional information to be gained from calculating a similar angle for μ_2.
- The velocity of the di-muon system, $\beta(\mu\mu)$, where $\beta = \frac{v}{c}$.
- The transverse momentum of the di-muon system, $p_T(\mu\mu)$.
- The polar angle of the di-muon system, $\theta(\mu\mu)$.

The most powerful variable is the visible energy whenever there is an electron within the detector acceptance. Otherwise the background can be rejected by the transverse momentum of the di-muon system or the sum of the two individual transverse momenta. According to the correlation matrices shown in Fig. 10.3 the two latter variables are highly correlated. The level of correlation is different for signal and background samples, which means that both variables are useful for the background rejection.

Fig. 10.4 shows the response of the BDT classifier for the different samples. It also shows the dependence of the signal selection efficiency N_S/N_S^{total}, signal purity $N_S/(N_S + N_B)$, background efficiency

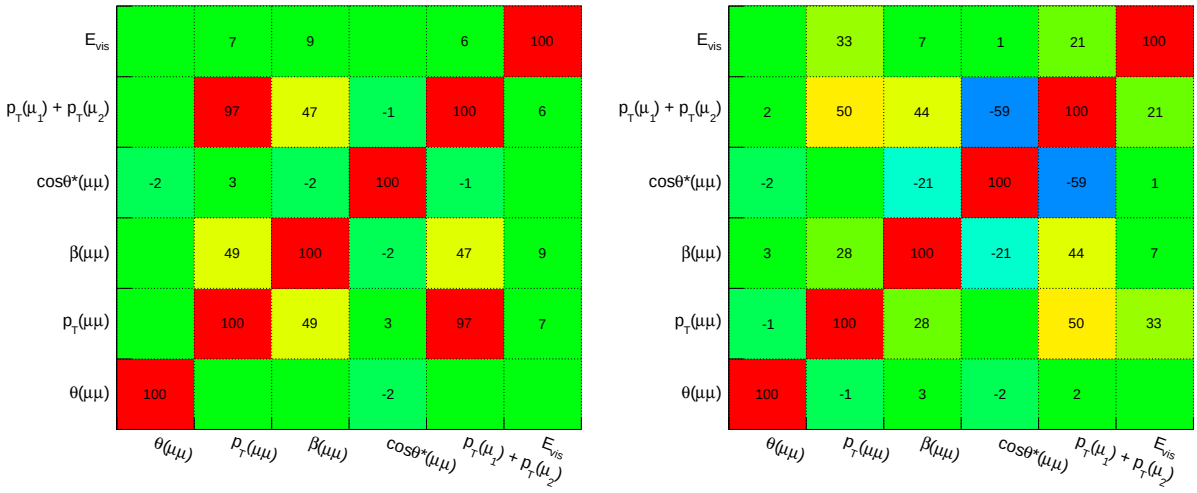

Figure 10.3: Correlation matrices for the kinematic variables used in the boosted decision tree classifier for $h \to \mu^+\mu^-$ events (left) and $\mu^+\mu^-e^+e^-$ events (right).

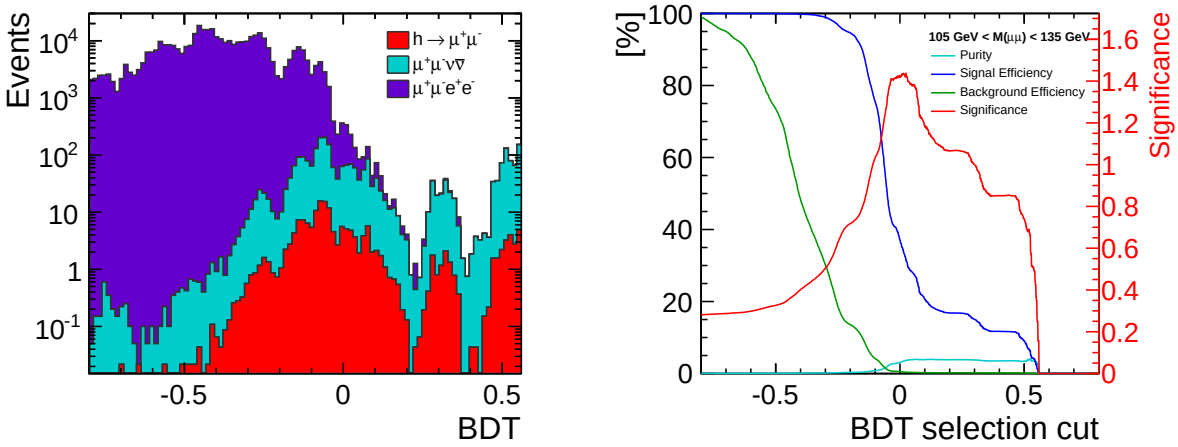

Figure 10.4: Response of the boosted decision tree classifier for the signal and the two most important background processes (left) and the resulting significance, purity, signal efficiency and background efficiency (right). See text for details.

N_B/N_B^{total} and significance[1] $N_S/\sqrt{N_S + N_B}$ on the BDT cut value, where N_S and N_B are the number of selected signal and selected background events, respectively. N_S^{total} and N_B^{total} are the number of events before the event selection for signal and background samples, respectively.

The final BDT selection cut is chosen such that the significance is maximized, which is usually at a BDT value of around 0. The distribution of all input variables before and after the BDT selection are shown in Fig. 10.6 and Fig. 10.7. The distribution of the invariant mass of the di-muon system before and after the event selection is shown in Fig. 10.5. The Higgs mass peak is clearly visible after the event selection.

[1] It should be noted that this is the significance over the arbitrarily chosen range of 105 GeV $< M(\mu\mu) <$ 135 GeV and should not be confused with the significance of the signal peak.

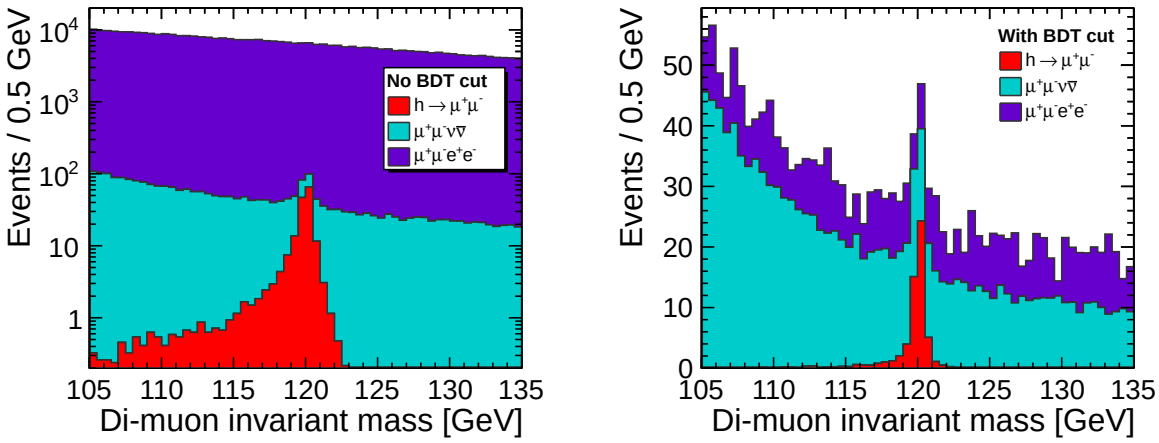

Figure 10.5: Distribution of the invariant mass of the di-muon system for the signal and the two main background channels before the event selection (left) and after the event selection (right). Histograms are stacked and normalized to $\mathcal{L} = 2\,\text{ab}^{-1}$.

10.2.3 Additional Background Samples

Although not used in the BDT training, the background selection efficiency was checked for all background samples.

Only 4 events of the $e^+e^- \to \tau^+\tau^-$ sample and 3 events of the $e^+e^- \to \tau^+\tau^-\nu\bar{\nu}$ sample pass the final event selection. Assuming a total integrated luminosity of $2\,\text{ab}^{-1}$ this corresponds to approximately 20 selected events from the $e^+e^- \to \tau^+\tau^-$ channel and 8 selected events from the $e^+e^- \to \tau^+\tau^-\nu\bar{\nu}$ channel with an invariant di-muon mass between 105 GeV and 135 GeV. It is reasonable to assume that their distribution is flat within that invariant mass region, which implies that their influence on the fit of the Higgs peak is negligible.

None of the $e^+e^- \to \mu^+\mu^-$ background events passes the final event selection. In fact, these events can be effectively rejected just by removing events with $p_T(\mu\mu) < 25\,\text{GeV}$ which is well below the selection cut introduced by the BDT, as shown in Fig. 10.6.

The $\gamma\gamma \to \mu^+\mu^-$ sample was studied at generator level. Fig. 10.8 shows the $p_T(\mu\mu)$ distribution of all samples at generator level and—despite the large event weights and low statistics in the tail—it can be seen that this variable can be used to effectively reject the $\gamma\gamma \to \mu^+\mu^-$ background, well below the selection cut introduced by the BDT (see Fig. 10.6).

10.3 Invariant Mass Fit

The number of signal events is obtained by fitting the expected shape of signal and background to the invariant mass distribution. This is a viable procedure since the Higgs mass can be obtained from other measurements with much higher precision. All the fits that are described in the following section are unbinned likelihood fits performed with the RooFit package [162].

10.3.1 Invariant Mass Shapes

In order to fit the invariant mass, the shapes of the invariant mass distributions for all channels are fitted individually first, using the full statistics available. The resulting Probability Density Functions

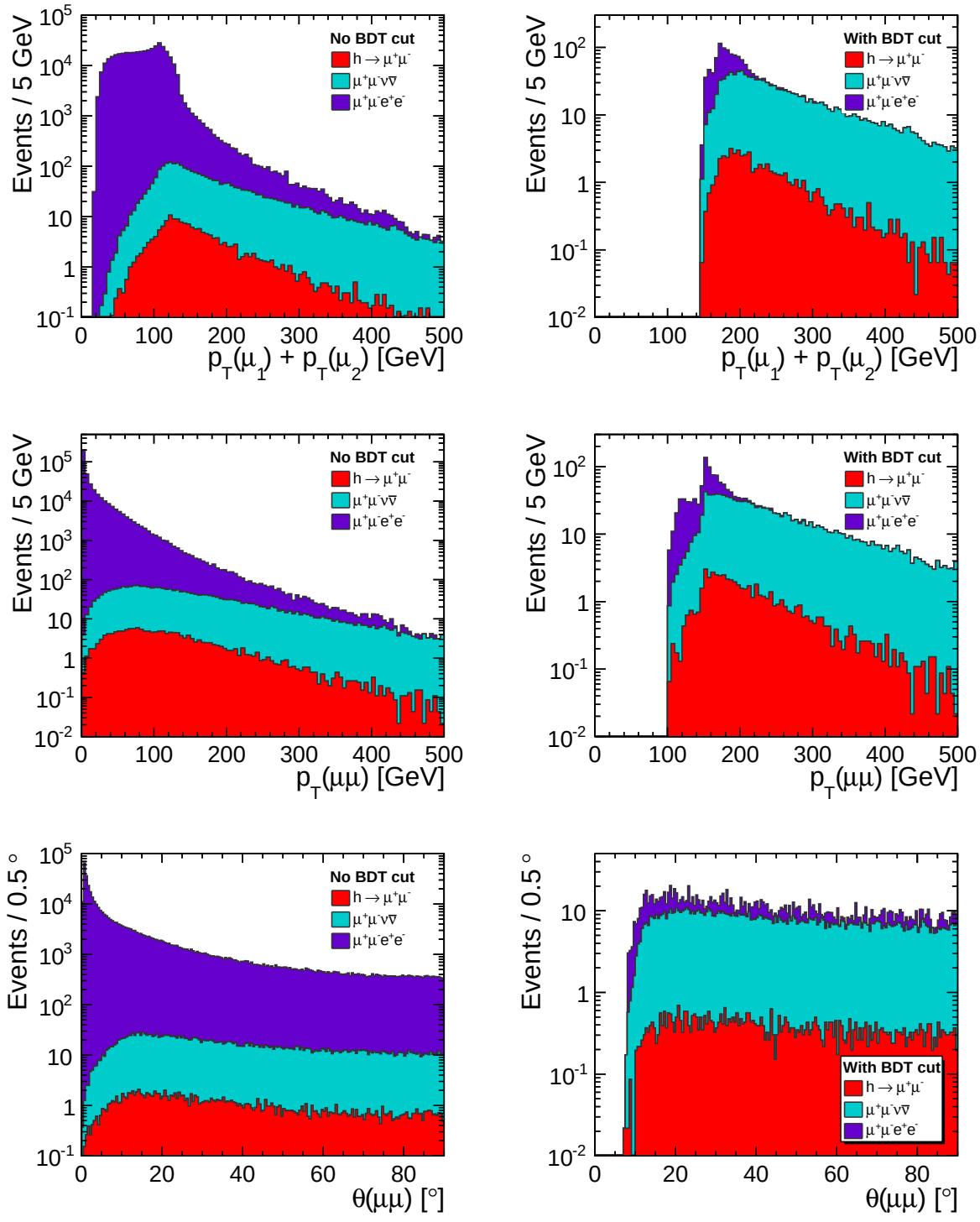

Figure 10.6: Distribution of the sum of the transverse momenta of the two muons $p_T(\mu_1) + p_T(\mu_2)$, the transverse momentum of the di-muon system $p_T(\mu\mu)$ and the polar angle of the di-muon system $\theta(\mu\mu)$ for the signal and the two main background channels before the event selection (left) and after the event selection (right). Histograms are stacked and normalized to $\mathcal{L} = 2\,\text{ab}^{-1}$.

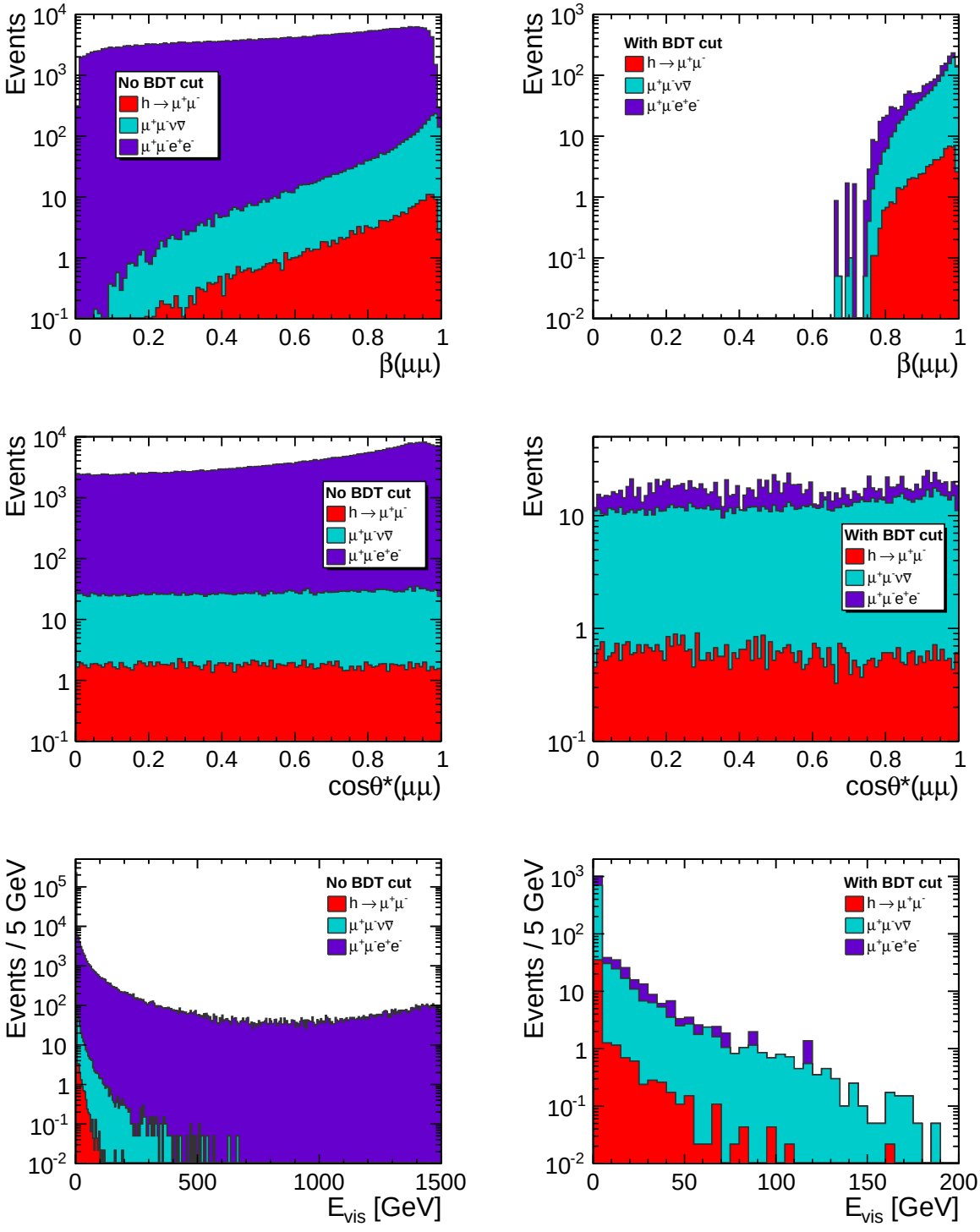

Figure 10.7: Distribution of the velocity β of the di-muon system, the helicity angle $\cos\theta^*$ and the visible energy without the two muons E_{vis} for the signal and the two main background channels before the event selection (left) and after the event selection (right). Histograms are stacked and normalized to $\mathcal{L} = 2\,\text{ab}^{-1}$.

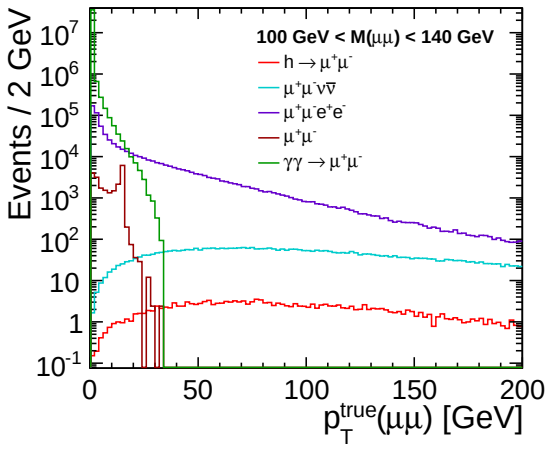

Figure 10.8: Distribution of the true transverse momentum of the di-muon system for all channels normalized to $\mathcal{L} = 2\,\text{ab}^{-1}$. No detector acceptance effects are taken into account.

(PDFs) then serve as templates to fit the simulated data. They also serve to generate more, statistically independent data sets for the background channels to perform multiple toy Monte Carlo experiments. The normalization is irrelevant for determining the shape and is thus not part of the PDFs.

The reconstructed Higgs mass peak can be described by a Gaussian distribution, which is determined completely by the momentum resolution of the detector. The detector resolution is in fact a convolution of several Gaussian distributions, since the momentum resolution is strongly depending on the transverse momentum and the polar angle of the reconstructed muon (see Section 10.5). The distribution has a tail towards lower masses because of final state radiation. In principle, this can be corrected for by identifying and matching reconstructed photons with the muons. This correction was not applied in this analysis because the overall effect on the shape is rather small. Instead, the shape is described well by two half Gaussian distributions with an exponential tail. Together with the mean value this results in five free parameters in the fitted function, which can be written as

$$f(x) = n \begin{cases} e^{\frac{-(x-m_0)^2}{2\sigma_L^2+\alpha_L(x-m_0)^2}}, & x \leq m_0 \\ e^{\frac{-(x-m_0)^2}{2\sigma_R^2+\alpha_R(x-m_0)^2}}, & x > m_0 \end{cases} \tag{10.1}$$

where m_0 is the mean of both Gaussian distributions, σ_L and σ_R are the widths, and α_L and α_R are the tail parameters of the left and the right Gaussian distribution, respectively. The normalization n is required to normalize the total integral to 1 and transform the function into a probability distribution. The best fit of Eq. (10.1) to the invariant mass distribution after event selection is shown in Fig. 10.9 (left). The values for the best fit are $m_0 = 120.1\,\text{GeV}$, $\sigma_L = 0.379\,\text{GeV}$, $\sigma_R = 0.293\,\text{GeV}$, $\alpha_L = 0.203$ and $\alpha_R = 0.133$.

Both main background channels can be described by a combination of an exponential PDF and a flat PDF

$$f(x) = r\, n_0\, e^{\lambda x} + (1 - r)\, n_1, \tag{10.2}$$

where the two free parameters are λ, describing the exponential behavior, and the fraction r, describing the amount of the exponential and the flat contributions. The two normalization constants n_0 and n_1 are required to normalize each individual probability distribution to 1.

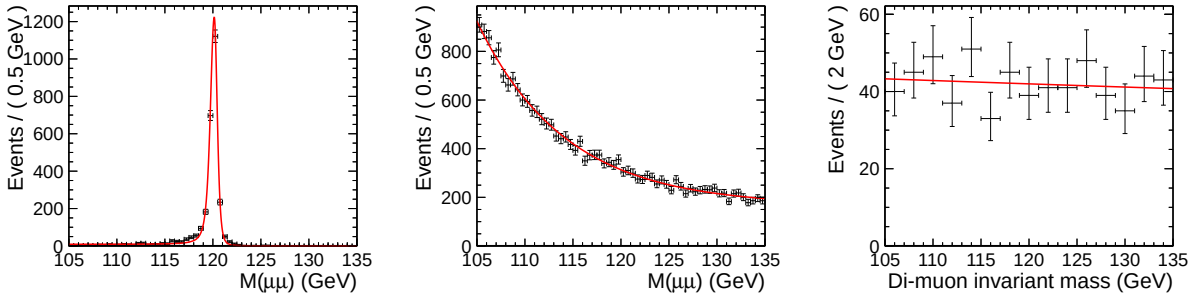

Figure 10.9: The invariant mass distribution of the signal events after event selection fitted with the function given in Eq. (10.1) (left). The invariant mass distribution of the $e^+e^- \to \mu^+\mu^-\nu\bar{\nu}$ events (middle) and the $e^+e^- \to \mu^+\mu^-e^+e^-$ events (right) after event selection, both fitted with a combination of a flat and an exponential probability density function.

As shown in Fig. 10.9 the distribution of the di-muon invariant mass in the $e^+e^- \to \mu^+\mu^-\nu\bar{\nu}$ events after the event selection using the BDT is mostly described by an exponential drop with $\lambda = -0.109$ and $r = 0.573$. The di-muon invariant mass distribution of the $e^+e^- \to \mu^+\mu^-e^+e^-$ events is almost flat after the event selection. The best fit is $\lambda = -0.004$ and $r = 0.493$.

After determining the shapes of the three contributing channels, the three PDFs are added into a combined PDF which describes the signal plus background hypothesis in case of a SM Higgs decaying into two muons. The parameters defining the shape of the individual PDFs are fixed and three free parameters for the number of events contributed by the individual channels are introduced.

10.3.2 Toy Monte Carlo

The fit of the Higgs mass peak is done on a very small event sample and upward or downward fluctuations of the number of signal events can strongly influence the measurement. Therefore, it is useful to perform the measurement on several independent event samples to estimate the average expected measurement accuracy. Since the available statistics from full simulation, especially for the $\mu^+\mu^-e^+e^-$ sample, is not sufficient to create enough independent samples corresponding to an integrated luminosity of $2\,\text{ab}^{-1}$, the toy Monte Carlo method is used instead. For this, the PDFs for the different channels determined in Section 10.3.1 are used to generate random event samples corresponding to the desired integrated luminosity. The number of events to be generated for each process is drawn from a Poisson distribution with a most probable value of $N = \sigma \cdot \epsilon \cdot \mathcal{L}$, where ϵ is the total selection efficiency for the respective process. Since the $h \to \mu^+\mu^-$ sample has sufficient statistics, those events are drawn from the fully simulated sample instead. This method allows to generate a large number of independent samples that each correspond to a realistic measurement. It also allows to generate data sets corresponding to larger integrated luminosities than possible with the original samples, provided the original sample is large enough to extract the shape.

The randomly generated event sample is then fitted with the combined PDF using an unbinned likelihood fit to obtain the number of signal events. An example of this fit for an integrated luminosity of $2\,\text{ab}^{-1}$ is shown in Fig. 10.10 (left). The cross section times branching ratio is then determined by

$$\sigma_{h\nu_e\bar{\nu}_e} \times \text{BR}_{h\to\mu^+\mu^-} = \frac{N_S}{\mathcal{L}\,\epsilon_S}, \tag{10.3}$$

where ϵ_S is the total signal selection efficiency

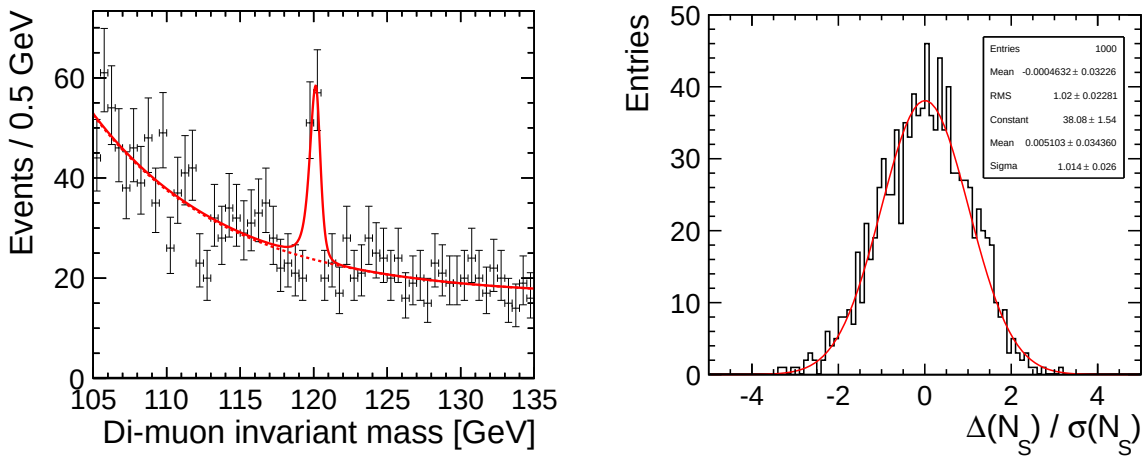

Figure 10.10: One example of the Higgs mass peak fit for a data set corresponding to $\mathcal{L} = 2\,\mathrm{ab}^{-1}$ (left). Pull distribution for 1000 toy Monte Carlo experiments extracting the number of signal events N_S assuming a total integrated luminosity of $2\,\mathrm{ab}^{-1}$ and fitted with a Gaussian distribution (right).

The large number of samples that can be generated with the toy Monte Carlo method also allows to test the shape assumed for the signal distribution, since the $h \to \mu^+\mu^-$ events are drawn from the full simulation sample. If the shape describes the distribution well, the resulting pull distribution should follow a Gaussian distribution centered around 0 with a width of 1. The pull is defined as $\Delta N_S/\sigma(N_S)$, where ΔN_S is the difference between the number of signal events extracted from the respective fit and the mean expected signal events. $\sigma(N_S)$ is the uncertainty of the number of signal events for that fit. Fig. 10.10 (right) shows the pull distribution obtained from 1000 toy Monte Carlo experiments which has been fitted with a Gaussian distribution. It can be seen that the invariant mass distribution is well described by the assumed shapes.

10.3.3 Result

In order to estimate the achievable precision, 100 toy Monte Carlo experiments are performed. The resulting cross section times branching ratio of 0.122 fb is the average obtained from those 100 fits. The relative statistical uncertainty of 23% is the average of the relative uncertainties of the individual measurements. The results are summarized in Table 10.3. Here, we assumed a SM-like cross section times branching ratio. If the true value differs from the SM prediction by a factor a, then the achievable uncertainty scales with a factor $1/\sqrt{a}$ due to the different amount of available signal events. The observed signal would correspond to a significance of 4.3σ, which would be slightly to low to actually claim a discovery of the muon decay channel.

There are several systematic uncertainties that have to be taken into account in such an experiment. The expected uncertainty of the peak luminosity is currently being studied but is estimated to be around 1% or less. The systematic uncertainties originating from detector effects are difficult to estimate and a detailed study goes beyond the scope of this thesis. The most important detector effects will be the uncertainty on the momentum resolution, the uncertainty on the resolution of the track angle and the uncertainty on the muon identification efficiency directly influencing the uncertainty of the signal selection efficiency and the expected signal shape.

An estimate of the detector related systematic uncertainties can be found from the experience at the

Table 10.3: Summary of the results for the $h \to \mu^+\mu^-$ branching ratio measurement for an integrated luminosity of $2\,ab^{-1}$.

Signal events	62 ± 14
Signal efficiency	25.2%
$\sigma_{h\nu_e\bar{\nu}_e} \times BR_{h\to\mu^+\mu^-}$	0.122 fb
Stat. uncertainty	23.3%

LEP experiments. For the measurement of $\sigma_{Z\to\mu^+\mu^-}$ at LEP, the systematic uncertainty due to detector effects was between 0.1 and 0.4%, depending on the experiment [33]. Together with the estimate on the uncertainty due to the luminosity measurement, one can expect that the systematic uncertainty of this analysis will be negligible compared to the statistical uncertainty.

10.4 Impact of Beam-Induced Background

The beam-induced electron pair background with particles at very low angles and low transverse momenta leads to high occupancies in the vertex detector and the forward calorimeters (see Sections 3.1.3 and 5.6). This has to be considered when designing those sub-detectors but is of no concern for this analysis. The $\gamma\gamma \to$ hadrons background, on the other hand, introduces particles at higher p_T and has to be dealt with at the analysis level (see also Section 3.1.3). The default event overlay settings for the $\gamma\gamma \to$ hadrons background are used, as defined in Section 6.3.1. The impact of this background is studied by adding the background only to the signal events due to the large statistics of the background samples.

In case of the signal sample, the reconstructed event topology of two muons with a typical transverse momentum of 100 GeV and more (see Fig. 10.6) is not affected by the addition of the $\gamma\gamma \to$ hadrons background. Nevertheless a cut requiring a minimum transverse momentum of 5 GeV for each reconstructed particle is introduced to remove low-p_T background particles and retain the clean event topology. None of the distributions of the kinematic variables of the muons and the di-muon system are affected by the addition of the $\gamma\gamma \to$ hadrons background, see Fig. 10.11. On the other hand, the distribution of the visible energy, which is shown in Fig. 10.12 (left), is affected. Without background, non-zero E_{vis} is solely due to final state radiation. Despite the cut on the p_T of the reconstructed particles, the reconstructed energy is increased due to background, since the $\gamma\gamma \to$ hadrons events can contain some particles with higher p_T that may add up to 100 GeV to the total visible energy, after cuts. The fraction of $h \to \mu^+\mu^-$ events with $E_{vis} > 0$ increases from 9% to about 52% when the background is added.

The muon reconstruction efficiency in the signal sample is slightly reduced in the barrel region, as shown in Fig. 10.12 (right). The average muon reconstruction efficiency for polar angles greater than 10° is 98.4% with background compared to 99.6% without. The inefficiency is due to failed muon identification in the calorimeters which was tuned without background overlay and can most likely be improved. The total reconstruction efficiency, requiring two reconstructed muons with an invariant mass between 105 GeV and 135 GeV, is reduced to 72% in the presence of background.

The event selection is performed with a BDT, similar to the selection procedure described in Section 10.2. Since the E_{vis} distribution of the signal sample is modified by the addition of the $\gamma\gamma \to$ hadrons background, which was not added to the other physics processes, this variable can not be used in the classifier. Instead, a pre-selection cut of $E_{vis} < 150$ GeV is used to reject $e^+e^- \to \mu^+\mu^-e^+e^-$ events with electrons at large polar angles. This cut removes only 0.6% of the $h \to \mu^+\mu^-$ events that passed the

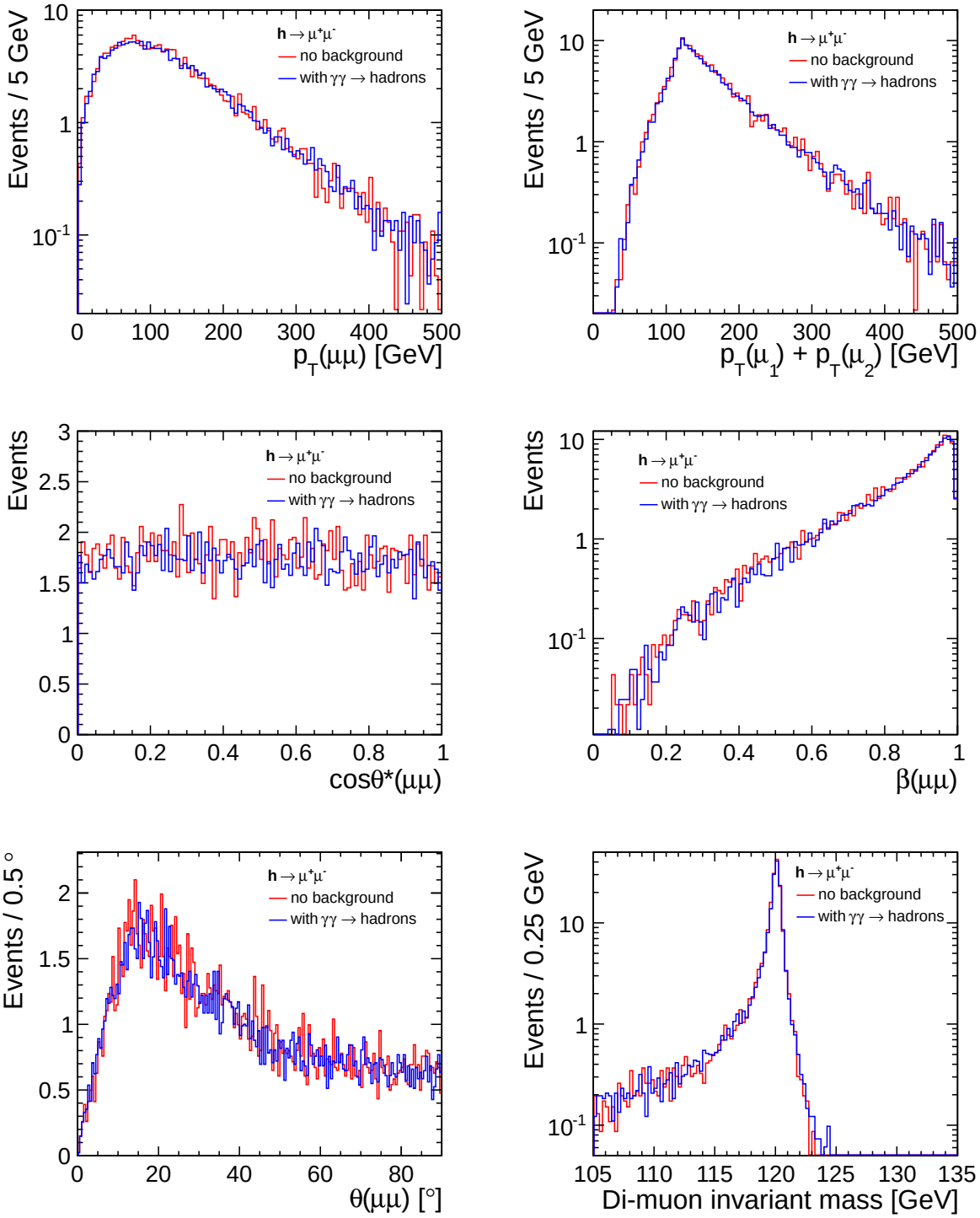

Figure 10.11: Impact of the $\gamma\gamma \to$ hadrons background on the distributions of the kinematic variables used in the event selection in $h \to \mu^+\mu^-$ events. Histograms are normalized to a total integrated luminosity of 2 ab^{-1}.

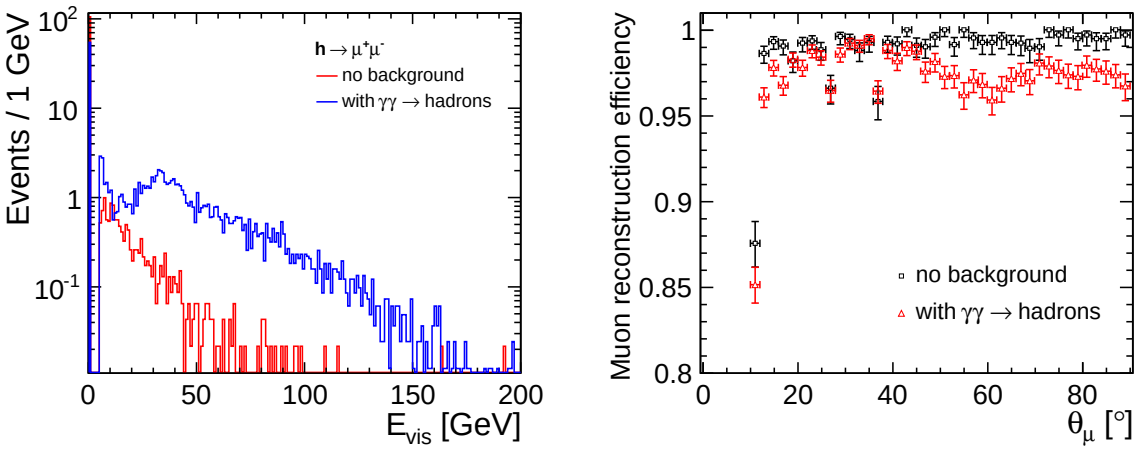

Figure 10.12: Impact of the $\gamma\gamma \to$ hadrons background on the distribution of E_{vis} of the signal sample, normalized to $\mathcal{L} = 2\,\text{ab}^{-1}$ (left). Muon reconstruction efficiency for the signal sample with and without $\gamma\gamma \to$ hadrons overlay (right).

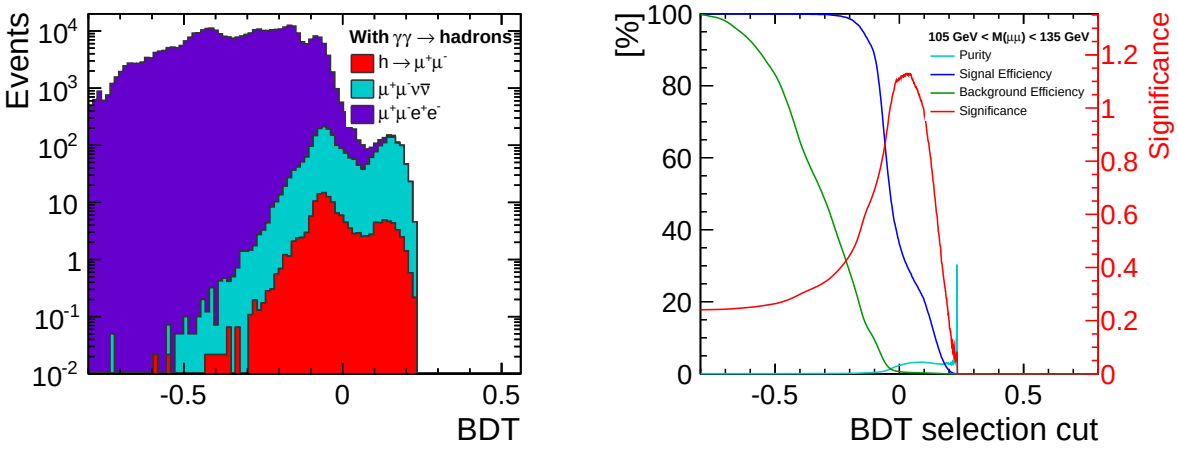

Figure 10.13: Response of the boosted decision tree classifier for the signal including the $\gamma\gamma \to$ hadrons background and the two most important background processes (left) and the resulting significance, purity, signal efficiency and background efficiency (right).

original pre-selection cut. Applying a pre-selection cut on a variable instead of using it in a multivariate classifier leads to a worse signal and background separation since correlations are no longer taken into account. In addition, the fact that E_{vis} is underestimated for the background processes means that the number of selected background events is overestimated. This means that our estimate of the impact of the $\gamma\gamma \to$ hadrons background is conservative.

Fig. 10.13 shows the response of the BDT classifier including the $\gamma\gamma \to$ hadrons background. The BDT selection cut that yields the highest significance corresponds to a signal selection efficiency of 21.7%. Using the fitting procedure explained in Section 10.3 in 100 toy Monte Carlo experiments results in an expected relative statistical uncertainty of 26.3%, see Table 10.4. This is worse than the result obtained in Section 10.3.3 but probably too pessimistic due to the reasons stated above.

Table 10.4: Summary of the results for the $h \to \mu^+\mu^-$ branching ratio measurement with $\gamma\gamma \to$ hadrons background overlaid for an integrated luminosity of $2\,\text{ab}^{-1}$.

Signal events	53 ± 14
Signal efficiency	21.7%
$\sigma_{h\nu_e\bar{\nu}_e} \times \text{BR}_{h\to\mu^+\mu^-}$	0.121 fb
Stat. uncertainty	26.3%

In addition to the systematic uncertainties discussed in Section 10.3.3, no systematic uncertainties due to the $\gamma\gamma \to$ hadrons background are expected. The huge statistics of all machine-induced backgrounds will allow to understand those process with almost unlimited precision and will allow to remove any systematic uncertainty on E_{vis}. The impact of these backgrounds on the muon reconstruction efficiency can be studied in Z boson production events. If the reduced reconstruction efficiency due to the presence of $\gamma\gamma \to$ hadrons background can not be removed by an improved muon finding algorithm, a larger cross section of the $\gamma\gamma \to$ hadrons process than expected here will lead to a lower significance of the branching ratio measurement.

10.5 Impact of the Momentum Resolution

The momentum resolution is the most important detector parameter that directly influences the branching ratio measurement. It determines the width of the Higgs boson mass peak observed in the signal sample, which then translates into the significance of the observed peak over the background.

The momentum resolution $\sigma(\Delta(p_T)/p_T^2)$ depends strongly on the particle momentum and its polar angle θ. Fig. 10.14 (left) shows the momentum resolution as a function of those two variables obtained from the muons in all of the fully simulated samples used in this analysis. For each bin in θ and p_T the resulting $\Delta(p_T)/p_T^2$-distribution was fitted to a Gaussian distribution to obtain its width. Outliers are rejected by a cut at five times the RMS around the mean of the distribution prior to the fitting. As expected, the momentum resolution has a $1/p_T$-dependence due to multiple scattering. For transverse momenta above 100 GeV the constant term driven by the magnetic field and the lever arm becomes more important and the distribution flattens out. It can be seen that the momentum resolution throughout the barrel region, $\theta > 40\,^\circ$, only depends on the transverse momentum. It degrades sharply for polar angles below 30°. Fig. 10.14 (right) shows the momentum resolution of the reconstructed muons in the signal sample and for the two subsets where the polar angle of the muon is either above or below 30°. The average momentum resolution for reconstructed muons with $\theta > 30^\circ$ is $3.5 \times 10^{-5}\,\text{GeV}^{-1}$ but only $1.1 \times 10^{-4}\,\text{GeV}^{-1}$ for reconstructed muons with $\theta < 30^\circ$. The average momentum resolution for all reconstructed tracks in the signal sample is $5.2 \times 10^{-5}\,\text{GeV}^{-1}$. Those events that pass the final event selection, as discussed in Section 10.2, are biased towards the central region, such that the average momentum resolution for the selected signal sample is $3.9 \times 10^{-5}\,\text{GeV}^{-1}$.

To assess the impact of the momentum resolution, various samples were created using fast simulation and assuming different widths of the $\Delta p_T/p_T^2$ distribution. For simplicity, flat momentum resolutions are assumed without any dependence on the transverse momentum or the polar angle of the particle. A Gaussian smearing with the width corresponding to the desired momentum resolution has been applied to the true momenta of the reconstructed muons to generate the reconstructed momenta. The reconstructed track angles are unchanged. The broadening of the Higgs peak due to increasing momentum resolution is shown in Fig. 10.15 (left).

The event selection and fit of the invariant mass distribution follows the procedure explained in the

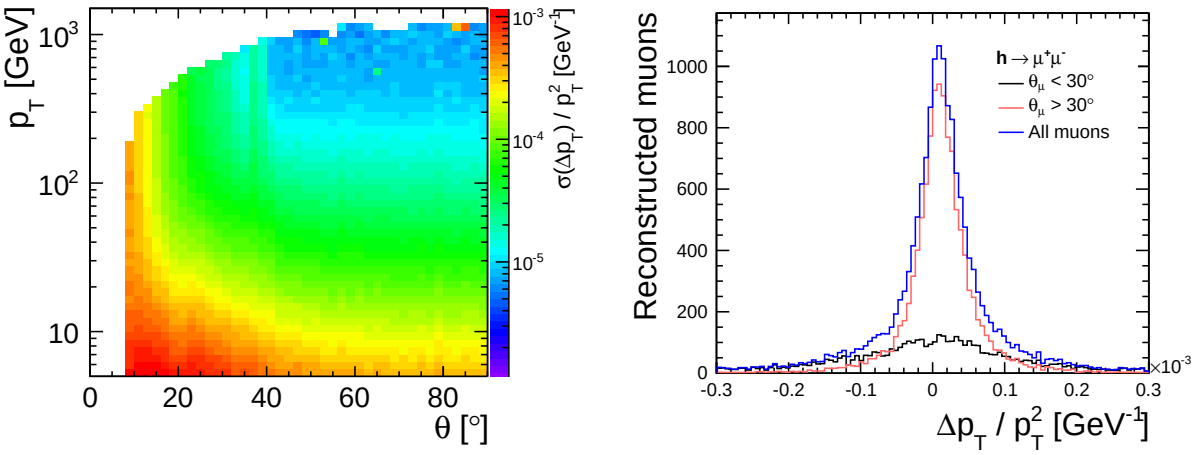

Figure 10.14: $\Delta p_T/p_T^2$ resolution of muons depending on the polar angle θ and the transverse momentum extracted from all fully simulated samples (left) and $\Delta p_T/p_T^2$ resolution in $h \to \mu^+\mu^-$ events for different regions in θ (right).

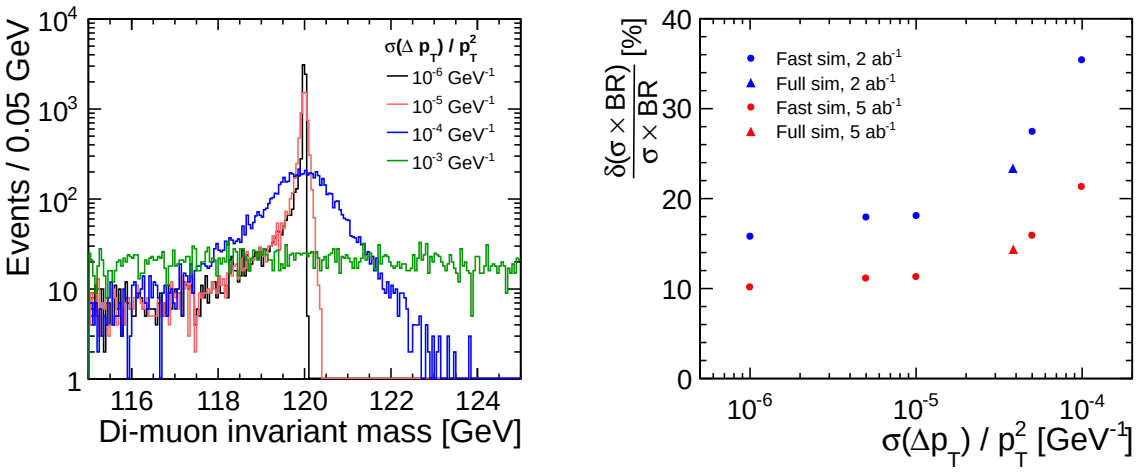

Figure 10.15: Di-muon invariant mass distribution for different $\Delta p_T/p_T^2$ resolutions (left) and relative statistical uncertainty on the $h \to \mu^+\mu^-$ cross section times branching ratio measurement depending on the $\Delta p_T/p_T^2$ resolution for an integrated luminosity of 2 and 5 ab^{-1} (right).

previous sections using the same boosted decision tree. Only the BDT selection cut has been changed to optimize the significance. The di-muon invariant mass distribution of the signal and background contributions are fitted to obtain their expected shapes and the cross section times branching ratio is extracted from 100 toy Monte Carlo experiments. The impact of the $\gamma\gamma \to$ hadrons background is not included but expected to be similar to the results obtained in Section 10.4.

Fig. 10.15 (right) shows the resulting statistical uncertainty on the cross section times branching ratio measurement depending on the momentum resolution, assuming a total integrated luminosity of 2 ab^{-1} and 5 ab^{-1}, respectively. The points corresponding to the result from the full simulation sample obtained in Section 10.3.3 are consistent with the results obtained from fast simulations. The relative statistical uncertainty degrades noticeably for momentum resolutions worse than a few times 10^{-5} GeV^{-1}. The measurement does not improve for better momentum resolutions because of the intrinsic statistical fluc-

Table 10.5: Summary of the results for the $h \to \mu^+\mu^-$ branching ratio measurement using fast simulation samples with different momentum resolutions $\sigma(\Delta p_T)/p_T^2$ assuming an integrated luminosity of $2\,ab^{-1}$. Given is the corresponding invariant mass resolution $\sigma(\Delta M(\mu\mu))$ and the resulting statistical uncertainty of the $\sigma_{h\nu_e\bar{\nu}_e} \times BR_{h\to\mu^+\mu^-}$ measurement.

$\sigma(\Delta p_T)/p_T^2$	$\sigma(\Delta M(\mu\mu))$	Stat. uncertainty
$10^{-3}\,GeV^{-1}$	6.5 GeV	-
$10^{-4}\,GeV^{-1}$	0.70 GeV	34.3%
$10^{-5}\,GeV^{-1}$	0.068 GeV	18.2%
$10^{-6}\,GeV^{-1}$	0.022 GeV	16.0%

tuations in the number of selected signal events. The results of the cross section times branching ratio measurement for different momentum resolutions are summarized in Table 10.5.

10.6 Impact of Forward Electron Tagging

The results presented in Section 10.3.3 can be improved further by rejecting $\mu^+\mu^-e^+e^-$ events through electron tagging in the forward calorimeters, thus improving the signal to background ratio. The forward calorimeters LumiCal and BeamCal were not part of the full simulation, since this would have required the addition of the incoherent pair background to every event in order to be realistic. To estimate the possible improvement by including this information, several electron tagging efficiencies are assumed and events are rejected based on the Monte Carlo truth information. The electron tagging efficiency in the forward calorimeters at CLIC in the presence of realistic beam-induced backgrounds is currently being investigated in a dedicated full simulation study.

10.6.1 Event Rejection

The event rejection of the $e^+e^- \to \mu^+\mu^-e^+e^-$ events is based on the Monte Carlo truth information of the two electrons, where e_1 is the most energetic electron and e_2 is the second most energetic electron. Fig. 10.16 shows the polar angle θ and the azimuthal angle ϕ of the two electrons in $e^+e^- \to \mu^+\mu^-e^+e^-$ events. The electrons are mostly going very forward and peak at a polar angle of 10 mrad, which is half of the crossing angle of the two beams. The ϕ distribution peaks at 0° due to the inclusion of the crossing angle. The outgoing beam pipe is displaced in the x-z-plane, which corresponds to an azimuthal angle of 0°.

For this study we use the electron directions with respect to the outgoing beam axis instead of the directions with respect to the detector axis. This requires a rotation of the coordinate system around the y-axis by 10 mrad for $z > 0$ and a rotation by -10 mrad for $z < 0$. The resulting angles are referred to as θ' for the polar angle and ϕ' for the azimuthal angle. Their distributions are shown in Fig. 10.17.

In order to reject the $e^+e^- \to \mu^+\mu^-e^+e^-$ background events, the electrons have to be tagged by identifying their energy deposition in presence of the beam-induced backgrounds. As shown in Fig. 10.18 (left), the energy of the electrons is usually of the order of several hundreds of GeV up to the full beam energy. We assume an ad-hoc tagging efficiency of 95% or 99% is for electrons with a polar angle greater then 44 mrad, which corresponds to the inner radius of the fiducial volume of the LumiCal. The two cases are referred to as LumiCalCut_{95}, for 95% efficiency, and LumiCalCut_{99}, for 99% efficiency. The BeamCal on the other hand has a much higher occupancy and electron tagging at these polar angles is thus less efficient. Two cases have been studied, one assuming 30% electron tagging efficiency for polar angles

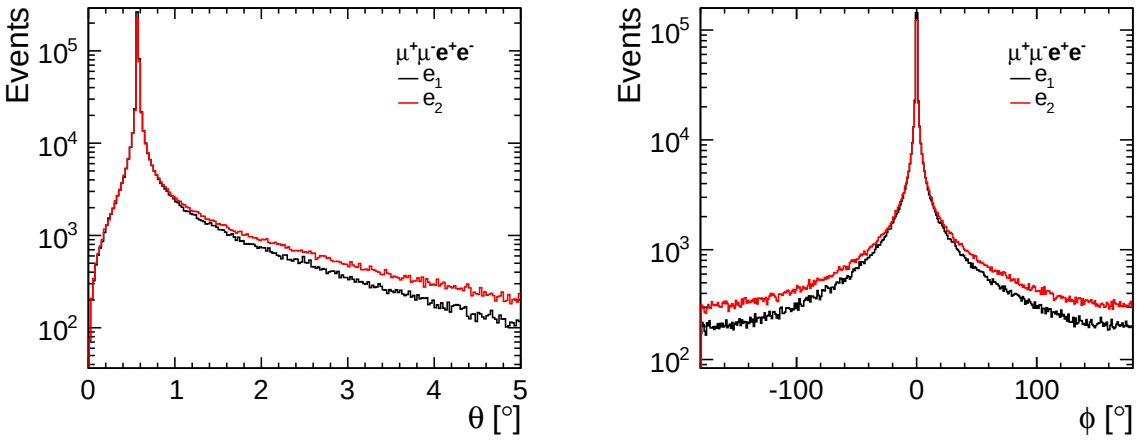

Figure 10.16: Distribution of the polar angle θ (left) and azimuthal angle ϕ (right) of the most energetic electron (e_1) and the second most energetic electron (e_2) in $e^+e^- \to \mu^+\mu^-e^+e^-$ events.

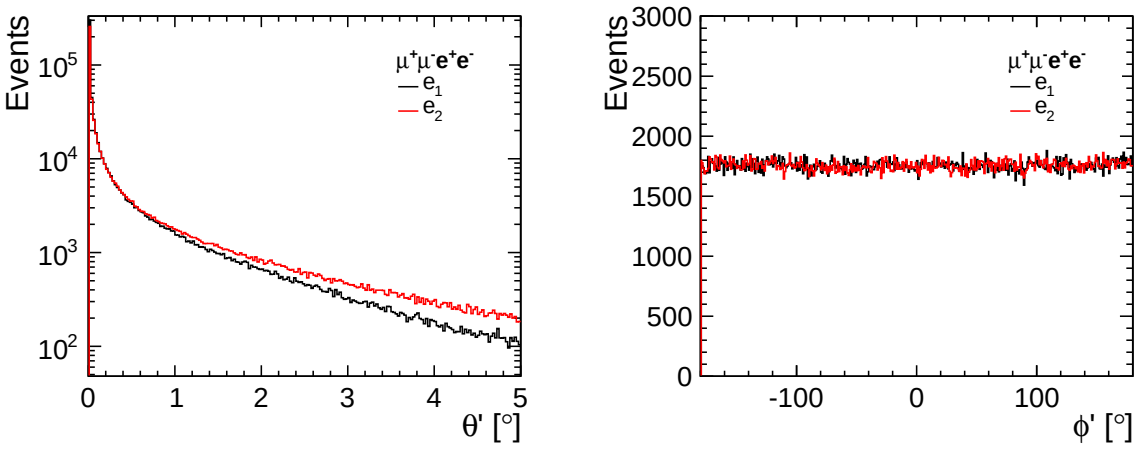

Figure 10.17: Distribution of the electron angles with respect to the outgoing beam axis. Polar angle θ' (left) and azimuthal angle ϕ' (right) of the most energetic electron (e_1) and the second most energetic electron (e_2) in $e^+e^- \to \mu^+\mu^-e^+e^-$ events.

θ' greater than 15 mrad and one assuming 70% electron tagging efficiency in the same angular region. These selection cuts are referred to as BeamCalCut_{30} and BeamCalCut_{70}, both implicitly including the LumiCalCut_{99} to account for the higher tagging efficiency at larger polar angles. For simplicity, no further dependence of the electron tagging efficiency on the polar angle is assumed and no dependence of the tagging efficiency on the electron energy was introduced. A dedicated full simulation study of the electron tagging efficiency in the BeamCal, including the incoherent pair background, found that tagging efficiencies of more than 80% seem feasible for electron energies of 1 TeV and higher [111].

To model the tagging efficiency, two random numbers between 0 and 1 are assigned to each event, one for each electron. An event is rejected if any of the two most energetic electrons has a polar angle θ' greater than the assumed acceptance angle and the corresponding random number is above the assumed efficiency. Fig. 10.18 (right) shows the impact of the BeamCalCut_{70} event selection on the

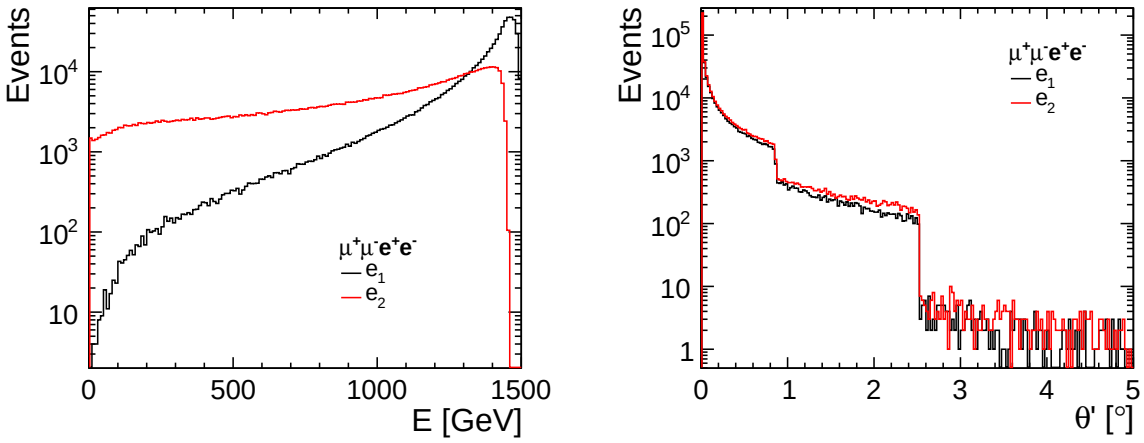

Figure 10.18: Distribution of the energy of the most energetic electron (e_1) and the second most energetic electron (e_2) in $e^+e^- \to \mu^+\mu^-e^+e^-$ events (left). Distribution of the polar angle θ' of the most energetic electron (e_1) and the second most energetic electron (e_2) in $e^+e^- \to \mu^+\mu^-e^+e^-$ events after applying the BeamCalCut$_{70}$ selection cut (right).

Table 10.6: Event selection cuts for removing $e^+e^- \to \mu^+\mu^-e^+e^-$ events. The assumed single electron tagging efficiency ϵ_e, the minimum polar angle required to tag the electron θ'_{min} and the resulting efficiency to reject events ϵ_{reject} are given.

	ϵ_e [%]	θ'_{min} [mrad]	ϵ_{reject} [%]
LumiCalCut$_{95}$	95	44	15.1
LumiCalCut$_{99}$	99	44	15.7
BeamCalCut$_{30}$*	30	15	21.5
BeamCalCut$_{70}$*	70	15	29.0

* Implicitely includes LumiCalCut$_{99}$.

distribution of the polar angles of the electrons. The number of events drops sharply at the polar angles corresponding to the assumed BeamCal and LumiCal acceptance, but most of the $e^+e^- \to \mu^+\mu^-e^+e^-$ events are unaffected by these selection cuts, since in most cases both electrons are leaving the detector outside of the BeamCal acceptance. For example, more than 70% of the events pass the BeamCalCut$_{70}$ rejection cut. The resulting total event rejection efficiencies for the different cuts are summarized in Table 10.6.

10.6.2 Coincidence with Bhabha Scattering Events

Vetoing events based on low-angle electrons bears of course the danger of rejecting signal events if they coincide within the readout time window for example with a Bhabha scattering event. The total cross section for the $e^+e^- \to e^+e^-$ process with a minimum electron polar angle of 44 mrad and a minimum electron energy of 100 GeV is approximately 60 pb. With a nominal luminosity of $5.9 \times 10^{34}\,\mathrm{cm}^{-2}\mathrm{s}^{-1}$ and a rate of 50 bunch trains per second, 0.071 events of this kind are expected per bunch train. Each bunch train consists of 312 bunches and has a length of 156 ns. If a time stamping of 10 ns is assumed in addition, the probability of coincidence with a signal event within this time window is less than 0.5%

Table 10.7: Summary of the results for the $h \to \mu^+\mu^-$ branching ratio measurement assuming different electron tagging efficiencies in the forward calorimeters for an integrated luminosity of $2\,ab^{-1}$.

	$LumiCalCut_{95}$	$LumiCalCut_{99}$	$BeamCalCut_{30}$	$BeamCalCut_{70}$
Signal events	120 ± 17	127 ± 18	130 ± 18	132 ± 18
Signal efficiency	49.3%	53.2%	55.1%	55.9%
$\sigma_{h\nu_e\bar{\nu}_e} \times BR_{h\to\mu^+\mu^-}$	0.121 fb	0.119 fb	0.118 fb	0.118 fb
Stat. uncertainty	15.0%	14.3%	14.1%	13.8%

and of no concern.

If a minimum electron polar angle of only 15 mrad is required, the total cross section of the $e^+e^- \to e^+e^-$ process rises to approximately 650 pb. This corresponds to 0.767 events per bunch train and 0.051 events within a 10 ns time window. This means that a significant amount of signal events of about 5% would be rejected.

The cross section for the $e^+e^- \to e^+e^- f\bar{f}$ process, with similar cuts on the electrons and a maximum fermion polar angle of 100 mrad, is always more than one order of magnitude smaller than the cross section of the e^+e^- process and can be neglected.

10.6.3 Event Selection

The final event selection is done similarly to the strategy introduced in Section 10.2 using boosted decision trees. Since the electron angles are correlated with the angle of the di-muon system as well as the muon angles, the distributions of the input variables used in the boosted decision tree change when the electron cuts are applied during the event pre-selection. Dedicated BDTs are thus trained for each of the electron cuts and the BDT value of the final event selection cut is determined as the value with the highest significance $N_S/\sqrt{N_S + N_B}$.

Since most of the $e^+e^- \to \mu^+\mu^-e^+e^-$ events with a high p_T of the di-muon system are removed a priori by the electron rejection cuts, the background rejection by the BDT is largely improved. The signal selection efficiency increases to about 49% with the $LumiCalCut_{95}$ and almost 56% with the $BeamCalCut_{70}$ selection.

10.6.4 Branching Ratio Measurement

The statistical uncertainty on the cross section times branching ratio measurement is determined similarly to Section 10.3. First the shapes of the di-muon invariant mass distributions for the individual signal and background contributions are determined. Then the signal plus background model is used to measure the number of signal events in 100 toy Monte Carlo experiments and finally the cross section times branching ratio is calculated using the selection efficiency. Fig. 10.19 shows the uncertainty that can be achieved, depending on the integrated luminosity and the electron rejection cut applied. The results for an integrated luminosity of $2\,ab^{-1}$ are given in Table 10.7.

Since the statistical uncertainty is directly related to the number of signal events selected, the higher selection efficiency that can be achieved when rejecting some of the $e^+e^- \to \mu^+\mu^-e^+e^-$ events a priori leads to a big improvement of the cross section times branching ratio measurement from a relative uncertainty of 23% down to 15% when using the $LumiCalCut_{95}$. Assuming even higher electron tagging efficiencies and also electron tagging in the BeamCal can improve the statistical uncertainety of the cross section times branching ratio measurement to less than 14%. The additional improvement is only modest

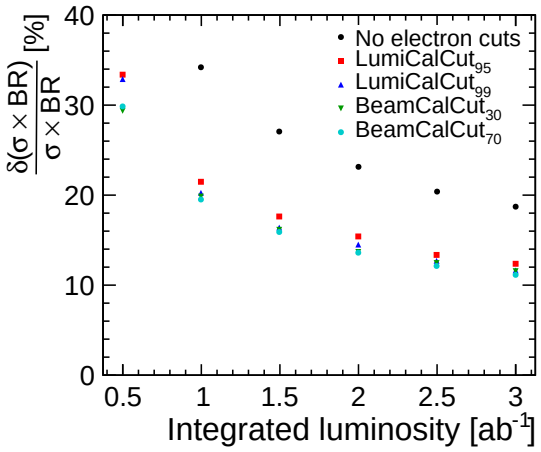

Figure 10.19: Relative statistical uncertainty on the $h \to \mu^+\mu^-$ cross section times branching ratio measurement depending on the integrated luminosity with and without assuming electron tagging in the forward calorimeters.

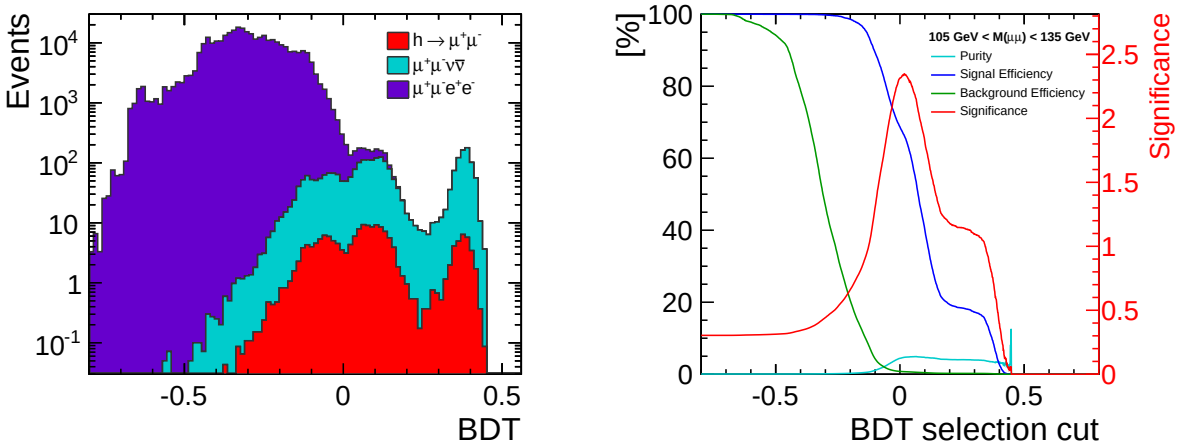

Figure 10.20: Response of the boosted decision tree classifier for the signal and the two most important background processes (left) and the resulting significance, purity, signal efficiency and background efficiency (right), in case of the LumiCalCut$_{95}$.

since the background rejection based on the transverse momentum of the di-muon system is already very efficient for low $p_T(\mu\mu)$. This is also reflected in the small differences in significance achievable by the BDT event selection shown in Figures 10.20, 10.21, 10.22 and 10.23.

Similar to the study in Section 10.4, the analysis was repeated with the signal sample that had been overlaid with the $\gamma\gamma \to$ hadrons background for the case of the LumiCalCut$_{95}$ selection cut. A different BDT without the E_{vis} variable was trained and instead a pre-selection cut of $E_{\text{vis}} < 150\,\text{GeV}$ was used. The most significant selection cut yields a signal selection efficiency of 49.7% and results in a relative statistical uncertainty on the $\sigma_{h\nu_e\bar{\nu}_e} \times \text{BR}_{h\to\mu^+\mu^-}$ measurement of 15.7%. The result degrades only by a small amount since the E_{vis} variable is mostly used to reject background events with electrons within the detector acceptance which are mostly removed by the LumiCalCut$_{95}$ cut instead. This result would correspond to a significance of almost 6.4σ.

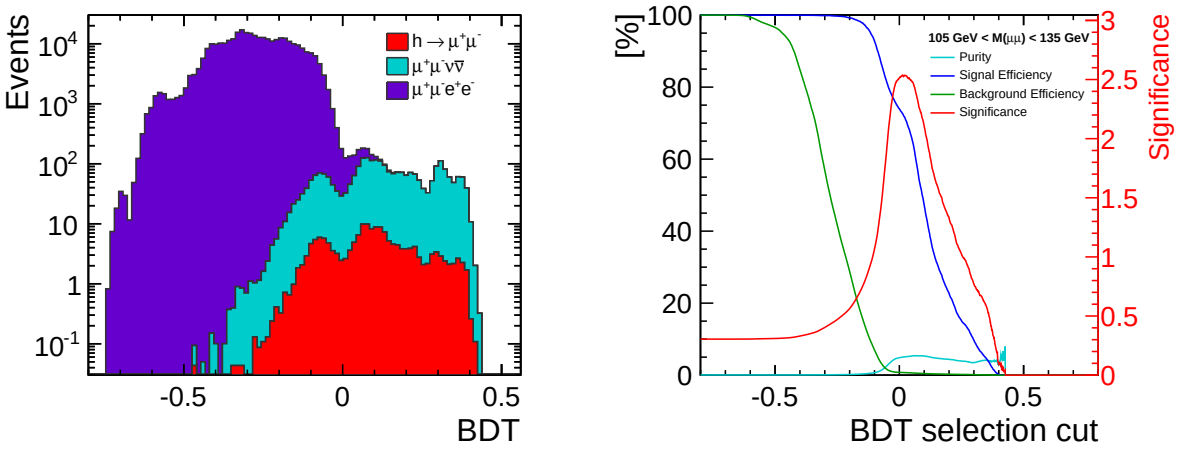

Figure 10.21: Response of the boosted decision tree classifier for the signal and the two most important background processes (left) and the resulting significance, purity, signal efficiency and background efficiency (right), in case of the LumiCalCut_{99}.

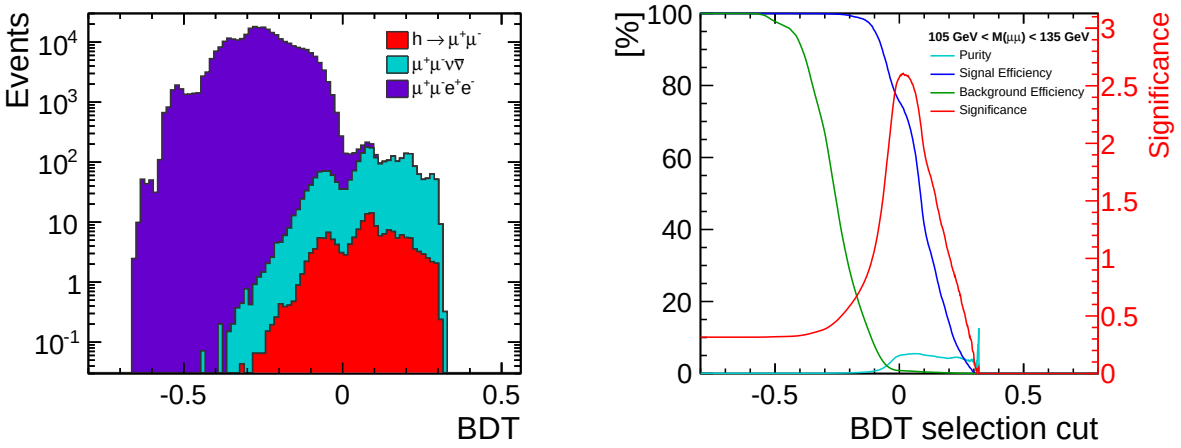

Figure 10.22: Response of the boosted decision tree classifier for the signal and the two most important background processes (left) and the resulting significance, purity, signal efficiency and background efficiency (right), in case of the BeamCalCut_{30}.

These results show that a high electron tagging in the LumiCal can improve the measurement substantially. Efficient electron tagging in the BeamCal would improve the results only by a small amount. It also significantly increases the probability of rejecting signal events if they coincide with low-angle $e^+e^- \to e^+e^-$ events.

10.7 Extracting the Higgs Coupling

Once the cross-section times branching ratio has been measured the Yukawa coupling constant g_μ can be determined. In general this has to be done by performing a global fit to all branching ratio measurements involving the Higgs. This allows to determine all coupling constants simultaneously including their

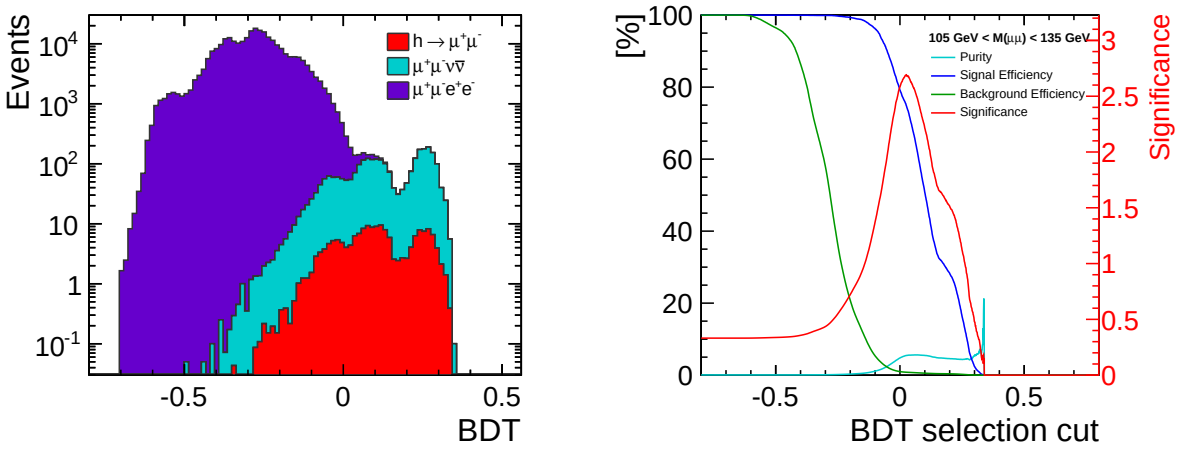

Figure 10.23: Response of the boosted decision tree classifier for the signal and the two most important background processes (left) and the resulting significance, purity, signal efficiency and background efficiency (right), in case of the BeamCalCut_{70}.

correlations. An example of such a global fit is presented in [163] or more recently in [164].

If we assume that all Higgs couplings are exactly as in the SM except for the coupling to muons, we can estimate the sensitivity on this coupling just from the branching ratio measurement presented here. If the coupling to muons differs from the SM expectation by a value δ_g, i.e. $g_\mu / g_{\mu,\,\text{SM}} = 1 + \delta_g$, the partial width can be written as $\Gamma_\mu / \Gamma_{\mu,\,\text{SM}} = \left(1 + \delta_g\right)^2$, using Eq. (2.26). The branching ratio is then given by

$$\text{BR}_{\text{h}\to\mu^+\mu^-} = \frac{\Gamma_\mu}{\Gamma} \tag{10.4}$$

$$= \frac{\Gamma_{\mu,\,\text{SM}} \left(1 + \delta_g\right)^2}{\Gamma_{\text{SM}} - \Gamma_{\mu,\,\text{SM}} + \Gamma_{\mu,\,\text{SM}} \left(1 + \delta_g\right)^2} \tag{10.5}$$

$$= \frac{\left(1 + \delta_g\right)^2}{\frac{1}{\text{BR}_{\mu,\,\text{SM}}} - 1 + \left(1 + \delta_g\right)^2}. \tag{10.6}$$

Since we assumed all other couplings to be as in the SM, the production cross section is also as in the SM and thus

$$\frac{\sigma_{\text{h}\nu_\text{e}\bar{\nu}_\text{e}} \times \text{BR}_{\text{h}\to\mu^+\mu^-}}{\left(\sigma_{\text{h}\nu_\text{e}\bar{\nu}_\text{e}} \times \text{BR}_{\text{h}\to\mu^+\mu^-}\right)_{\text{SM}}} = \frac{\text{BR}_{\text{h}\to\mu^+\mu^-}}{\text{BR}_{\text{h}\to\mu^+\mu^-,\,\text{SM}}}. \tag{10.7}$$

If δ_g is small, we can use Eq. (10.6) and expand it around 0

$$\frac{\text{BR}_{\text{h}\to\mu^+\mu^-}}{\text{BR}_{\text{h}\to\mu^+\mu^-,\,\text{SM}}} = 1 + 2(1 - \text{BR}_{\text{h}\to\mu^+\mu^-,\,\text{SM}})\delta_g + O(\delta_g^2) + \ldots \tag{10.8}$$

The measured relative uncertainty on the cross section times ratio thus translates to a sensitivity on the

coupling as

$$\frac{\delta(\sigma_{h\nu_e\bar{\nu}_e} \times BR_{h\to\mu^+\mu^-})}{\sigma_{h\nu_e\bar{\nu}_e} \times BR_{h\to\mu^+\mu^-}} = 2(1 - BR_{h\to\mu^+\mu^-,\,SM})\delta_g \approx 2\,\delta_g. \tag{10.9}$$

For example, the relative statistical uncertainty of 15.7% obtained in Section 10.6.4, translates to an uncertainty on g_μ of approximately 7.9%.

10.8 Measurement Potential at other Accelerators

10.8.1 Comparison with ILC Potential

The measurement of Higgs decays into muons at the ILC was studied in the SiD detector concept in [22]. In that study a center-of-mass energy of 250 GeV and an integrated luminosity of 250 fb^{-1} is assumed. Like in our study, a SM Higgs boson with a mass of 120 GeV is assumed. At that $\sqrt{s}$ the Higgsstrahlung process is the dominating Higgs production process. In the hadronic decay channel of the Z boson, $e^+e^- \to Zh \to q\bar{q}\mu^+\mu^-$, 7.7 signal events are left after the final event selection, resulting in a significance of only 1.1σ is achieved. The final state where the Z decays invisibly, $e^+e^- \to Zh \to \nu\bar{\nu}\mu^+\mu^-$, has an even lower number of signal events left after the event selection. Nevertheless, these 2.7 events correspond to a significance of 1.8σ, since the backgrounds can be removed very efficiently

A combination of these two analyses will improve the significance but ultimately more luminosity will be required. For example, in order to reach 5σ in the neutrino channel, 7.7 times more luminosity would be required, all collected at $\sqrt{s} = 250$ GeV. For higher center-of-mass energies the Higgs production cross section drops significantly until the W^+W^- fusion process becomes dominating. At around $\sqrt{s} =$ 250 GeV the Higgs production cross section would be comparable to that at the Zh threshold, but the impact of the backgrounds at that energy can not be easily estimated.

From this comparison one can see that a multi-TeV CLIC has two advantages over a low energy linear collider for measuring this rare decay. First, the Higgs production cross section is larger at high energies due to the $\sqrt{s}$ dependence. Secondly, CLIC has a higher total luminosity which can, at least in this channel, be fully exploited despite the long tail in the luminosity spectrum.

10.8.2 Comparison with LHC Potential

The main production process for a light SM Higgs boson at the LHC is the gluon fusion process shown in Fig. 10.24 (left). This process and the vector boson fusion process shown in Fig. 10.24 (right) might allow for the measurement of the Higgs branching ratio into muons at the LHC. The prospects of measuring the Higgs branching ratio into muons at the LHC using these channels has been investigated in several studies [165–167]. The different results are summarized below for a light SM Higgs boson with a mass of 120 GeV, assuming a center-of-mass energy of 14 TeV and an integrated luminosity of 300 fb^{-1} [2].

The measurement in the W and Z boson fusion channel has been studied in [165]. The significance of the signal is estimated to be around 1.8 σ per experiment, translating to an uncertainty on the cross section times branching ratio measurement of approximately 60%.

The Higgs production through the gluon fusion channel is investigated in [166]. The estimated significance for measuring the Higgs decay into two muons is 2.51σ per experiment. They also find a better significance compared to [165] of 2.37σ using the vector boson fusion channel. The combined

[2] Expected total integrated luminosity per experiment for the LHC without a possible luminosity upgrade.

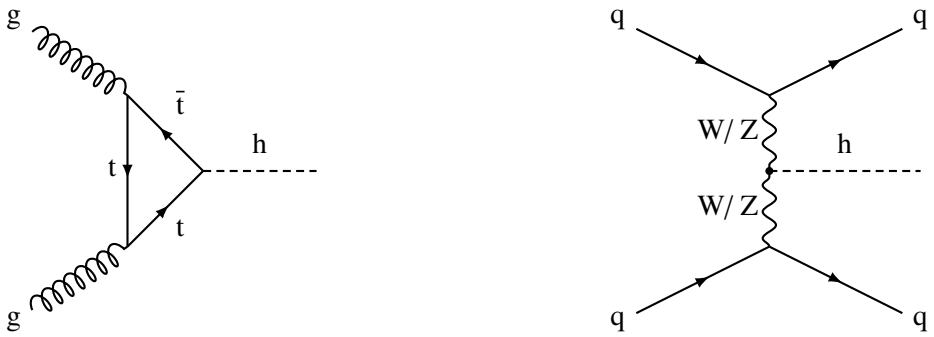

Figure 10.24: Feynman diagrams of the Higgs production processes at the LHC suitable for measuring Higgs decays into muons. Gluon fusion process (left) and vector boson fusion process (right).

significance using both channels is given as 3.45σ per experiment, which corresponds to an uncertainty on the cross section times branching ratio measurement of about 29%.

Ref. [167] presents a method of calculating the maximum significance of a measurement using all phase space information on generator level. This method is applied to the Higgs into muons branching ratio measurement using the vector boson fusion channel. A large improvement compared to the cut based analysis presented in [165] is achieved. The maximum significance for an integrated luminosity of 300 fb^{-1} is reported as 3.54σ per experiment. Any realistic analysis will necessarily result in a lower significance.

It should be noted that all LHC studies listed above are done on generator level. Gaussian smearing is applied to the di-muon mass distribution to model the detector resolution and additional kinematic cuts on the muons are introduced to model the detector acceptance. The impact of pile-up and minimum bias events is not taken into account.

10.9 Summary

It has been shown that the measurement of the cross section times branching ratio of a light Standard Model Higgs boson with a mass of 120 GeV decaying into two muons can be performed at CLIC with a center-of-mass energy of 3 TeV and total integrated luminosity of 2 ab^{-1} with a statistical uncertainty of about 23%[3]. Systematic uncertainties will be negligible compared to the statistical uncertainties. This result has been obtained using full detector simulation and taking into account all relevant Standard Model backgrounds.

The $\gamma\gamma \rightarrow$ hadrons background present at CLIC degrades the statistical uncertainty of the measurement to about 26%. This result was obtained overlaying realistic amounts of $\gamma\gamma \rightarrow$ hadrons events over the signal sample. The background samples were not overlayed with $\gamma\gamma \rightarrow$ hadrons background events, meaning that background rejection based on the visible energy in the event was underestimated and the estimated uncertainty on the branching ratio measurement is conservative.

A fast simulation study was performed to assess the required momentum resolution and it was found that a resolution of a few $10^{-5}\,\text{GeV}^{-1}$ is required, otherwise the result will degrade significantly. The results from fast simulation are consistent with the results from full simulation, where an average momentum resolution of $3.9 \times 10^{-5}\,\text{GeV}^{-1}$ is achieved for the selected signal events.

[3] The results reported in [168], scaled to the same integrated luminosity, quote a smaller error than is reported here, since the $e^+e^- \rightarrow \mu^+\mu^- e^+e^-$ background was neglected in that study.

The impact of forward electron tagging was studied by randomly rejecting $e^+e^- \to \mu^+\mu^-e^+e^-$ background events based on the true electron angles. Assuming an electron tagging efficiency of 95% in the LumiCal, the statistical uncertainty of the cross section times branching ratio measurement can be improved to about 15% or 15.7% when including the effect of the $\gamma\gamma \to$ hadrons background. If we assume that all other Higgs couplings are as predicted by the SM, this translates to an uncertainty on the coupling g_μ of approximately 7.5% or 7.9%, when including the degradation due to $\gamma\gamma \to$ hadrons.

CHAPTER 11

Conclusion and Outlook

The basic detector requirements of any experiment are derived from its physics goals. In addition, there are additional requirements that come from experimental conditions at the interaction region. In case of CLIC the short time between two bunch crossings, the amount of beam-related backgrounds originating from beamstrahlung, and the requirements of the placement and stability of the final focusing quadrupole have important consequences for the design of the detector as well as the choice of detector technologies. Based on the SiD concept we have developed a simulation model that takes into account the requirements specific to CLIC at a center-of-mass energy of 3 TeV as well as the performance goals required for the desired precision measurements.

We have shown in simulation studies that the performance of the proposed all-silicon tracking system is robust even in the presence of the $\gamma\gamma \rightarrow$ hadrons background. A transverse momentum resolution of $\sigma(p_T) = 1.9 \times 10^{-5}\, p_T/\text{GeV} \oplus 3.8 \times 10^{-3}/\sin\theta$ or better is achieved for polar angles $\theta > 30$. Although we assume a low material budget, it is still the limiting factor for the momentum resolution for track momenta of up to ~ 200 GeV. The track finding efficiency in high energetic jets is 95–98%, depending on the polar angle and the track momentum. The efficiency is lower in regions of very high local occupancies, e.g. in the center of a jet. Increasing the segmentation in the barrel strip detectors is expected to improve this. In addition, we have discussed the total occupancies in the tracking detectors from the incoherent pair background and the $\gamma\gamma \rightarrow$ hadrons background, and identified a possible problem with the occupancies in the innermost strip detectors. This originates from the long strip sizes and can be avoided by increasing the segmentation. Nevertheless, a time resolution of the order of 5 ns and multi-hit capabilities will be necessary to mitigate the effects of beam-related backgrounds. Dedicated R&D is necessary especially for fast low material pixel technologies for the vertex detectors, since no current technology fulfills all prerequisits for a CLIC detector.

Tungsten was chosen as the absorber material in the HCal barrel region to allow for sufficient shower containment for jet energies typical for a multi-TeV collider experiment. In this way, an HCal corresponding to approximately 7.5 λ_I can be accommodated within a free bore radius of the coil of 2.9 m. A simulation study using a Neural Network, taking several shower shape variables as input and which was trained for various calorimeter configurations, has been performed to identify the optimal configuration. In the mean time, two test beam campaigns with a tungsten HCal prototype using analog readout have been succesfully completed and preliminary results show promising results. Further test beams using other readout technologies will follow to validate the simulation results.

The current default for the SiD concept is to use a linear energy reconstruction. We have presented the

calibration method to obtain the correction factors used to reconstruct the energy. The energy resolution for single neutral particles was determined to be $\sigma(E)/E = 19.1\%/\sqrt{E/\mathrm{GeV}} \oplus 1.0\%$ in case of photons and $\sigma(E)/E = 50.3\%/\sqrt{E/\mathrm{GeV}} \oplus 6.5\%$ in case of K_L^0. The jet-energy resolution achievable with the current particle flow algorithm was studied in di-jet events and was found to be between $\sigma(E)/E = 5\%$ and $\sigma(E)/E = 3.5\%$, using RMS_{90}, for jet energies between 45 GeV and 1.5 GeV. The mean reconstructed jet energy is underestimated by approximately 5% which can be corrected by adjusting the jet energy scale. It is assumed that this systematic bias is due to confusion, but further studies are required.

Future simulation studies will have to be refined and made more realistic in order to arrive at an optimal detector concept for the next collider experiment. We have pointed out several issues that could be improved beyond those software tools that we have implemented for the studies presented here. For example the PandoraPFA algorithms will have to be specifically tuned for SiD-like detector geometries, and additional track finding algorithms to recover non-prompt tracks should be explored.

Finally, we have presented one of the benchmark analyses that have been selected for the CLIC CDR, the measurement of the decays of a 120 GeV SM Higgs boson into two muons. The study was performed in full simulation, taking into account all relevant SM background processes as well as the most important beam-related background from $\gamma\gamma \to$ hadrons processes. It was found that for an integrated luminosity of $2\,\mathrm{ab}^{-1}$ taken at CLIC with a center-of-mass energy of 3 TeV a statistical uncertainty of approximately 26% can be achieved. The sensitivity of the result on the momentum resolution has been determined in a fast simulation study and it was found that an average momentum resolution of $\sigma(p_\mathrm{T})/p_\mathrm{T}^2 < 5 \times 10^{-5}\,\mathrm{GeV}^{-1}$ is desirable. If the forward calorimeters are used to reject the dominant reducible SM background $\mathrm{e}^+\mathrm{e}^- \to \mu^+\mu^-\mathrm{e}^+\mathrm{e}^-$, the statistical uncertainty can be improved to approximately 15%. If all other branching ratios are assumed to be exactly as predicted by the SM, this corresponds to an uncertainty on the Higgs Yukawa coupling to muons of approximately 7.5%. This measurement would be significantly more accurate than what is achievable at the ILC or the LHC, at least without a possible high luminosity upgrade.

The results that the LHC will produce in the next years will answer the question if the Higgs mechanism can be the reason for the electroweak symmetry breaking in the SM. In addition, there might be hints for new physics beyond the SM. A linear $\mathrm{e}^+\mathrm{e}^-$ collider like CLIC will complement the measurements possible at the LHC and will probably be necessary to decide between different concurrent models. If discovered, the energy scale of the new physics will guide the decision for the scope of the next linear collider.

Appendix

APPENDIX A

Units, Conventions and Notations

A.1 Units

Throughout this thesis we use the *natural* units for the speed of light, c, and the reduced Planck constant, $\hbar = \frac{h}{2\pi}$ with

$$c \equiv 1 \text{ and } \hbar \equiv 1.$$

With the respective values in SI units, taken from [78],

$$\begin{aligned} c &= 299792458\,\mathrm{m/s}, \\ \hbar &= 1.054571628(53) \times 10^{-34}\,\mathrm{J \cdot s}, \\ 1\,\mathrm{GeV} &= 1.602176487(40) \times 10^{-10}\,\mathrm{J} \end{aligned}$$

we can translate the units of common dimensions:

$$\begin{aligned} 1\,\mathrm{GeV} &\equiv 1\,\mathrm{GeV}/c^2 \approx 1.783 \times 10^{-27}\,\mathrm{kg} \\ 1\,\mathrm{GeV} &\equiv 1\,\mathrm{GeV}/c \approx 5.344 \times 10^{-19}\,\mathrm{kg \cdot m/s} \\ 1\,\mathrm{GeV}^{-1} &\equiv 1\,\hbar \cdot c/\mathrm{GeV} = 1.973 \times 10^{-15}\,\mathrm{m} \\ 1\,\mathrm{GeV}^{-1} &\equiv 1\,\hbar/\mathrm{GeV} = 6.582 \times 10^{-25}\,\mathrm{s}. \end{aligned}$$

The cross section of particle interactions is usually expressed in barn

$$1\,\mathrm{fb} = 10^{-43}\,\mathrm{m}^2.$$

A.2 Conventions

For convenience we use $\oplus$ to denote quadratic addition, e.g. in case of uncorrelated errors

$$a^2 + b^2 = c^2 \qquad \Leftrightarrow \qquad a \oplus b = c.$$

The following conventions are only relevant to Chapter 2. Our metric is defined by the tensor

$$g_{\mu\nu} = g^{\mu\nu} = \begin{pmatrix} 1 & 0 & 0 & 0 \\ 0 & -1 & 0 & 0 \\ 0 & 0 & -1 & 0 \\ 0 & 0 & 0 & -1 \end{pmatrix}.$$

The Greek indices denote the four components t, x, y, z and are lowered or raised by multiplication with the metric tensor

$$x_\mu = g_{\mu\nu} x^\nu.$$

The Latin indices denote the three spatial components. The partial derivative ∂_μ is defined as

$$\partial_\mu = \frac{\partial}{\partial x^\mu}.$$

The three Pauli matrices σ^a are defined as

$$\sigma^1 = \begin{pmatrix} 0 & 1 \\ 1 & 0 \end{pmatrix}, \qquad \sigma^2 = \begin{pmatrix} 0 & -i \\ i & 0 \end{pmatrix}, \qquad \sigma^3 = \begin{pmatrix} 1 & 0 \\ 0 & -1 \end{pmatrix}.$$

We use the chiral representation of the Dirac matrices

$$\gamma^0 = \begin{pmatrix} 0 & 0 & 1 & 0 \\ 0 & 0 & 0 & 1 \\ 1 & 0 & 0 & 0 \\ 0 & 1 & 0 & 0 \end{pmatrix}, \quad \gamma^1 = \begin{pmatrix} 0 & 0 & 0 & 1 \\ 0 & 0 & 1 & 0 \\ 0 & -1 & 0 & 0 \\ -1 & 0 & 0 & 0 \end{pmatrix}, \quad \gamma^2 = \begin{pmatrix} 0 & 0 & 0 & -i \\ 0 & 0 & i & 0 \\ 0 & i & 0 & 0 \\ -i & 0 & 0 & 0 \end{pmatrix}, \quad \gamma^3 = \begin{pmatrix} 0 & 0 & 1 & 0 \\ 0 & 0 & 0 & -1 \\ -1 & 0 & 0 & 0 \\ 0 & 1 & 0 & 0 \end{pmatrix}.$$

In addition we use the Einstein notation, i.e. all terms with an index occurring twice implies a sum over the range of the index.

A.3 Detector Coordinate Systems

Throughout this thesis we are using Cartesian, cylindrical and spherical coordinate systems which are defined as follows.

Cartesian Coordinates

Right handed euclidean coordinate system defined by the orthogonal axes x, y and z. The detector axis is identical to z, x is in the horizontal plane and y is in the vertical plane pointing upwards. The Interaction Point in the center of the detector is located at the origin $(0, 0, 0)$.

Cylindrical Coordinates

Coordinate system defined by the detector axis z, the azimuthal angle ϕ and the distance from the detector axis r. The azimuthal angle ϕ is defined in the interval $[0, 2\pi] = [0°, 360°]$. The transformation

from Cartesian coordinates are

$$r = \sqrt{x^2 + y^2},$$
$$\phi = \tan^{-1} \frac{y}{x}.$$

The coordinate transformations to the Cartesian coordinates are

$$x = r \cos \phi,$$
$$y = r \sin \phi.$$

Spherical Coordinates

Coordinate system defined by the polar angle θ, the azimuthal angle ϕ and the distance from the origin R. The azimuthal angle is defined identical to the cylindrical case. The polar angle θ is defined in the interval $[0, \pi] = [0°, 180°]$.

$$R = \sqrt{x^2 + y^2 + z^2} = \sqrt{r^2 + z^2},$$
$$\theta = \arctan \frac{\sqrt{x^2 + y^2}}{z} = \arctan \frac{r}{z}.$$

Due to the symmetry of the detector it is often convenient to use a slightly different definition of the polar angle

$$\theta = \arctan \frac{\sqrt{x^2 + y^2}}{|z|} = \arctan \frac{r}{|z|}$$

in the interval $[0, \frac{\pi}{2}] = [0°, 90°]$. We mostly use the latter definition. It should be evident from the context which definition was used.

APPENDIX B

RMS and RMS_{90}

For a finite sample of N values $x_1, ..., x_N$, the arithmetic mean is defined as

$$\text{MEAN} = \overline{x} = \frac{1}{N}\sum_{i=0}^{N} x_i. \tag{B.1}$$

We define the RMS as

$$\text{RMS} = \sqrt{\frac{1}{N}\sum_{i=0}^{N} (x_i - \overline{x})^2}, \tag{B.2}$$

which is identical to the standard deviation of the sample and the square root of the variance. When estimating the mean and the RMS of a larger sample from a small sample, the expressions given in Equation B.1 and Equation B.2 are biased. An unbiased estimate of the standard deviation is instead given by replacing $1/N$ with $1/(N-1)$ in Equation B.2. This correction is negligible for sufficiently large samples, which is the case for all RMS values calculated in this thesis.

The mean and RMS are very sensitive to strong outliers. Especially for an otherwise narrow distribution with several strong outliers they can lead to a poor description of the majority of the distribution. When characterizing for example the resolution of a measurement, the distribution of the majority is of most interest. In these cases it is useful to restrict the sample to the interval which contains the majority of the values. A commonly used quantity is the RMS_{90} which is defined as the standard deviation of the values in the smallest interval that contains at least 90% of the values. The mean of this interval is denoted as $MEAN_{90}$.

One has to keep in mind that the RMS_{90} is systematically smaller than the RMS. The size of the difference of these two measures of the spread depends on the respective distribution. For a normal distribution the Gaussian width and the RMS are identical. The RMS_{90} is then approximately 79% of the RMS.

In addition, we use the interval defined by the RMS_{90} method as the fit range for Gaussian fits. This ensures useful fit results in cases of long non-Gaussian tails.

APPENDIX C

Track Parametrization

The tracks in LCIO are helices which are defined by 5 parameters [169]. This definition is based on the L3 convention [170]. For a uniform magnetic field, the axis of the helix is always parallel to the direction of the magnetic field. A solenoid field along z with $\vec{B} = (0, 0, B)$ is assumed. The parameters are defined with respect to an arbitrary reference point, which we define as the origin $P_{\text{ref}} = (0, 0, 0)$. The point of closest approach of the track projection in the xy plane to the reference point defines the starting point of the helix $P_0 = (x_0, y_0, z_0)$. The arc length along the curvature of the helix in the xy projection starting at P_0 is called S. The track projection into Sz is a straight line. Figure C.1 gives an illustration of the track parameters which are defined as follow.

- The distance of closest approach to the reference point in the xy plane, $d_0 = \sqrt{x_0 + y_0}$.
- The track curvature in the xy plane, κ, which is the inverse of the radius ρ of the track projection in the xy plane. The sign of κ gives the orientation of the helix.
- The track direction at P_0 in the xy plane, ϕ_0.
- The slope of the particle trajectory in the Sz projection, $\tan\lambda = \cot\theta$.
- The z coordinate of the point of closest approach to the reference point in the xy plane, z_0.

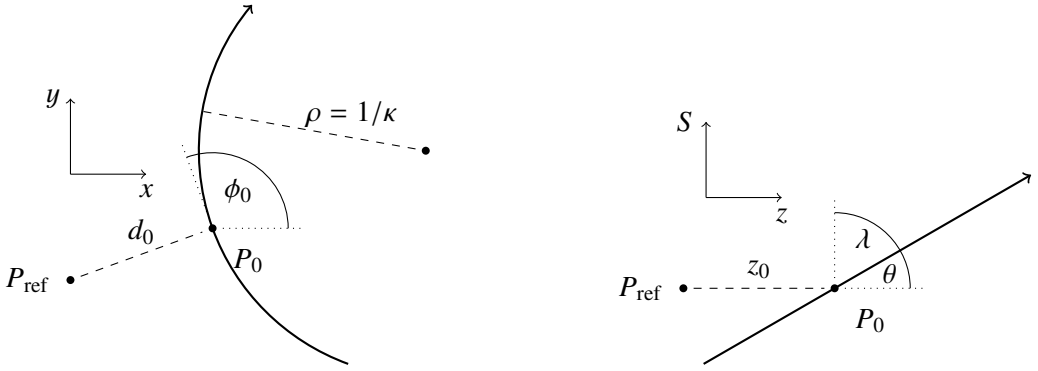

(a) xy plane (b) Sz plane

Figure C.1: Illustration of the track parameters as defined in LCIO.

C.1 Converting Track Parameters

Assuming a constant magnetic field along z with $\vec{B} = (0, 0, B)$ and a particle with a charge of $q = \pm e$, the track parameters can be translated into physical quantities using the following formulas

$$\begin{aligned} p_{\text{T}} &= \frac{k\,B}{|\kappa|} \\ p_x &= p_{\text{T}}\ \cos\phi_0, \\ p_y &= p_{\text{T}}\ \sin\phi_0, \\ p_z &= p_{\text{T}}\ \tan\lambda, \\ p &= \frac{p_{\text{T}}}{\cos\lambda} = p_{\text{T}}\sqrt{1+\tan^2\lambda}, \\ q &= \frac{\kappa}{|\kappa|}. \end{aligned} \tag{C.1}$$

The constant k is introduced to absorb the units and is defined as

$$k \approx 0.3\left[\frac{\text{GeV}}{\text{T m}}\right]. \tag{C.2}$$

C.2 Track Parameter Uncertainties

If we define a vector $\vec{x} = (d_0, \kappa, \phi_0, \tan\lambda, z_0)$ the corresponding uncertainties from the track fit are given by the symmetric covariance matrix

$$C = \begin{pmatrix} \sigma^2(d_0) & \sigma(d_0,\kappa) & \sigma(d_0,\phi_0) & \sigma(d_0,\tan\lambda) & \sigma(d_0,z_0) \\ \sigma(\kappa,d_0) & \sigma^2(\kappa) & \sigma(\kappa,\phi_0) & \sigma(\kappa,\tan\lambda) & \sigma(\kappa,z_0) \\ \sigma(\phi_0,d_0) & \sigma(\phi_0,\kappa) & \sigma^2(\phi_0) & \sigma(\phi_0,\tan\lambda) & \sigma(\phi_0,z_0) \\ \sigma(\tan\lambda,d_0) & \sigma(\tan\lambda,\kappa) & \sigma(\tan\lambda,\phi_0) & \sigma^2(\tan\lambda) & \sigma(\tan\lambda,z_0) \\ \sigma(z_0,d_0) & \sigma(z_0,\kappa) & \sigma(z_0,\phi_0) & \sigma(z_0,\tan\lambda) & \sigma^2(z_0) \end{pmatrix}. \tag{C.3}$$

The off-diagonal elements are the covariances which are defined as

$$\sigma(a,b) = \sigma(a)\sigma(b)\delta(a,b), \tag{C.4}$$

where $\delta(a,b)$ is the correlation coefficient which is defined in the interval $[-1,1]$. Estimations for the diagonal elements of the covariance matrix from detector resolutions are given in section 4.1. For a full derivation of all terms in the covariance matrix we refer to [72, 76, 171].

The track fitting that is explained in subsection 6.3.5 does an independent circle fit to obtain d_0, κ and ϕ_0 followed by a linear fit to obtain $\tan\lambda$ and z_0. The correlation coefficients between the parameters of the two fits are thus 0 and the covariance matrix is given by two independent sub-matrices of dimensions 3×3 and 2×2

$$C = \begin{pmatrix} \sigma^2(d_0) & \sigma(d_0,\kappa) & \sigma(d_0,\phi_0) & 0 & 0 \\ \sigma(\kappa,d_0) & \sigma^2(\kappa) & \sigma(\kappa,\phi_0) & 0 & 0 \\ \sigma(\phi_0,d_0) & \sigma(\phi_0,\kappa) & \sigma^2(\phi_0) & 0 & 0 \\ 0 & 0 & 0 & \sigma^2(\tan\lambda) & \sigma(\tan\lambda,z_0) \\ 0 & 0 & 0 & \sigma(z_0,\tan\lambda) & \sigma^2(z_0) \end{pmatrix}. \tag{C.5}$$

C.3 Propagation of Track Parameter Uncertainties

For a linear combinations of the track parameters

$$f(d_0,\kappa,\phi_0,\tan\lambda,z_0) = A\vec{x} \tag{C.6}$$

the uncertainty is given by

$$\sigma^2(f) = A\,C\,A^{\mathrm{T}}. \tag{C.7}$$

For a non-linear combination of variables, which is needed to calculate the uncertainties of the quantities described in Equation C.1, the function has to be expanded into a Taylor series. The first order approximation for the expansion around the vector $\vec{x}_0$ is then given by

$$f(d_0,\kappa,\phi_0,\tan\lambda,z_0) \approx f(\vec{x}_0) + J(\vec{x}-\vec{x}_0), \tag{C.8}$$

where J is the Jacobian matrix

$$J = \left(\frac{\partial f}{\partial d_0}, \frac{\partial f}{\partial \kappa}, \frac{\partial f}{\partial \phi_0}, \frac{\partial f}{\partial \tan\lambda}, \frac{\partial f}{\partial z_0}\right). \tag{C.9}$$

It should be noted that the first order approximation is only valid for small uncertainties. The term $f(\vec{x}_0)$ is constant and does not contribute to the uncertainty. The uncertainty for f is then given by

$$\sigma^2(f) \approx J\,C\,J^{\mathrm{T}}. \tag{C.10}$$

As an example, for an arbitrary function of two parameters, $f(a,b)$, the uncertainty is given by

$$\sigma^2(f) \approx \left(\frac{\partial f(a,b)}{\partial a}\right)^2 \sigma^2(a) + \left(\frac{\partial f(a,b)}{\partial b}\right)^2 \sigma^2(b) + 2\frac{\partial f(a,b)}{\partial a}\frac{\partial f(a,b)}{\partial b}\sigma(a,b). \tag{C.11}$$

Using Equation C.11 we can now estimate the uncertainties of the quantities given in Equation C.1:

$$\sigma^2(p_\mathrm{T}) \approx \left(\frac{k\,B}{\kappa^2}\right)^2 \sigma^2(\kappa) \tag{C.12}$$

$$\sigma^2(p_x) \approx \left(\frac{k\,B}{\kappa^2}\right)^2 \left(\left(\frac{\cos\phi_0}{\kappa}\right)^2 \sigma^2(\kappa) + \sin^2\phi_0 \sigma^2(\phi_0) + \frac{2\,\sin\phi_0\,\cos\phi_0}{\kappa}\sigma(\kappa,\phi_0)\right) \tag{C.13}$$

$$\sigma^2(p_y) \approx \left(\frac{k\,B}{\kappa^2}\right)^2 \left(\left(\frac{\sin\phi_0}{\kappa}\right)^2 \sigma^2(\kappa) + \cos^2\phi_0 \sigma^2(\phi_0) + \frac{2\,\sin\phi_0\,\cos\phi_0}{\kappa}\sigma(\kappa,\phi_0)\right) \tag{C.14}$$

$$\sigma^2(p_z) \approx \left(\frac{k\,B}{\kappa^2}\right)^2 \left(\left(\frac{\tan\lambda}{\kappa}\right)^2 \sigma^2(\kappa) + \sigma^2(\tan\lambda) + \frac{2\,\tan\lambda}{\kappa}\sigma(\kappa,\tan\lambda)\right) \tag{C.15}$$

$$\sigma^2(p) \approx \left(\frac{k\,B}{\kappa^2}\right)^2 \left(\frac{1+\tan^2\lambda}{\kappa^2}\sigma^2(\kappa) + \frac{\tan^2\lambda}{1+\tan\lambda}\sigma^2(\tan\lambda) + \frac{2\,\tan\lambda}{\kappa\,\sqrt{1+\tan^2\lambda}}\sigma(\kappa,\tan\lambda)\right) \tag{C.16}$$

APPENDIX D

Tracking Efficiency in Top Pair Production

Here we want to briefly discuss the tracking efficiencies and fake rates observed in simulations of $e^+e^- \to t\bar{t}$ at $\sqrt{s} = 3\,\text{TeV}$ and compare them to the results found for the di-jet events discussed in Chapter 7. 10000 simulated events with and without background are used for the study.

The highest tracking efficiency of 98% is achieved for tracks of intermediate momentum below 100 GeV which is very similar to what is achieved in di-jet events. The dependency towards higher transverse momenta is very different though, as shown in Fig. D.1. The drop in efficiency is less sharp for momenta below 100 GeV but becomes stronger than in the case of the di-jet events for higher energies dropping as low as only 50% for transverse momenta of 500–1000 GeV. This is due to the different average particle moment in the $t\bar{t}$ events which contain more lower energetic tracks. The angular dependence of the tracking efficiency is very similar between the two topologies.

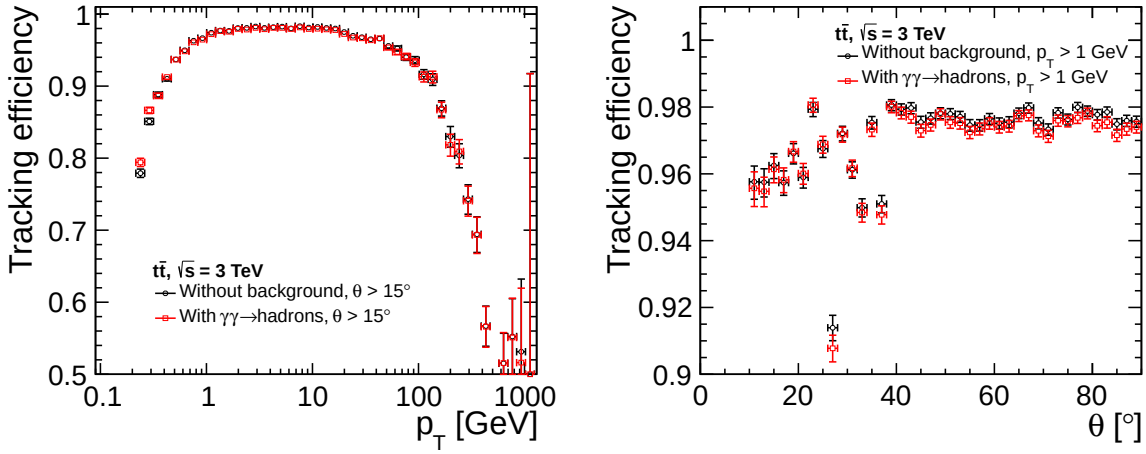
Tracking efficiency
tt̄, √s = 3 TeV
Without background, θ > 15°
With γγ→hadrons, θ > 15°
p_T [GeV]
tt̄, √s = 3 TeV
Without background, p_T > 1 GeV
With γγ→hadrons, p_T > 1 GeV
θ [°]

Figure D.1: Tracking efficiency depending on the transverse momentum p_T (left) and the polar angle θ (right) in $t\bar{t}$ events at a center-of-mass energy of 3 TeV with and without $\gamma\gamma \to$ hadrons background.

The results for the fake rate are also very similar, as shown in Fig. D.2. The only difference between di-jet and $t\bar{t}$ events is for tracks of medium transverse momentum. At these momenta the fake rates in $t\bar{t}$ are slightly lower. In general, like in case of the di-jet events, the impact of the $\gamma\gamma \to$ hadrons background is negligible except for lowest track momenta.

This comparison shows that there is no strong dependency of the results presented in Chapter 7 on the event topology.

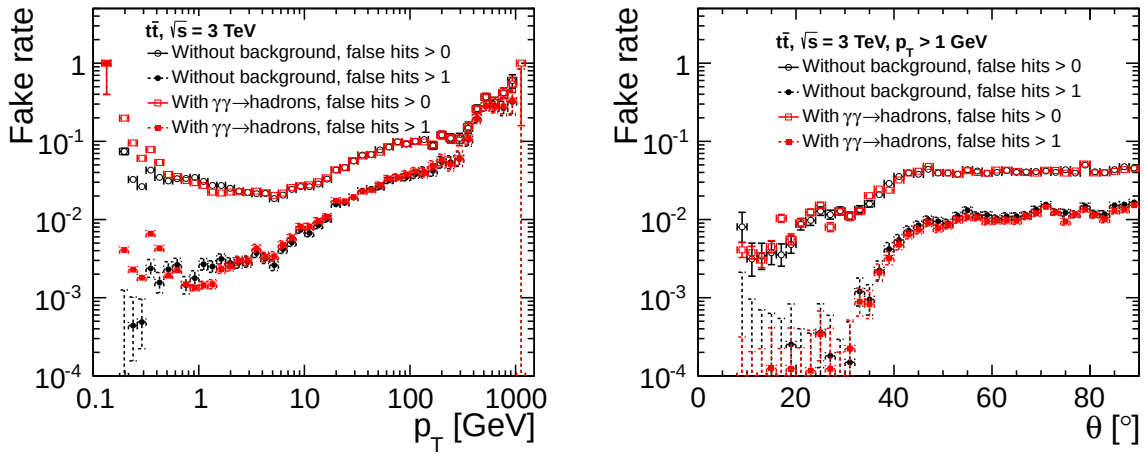
Fake rate
$t\bar{t}$, $\sqrt{s}$ = 3 TeV
Without background, false hits > 0
Without background, false hits > 1
With γγ→hadrons, false hits > 0
With γγ→hadrons, false hits > 1
p_T [GeV]
$t\bar{t}$, $\sqrt{s}$ = 3 TeV, p_T > 1 GeV
θ [°]

Figure D.2: Fake rate depending on the transverse momentum p_T (left) and the polar angle θ (right) in $t\bar{t}$ events at a center-of-mass energy of 3 TeV with and without $\gamma\gamma \rightarrow$ hadrons background.

List of Acronyms

ADC	Analog to Digital Converter
ALEPH	Experiment at LEP
ALICE	Experiment at the LHC
ASIC	Application-Specific Integrated Circuit
ATLAS	Experiment at the LHC
BeamCal	Beam Calorimeter
BDS	Beam Delivery System
BDT	Boosted Decision Tree - a multi variate classifier
BSM	Beyond the Standard Model
BX	Bunch Crossing
CDR	Conceptual Design Report
CERN	European Organization for Nuclear Research, Geneva, Switzerland
CHIPS	Chiral Invariant Phase Space model
CKM	Cabibbo-Kobayashi-Maskawa- name of the quark mixing matrix in the SM in flavor changing electroweak interactions
CLIC	Compact Linear Collider
CMS	Compact Muon Solenoid
CTF3	CLIC test facility 3
DELPHI	Experiment at LEP
DESY	Deutsches Elektronen Synchrotron, Hamburg, Germany
ECal	Electromagnetic Calorimeter
GPS	General Particle Source
H1	experiment at HERA

HERA Hadron Elektron Ring Anlage - lepton-proton collider at DESY

HCal Hadronic Calorimeter

HEP High Energy Physics

ILC International Linear Collider - concept for a future e^+e^- linear collider

ILD International Large Detector - concept for an experiment at the ILC or CLIC

IP Interaction Point

L3 Experiment at LEP

LCIO Linear Collider Input/Output

LEP Large Electron-Positron Collider

LHC Large Hadron Collider - proton-proton collider at CERN

LHCb LHC beauty

LINAC Linear Accelerator

LumiCal Luminosity Calorimeter

LSP lightest supersymmetric particle

MIP Minimum Ionizing Particle

MPGD Micro-Pattern Gas Detectors

MSSM Minimal Supersymmetric Standard Model

NN Neural Network

OPAL Experiment at LEP

PDF Probability Density Function

PETS Power Extraction and Transfer System

PFA Particle Flow Algorithm

PFO Particle Flow Object

PS Proton Synchrotron - accelerator at CERN

QCD Quantum Chromodynamics

QD0 final focusing quadrupole

QED Quantum Electrodynamics

QFT Quantum Field Theory

RF Radio Frequency

RMS Root Mean Square

RPC Resistive Plate Chamber

SiD Silicon Detector - concept for an experiment at the ILC or CLIC

SiPM Silicon Photomultiplier

SLAC National Accelerator Laboratory, Stanford, USA

SLC Stanford Linear Collider - e^+e^- collider at SLAC

SLD SLAC Large Detector - experiment at the SLC

SLIC Simulator for the Linear Collider

SM Standard Model

SPS Super Proton Synchrotron - accelerator at CERN

SUSY Supersymmetry

SUGRA Supergravity

TESLA Concept for a future e^+e^- linear collider

Tevatron Proton-antiproton collider at FermiLab

TMVA Toolkit for Multivariate Data Analysis

UA1 Experiment at the SPS

UA2 Experiment at the SPS

XML Extensible Markup Language

Bibliography

[1] S. Glashow, "Partial Symmetries of Weak Interactions", *Nucl.Phys.* 22 (1961) pp. 579–588, DOI: 10.1016/0029-5582(61)90469-2.

[2] S. Weinberg, "A Model of Leptons", *Phys.Rev.Lett.* 19 (1967) pp. 1264–1266, DOI: 10.1103/PhysRevLett.19.1264.

[3] A. Salam, "Weak and Electromagnetic Interactions", *Proceedings of the Eighth Nobel Symposium*, ed. by N. Svartholm, Lerum, Sweden, 1968 pp. 367–377.

[4] F. Englert and R. Brout, "Broken Symmetry and the Mass of Gauge Vector Mesons", *Phys.Rev.Lett.* 13 (1964) pp. 321–323, DOI: 10.1103/PhysRevLett.13.321.

[5] P. W. Higgs, "Broken Symmetries and the Masses of Gauge Bosons", *Phys.Rev.Lett.* 13 (1964) pp. 508–509, DOI: 10.1103/PhysRevLett.13.508.

[6] G. Guralnik, C. Hagen, and T. Kibble, "Global Conservation Laws and Massless Particles", *Phys.Rev.Lett.* 13 (1964) pp. 585–587, DOI: 10.1103/PhysRevLett.13.585.

[7] D. Gross and F. Wilczek, "Ultraviolet Behavior of Nonabelian Gauge Theories", *Phys.Rev.Lett.* 30 (1973) pp. 1343–1346, DOI: 10.1103/PhysRevLett.30.1343.

[8] H. D. Politzer, "Reliable Perturbative Results for Strong Interactions?", *Phys.Rev.Lett.* 30 (1973) pp. 1346–1349, DOI: 10.1103/PhysRevLett.30.1346.

[9] H. Fritzsch, M. Gell-Mann, and H. Leutwyler, "Advantages of the Color Octet Gluon Picture", *Phys.Lett.* B47 (1973) pp. 365–368, DOI: 10.1016/0370-2693(73)90625-4.

[10] H. Fritzsch and M. Gell-Mann, "Current algebra: Quarks and what else?", *16th International Conference on High-energy Physics*, Chicago, IL, 1972 pp. 135–165, arXiv:hep-ph/0208010 [hep-ph].

[11] J. D. Lykken, "Beyond the Standard Model", *2009 European School of High-energy Physics*, CERN-2010-002, Geneva, 2010 pp. 101–109, arXiv:1005.1676 [hep-ph].

[12] M. Trodden and S. M. Carroll, "Introduction to cosmology", *TASI Lectures 2002/2003*, Boulder, CO, 2004 pp. 703–793, arXiv:astro-ph/0401547 [astro-ph].

[13] A. A. Penzias and R. W. Wilson, "A Measurement of excess antenna temperature at 4080 Mc/s", *Astrophys. J.* 142 (1965) pp. 419–421, DOI: 10.1086/148307.

[14] E. Komatsu et al., "Five-Year Wilkinson Microwave Anisotropy Probe (WMAP) Observations: Cosmological Interpretation", *Astrophys.J.Suppl.* 180 (2009) pp. 330–376, DOI: 10.1088/0067-0049/180/2/330, arXiv:0803.0547 [astro-ph].

[15] R. Alpher, H. Bethe, and G. Gamow, "The origin of chemical elements", *Phys.Rev.* 73 (1948) pp. 803–804, DOI: 10.1103/PhysRev.73.803.

[16] G. Steigman, "Primordial nucleosynthesis: successes and challenges", *Int.J.Mod.Phys.* E15 (2006) pp. 1–36, DOI: 10.1142/S0218301306004028, arXiv:astro-ph/0511534 [astro-ph].

[17] G. Bertone, D. Hooper, and J. Silk, "Particle dark matter: Evidence, candidates and constraints", *Phys.Rept.* 405 (2005) pp. 279–390, DOI: 10.1016/j.physrep.2004.08.031, arXiv:hep-ph/0404175 [hep-ph].

[18] J. Brau et al., eds., *International Linear Collider reference design report: ILC Global Design Effort and World Wide Study*, 1: Executive summary. 2: Physics at the ILC. 3: Accelerator. 4: Detectors vols., ILC-REPORT-2007-001, Geneva, 2007.

[19] R. Corsini, "An Overview of the new CLIC test facility (CTF3)", *19th IEEE Particle Accelerator Conference*, Chicago, IL, 2001 pp. 412–414.

[20] H. Schmickler et al., eds., *CLIC Conceptual Design Report: The CLIC accelerator and site facilities*, to appear, Geneva, 2012.

[21] T. Abe et al., eds., *The International Large Detector: Letter of Intent*, FERMILAB-LOI-2010-03, 2010, arXiv:1006.3396 [hep-ex].

[22] H. Aihara et al., eds., *SiD Letter of Intent*, FERMILAB-LOI-2009-01, 2009, arXiv:0911.0006 [physics.ins-det].

[23] L. Linssen et al., eds., *CLIC Conceptual Design Report: Physics and Detectors at CLIC*, CERN-2012-003, Geneva, 2012, arXiv:1202.5940 [physics.ins-det].

[24] M. A. Thomson et al., "The physics benchmark processes for the detector performance studies of the CLIC CDR", LCD-Note 2011-026, CERN, 2011.

[25] C. Grefe and A. Münnich, "The CLIC_SiD_CDR Geometry for the CDR Monte Carlo Mass Production", LCD-Note 2011-009, CERN, 2011.

[26] C. Grefe, "OverlayDriver: An event mixing tool for org.lcsim", LCD-Note 2011-032, CERN, 2011.

[27] P. Speckmayer and C. Grefe, "Comparison of Performance of Hadronic Tungsten and Steel Sampling Calorimeters", LCD-Note 2010-001, CERN, 2010.

[28] C. Grefe, "Light Higgs decay into muons in the CLIC_SiD_CDR detector", LCD-Note 2011-035, CERN, 2011.

[29] C. Grefe et al., "Measurement of the Cross Section Times Branching Ratio of Light Higgs Decays at CLIC" (2012), arXiv:1202.5647 [hep-ex].

[30] D. J. Griffiths, *Introduction to elementary particles*, 2nd ed., New York, NY: Wiley, 2008.

[31] M. E. Peskin and D. V. Schroeder, *An Introduction to Quantum Field Theory*, Boulder, CO: Westview, 1995.

[32] W. Hollik, "Quantum field theory and the Standard Model", *2009 European School of High-energy Physics*, CERN-2010-002, Geneva, 2010 pp. 1–44, arXiv:1012.3883 [hep-ph].

[33] ALEPH Collaboration et al., "Precision electroweak measurements on the Z resonance", *Phys.Rept.* 427 (2006) pp. 257–454, DOI: 10.1016/j.physrep.2005.12.006, arXiv:hep-ex/0509008 [hep-ex].

[34] N. Cabibbo, "Unitary Symmetry and Leptonic Decays", *Phys.Rev.Lett.* 10 (1963) pp. 531–533, DOI: 10.1103/PhysRevLett.10.531.

[35] M. Kobayashi and T. Maskawa, "CP Violation in the Renormalizable Theory of Weak Interaction", *Prog.Theor.Phys.* 49 (1973) pp. 652–657, DOI: 10.1143/PTP.49.652.

[36] W Kilian, M Kramer, and P. Zerwas, "Higgsstrahlung and W W fusion in e+ e- collisions", *Phys.Lett.* B373 (1996) pp. 135–140, DOI: 10.1016/0370-2693(96)00100-1, arXiv:hep-ph/9512355 [hep-ph].

[37] B. A. Kniehl, "Radiative corrections for associated ZH production at future e^+e^- colliders", *Z.Phys.* C55 (1992), Revised version pp. 605–618, DOI: 10.1007/BF01561297.

[38] A. Denner et al., "Electroweak radiative corrections to $e^+e^- \to \nu\bar{\nu}H$", *Nucl.Phys.* B660 (2003) pp. 289–321, DOI: 10.1016/S0550-3213(03)00269-4, arXiv:hep-ph/0302198 [hep-ph].

[39] A. Djouadi, J. Kalinowski, and P. Zerwas, "Higgs radiation off top quarks in high-energy e+ e- colliders", *Z.Phys.* C54 (1992) pp. 255–262, DOI: 10.1007/BF01566654.

[40] W. Kilian, T. Ohl, and J. Reuter, "WHIZARD: Simulating Multi-Particle Processes at LHC and ILC", *Eur.Phys.J.* C71 (2011) p. 1742, DOI: 10.1140/epjc/s10052-011-1742-y, arXiv:0708.4233 [hep-ph].

[41] A. Djouadi, "The Anatomy of electro-weak symmetry breaking. I: The Higgs boson in the standard model", *Phys.Rept.* 457 (2008) pp. 1–216, DOI: 10.1016/j.physrep.2007.10.004, arXiv:hep-ph/0503172 [hep-ph].

[42] A. Denner et al., "Standard Model Higgs-Boson Branching Ratios with Uncertainties", *Eur.Phys.J.* C71 (2011) p. 1753, DOI: 10.1140/epjc/s10052-011-1753-8, arXiv:1107.5909 [hep-ph].

[43] S. Dittmaier et al., eds., *Handbook of LHC Higgs Cross Sections: 1. Inclusive Observables*, CERN-2011-002, Geneva, 2011, arXiv:1101.0593 [hep-ph].

[44] H. Li, R. Poschl, and F. Richard, "HZ Recoil Mass and Cross Section Analysis in ILD" (2012), arXiv:1202.1439 [hep-ex].

[45] ALEPH Collaboration et al., "Precision Electroweak Measurements and Constraints on the Standard Model" (2010), 18 pages, arXiv:1012.2367 [hep-ex].

[46] M. Baak et al.,
"Updated Status of the Global Electroweak Fit and Constraints on New Physics" (2011), arXiv:1107.0975 [hep-ph].

[47] CMS Collaboration, "Searches for the SM Scalar Boson at CMS",
Proceedings of the 47th Rencontres de Moriond, to appear, La Thuile, Italy, 2012.

[48] ATLAS Collaboration, "SM Scalar Boson search with the ATLAS detector",
Proceedings of the 47th Rencontres de Moriond, to appear, La Thuile, Italy, 2012.

[49] V. Rubin, N. Thonnard, and J. Ford W.K., "Rotational properties of 21 SC galaxies with a large range of luminosities and radii, from NGC 4605 /R = 4kpc/ to UGC 2885 /R = 122 kpc/",
Astrophys.J. 238 (1980) p. 471, DOI: 10.1086/158003.

[50] X.-P. Wu et al.,
"A comparison of different cluster mass estimates: consistency or discrepancy ?" (1998), arXiv:astro-ph/9808179 [astro-ph].

[51] D. Clowe et al., "A direct empirical proof of the existence of dark matter",
Astrophys.J. 648 (2006) pp. L109–L113, DOI: 10.1086/508162,
arXiv:astro-ph/0608407 [astro-ph].

[52] V. Springel et al.,
"Simulating the joint evolution of quasars, galaxies and their large-scale distribution",
Nature 435 (2005) pp. 629–636, DOI: 10.1038/nature03597,
arXiv:astro-ph/0504097 [astro-ph].

[53] Y. Fukuda et al.,
"Measurements of the solar neutrino flux from Super-Kamiokande's first 300 days",
Phys.Rev.Lett. 81 (1998) pp. 1158–1162,
DOI: 10.1103/PhysRevLett.81.1158,10.1103/PhysRevLett.81.1158,
arXiv:hep-ex/9805021 [hep-ex].

[54] Q. Ahmad et al., "Measurement of the rate of $\nu_e + d \rightarrow p + p + e^-$ interactions produced by B-8 solar neutrinos at the Sudbury Neutrino Observatory", *Phys.Rev.Lett.* 87 (2001) p. 071301, DOI: 10.1103/PhysRevLett.87.071301, arXiv:nucl-ex/0106015 [nucl-ex].

[55] S. P. Martin, "A Supersymmetry primer" (1997), arXiv:hep-ph/9709356 [hep-ph].

[56] G. Jungman, M. Kamionkowski, and K. Griest, "Supersymmetric dark matter",
Phys.Rept. 267 (1996) pp. 195–373, DOI: 10.1016/0370-1573(95)00058-5,
arXiv:hep-ph/9506380 [hep-ph].

[57] D. Z. Freedman, P. van Nieuwenhuizen, and S. Ferrara,
"Progress Toward a Theory of Supergravity", *Phys.Rev.* D13 (1976) pp. 3214–3218,
DOI: 10.1103/PhysRevD.13.3214.

[58] S. Deser and B. Zumino, "Consistent Supergravity", *Phys.Lett.* B62 (1976) p. 335,
DOI: 10.1016/0370-2693(76)90089-7.

[59] J. F. Gunion et al., *The Higgs hunter's guide*, Upton, NY: Brookhaven Nat. Lab., 1989.

[60] A. Djouadi, "The Anatomy of electro-weak symmetry breaking. II. The Higgs bosons in the minimal supersymmetric model", *Phys.Rept.* 459 (2008) pp. 1–241,
DOI: 10.1016/j.physrep.2007.10.005, arXiv:hep-ph/0503173 [hep-ph].

[61] G. Arnison et al., "Experimental Observation of Lepton Pairs of Invariant Mass Around 95 GeV/c^2 at the CERN SPS Collider", *Phys.Lett.* B126 (1983) pp. 398–410, DOI: 10.1016/0370-2693(83)90188-0.

[62] G. Arnison et al., "Experimental Observation of Isolated Large Transverse Energy Electrons with Associated Missing Energy at $\sqrt{s}$ = 540 GeV", *Phys.Lett.* B122 (1983) pp. 103–116.

[63] M. Banner et al., "Observation of Single Isolated Electrons of High Transverse Momentum in Events with Missing Transverse Energy at the CERN anti-p p Collider", *Phys.Lett.* B122 (1983) pp. 476–485, DOI: 10.1016/0370-2693(83)91605-2.

[64] P. Bagnaia et al., "Evidence for $Z^0 \to e^+e^-$ at the CERN anti-p p Collider", *Phys.Lett.* B129 (1983) pp. 130–140, DOI: 10.1016/0370-2693(83)90744-X.

[65] D. Schulte, "Study of Electromagnetic and Hadronic Background in the Interaction Region of the TESLA Collider", PhD thesis, Universität Hamburg, 1997.

[66] P. Chen, "Beamstrahlung and the QED, QCD backgrounds in linear colliders", *9th International Workshop on Photon-photon Collisions*, La Jolla, CA, 1992 pp. 418–429.

[67] P. Chen, T. L. Barklow, and M. E. Peskin, "Hadron production in gamma gamma collisions as a background for e+ e- linear colliders", *Phys.Rev.* D49 (1994) pp. 3209–3227, DOI: 10.1103/PhysRevD.49.3209, arXiv:hep-ph/9305247 [hep-ph].

[68] D. Schulte, "Beam-beam simulations with GUINEA-PIG", *5th International Computational Accelerator Physics Conference*, Monterey, CA, 1999 pp. 127–131.

[69] D. Schulte and F. Zimmermann, "The Crossing angle in CLIC", *19th IEEE Particle Accelerator Conference*, Chicago, IL, 2001 pp. 148–150.

[70] S. Stapnes et al., eds., *CLIC Conceptual Design Report: CLIC study summary*, to appear, Geneva, 2012.

[71] R. Gluckstern, "Uncertainties in track momentum and direction, due to multiple scattering and measurement errors", *Nucl.Instrum.Meth.* 24 (1963) pp. 381–389, DOI: 10.1016/0029-554X(63)90347-1.

[72] V. Karimaki, "Explicit covariance matrix for particle measurement precision", *Nucl.Instrum.Meth.* A410 (1998) pp. 284–292, DOI: 10.1016/S0168-9002(98)00279-4.

[73] G. Moliere, "Theory of the scattering of fast charged particles. 2. Repeated and multiple scattering", *Z.Naturforsch.* A3 (1948) pp. 78–97.

[74] V. L. Highland, "Some Practical Remarks on Multiple Scattering", *Nucl.Instrum.Meth.* 129 (1975) p. 497, DOI: 10.1016/0029-554X(75)90743-0.

[75] G. R. Lynch and O. I. Dahl, "Approximations to multiple Coulomb scattering", *Nucl.Instrum.Meth.* B58 (1991), Revised version pp. 6–10, DOI: 10.1016/0168-583X(91)95671-Y.

[76] M. Valentan, M. Regler, and R. Fruhwirth, "Generalization of the Gluckstern formulas II: Multiple scattering and non-zero dip angles", *Nucl.Instrum.Meth.* A606 (2009) pp. 728–742, DOI: 10.1016/j.nima.2009.05.024.

[77] R. Wigmans, *Calorimetry: Energy Measurement in Particle Physics*, International series of monographs on physics, Oxford: Clarendon Press, 2000.

[78] K. Nakamura, et al., eds., "Review of particle physics", *J.Phys.G* G37 (2010), DOI: 10.1088/0954-3899/37/7A/075021.

[79] L. Landau, "On the energy loss of fast particles by ionization", *J.Phys.(USSR)* 8 (1944) pp. 201–205.

[80] T. Behnke et al., eds., *TESLA: The superconducting electron positron linear collider with an integrated X-ray laser laboratory. Technical design report. Pt. 4: A detector for TESLA*, DESY-01-011, 2001.

[81] I. Laktineh, "Semi-digital hadronic calorimeter for future high energy physics experiments", *J.Phys.Conf.Ser.* 160 (2009) p. 012030, DOI: 10.1088/1742-6596/160/1/012030.

[82] J. Aguilar-Saavedra et al., eds., *TESLA: The Superconducting electron positron linear collider with an integrated X-ray laser laboratory. Technical design report. Pt. 3: Physics at an* e^+e^- *linear collider*, DESY-01-011, 2001, arXiv:hep-ph/0106315 [hep-ph].

[83] T. Barklow, A. Münnich, and P. Roloff, "Measurement of chargino and neutralino pair production at CLIC", LCD-Note 2011-037, CERN, 2011.

[84] T. Laštovička, "Light Higgs Production and Decays to Pairs of Bottom and Charm Quarks at 3 TeV", LCD-Note 2011-036, CERN, 2011.

[85] M. Thomson, "Particle Flow Calorimetry and the PandoraPFA Algorithm", *Nucl.Instrum.Meth.* A611 (2009) pp. 25–40, DOI: 10.1016/j.nima.2009.09.009, arXiv:0907.3577 [physics.ins-det].

[86] N. Akchurin et al., "Electron detection with a dual-readout calorimeter", *Nucl.Instrum.Meth.* A536 (2005) pp. 29–51, DOI: 10.1016/j.nima.2004.06.178.

[87] N. Akchurin et al., "Hadron and jet detection with a dual-readout calorimeter", *Nucl.Instrum.Meth.* A537 (2005) pp. 537–561, DOI: 10.1016/j.nima.2004.07.285.

[88] J.-C. Brient and H. Videau, "The calorimetry at the future e+ e- linear collider", *Summer Study on the Future of Particle Physics*, Snowmass, CO, 2001, arXiv:hep-ex/0202004.

[89] V. Morgunov, "Energy flow method for multi - jet effective mass reconstruction in the highly granulated TESLA calorimeter", *Summer Study on the Future of Particle Physics*, Snowmass, CO, 2001.

[90] D. Buskulic et al., "Performance of the ALEPH detector at LEP", *Nucl.Instrum.Meth.* A360 (1995) pp. 481–506, DOI: 10.1016/0168-9002(95)00138-7.

[91] I. Knowles and G. Lafferty, "Hadronization in Z^0 decay", *J.Phys.G* G23 (1997) pp. 731–789, DOI: 10.1088/0954-3899/23/7/003, arXiv:hep-ph/9705217 [hep-ph].

[92] CALICE Collaboration, "Tests of a particle flow algorithm with CALICE test beam data", *JINST* 6 (2011) P07005, DOI: 10.1088/1748-0221/6/07/P07005, arXiv:1105.3417 [physics.ins-det].

[93] F. Beaudette, "Performance of the particle flow algorithm in CMS", *PoS* ICHEP2010 (2010).

[94] K. Elsener et al., "CLIC detector concepts as described in the CDR: Differences between GEANT4 and engineering models", LCD-Note 2011-011, CERN, 2011.

[95] D. Dannheim and M. Vos,
"Simulation studies for the layout of the vertex and tracking regions of the CLIC detectors", LCD-Note 2011-031, CERN, 2011.

[96] X Llopart et al., "Timepix, a 65k programmable pixel readout chip for arrival time, energy and/or photon counting measurements",
Nucl. Instrum. Methods Phys. Res., A 581.1-2 (2008) 485–494. 10 p.

[97] R. Turchetta et al., "A monolithic active pixel sensor for charged particle tracking and imaging using standard VLSI CMOS technology", *Nucl.Instrum.Meth.* A458 (2001) pp. 677–689, DOI: 10.1016/S0168-9002(00)00893-7.

[98] C. Baltay et al., "Chronopixel Vertex Detectors for Future Linear Colliders" (2011), arXiv:1109.2811 [physics.ins-det].

[99] H. Ikeda et al., "Deep sub-micron FD-SOI for front-end application",
Nucl.Instrum.Meth. A579 (2007) pp. 701–705, DOI: 10.1016/j.nima.2007.05.280.

[100] S. I. Parker, C. J. Kenney, and J. Segal,
"3-D: A New architecture for solid state radiation detectors",
Nucl.Instrum.Meth. A395 (1997) pp. 328–343, DOI: 10.1016/S0168-9002(97)00694-3.

[101] D. Freytag et al., "KPiX, An Array of Self Triggered Charge Sensitive Cells Generating Digital Time and Amplitude Information", SLAC-PUB-13462, 2008.

[102] CALICE collaboration et al.,
"Construction and Commissioning of the CALICE Analog Hadron Calorimeter Prototype",
JINST 5 (2010) P05004, DOI: 10.1088/1748-0221/5/05/P05004,
arXiv:1003.2662 [physics.ins-det].

[103] B. Bilki et al., "Tests of a Digital Hadron Calorimeter", *J.Phys.Conf.Ser.* 293 (2011) p. 012075, arXiv:1005.0409 [physics.ins-det].

[104] J. Yu, "Development of GEM Based Digital Hadron Calorimeter",
International Linear Collider Workshop, Hamburg, Germany pp. 567–572.

[105] C. Adloff et al., "Development of MicroMegas for a Digital Hadronic Calorimeter" (2009), arXiv:0901.4927 [physics.ins-det].

[106] G. Acquistapace et al., "CMS, the magnet project: Technical design report",
CERN-LHCC-97-10, 1997.

[107] A Gaddi,
"Considerations about an improved superconducting cable for Linear Collider Detectors", LCD-Note 2009-001, CERN, 2009.

[108] B Cure, "Study of a 5-Tesla large aperture coil for the CLIC detector", LCD-Note 2011-007, CERN, 2011.

[109] C. Grah et al., "Polycrystalline CVD diamonds for the beam calorimeter of the ILC",
IEEE Trans.Nucl.Sci. 56 (2009) pp. 462–467, DOI: 10.1109/TNS.2009.2013853.

[110] D. Dannheim and A. Sailer, "Beam-induced Backgrounds in the CLIC Detectors",
LCD-Note 2011-021, CERN, 2011.

[111] A. Sailer, "Radiation and Background Levels in a CLIC Detector due to Beam-Beam Effects", to appear, PhD thesis, Humboldt-Universität zu Berlin, 2012.

[112] M. Moretti, T. Ohl, and J. Reuter, "O'Mega: An Optimizing matrix element generator" (2001), arXiv:hep-ph/0102195 [hep-ph].

[113] T. Sjostrand, S. Mrenna, and P. Z. Skands, "PYTHIA 6.4 Physics and Manual", *JHEP* 05 (2006), hep-ph/0603175 p. 026, DOI: 10.1088/1126-6708/2006/05/026.

[114] M. Berggren, "Tuning PYTHIA", 2010, URL: http://indico.cern.ch/contributionDisplay.py?contribId=3&confId=113752.

[115] Z. Was, "TAUOLA the library for tau lepton decay, and KKMC/KORALB/KORALZ/... status report", *Nucl. Phys. Proc. Suppl.* 98 (2001), hep-ph/0011305 pp. 96–102, DOI: 10.1016/S0920-5632(01)01200-2.

[116] *StdHep*, URL: http://cepa.fnal.gov/psm/stdhep.

[117] D. Schulte et al., "CLIC simulations from the start of the linac to the interaction point", CLIC-Note-529.

[118] T. Barklow et al., "Simulation of $\gamma\gamma$ to hadrons background at CLIC", LCD-Note 2011-020, CERN, 2011.

[119] N. Graf and J. McCormick, "Simulator for the linear collider (SLIC): A tool for ILC detector simulations", *AIP Conf. Proc.* 867 (2006) pp. 503–512, DOI: 10.1063/1.2396991.

[120] *SLIC*, URL: http://www.lcsim.org/software/slic.

[121] S. Agostinelli et al., "GEANT4: A Simulation toolkit", *Nucl.Instrum.Meth.* A506 (2003) pp. 250–303, DOI: 10.1016/S0168-9002(03)01368-8.

[122] J. Allison et al., "Geant4 developments and applications", *IEEE T. Nucl. Sci.* 53.1 (2006) pp. 270–278, DOI: 10.1109/TNS.2006.869826.

[123] F. Gaede et al., "LCIO: A Persistency framework for linear collider simulation studies", *Conference for Computing in High-Energy and Nuclear Physics*, La Jolla, CA, 2003, arXiv:physics/0306114 [physics].

[124] *LCIO*, URL: http://lcio.desy.de.

[125] S. Piperov, "Geant4 validation with CMS calorimeters test-beam data" (2008), arXiv:0808.0130 [physics.ins-det].

[126] V. Ivanchenko et al., "Recent Improvements in Geant4 Electromagnetic Physics Models and Interfaces", *Prog. in Nucl. Science and Tech.* 2 (2011) pp. 898–903.

[127] H. W. Bertini, "Low-Energy Intranuclear Cascade Calculation", *Phys. Rev.* 131.4 (1963) pp. 1801–1821, DOI: 10.1103/PhysRev.131.1801.

[128] G. Folger, V. N. Ivanchenko, and J. P. Wellisch, "The Binary Cascade - Nucleon nuclear reactions", *Eur. Phys. J. A* 21 (2004) pp. 407–417, DOI: 10.1140/epja/i2003-10219-7.

[129] V. Toneev, A. Amelin, and K. Gudima, "The Independent Quark-Gluon String Model for Heavy Ion Collisions ar Ultrelativistic Energies", GSI-89-52, Darmstadt, Germany, 1989.

[130] G. Folger and J. Wellisch, "String parton models in GEANT4", *Conference for Computing in High-Energy and Nuclear Physics*, La Jolla, CA, 2003, arXiv:nucl-th/0306007 [nucl-th].

[131] P. V. Degtyarenko, M. V. Kosov, and H. P. Wellisch, "Chiral invariant phase space event generator. I: Nucleon antinucleon annihilation at rest", *Eur. Phys. J.* A8 (2000) pp. 217–222, DOI: 10.1007/s100500070108.

[132] P. Degtyarenko, M. Kossov, and H. Wellisch, "Chiral invariant phase space event generator. II: Nuclear pion capture at rest and photonuclear reactions below the Delta(3,3) resonance", *Eur.Phys.J.* A9 (2000) pp. 411–420, DOI: 10.1007/s100500070025.

[133] P. Degtyarenko, M. Kossov, and H. Wellisch, "Chiral invariant phase space event generator. III: Modeling of real and virtual photon interactions with nuclei below pion production threshold", *Eur.Phys.J.* A9 (2000) pp. 421–424, DOI: 10.1007/s100500070026.

[134] GEANT4 Collaboration, *Physics Reference Manual*, 2011, URL: http://geant4.web.cern.ch/geant4/UserDocumentation/UsersGuides/PhysicsReferenceManual/fo/PhysicsReferenceManual.pdf.

[135] *Linear Collider simulations*, URL: http://lcsim.org/software/lcsim/1.18.

[136] *SiSim Digitization*, URL: http://www.lcsim.org/software/lcsim/1.18/apidocs/org/lcsim/recon/tracking/digitization/sisim/package-summary.html.

[137] M. Krammer and H. Pernegger, "Signal collection and position reconstruction of silicon strip detectors with 200-micrometer readout pitch", *Nucl.Instrum.Meth.* A397 (1997) pp. 232–242, DOI: 10.1016/S0168-9002(97)00802-4.

[138] G. F. Knoll, *Radiation detection and measurement*, 4th ed., New York, NY: Wiley, 2010.

[139] E. van der Kraaij and B. Schmidt, "Muon System Design Studies for Detectors at CLIC", LCD-Note 2011-008, CERN, 2011.

[140] *SeedTracker Algorithm*, URL: http://www.lcsim.org/software/lcsim/1.18/apidocs/org/lcsim/recon/tracking/seedtracker/SeedTracker.html.

[141] D. Onoprienko and E. von Toerne, "Calorimeter assisted tracking algorithm for SiD", *International Linear Collider Workshop*, Hamburg, Germany, 2007, arXiv:0711.0134 [physics.ins-det].

[142] V. Karimaki, "Effective circle fitting for particle trajectories", *Nucl.Instrum.Meth.* A305 (1991) pp. 187–191, DOI: 10.1016/0168-9002(91)90533-V.

[143] J. Marshall, "Redesign of PandoraPFA", *International Workshop on Future Linear Colliders*, Geneva, 2010.

[144] E. van der Kraaij and J. Marshall, "Development of the PANDORA PFA NEW muon reconstruction algorithm", LCD-Note 2011-004, CERN, 2011.

[145] *PFOSelector Algorithm*, URL: http://www.lcsim.org/software/lcsim/1.18/apidocs/org/lcsim/recon/util/PfoSelector.html.

[146] F. Simon, C. Soldner, and C. Joram, "Direct Coupling of SiPMs to Scintillator Tiles for Imaging Calorimetry and Triggering" (2010), arXiv:1011.5033 [physics.ins-det].

[147] *Truth Linker Algorithm*, URL: http://www.lcsim.org/software/lcsim/1.18/apidocs/org/lcsim/recon/util/McTruthLinker.html.

[148] J. P. Wellisch, "Object-oriented software for low-energy neutron reactions", *Conference on High Energy Physics*, Chicago, USA, 1998.

[149] P. Speckmayer, "Impact of the Choice of Physics List on GEANT4 Simulations of Hadronic Showers in Tungsten", LCD-Note 2010-002, CERN, 2010.

[150] F. Simon, "Operational Experience and First Results with a Highly Granular Tungsten Analog Hadron Calorimeter" (2011), arXiv:1111.5132 [physics.ins-det].

[151] F. Simon, "Measurements of the Time Structure of Hadronic Showers in a Scintillator-Tungsten HCAL" (2011), arXiv:1109.3143 [physics.ins-det].

[152] M. Hoppner and D. Wegener, "Applications of neural networks to shower analysis in a highly segmented LAr calorimeter", *Nucl.Instrum.Meth.* A389 (1997) pp. 154–156, DOI: 10.1016/S0168-9002(97)00068-5.

[153] J. Damgov and L. Litov, "Application of neural networks for energy reconstruction", *Nucl.Instrum.Meth.* A482 (2002) pp. 776–788, DOI: 10.1016/S0168-9002(01)01851-4, arXiv:hep-ex/0012003 [hep-ex].

[154] P. da Silva and J. de Seixas, "Energy reconstruction for a hadronic calorimeter using neural networks", *Nucl.Instrum.Meth.* A559 (2006) pp. 124–128, DOI: 10.1016/j.nima.2005.11.130.

[155] A. Hoecker et al., "TMVA - Toolkit for Multivariate Data Analysis", *PoS* ACAT (2007) p. 040, arXiv:physics/0703039 [PHYSICS].

[156] M. Chadeeva et al., "Hadron Energy Resolution of the CALICE AHCAL and Software Compensation Approaches" (2012), arXiv:1202.6184 [physics.ins-det].

[157] I. Marchesini, "Shower Leakage in a Highly Granular Calorimeter", CAN-029, CALICE, 2011.

[158] CALICE Collaboration, "Shower development of particles with momenta from 1 to 10 GeV in the CALICE Scintillator-Tungsten HCAL", CAN-036, CALICE, 2012.

[159] J. Marshal, A. Münnich, and M. Thomson, "Particle Flow Performance at CLIC", LCD-Note 2011-028, CERN, 2011.

[160] S. Catani et al., "Longitudinally invariant K_t clustering algorithms for hadron hadron collisions", *Nucl.Phys.* B406 (1993) pp. 187–224, DOI: 10.1016/0550-3213(93)90166-M.

[161] L. Weuste and F. Simon, "Mass and Cross Section Measurements of light-flavored Squarks at CLIC", LCD-Note 2011-027, CERN, 2011.

[162] W. Verkerke and D. P. Kirkby, "The RooFit toolkit for data modeling", *Conference for Computing in High-Energy and Nuclear Physics*.

[163] K. Desch and M. Battaglia, "Determination of the Higgs profile: HFITTER", *AIP Conf. Proc.* 578 (2000) pp. 312–316.

[164] M. Rauch, "Determination of Higgs-boson couplings (SFitter)" (2012), arXiv:1203.6826 [hep-ph].

[165] T. Plehn and D. L. Rainwater, "Higgs decays to muons in weak boson fusion", *Phys.Lett.* B520 (2001) pp. 108–114, DOI: 10.1016/S0370-2693(01)01157-1, arXiv:hep-ph/0107180 [hep-ph].

[166] T. Han and B. McElrath, "$h \to \mu^+\mu^-$ via gluon fusion at the LHC", *Phys.Lett.* B528 (2002) pp. 81–85, DOI: 10.1016/S0370-2693(02)01208-X, arXiv:hep-ph/0201023 [hep-ph].

[167] K. Cranmer and T. Plehn, "Maximum significance at the LHC and Higgs decays to muons", *Eur.Phys.J.* C51 (2007) pp. 415–420, DOI: 10.1140/epjc/s10052-007-0309-4, arXiv:hep-ph/0605268 [hep-ph].

[168] M. Battaglia, "Testing the Higgs Mechanism in the Lepton Sector with multi-TeV e+e- Collisions", *J. Phys.* G35 (2008) p. 095005, DOI: 10.1088/0954-3899/35/9/095005, arXiv:0807.1299 [hep-ex].

[169] T. Kramer, "Track parameters in LCIO", LC-DET-2006-004, 2006.

[170] J. Alcaraz, "Helicoidal Tracks", L3 Internal Note 1666, 1995.

[171] M. Regler and R. Fruhwirth, "Generalization of the Gluckstern formulas. I: Higher orders, alternatives and exact results", *Nucl.Instrum.Meth.* A589 (2008) pp. 109–117, DOI: 10.1016/j.nima.2008.02.016.

List of Figures

2.1 Feynman diagrams of the dominant Higgs production processes at an e^+e^- collider. . . 11
2.2 Higgs production cross section in the Standard Model. 12
2.3 Higgs branching ratios in the Standard Model. 12

3.1 Schematic view of the CLIC layout for a center-of-mass energy of 3 TeV. 19
3.2 Feynman diagrams of the coherent pair production and trident pair production processes. 20
3.3 Feynman diagrams of the most important processes that contribute to the incoherent pair production. 20
3.4 Distribution of the energy and the polar angle of the particles from beam-induced backgrounds. 21
3.5 Time structure of the beams at ILC and CLIC. 22
3.6 Luminosity spectrum at CLIC for a nominal center-of-mass energy of 3 TeV. 24

5.1 One quadrant of the CLIC_SiD_CDR detector model. 38
5.2 Coverage of the tracking systems with respect to the polar angle θ. 39
5.3 Layout of the tracking system in CLIC_SiD. 40
5.4 Layout of the vertex barrel detector in CLIC_SiD in the xy-plane. 41
5.5 Layout of the vertex region in CLIC_SiD in the zy-plane. 41
5.6 The material budget in the tracking region of CLIC_SiD. 45
5.7 Cut through the barrel region of the calorimeter in CLIC_SiD. 46
5.8 Layout of the forward region in CLIC_SiD. 48
5.9 Time dependence of the hit densities in the vertex barrel layers from incoherent pairs. . 50
5.10 Hit densities from incoherent pair background in the innermost vertex endcap layer depending on x and y. 51
5.11 Hit densities in the vertex barrel layers from incoherent pairs and the $\gamma\gamma \rightarrow$ hadrons background depending on z. 52
5.12 Hit densities in the main tracker barrel layers from incoherent pairs and the $\gamma\gamma \rightarrow$ hadrons background depending on z. 52
5.13 Hit densities in the vertex endcap layers from incoherent pairs and the $\gamma\gamma \rightarrow$ hadrons background depending on r. 53
5.14 Hit densities in the forward tracking pixel disks from incoherent pairs and the $\gamma\gamma \rightarrow$ hadrons background depending on r. 53
5.15 Hit densities in the main tracker endcap layers from incoherent pairs and the $\gamma\gamma \rightarrow$ hadrons background depending on r. 54
5.16 Distribution of the sizes of the reconstructed clusters in the tracking detectors. 55

6.1 Example of a bunch train structure created by the *OverlayDriver*. . . . 61
6.2 Time structure of the hits in the barrel detectors with and without applying readout time windows. . . . 62
6.3 Illustration of the charge deposition in the sensitive material of silicon detectors as simulated in the tracker hit digitization. . . . 65

7.1 Momentum resolution of single muons depending on the momentum and the polar angle. 74
7.2 Δp_T-distribution and pull distribution for single muons. . . . 75
7.3 Momentum resolution of single muons depending on the momentum and the polar angle. 75
7.4 Angular track resolutions for single muons. . . . 76
7.5 Impact parameter d_0 resolution for single muons. . . . 77
7.6 Impact parameter z_0 resolution for single muons depending on the polar angle. . . . 77
7.7 Distribution of polar angles and of transverse momenta of findable particles in jet events. 78
7.8 Distribution of number of findable particles and the distance to the closest hit in jet events. 78
7.9 Momentum resolution in di-jet events for different numbers of false hits. . . . 80
7.10 Impact parameter resolution in di-jet events for different numbers of false hits. . . . 80
7.11 Tracking efficiency for reconstructed tracks with different numbers of false hits in di-jet events. . . . 81
7.12 Tracking efficiency for different minimum hits requirements in di-jet events. . . . 82
7.13 Tracking efficiency for different χ^2_{max} requirements in di-jet events. . . . 82
7.14 Tracking efficiency in di-jet events with and without $\gamma\gamma \rightarrow$ hadrons background. . . . 83
7.15 Tracking efficiency depending on the distance to the closest hit. . . . 83
7.16 Algorithmic tracking efficiency in di-jet events. . . . 84
7.17 Fake rate in di-jet events with and without $\gamma\gamma \rightarrow$ hadrons background. . . . 85
7.18 Number of false hits on a track and track purity in di-jet events. . . . 85

8.1 Energy resolution for π^+ depending on the true particle energy for different tungsten absorber thicknesses. . . . 91
8.2 Linearity for π^+ depending on the true particle energy for different tungsten absorber thicknesses. . . . 92
8.3 Energy resolution for π^+ depending on the true particle energy for different steel absorber thicknesses. . . . 92
8.4 Linearity for π^+ depending on the true particle energy for different steel absorber thicknesses. . . . 93
8.5 Energy resolution for π^+ with an energy of 250 ± 20 GeV depending on the calorimeter depth for tungsten calorimeters. . . . 94
8.6 Energy resolution for π^+ with an energy of 250 ± 20 GeV depending on the calorimeter depth for steel calorimeters. . . . 94
8.7 Energy resolution for π^+ depending on the true particle energy for a calorimeter with tail catcher. . . . 95

9.1 Linearity for single neutral particles in the CLIC_SiD detector . . . 99
9.2 Energy resolution for single neutral particles in the CLIC_SiD detector. . . . 100
9.3 PFA response for single jets in di-jet decays depending on the jet energy. . . . 102
9.4 Calorimeter response for single jets in di-jet decays depending on the jet energy. . . . 102
9.5 Distribution of the reconstructed energy in di-jet decays depending on the jet energy. . . 103

9.6 Calorimeter response for single jets in di-jet decays depending on the polar angle of the jet. . . . 103

10.1 Feynman diagram of the Higgs production through W^+W^- fusion with the Higgs decaying into two muons. . . . 107
10.2 Polar angle distribution and reconstruction efficiency of the muons in $H \to \mu^+\mu^-$ events. 108
10.3 Correlation matrices for the kinematic variables used in the boosted decision tree classifier. 110
10.4 Response of the boosted decision tree classifier and resulting significance, purity, signal efficiency and background efficiency . . . 110
10.5 Distribution of the invariant mass of the di-muon system before and after the event selection. . . . 111
10.6 Distributions of kinematic variables before and after the event selection. . . . 112
10.7 Distributions of kinematic variables before and after the event selection. . . . 113
10.8 Distribution of the true transverse momentum of the di-muon system. . . . 114
10.9 Invariant mass distributions for signal and background events with fitted PDFs. . . . 115
10.10 Fit of the Higgs mass peak and pull distribution of the toy Monte Carlo. . . . 116
10.11 Kinematic variables with and without overlay of the $\gamma\gamma \to$ hadrons background. . . . 118
10.12 Impact of the $\gamma\gamma \to$ hadrons background on E_{vis} and on the muon reconstruction efficiency. 119
10.13 Response of the boosted decision tree classifier when including the $\gamma\gamma \to$ hadrons background. . . . 119
10.14 Momentum resolution of the muons depending on their polar angle and their transverse momentum. . . . 121
10.15 Di-muon invariant mass distribution and relative statistical uncertainty on the cross section times branching ratio measurement depending on the momentum resolution. . . . 121
10.16 Angular distributions of the electrons in $e^+e^- \to \mu^+\mu^-e^+e^-$. . . . 123
10.17 Angular distributions of the electrons in $e^+e^- \to \mu^+\mu^-e^+e^-$ with respect to the outgoing beam axis. . . . 123
10.18 Energy distributions of the electrons in $e^+e^- \to \mu^+\mu^-e^+e^-$ events. . . . 124
10.19 Relative statistical uncertainty on the $h \to \mu^+\mu^-$ cross section times branching ratio measurement depending on the integrated luminosity. . . . 126
10.20 Response of the boosted decision tree classifier in case of the LumiCalCut_{95} . . . 126
10.21 Response of the boosted decision tree classifier in case of the LumiCalCut_{99} . . . 127
10.22 Response of the boosted decision tree classifier in case of the BeamCalCut_{30} . . . 127
10.23 Response of the boosted decision tree classifier in case of the BeamCalCut_{70} . . . 128
10.24 Feynman diagrams of the Higgs production processes at the LHC suitable for measuring Higgs decays into muons. . . . 130

C.1 Illustration of the track parameters as defined in LCIO. . . . 144

D.1 Fake rate depending on the transverse momentum and the polar angle in $t\bar{t}$ events. . . . 147
D.2 Fake rate depending on the transverse momentum and the polar angle in $t\bar{t}$ events. . . . 148

List of Tables

2.1 Fermions in the Standard Model. 8

3.1 Parameters of the default CLIC layout for $\sqrt{s}$ = 3 TeV. 23

5.1 Parameters for the main elements of the CLIC_SiD_CDR detector model. 38
5.2 Parameters for the vertex detector barrel layers. 41
5.3 Parameters for the vertex endcap and forward tracking disks. 42
5.4 Parameters for the barrel tracker layers. 43
5.5 Materials in the tracker barrel modules. 43
5.6 Parameters for the tracker endcap disks in CLIC_SiD. 44
5.7 Parameters of the coil elements. 47

6.1 Correction factors used for the calculation of the tracker hit uncertainty. 65
6.2 One set of cuts used for the PFO selection at CLIC. 70

7.1 Transverse momentum resolution in CLIC_SiD for single muons. 74

8.1 List the HCal geometries used for calorimeter optimization. 88

9.1 Electromagnetic and hadronic sampling fractions used for the different calorimeters in CLIC_SiD. 98
9.2 Correction to the reconstructed particle energy to improve the linearity in CLIC_SiD. . 100
9.3 Energy resolution for single neutral particles in CLIC_SiD. 101

10.1 List of processes considered for the $h \to \mu^+\mu^-$ analysis. 106
10.2 Selection efficiencies forthe pre-selection cuts. 109
10.3 Summary of the results for the $h \to \mu^+\mu^-$ branching ratio measurement. 117
10.4 Summary of the results for the $h \to \mu^+\mu^-$ branching ratio measurement with $\gamma\gamma \to$ hadrons background overlaid. 120
10.5 Summary of the results for the $h \to \mu^+\mu^-$ branching ratio measurement for different momentum resolutions. 122
10.6 Event selection cuts for removing $e^+e^- \to \mu^+\mu^-e^+e^-$ events based on the electron angles. 124
10.7 Summary of the results for the $h \to \mu^+\mu^-$ branching ratio measurement assuming different electron tagging efficiencies in the forward calorimeters. 125